The rheological complexity of waxy crude oils: Yielding, thixotropy and shear heterogeneities

by

Christopher J. Dimitriou

B.S., Massachusetts Institute of Technology (2008)
S.M., Massachusetts Institute of Technology (2010)

Submitted to the Department of Mechanical Engineering
in partial fulfillment of the requirements for the degree of

Doctor of Philosophy in Mechanical Engineering

at the

MASSACHUSETTS INSTITUTE OF TECHNOLOGY

June 2013

Author .....
Department of Mechanical Engineering
April 23, 2013

Certified by .....
Gareth H. McKinley
Professor, Mechanical Engineering
Thesis Supervisor

Accepted by .....
David E. Hardt
Chairman, Department Committee on Graduate Students

The rheological complexity of waxy crude oils: Yielding, thixotropy and shear heterogeneities

by

Christopher J. Dimitriou

Submitted to the Department of Mechanical Engineering
on April 23, 2013, in partial fulfillment of the
requirements for the degree of
Doctor of Philosophy in Mechanical Engineering

Abstract

Precipitate-containing crude oils are of increasing economic importance, due to diminishing oil reserves and the increased need to extract hydrate and wax-containing crude oil from ultra deep-water resources. Despite this need, the rheological behavior of these types of crude oil is often poorly understood. In this thesis, we investigate some of the underlying complexities associated with the rheology of waxy crude oils. These complex phenomena are often difficult to both quantify experimentally and capture with existing constitutive models. The contribution of this thesis is therefore to develop a detailed understanding of three of these particular phenomena, through the development and use of several new experimental and theoretical tools. A better understanding of waxy crude oil rheology is critical for developing flow assurance strategies, which can in turn ensure continuous production of precipitate-containing crude oils under adverse conditions.

The three phenomena studied are, first: shear heterogeneities, i.e. the manifestation of wall slip, shear banding or other shear-localization events under imposed deformations that are assumed to be homogenous. For these purposes, flow visualization techniques capable of "Rheo-PIV" measurements are developed to detect these heterogeneities. Second: elasto-viscoplasticity, or the presence of an elastic response and a yield-like behavior in a non-Newtonian fluid. Constitutive modeling of this type of behavior is difficult to achieve using standard linear viscoelastic techniques, where the viscoelastic response is decomposed into a finite number of linear elements with a spectrum of relaxation times. For these reasons, additional concepts are adopted from plasticity models in order to describe this behavior. Finally: thixotropy, which refers to the ability of a fluid to continuously evolve, or age at rest and shear rejuvenate under a constant applied shear rate. A rigorous set of experimental tests is constructed which allow for the appropriate constitutive model parameters to be determined for a thixotropic fluid.

Through quantitative study of these phenomena, we reach several conclusions about how to characterize and model the rheology of a precipitate-containing crude oil. First, measurements of shear heterogeneities are important in these fluids, so

that rheological characterization may proceed with a knowledge of when these may arise and introduce artifacts into data. Second, new nonlinear rheometric techniques are necessary to develop quantitative data sets that describe the inherently nonlinear rheology of these fluids. The specific technique developed in this work is termed stress-controlled large amplitude oscillatory shear, or LAOStress. Finally, we show that the constitutive behavior of these materials is best prescribed using a framework which utilizes yielding and hardening mechanisms from plasticity theory. The resulting constitutive model for this nonlinear elasto-viscoplastic and thixotropic class of materials is expressed in a closed form that can be used in existing flow assurance simulation tools.

The most relevant applications for this work are in the flow assurance challenges associated with crude oil production. Consequently, a large portion of the experimental work is carried out on a model waxy crude oil, containing a total wax content ranging from 5 to 10% by weight. However the phenomena studied here occur ubiquitously in a number of complex fluids. For this reason, the same rheological complexities are studied in the context of several other fluids, including a swollen microgel paste (Carbopol) and a shear-banding wormlike micellar solution.

Thesis Supervisor: Gareth H. McKinley
Title: Professor, Mechanical Engineering

Acknowledgments

The work in this thesis would not have been possible without the support (both emotional and scientific) from a number of different individuals:

Gareth has been a superb advisor over the course of my graduate studies - Not only is he a great guy, but his enthusiasm for research has been a source of inspiration. After 5 years, I have finally internalized what the PhD is all about - learning to independently identify a research problem you find interesting, and taking the initiative (on your own) to solve it. Having an advisor as good as Gareth, who realizes that this is an integral part of the process, makes that piece of paper you get at the end seem all the more valuable.

I also have to thank the different groups of friends that I have made since starting at MIT as an undergrad. My most fond memories from the undergrad days are those with fellow sixers, many of whom I still keep in touch with to the present day. Whenever we hang out it seems like zero time has elapsed since we left that great place a number of years ago.

More recently, the friends I have made in the HML/NNF lab have been a great group to hang out with. Fun times were always being had, whether it was getting a beer at the Miracle while analyzing the story of the Dude, hiking up in the mountains of NH, or just shooting the breeze between experiments.

I've also had the good luck to climb with a number of different people over the past few years. Those experiences were always fun, but most importantly, I have always been able to count on them giving me perspective to what is and what is not important in my own life. I'm glad to have shared them with such a cool bunch of people.

My family has been an amazing source of support over the past 9 years since I moved to Boston - they have always been behind me with the decisions I've made, and for that I am extremely grateful. My days at MIT would undoubtedly been much harder without them being there for me, so they deserve a lot of credit for that and should be proud!

Finally, over the past 8 years I have always been able to rely on Angie being there for me. We both know how intense the whole PhD process can be, and I have always valued your perspective on it the most. And now that it's over, I'm excited about starting our new lives together!

Contents

List of Figures

List of Tables

Chapter 1

Motivation & Scope of Thesis

1.1 Motivation

Petroleum (or crude oil) is a widely traded and important commodity in the global economy, and in the context of petroleum production, the rheological response of structured fluids can play a very important role. While in many cases crude oil itself exhibits highly non-Newtonian flow behavior, there are also other fluids which are of interest to rheologists in the field of petroleum engineering. For example, drilling fluids are often designed in order to exhibit a wide range of complex rheological behaviors, from thixotropy to elasto-viscoplastic yield-like behavior at large deformations [30]. Non-Newtonian surfactant solutions are frequently utilized in enhanced oil recovery scenarios [9] in order to maximize output from a particular oilfield. In order for these fluids to be of use to the practicing petroleum engineer, a working knowledge of their rheology is required.

The problem of understanding the rheology of these fluids is of greater relevance today than ever before. Predictions made in the mid-20th century such as those by Hubbert showed that the production of crude oil within a given region would follow a bell shaped curve which, after peaking, would decrease slowly over time [102]. While Hubbert's peak theory predicts that eventually global production of crude oil will reach a peak, the point in time at which this peak will occur is still unclear - although estimates are typically on the order of several decades [40]. One of the reasons for

the peak point being difficult to predict is that modern oil exploration techniques have been uncovering new reserves of petroleum in remote locations [49]. As the technology used to both find these reserves and extract oil in more efficient manners continues to develop, total global production of oil can continue to grow. Hence, a significant segment of the oil industry today is focused solely on developing technology that both allows extraction of crude oil from remote reserves, but also allows more efficient extraction of petroleum from current and future reserves. Complex fluids and smart material systems will feature heavily in these developments.

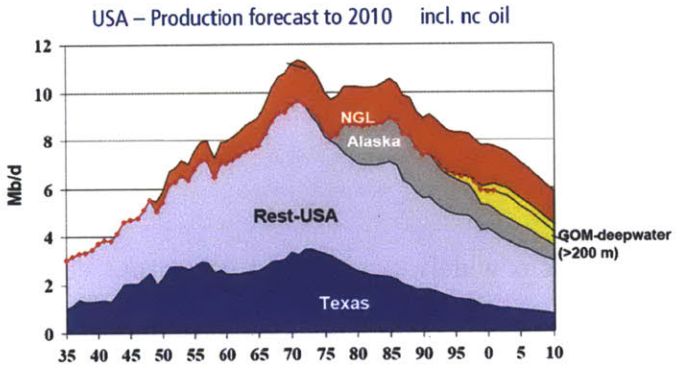

Figure 1-1: Production of crude oil in the United States, shown for different sources. Image from a paper by Tsoskounogiou [200]. Total production peaked in the 1970's, while deepwater production has seen an increase in the past decade

In this context, the rheological characterization of *precipitate-containing* crude-oils is of increased importance. Precipitate-containing oils tend to exhibit highly non-Newtonian flow behavior, due to the inherent microstructure associated with the presence of a number of possible solid phases. The most commonly encountered precipitates are waxes, hydrates (or clathrates) and asphaltenes [195, 27]. In the case of ultra-deep water oil production, precipitates such as waxes may pose significant problems towards the goal of ensuring continuous flow of the fluid from a reserve. In particular, the fluid may experience large drops in temperature due to the cool ambient sea-water and extremely long pipelines (several kilometers) [47], resulting in a waxy crude oil being cooled to below its wax appearance temperature, denoted T_{wa}. Once the waxy crude is cooled to below T_{wa}, it may form an viscoelastic gel, and much larger pressure drops are then required in order to ensure the same flow

rate. This issue is often so problematic that field workers will insulate and/or heat pipelines to prevent this cooling from occurring [27].

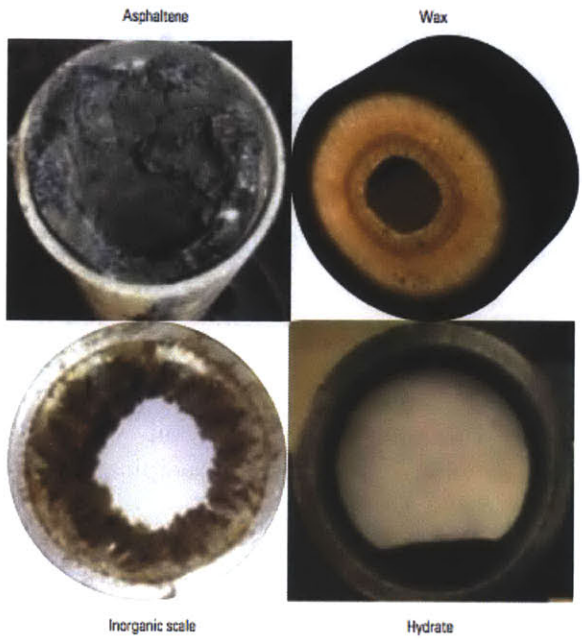

Figure 1-2: Images from [27] showing the effect that various types of precipitates may have on a pipeline cross-section.

Within the oil industry, there is an entire sub-discipline that deals with the problems encountered while attempting to ensure the continuous flow of crude oil through production lines. This research area is called *Flow Assurance* [8, 49]. Many of the problems flow assurance specialists must deal with are associated with preventing the occurrence of a gelled pipeline. A gelled pipeline may occur in the case where the temperature of the crude oil drops locally (near the wall) below a given point at which wax, or other precipitates begin to form. Gelled waxy crude oils often exhibit rheological behavior akin to yield stress fluids. Specifically, there exists a critical stress, or range of stresses, beyond which the viscosity of the gelled system decreases by several orders of magnitude, but below which no flow occurs [18]. Thus, in order to restart flow of a gelled pipeline, a pressure larger than the typical operating pressure is required to exceed the yield stress of the fluid at the wall. However, due to a lack of appropriate rheological constitutive equations for these types of fluids, current flow assurance strategies tend to be overly conservative, and thus too costly of an option

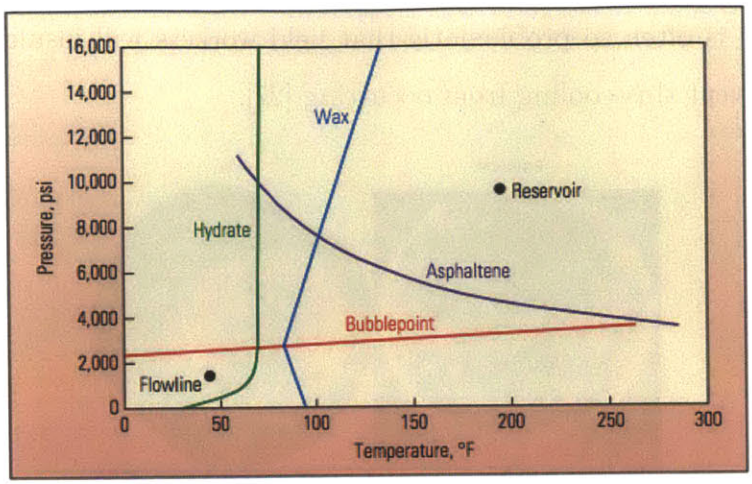

Figure 1-3: Figure from [27] showing the phase boundaries for different types of precipitates for a typical Gulf of Mexico crude oil. Typical flow lines operate at temperatures and pressures where all of these precipitates may be present

to make oil production under adverse conditions viable [175]. A better understanding of the thermorheological behavior of waxy crude oils would facilitate the improvement of these strategies. One of the main limitations of current flow assurance strategies is that they are based on simple empirical models that describe the rheological behavior of precipitate-containing production fluids. An in-depth experimental approach, that would uncover how the rheology of these fluids is affected by the presence of precipitates, would therefore be of great practical importance.

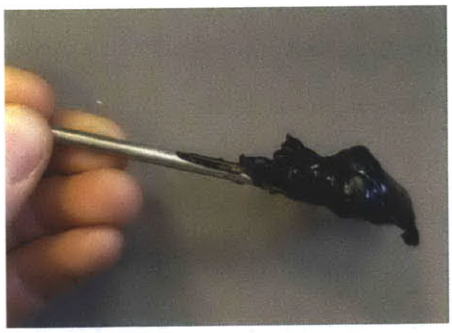

Figure 1-4: Image of a typical waxy crude oil below its wax appearance temperature T_{wa} (sample provided by Chevron). The material clearly holds its shape and does not flow - behavior indicative of a yield stress fluid.

Rheology - which is the study of how materials flow and deform, relies on well-defined experimental techniques and protocols. For example, a linear viscoelastic

material, which exhibits behavior intermediate to that of a solid and liquid, can be characterized using a number of techniques in the rheologist's toolbox. Small amplitude oscillatory shear can be used to extract quantitative measures that characterize both elastic behavior and viscous behavior. Creep tests or stress relaxation tests can be used to extract creep compliances and relaxation moduli respectively. Equally important to these experimental techniques are the quantitative material functions which can be extracted from the specific experimental protocol. An important component of the study of complex fluids is therefore *rheometry*, which broadly encompasses the development of specific experimental techniques and quantitative material measures for characterizing the rheology of a particular material.

However, one of the issues faced when dealing with highly nonlinear materials, such as those encountered in the petroleum industry, is that complexities may arise in their response to deformations that render traditional rheometric approaches of either limited use or no use whatsoever. For example, a typical rheometer will deform a material and extract material measures (such as a viscosity, or modulus) based on an assumption about the homogeneity of the underlying kinematic field within the material [29]. These assumptions may break down with highly nonlinear materials which are known to experience shear heterogeneities under configurations which impose a (nominally) spatially homogenous stress distribution. The framework of small amplitude oscillatory shear (SAOS) mentioned previously assumes that deformations are in the linear range of material behavior. For wax-oil mixtures this assumption may only hold for a very small range of applied strains. Thixotropy [17] can introduce artifacts in rheological data which are difficult to account for in constitutive models.

These types of behaviors are the main focus of this thesis and they are broadly referred to as "complex phenomena". They all have the distinction of requiring advanced rheometric techniques to study and are frequently encountered in the rheological response of precipitate-containing crude oils. However these phenomena are also interesting from a fundamental viewpoint, as their study may lead towards a deeper and fuller understanding of the nonlinear rheology of a whole range of complex fluids. The main goal of this thesis will be to develop quantitative experimental

and analytical tools to study these phenomena. In some cases, we go as far as to formulate constitutive equations which encapsulate the essential features associated with these phenomena. The particular equations are immediately relevant to industrial processes involving crude oil, however we also anticipate that the framework (experimental, theoretical, constitutive) used throughout this thesis will be useful in non-petroleum related industrial applications where these complex phenomena may arise.

1.2 Scope of thesis & Roadmap

This thesis will deal with three particular complex phenomena, and is therefore divided into three parts. The first part concerns the study of "shear heterogeneities". The term shear heterogeneities will be used broadly to refer to the presence of non-idealities in the kinematics of flows which are nominally viscometric. For example, certain yield stress fluids are known to violate the no-slip condition [16], while other fluids may experience shear banding [128]. The study of these shear heterogeneities is included in Chapters 3-5, where these heterogeneities are studied in the context of surfactant-containing wormlike micellar solutions, as well as in a model waxy crude oil. The second principal contribution of this thesis consists of a study of "Elasto-Viscoplastic" behavior (abbreviated as EVP behavior), which entails the presence of a nonlinear yielding transition which may occur in some materials above a critical stress. Chapters 6-7 discuss this second rheological phenomenon in a model "yield stress fluid" that is commonly utilized by rheologists. The third and final part of this thesis concerns a study of thixotropy. Thixotropy generally refers to the ability of complex fluids to undergo a change in structure under the presence and absence of shear, and it is a commonly encountered phenomenon among structured fluids. Chapter 8 presents this study of thixotropic behavior in a model waxy crude oil.

Several new experimental and theoretical tools are developed throughout the course of this thesis. These include an experimental apparatus (a RheoPIV device) which allows for in-situ flow visualization to be performed on a sample whilst undergo-

ing imposed shearing (steady or transient) in a rheometer. We also develop techniques to quantify nonlinear viscoelasticity in these types of materials - specifically a framework is developed for carrying out stress controlled large amplitude oscillatory shear (LAOStress) measurements. Third, constitutive modeling tools are also adopted from the plasticity literature in order develop new models that can capture the complex thixotropic yielding behavior in non-Newtonian fluids.

Fig. 1-5 serves as a visual roadmap for the content that is contained within this thesis. The three main topics are in the outer circle, with the particular tools that are utilized/developed being placed in the inner circle. These tools are, for the most part, utilized in studying each of the three phenomena described here.

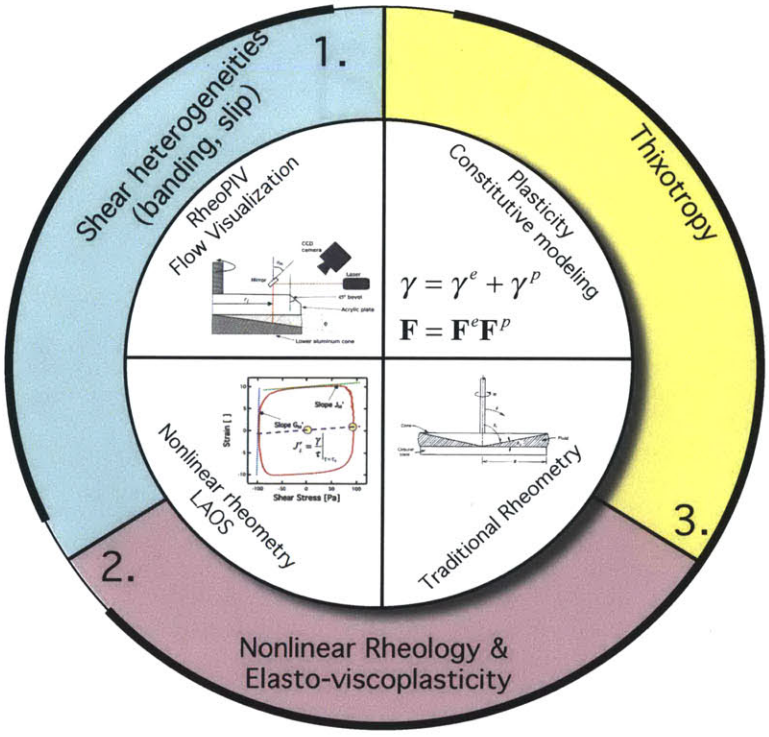

Figure 1-5: A visual overview of the topics covered in this thesis

Chapter 2

Background & Literature Review

2.1 Rheology of Waxy Crude Oils

Wax is a commonly occurring component of crude oil. It is generally characterized as consisting of large n-paraffins that are solid at room temperature when isolated, yet soluble in the crude oil mixture at elevated temperatures [195]. Waxy crude oils are crude oils with relatively high amounts of wax suspended in them [209]. The rheology of such materials is extremely sensitive to temperature, because at lowered temperatures it is possible for wax to precipitate out of the crude oil mixture and form a sample-spanning gel-like structure composed of crystallites with a high aspect ratio [203, 202]. The sample spanning network formed by these crystallites is akin to a physical gel network in which the correlation length has diverged towards infinity [213, 214], and the high aspect ratio of the crystallites allows for gelation to occur at low volume fractions of precipitated wax [167, 109, 108]. Some studies have also suggested that the gel structure formed by the precipitates is a fractal network [81].

In order to understand the yielding of these gel structures during a pipeline restart it is necessary to study the behavior of waxy crude oils at temperatures below the wax appearance temperature (T_{wa}), which can be defined as the temperature at which wax precipitates first begin to form in the mixture. The formation of these precipitates affects the flow of the resulting multiphase system. Several approaches have been taken towards understanding the impact of wax precipitates on the rheology of these

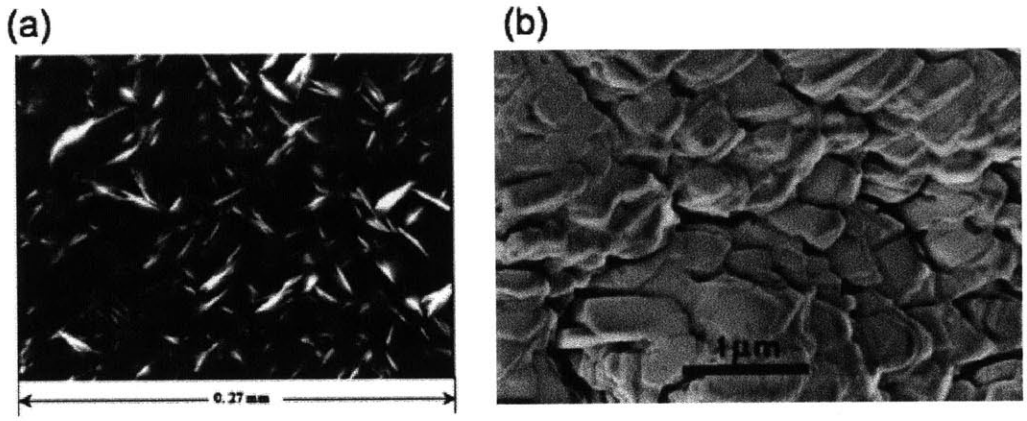

Figure 2-1: Microscopy images of wax precipitates in a paraffin gel reproduced from [202] in (a). The precipitates appear as bright in this image, and have a needle like shape. In (b), transmission electron microscopes of cryo-fractured wax precipitates are shown from [109]. In this image, the three dimensional discotic morphology of the precipitates is evident.

fluids and the practical applications thereof. Rheometric studies of waxy crude oils and waxy crude oil emulsions below their wax appearance temperature have been carried out by Visintin et al. [204, 205]. Visintin and coauthors demonstrated that waxy crude oils exhibit a strongly temperature-dependent yield stress (σ_y) when they are below their wax appearance temperature. The yield stress represents the stress which must be exceeded in order for the oil to exhibit steady flow and is important because it plays a critical role in determining the applied pressure drop required for restart of a gelled pipeline.

From data such as that presented by Visintin et al., it is relatively straightforward to obtain an estimate for the yield stress of a gelled waxy crude oil. However, it is not clear how the value of a bulk yield stress σ_y determines the pressure required to restart a gelled pipeline. For the restart of pipelines containing gelled waxy oil, complex spatial and temporal yielding behavior must be accounted for. Chang considered this type of yielding behavior by observing the different stages of a flow restart in an isothermal pipeline [46]. However, other factors may also affect restart behavior. For example, Perkins and Turner studied the restart behavior of gelled pipelines and determined that compressibility of the gel can play an important role in the

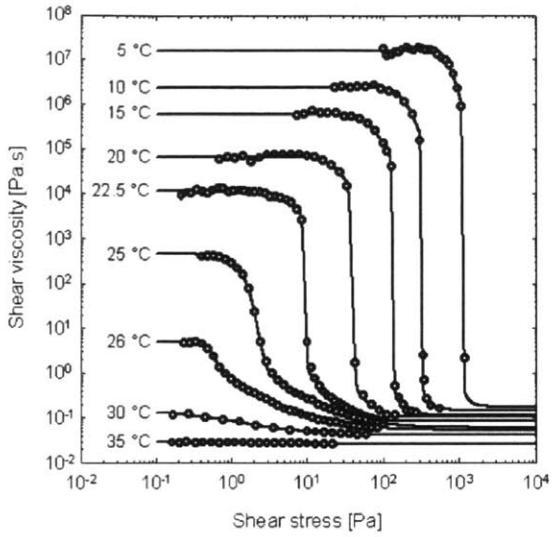

Figure 2-2: Plot from Visintin et al. [204] showing the narrow range of stresses over which the viscosity of a waxy crude oil gel drops considerably - this is indicative of a yielding behavior.

restart procedure [165]. Furthermore, Lee et al. have shown that it is possible for a gelled waxy crude oil to "break" or yield through either the mechanism of cohesive or adhesive failure [119]. These latter results suggest that when modeling the restart of a pipeline, the nature of the gel-wall interactions must be considered in detail as these can significantly affect the microstructure deformation processes that disrupt the gel.

The issue of determining a restart pressure from a simple measure of yield stress is also complicated by the fact that in most practical instances, the gel strength is not spatially uniform over the cross section of a pipe. This has been demonstrated by studying the process whereby wax precipitates deposit on pipeline walls. It is possible for waxes to "deposit" on the inner surface of a pipe if the temperature of the pipe wall is below the cloud point of the oil (or the wax appearance temperature T_{wa}) [191]. This incipient wax layer is the first step towards deposition of the gel on the pipe wall. The combined presence of spatial temperature gradients and diffusion of wax-forming molecules towards the cold wall has been shown to be responsible for the hardening of the wax deposits closest to the pipeline wall [192]. In addition to this, non-uniformity in cooling rates across a pipeline can result in a spatially non-homogenous gel.

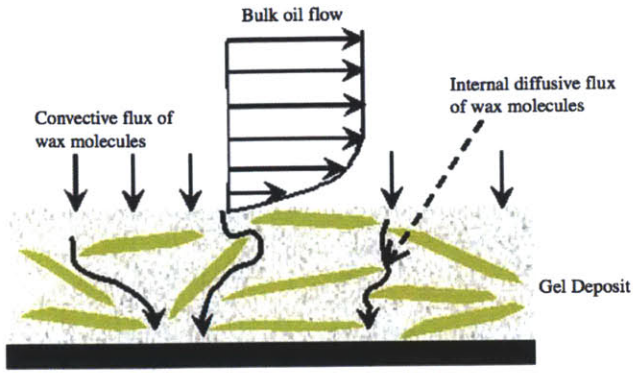

Figure 2-3: Diagram from Venkatesan et al. [202] showing the process whereby wax layers "deposit" on pipe walls due to the presence of a temperature gradient.

Even putting these considerations aside, substantial rheological complexity is still exhibited by homogenous waxy crude oils (i.e. oils that are formed under spatially homogenous temperatures). It is this rheological complexity that is the focus of this thesis, and we will separate this into three different phenomena. In what follows, we provide a review of past studies of each of these particular phenomena.

2.2 Shear heterogeneities (wall slip, banding)

One of the experimental tools most frequently used by rheologists is the cone and plate rheometer, which is shown schematically in Fig. 2-4. The main advantage of the cone and plate geometry (compared to say, a cylindrical Couette or plate-plate geometry) is that for small enough cone angles, the shear rate within the sample can be assumed to be spatially homogenous. As a result, the velocity profile is locally Couette-like everywhere, i.e. linear with a slope equal to the shear rate that the material is undergoing. Using this assumption, the viscosity of a fluid can be determined through the following equation:

$$\eta = \frac{3\mathcal{T}\Theta_0}{2\Omega\pi R^3} \tag{2.1}$$

Where $\mathcal{T}$ is the torque applied on the geometry, Ω is the angular rotation rate of the geometry, R is the geometry radius and Θ_0 is the cone angle.

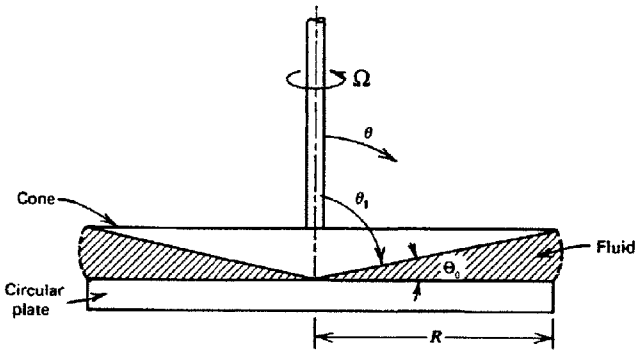

Figure 2-4: Diagram of a cone and plate geometry, reproduced from [29]

However, Eq. 2.1 no longer holds when the velocity field is not locally Couette-like or viscometric. This is known to occur in certain classes of non-Newtonian fluids. Throughout this thesis, we will generally use the term "shear heterogeneities" to refer to deviations from a Couette-like velocity profile with a spatially uniform shear rate.

2.2.1 Wall slip

Perhaps the first shear heterogeneity to be acknowledged in the rheology literature is wall slip, which was first studied by Mooney in 1931 [150]. Mooney acknowledged that wall slip is "in reality an abnormally large velocity gradient in a thin layer adjacent to the wall". This means that for Couette flow, for example, the shear rate $\dot{\gamma}$ will actually vary with the gap height rather than being a constant. However, Mooney argued that this variation in shear rate (i.e. velocity gradient) can essentially be modeled as a velocity discontinuity between the fluid and the wall. Fig. 2-5 (reproduced from Yoshimura and Prud'Homme [216]) illustrates this assumption.

In Fig. 2-5, a fluid is contained within a parallel plate-plate geometry, with the upper surface moving at a velocity Ωr, where Ω is the angular rotation rate of the upper surface, and r is the radial position under consideration. At that particular position r and with the given rotation rate Ω, the *apparent* shear rate is given as $\dot{\gamma}_a = \Omega r/H$, where H is the gap height. Due to the discontinuity in velocity at the upper and lower surface (slip velocity v_s), the true shear rate $\dot{\gamma}$ experienced by the

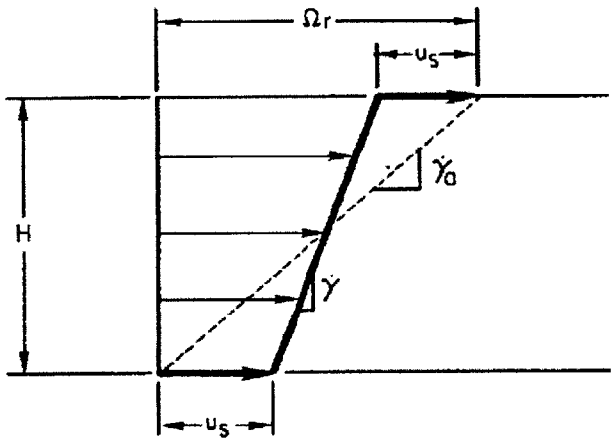

Figure 2-5: Wall slip in a plate-plate geometry. The figure is reproduced from Yoshimura and Prud'Homme [216]

fluid is as follows:

$$\dot{\gamma} = \frac{\Omega r - 2v_s}{H} \tag{2.2}$$

Thus, in order to determine the bulk viscosity of the fluid under question, knowledge of the slip velocity v_s is also required because it will determine the true shear rate $\dot{\gamma}$.

Following Mooney's contribution, many other workers addressed the question of wall slip [166, 94, 177, 60, 138]. The review article by Barnes [16] discusses the physics of slip in detail, including the existence of a "depletion layer" near the wall leading to a local region within the fluid with a large shear rate. This type of depletion layer is manifested in a number of different complex fluids. Barnes also discusses the use of a *slip law* to relate the velocity discontinuity at the wall-fluid interface, to shear stress within the fluid. A linear slip law (often referred to as the Navier slip law) would be given by the following equation:

$$v_s = \beta\sigma \tag{2.3}$$

Where v_s is the slip velocity, and β is the linear slip coefficient. Other types of slip laws can be employed - e.g. a power-law dependency of v_s on σ - in many cases these laws are empirical in nature.

Some of the more interesting recent contributions include Yoshimura and Prud'Homme's gap dependent methods for measuring wall slip in parallel plate geometries [216, 218].

Yoshimura and Prud'Homme introduced useful rheometric techniques which can be used to determine slip laws such as Eq. 2.3, without having to resort to direct measurements of slip velocity. Graham [91] looked at the effects of wall slip on large amplitude oscillatory flows, and showed that wall slip can have a considerable impact on the rheometric signature of a material. With more recent developments in flow-visualization technologies [128], some workers have even been able to directly measure wall slip in non-Newtonian fluids. The work by Seth et al. [189] established a theoretical model which predicts the functional form of the slip law in microgel pastes, and also used direct flow visualization measurements to verify the accuracy of their derived slip law.

Wall slip can play an important role in the context of waxy crude oil rheology. The work by Lee et al. [119] showed how a wax-oil gel can mechanically fail either through an adhesive (slip-like) mechanism, or a cohesive mechanism where the gel fails within its bulk. This type of behavior is not surprising, given that wax-oil gels consist of solid wax precipitates suspended in a Newtonian oil. Near the solid wall, it is possible for a depletion layer of low viscosity oil to form which would facilitate the occurrence of slip. The likelihood of slip is also affected by the roughness of the surface that the fluid is in contact with [202]. Other than the work by Lee et al. [119], there are few detailed quantitative studies of wall slip in waxy crude oils. A better understanding of this wall slip phenomenon may have implications for flow assurance strategies. For this reason, part of this thesis will focus on understanding wall slip in the context of waxy crude oils.

2.2.2 Shear Banding

Shear banding refers broadly to the phenomenon whereby a complex fluid subjected to a simple homogenous shearing deformation exhibits two or more neighboring regions of markedly differing shear rates. Numerous classes of non-Newtonian fluids are known to exhibit shear banding behavior [159], from various kinds of yield stress fluids (or EVP materials) [149, 64] to entangled polymer melts [197, 99] and wormlike micellar solutions [36, 185, 131, 130, 124, 33, 122]. Wormlike micelles are a particularly

interesting class of shear banding systems because they are widely used in consumer products, and they have become a canonical model system for understanding the shear banding phenomenon. The bulk rheology of these particular systems has also been studied extensively [176, 25, 187, 42, 121]

Whether or not a non-Newtonian fluid will exhibit shear banding is usually determined by the nature of the material flowcurve, i.e. the dependency of the shear stress σ on the shear rate $\dot{\gamma}$. Materials that shear band are typically assumed to have an underlying non-monotonic flowcurve (NMFC). This implies that there are unstable regions in the flowcurve where the stress can decrease as shear rate is increased. This is illustrated in Fig. 2-6, reproduced from Lerouge [121].

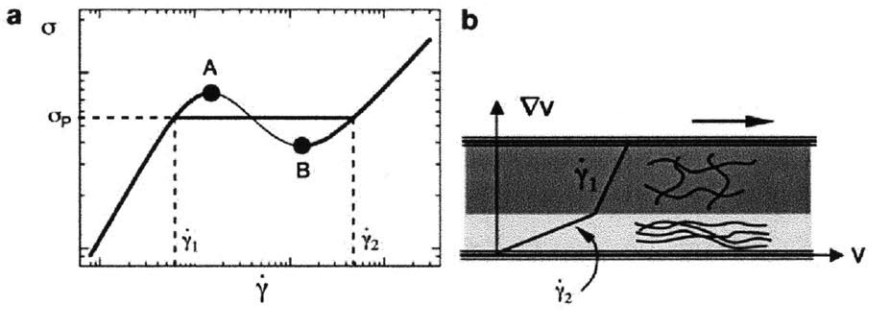

Figure 2-6: Typical example of a non-monotonic flowcurve in **a**, where between the shear rates $\dot{\gamma}_1$ and $\dot{\gamma}_2$ the stress σ increases up to point A, then subsequently decreases to point B. When a shear rate between $\dot{\gamma}_1$ and $\dot{\gamma}_2$ is applied to the fluid, the shear stress within the fluid remains at a plateau value σ_p and the material exhibits a shear banded velocity profile, as shown in **b**.

The NMFC illustrated in Fig. 2-6 (a) shows that for the plateau stress σ_p, there are two allowable shear rates, $\dot{\gamma}_1$ and $\dot{\gamma}_2$. One might therefore expect that at this stress, the material will split into two spatially distinct regions with different values of the local shear rate, as shown in Fig. 2-6 (b). When one controls the applied shear rate $\dot{\gamma}_a$ in an attempt to measure the flowcurve of such materials, a stress plateau σ_p is observed for applied shear rates between A and B. The stress therefore remains constant at σ_p as the applied shear rate $\dot{\gamma}_a$ is changed. Hence, these flowcurves are often referred to as underlying NMFC's, because they cannot usually be measured. Within the non-monotonic region of the flowcurve, the lever rule can be used to

determine the relative volume of fluid undergoing a particular shear rate, f [121]:

$$\dot{\gamma}_a = (1 - f)\dot{\gamma}_1 + f\dot{\gamma}_2 \tag{2.4}$$

Wormlike micellar solutions are one of the most frequently studied shear banding fluids. These fluids are solutions of surfactant molecules which have a hydrophilic head and a hydrophobic tail. The micelles are long cylindrical aggregates that are formed by these molecules, and can form into different shapes depending on the presence of additional screening molecules such as salts [42]. The earliest investigations studied the shear banding phenomenon in micelles using Rheo-NMR in a cone–plate geometry [36, 37]. This approach is reasonable because it is well known that when viscometric approximations hold, spatial variations in the stress in a cone–plate geometry are very small [29]. Subsequent velocimetric studies have focused more often on observing banding in cylindrical Couette geometries [185, 130, 145]. These velocimetry studies have shown that there is a clear difference between the structure of the shear-banded profiles observed in the two cases. Typically a double banded profile develops in the Couette case above a critical shear rate (i.e. one low and one high shear rate band) whereas 3-banded profiles appear in the cone–plate geometry (two low shear rate bands near the upper and lower rigid plates, and a higher shear rate band at midgap). These differences arise presumably because of the curvilinear nature of the flow fields in each device. The theoretical study by Adams et al. [1] has discussed the different shear banding scenarios for cone-plate and cylindrical Couette geometries for a particular case of the Johnson-Segalman constitutive model.

In addition to studies of banding in wall-bounded Couette cells, there have also been velocimetric studies of the onset of shear banding in these fluids within pressure driven microchannel flows [140, 133, 155, 156]. Although the kinematics of steady complex fluid flow in microchannels are spatially inhomogeneous, these experiments have been useful because they can be used to probe the nonlinear rheology of the fluids at much higher shear rates than is usually possible on a torsional rheometer. They can also probe the onset of "non-local" effects, which arise when the characteristic

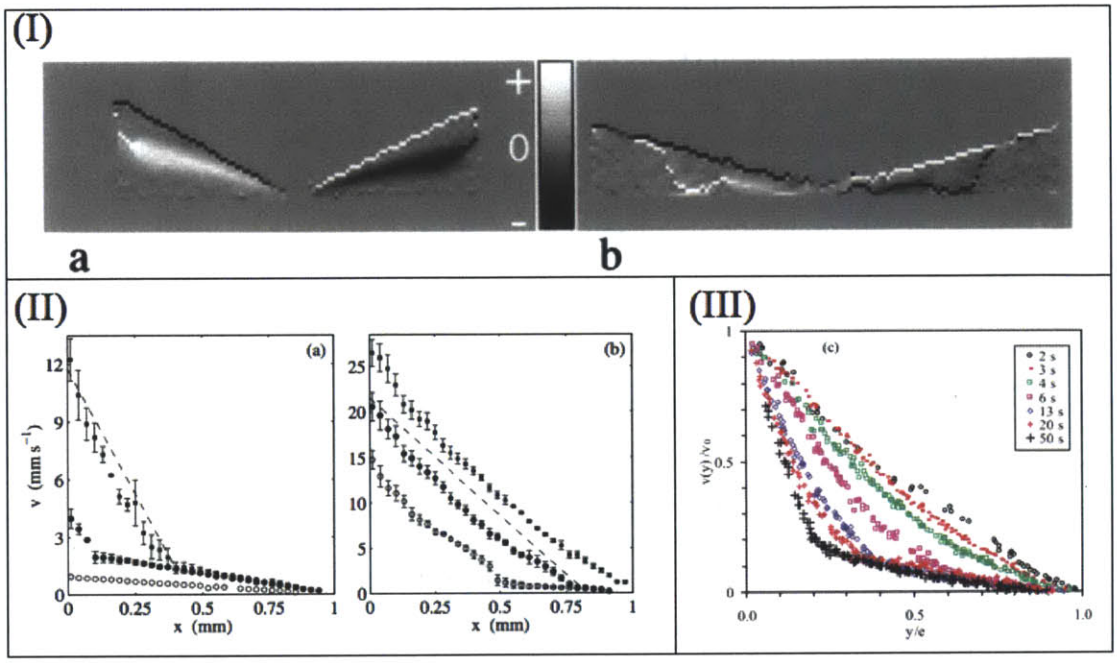

Figure 2-7: Set of figures showing the difference between the nature of shear banded velocity profiles in cylindrical Couette geometries and cone-plate geometries. In (I) a and b, shear rate contour plots are reproduced from Britton and Callaghan [36]. These show a high shear rate regime at the mid-gap, with low shear rate regimes near the upper and lower surfaces (3 banded profiles). The fluid is a cetylpyridinium chloride/NaSal wormlike surfactant solution. In (II) a. and b., velocity fields are reproduced from Salmon et al. [185], for flow of a similar wormlike micellar solution in a cylindrical Couette geometry. These velocity profiles show two regimes of different shear rates (double banded profile). The figure in (III) (reproduced from Hu and Lips [101]), also shows a double banded profile for flow in a cylindrical Couette geometry.

length scale of the geometry and of the shear band become comparable [136, 135].

Finally, we note that some recent studies have suggested that both wall slip [33, 122, 76] and unsteady secondary flows [74, 75] play an important role in the shear banding behavior of wormlike micellar solutions. The work by Feindel and Callaghan [76] questions the validity of the lever rule as a way to determine the steady state, banded configuration in the non-monotonic region of the fluids flowcurve. Feindel and Callaghan suggest that the shear banding phenomenon in wormlike micelles is actually more complex, and that the shear banded velocity profiles in these fluids can exhibit considerable spatiotemporal fluctuations.

Within this thesis we will utilize wormlike micellar solutions as a canonical shear-banding fluid to achieve a number of goals. First, we will test the experimental capabilities of a flow visualization apparatus (design discussed in Chap. 3) using a wormlike micellar solution in Chap. 4. In Chap. 4, we will also show original results demonstrating the shear banding behavior of these fluids under large amplitude oscillatory flow. A quantitative analysis of the dynamics of this shear banded flow will be given. Such results may prove useful for future researchers hoping to develop constitutive models that can predict the complex rheology of wormlike micellar fluids. While the behavior of these surfactant solutions is different from precipitate containing crude oils, they are nonetheless interesting from a petroleum-production standpoint because they are already frequently used for enhanced oil recovery [9].

2.2.3 Yield stress fluids - shear banding and other heterogeneities

Shear banding or shear heterogeneities are by no means unique to wormlike micellar fluids. An abundance of recent work has pointed towards the presence of shear banding in yield stress fluids (YSFs) or Elasto Viscoplastic (EVP) materials as well. The work by Coussot and coworkers [54] is one of the first instances of direct observations of shear banding in a yield stress fluid. Coussot et al. used NMR velocimetry to point towards shear banding in four different elasto-viscoplastic materials (a cement paste,

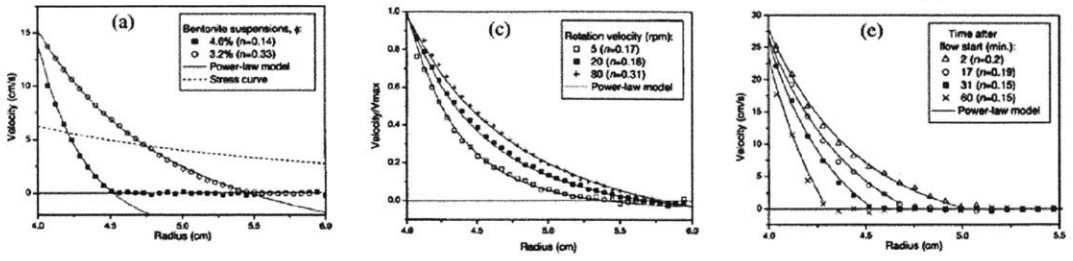

Figure 2-8: Shear banding in various yield stress fluids, reproduced from Coussot and coworkers [54]. Shear banding behavior is observed in a cylindrical Couette geometry for a bentonite-water suspension (left), for a mayonnaise/concentrated emulsion (center) and a cement paste (right).

concentrated emulsion, a natural clay suspension and a silica suspension). Møller and coworkers [149] observed similar behavior in a suspension of charged colloidal particles, and attempted to determine the underlying non-monotonic flowcurve of the fluid.

In another contribution, Møller and coworkers argued for a distinction between "simple" yield stress fluids and thixotropic yield stress fluids [147]. This distinction was tied to the presence or lack of shear banding - thixotropic YSFs are expected to exhibit banding, while simple YSFs do not. The work by Coussot [55] seemed to experimentally verify this using a Carbopol microgel, however Divoux and coworkers [64, 63, 62] indicated that Carbopol microgels are not so "ideal" because they appear to exhibit some transient shear banding.

One recent contribution that is relevant to the rheology of crude oils comes from Gibaud and coworkers [85, 86, 87]. Gibaud et al. studied a suspension of discotic, charged Laponite particles. This elasto-viscoplastic material exhibited shear heterogeneities which strongly depended on the roughness of the confining walls. Under the start-up of a steady shear flow, these materials generally show a gradual decay in stress. This decay in stress occurs due to an "erosion" process whereby the material microstructure breaks apart. The erosion process is accompanied by pronounced spatial and temporal fluctuations in the velocity profile within the fluid, which is confined to a cylindrical Couette geometry. Both variations in the slip velocity, as

well as in the shear rate in the bulk of the material are observed. One would expect waxy crude oils, which consist of suspensions of discotic wax crystallites, to exhibit similar types of spatiotemporal fluctuations and shear heterogeneities. Chap. 6 will present a detailed study of this type of behavior in a model waxy crude oil.

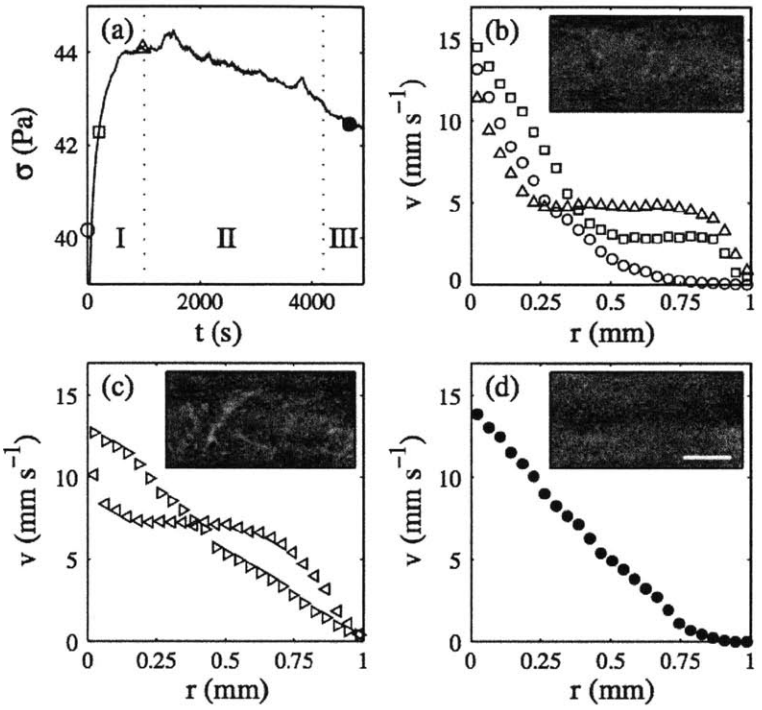

Figure 2-9: Figure from Gibaud et al. [85] showing startup of steady shear in a Laponite suspension. Applied shear rate is $\dot{\gamma} = 17\ s^{-1}$. Bulk stress in the material is shown in (a) while velocity fields within the fluid in different temporal regimes (I, II and III) are shown in (b)-(d). Generally the material exhibits spatiotemporal fluctuations in the velocity field, which only approaches a linear profile at very long times. A decrease in the stress/viscosity occurs alongside an erosion of the material microstructure.

2.2.4 Experimental techniques

There are numerous experimental techniques that have been used to study shear heterogeneities in complex fluids. These include NMR velocimetry [39, 149, 56], where velocity fields are extracted from the spin polarization of nuclei that interact with a strong external magnetic field gradient. Another method that has been used

is ultrasound velocimetry [129, 85], which utilizes high frequency ultrasonic pulses to produce ultrasonic speckle patterns and velocity fields. Finally, numerous workers have used particle tracking methods [138, 139, 197, 74, 95] in order to quantify local velocity/deformation fields.

The basic idea behind particle tracking techniques are to introduce a small amount of tracer particles into the test fluid. The concentration of these tracer particles must be low enough so that they do not affect the rheology of the fluid under question. These tracer particles may be either fluorescent or reflective, so that when they are illuminated (typically by a laser source), they scatter or emit a substantial amount of light. A CCD camera with a lens focused onto the particles can then be used to quantify the movement of particles over time. A simple diagram illustrating how this might be done in a cone and plate setup (reproduced from Meeker and coworkers [138]) is given in Fig. 2-10.

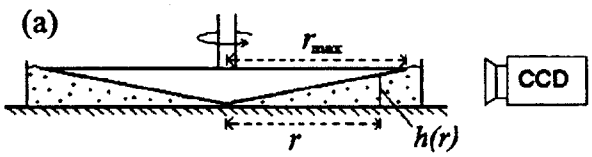

Figure 2-10: Experimental setup employed by Meeker et al. to evaluate velocity profiles for emulsions and pastes of microgel particles. Although Meeker and coworkers did not use a laser light source, typically one would direct a vertical light sheet at the radial position r, and focus the CCD camera onto that sheet.

In much of the recent work involving particle tracking in complex fluids, experiments have been carried out in the limit of low seeding density, where individual particles are tracked in order to determine the velocity field within the fluid. This type of tracking method is called particle tracking velocimetry (PTV) [5]. When the seeding density in the fluid is higher, the displacement of local groups of particles is determined by spatial correlations rather than tracking individual particles. This method is referred to as particle image velocimetry, or PIV [3, 4].

In the PIV approach, the velocity field is obtained by carrying out a cross correlation operation between "interrogation windows" in two subsequent images. Each interrogation window is a grid of $q \times p$ pixels which must contain a minimum number

of seed particles. In a dark field image, these particles will show up as bright spots since they are reflecting light (typically from a laser source) which is directed onto them. The procedure is shown diagrammatically in Figure 2-11. The red box in the full image on the left is the interrogation window (size $q \times p$ pixels). The optimum displacement is determined for the window from time t_1 to line up with the window from the next frame (at time t_2) by using the cross correlation operation. Wereley and Meinhart give the following equation for the cross correlation operation, which must be evaluated for each interrogation window [35].

$$\Phi_k(m,n) = \sum_{j=1}^{q} \sum_{i=1}^{p} f_k(i,j) \cdot g_k(i+m, j+n) \tag{2.5}$$

In Eq. 2.5 q and p give the size of each interrogation window in pixels, while $f_k(i,j)$ and $g_k(i,j)$ are the grayscale values for each of the pixels in the interrogation windows of the two frames. When the value of Φ_k is calculated for a number of different values of m and n, then a two dimensional intensity field shows Φ_k as a function of m and n. The point at which this is a maximum is the value of m and n which correspond to the average displacement which optically matches with the interrogation windows of the two frames. This displacement can then be computed into a point value of the in-plane velocity, assuming the time spacing between the frames is known.

There are some limitations associated this technique. One limitation is that each interrogation window must contain an adequate number of seed particles (typically 10 or more [3]), otherwise the function Φ_k will not give a distinct peak corresponding to the the actual displacement for the region given by that window. It is possible to track individual particles in the flow, however this approach is the basis of particle tracking velocimetry (or PTV).

Both PTV and PIV are well suited for observing transient responses in fluid flows, due to the good temporal and spatial resolution of these methods [128], and this has been exploited by some workers to study transient evolution of shear banded flows [145]. Both PTV and PIV are therefore a good choice of a tool for probing shear banding in oscillatory flows, although recent developments in Rheo-NMR techniques

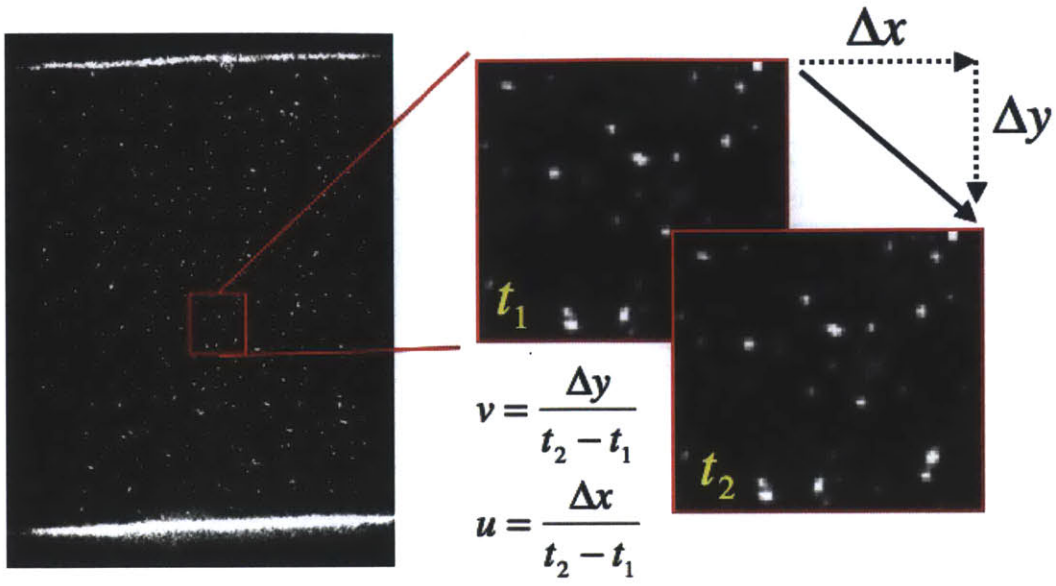

Figure 2-11: Diagram showing how images are divided up into interrogation windows, which are shifted such that they align with the windows of the next frame. The displacements Δx and Δy can be used to determine the velocity, given that the time spacing between each frame is known. The upper and lower horizontal lines are due to specular reflection, and they indicate the location of the bounding walls of the flow.

discussed by Callaghan [39] and Davies et al. [56] have provided spatial and temporal resolutions that rival those of PIV/PTV methods. One advantage of PIV over PTV is that it is a whole field technique, returning velocimetric data on a uniform spaced grid [174]. Vector fields obtained from PTV tend to be sparser than those obtained from PIV, and the individual vectors are located randomly throughout the imaged domain due to the randomly positioned particles in the flow [5]. This disadvantage in general makes subsequent data analysis, including computation of differential quantities such as shear rate and vorticity, more cumbersome in the case of PTV.

The flow visualization tool of choice that will be adopted in this thesis is PIV. In Chaps. 3, we will discuss in detail the design of a Rheo-PIV device, which allows for in-situ velocimetric measurements to be taken within a fluid undergoing shear in a rheometer. This device will be utilized throughout Chaps. 4-5 in order to observe shear heterogeneities in a wormlike micellar fluid and in a model waxy crude oil.

2.3 Elasto-Viscoplasticity

2.3.1 The Yield Stress - Myth or reality?

Throughout this thesis, we adopt the use of the term "Elasto-Viscoplastic" (which we have abbreviated so far as EVP) to refer to yield-like behavior in complex fluids beyond a critical stress. However, the inclusion of the "elasto-" component in this term implies the added presence of a primarily elastic behavior below the yield stress. The presence of "visco" in this terminology further implies a rate-dependency in the irreversible plastic flow which occurs above the critical stress. Hence, in contrast to viscoelastic materials, the response of EVP materials to deformations is highly dependent on the *extent* of the deformation, i.e. the magnitude of the applied stress or the magnitude of the imposed strain. EVP materials can therefore transition very abruptly (i.e. over a small range of stresses) from what appears to be an elastic solid, to a flowing liquid.

In the rheology literature, there has been considerable debate as to whether the concept of the yield stress is a reality or not [20, 18]. Barnes [18] goes into a substantial amount of detail about the arguments for and against the existence of the yield stress. The central tenet of Barnes' discussion is that the yield stress is a useful engineering concept, but is not a reality in the sense that most all materials exhibit measurable creep (or flow) for even the smallest stresses. If the yield stress is therefore defined as the stress below which zero flow occurs, then one will never be able to identify this stress due to the ubiquity of creep behavior (which Barnes provided evidence for in a number of different materials).

In this work, we adopt the same tenet; the yield stress is approached as an engineering concept, i.e. a mathematical approximation that helps demarcate between the "elasto" regime of EVP materials and the "viscoplastic" regime. Such a picture does not necessarily negate the possibility of flow (or irreversible creep) at stresses below the yield stress. In this thesis, we will introduce constitutive models with a yield stress term that do predict slow creeping flow below the yield stress. This will be accomplished by additively decomposing the material deformation into elastic

and plastic components. For small stresses and short enough time-scales, the elastic component may be much larger than the plastic creeping flow component, so the engineering approximation of zero flow (but nonzero deformation!) below a critical stress is a useful one.

Barnes assessment of the yield stress concept lead him to discuss the use of generalized Newtonian fluid (GNF) constitutive equations in order to account for the slow creeping flow which is observed in many complex fluids [19]. One such GNF model is the Cross model, which gives the following functional form for the viscosity of the material:

$$\frac{\eta - \eta_\infty}{\eta_0 - \eta_\infty} = \frac{1}{1 + \left(\frac{|\dot{\gamma}|}{\dot{\gamma}^*}\right)^m} \tag{2.6}$$

Where η_0 is the zero shear rate viscosity, η_∞ is the high shear rate viscosity, and m and $\dot{\gamma}^*$ are fitting coefficients. Another GNF model is the Bingham or Herschel-Bulkley model [97], which is given as follows:

$$\eta = \begin{cases} \frac{\sigma_y + k|\dot{\gamma}|^m}{|\dot{\gamma}|} & \text{for } |\sigma| > \sigma_y \\ \infty & \text{for } |\sigma| \leq \sigma_y \end{cases} \tag{2.7}$$

The special case of $m = 1$ in Eq. 2.7 reduces to the Bingham model [28]. Barnes argues that the Cross model is better suited for describing EVP materials than say, the Herschel-Bulkley model, because it predicts a finite viscosity for all finite values of stress. Fig. 2-12 below illustrates this on 2 plots reproduced from Barnes [18], which indicate how the Cross model can predict an "apparent" yield stress, with a Newtonian, high viscosity regime below this stress.

A significant drawback to Barnes' approach is that it fails to account for elastic deformations, which may take up a substantial portion of the total material deformation. These elastic deformations will also differ substantially from any viscoplastic deformations, due to the fundamental property of elastic deformations being reversible. This results in the material having some memory of its undeformed state. An (albeit extreme) example that illustrates this deficiency is that of any solid material under

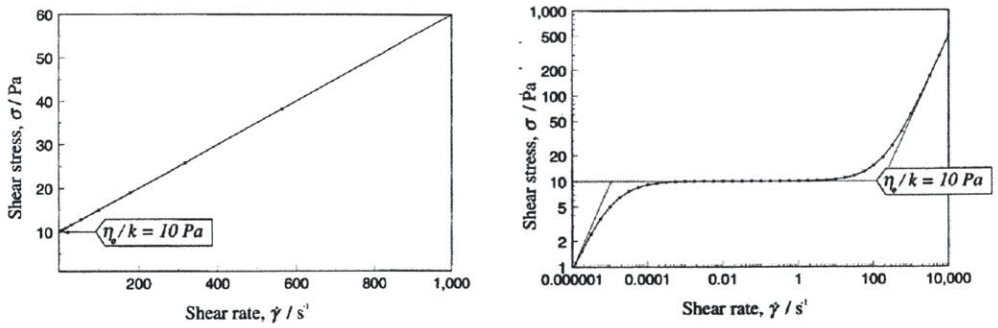

Figure 2-12: Predicted response of the Cross model reproduced from Barnes [18] on a linear scale (left) and logarithmic scale (right). The model parameters are $m = 1$, $\eta_\infty = 50$ mPa.s, $\eta_0 = 1 \times 10^6$ Pa.s and $\dot{\gamma}^* = 1 \times 10^{-5}$ s^{-1} (In the figure Barnes uses $1/k$ for $\dot{\gamma}^*$). The beginning and end of the shear thinning regime occur (approximately) where the low and high shear rate viscosity curves intercept the apparent yield stress, $\gamma^* \eta_0$.

load for a short period of time. The primary material variable used to determine the response of the structure is the elastic modulus. Creep flow viscosity will play a negligible role, and may even be a transient parameter which cannot be accounted for by a single zero shear rate viscosity parameter like η_0.

The use of GNF models therefore also lacks the ability to account for any transients in the response of a material which may be due to material memory and relaxation mechanisms. These relaxation mechanisms result from the interaction of elasticity and viscoplasticity, and are thus typically present in EVP materials. A recent paper by Møller et al. [147] showed that Carbopol, a commonly tested and favorite EVP material of rheologists [168], shows an interesting creep behavior below a critical stress. Under creeping flow the material tends (in an asymptotic limit) towards a material with infinite viscosity (which does not flow). This behavior is illustrated in Fig. 2-13. Møller and co-authors used this data to argue that Carbopol is an "ideal" yield stress fluid, because in the asymptotic limit $t \to \infty$ and for stresses $\sigma < \sigma_y$ the creeping flow ceases. The plateau viscosity for Carbopol (defined as $\eta^+ \equiv \sigma/\dot{\gamma}(t)$) shows a power law like growth in time, so it is unbounded. Some authors have referred to this different viscosity growth for $\sigma < \sigma_y$ and $\sigma > \sigma_y$ as a viscosity "bifurcation" [53].

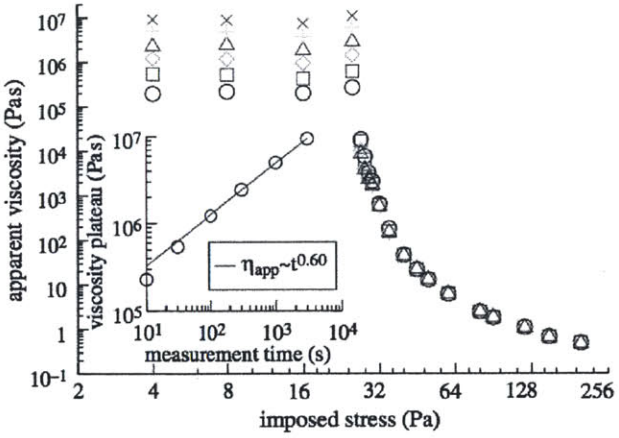

Figure 2-13: Plot from Møller et al. [147] illustrating time growth of a viscosity plateau below the yield stress for a Carbopol microgel. The inset shows a power law growth in this transient plateau viscosity.

2.3.2 Constitutive Models

A few workers have attempted to address the deficiencies of the GNF approach by introducing more sophisticated constitutive models to describe EVP behavior. Yoshimura and Prud'Homme [217] utilized their Elastic Bingham model in order to predict the complex response of an EVP material under large amplitude oscillatory shear (or LAOS). Doraiswamy et al. [65] further modified this model, so as to account for thixotropic effects and to remove some artifacts from the elastic Bingham model.

Other constitutive models that have been employed to predict EVP behavior include the soft glassy rheology (SGR) model, which was discussed in detail by Sollich [194]. The SGR model envisions EVP behavior in complex fluids as being a result of elements trapped in cages. These elements can be drops in emulsions, bubbles in foams or solid particles in a paste. The cages are formed by the neighboring elements, and the fundamental equation for the SGR model specifies the evolution of the probability of a finding an element in a cage of certain depth (or characteristic energy). Several workers have shown that the SGR model can exhibit many of the generic features associated with EVP behavior [194, 78]. However, the SGR model is difficult to evaluate for rheological flows, due to the fundamental equation of motion describing evolution of probability, rather than bulk measurable parameters such as

stress or strain. Additional effort is also required to cast this model into a tensorial form [194].

Saramito [186] proposed another constitutive model to account for EVP behavior. Saramito's modified Herschel Bulkley like model combines linear viscoelastic behavior below the yield stress, with a Herschel Bulkley like yielding behavior above a critical stress. Saramito also expressed the model in tensorial form (which involved the use of frame invariant derivatives), and verified that the model is thermodynamically admissible.

The simpler elastic Bingham model has received considerable attention in recent years, and has formed the basis for several studies (e.g. see the work by Ewoldt et al. [73] and Rogers and Lettinga [183]). However, the works of Doraiswamy et al. [65] and Yoshimura and Prud'Homme [217] (where this model was first introduced) lack a discussion of the relation between the elastic-Bingham–type models and the classical elasto-plastic models employed in plasticity. The standard approach used in the plasticity literature to describe yielding materials is to mathematically decompose the total strain that a material experiences (denoted γ) into an elastic and plastic component [120, 93]. For one-dimensional shearing deformations, this can be expressed as follows:

$$\gamma = \gamma^e + \gamma^p \tag{2.8}$$

Where γ^e is the elastic part of the deformation, and γ^p is the plastic part of the deformation. This strain decomposition is visually illustrated in Fig. 2-14, which is reproduced from Gurtin et al. [93]. This figure illustrates the typical stress-strain loading curve of an elasto-plastic material (for example, a metal) to a one-dimensional tension test (here s is used as stress and e as strain).

Stress strain curves such as that given in Fig. 2-14 are not the ideal candidates for illustrating rate dependency in a material. However, if the portion of the curve between B and C (and onward) were to depend on the rate of straining, $\frac{de}{dt}$, then the material would be classified as EVP (and not just elasto-plastic). For metals at

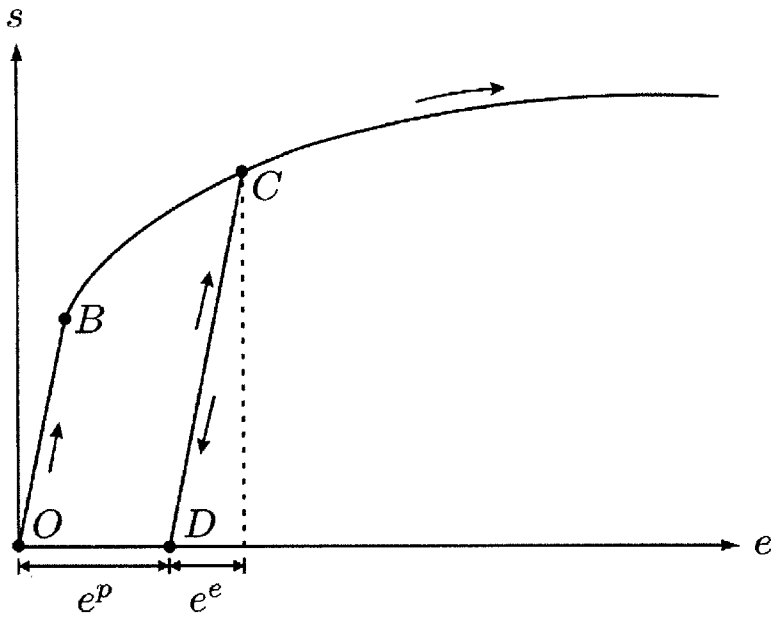

Figure 2-14: Stress-strain curve of a typical elasto-plastic material reproduced from Gurtin et al. [93]. The decomposition of strain is graphically indicated, as well as the elastic unloading path that the material goes through when the deformation is reversed.

low temperatures, rate dependency is usually negligible, so the portion of the stress-strain curve from B onwards (also known as the *hardening curve*) is assumed to be rate independent. However, rate dependency is easily and frequently introduced into plasticity models - for example when characterizing the mechanical response of polymers [11, 10].

Complex fluids that exhibit EVP behavior will show the same qualitative features of the stress-strain curve in Fig. 2-14, so a strain decomposition approach outlined in Eq. 2.8 is a reasonable starting point for building a constitutive model. Unfortunately, Doraiswamy et al. [65] and Yoshimura and Prud'Homme [217] do not begin with this approach in the development of their models. Doraiswamy et al. [65] explicitly reject the generalized 3 dimensional version of Eq. 2.8 as a possible avenue for exploration, because they (incorrectly) argue that it cannot account for viscous or rate-dependent effects. One central goal of this thesis will be the application of modeling tools from plasticity to explore these avenues. The benefit of this approach is that these constitutive models can be generalized to 3-dimensional form (which is more useful

in simulations of complex flows, such as the restart of a pipeline filled with waxy crude oil). To implement this 3D generalization, the strain decomposition of Eq. 2.8 is extended to a multiplicative decomposition of the deformation gradient $\mathbf{F}$ into individual elastic and plastic components (also known as the Kroner decomposition [114]):

$$\mathbf{F} = \mathbf{F}^e\mathbf{F}^p \tag{2.9}$$

The deformation gradient itself is defined as follows:

$$\mathbf{F}(\mathbf{X}, t) = \nabla\chi(\mathbf{X}, t) \tag{2.10}$$

Where $\chi(\mathbf{X}, t)$ is the motion function of the material, as a function of time t and material position $\mathbf{X}$. After a particular motion, a material point is moved to a new position $\mathbf{x} = \chi(\mathbf{X}, t)$. Gurtin et al. [93] discuss the significance of the Kroner decomposition in considerable depth. Generally, the plastic part of the deformation gradient $\mathbf{F}^p$ can be thought of an operator that transforms material vectors in a reference undeformed space to a vectors in a structural space. The structural space is generally associated with the actual material structure. For example, for a single crystal, the structural space contains an undistorted crystal lattice. Elastic deformations will then cause (reversible) distortions of the lattice. This transformation procedure is illustrated in Fig. 2-15.

The concept of the "structural space" which is illustrated in Fig. 2-15 is similar to the concept of cages formed by neighboring elements in the SGR model. Just as the SGR model accounts for an evolution in the energy landscape formed by these cages, a model based on Eq. 2.8 would account for an evolution of the plastic deformation gradient tensor $\mathbf{F}^p$. The plastic deformation gradient tensor $\mathbf{F}^p$ can therefore account for a change in the material structure with time. This material structure will evolve differently depending what it consists of (e.g. droplets in an emulsion, solid particles in a paste, etc.), however the framework in Eq. 2.8 is general enough to account for these types of variations.

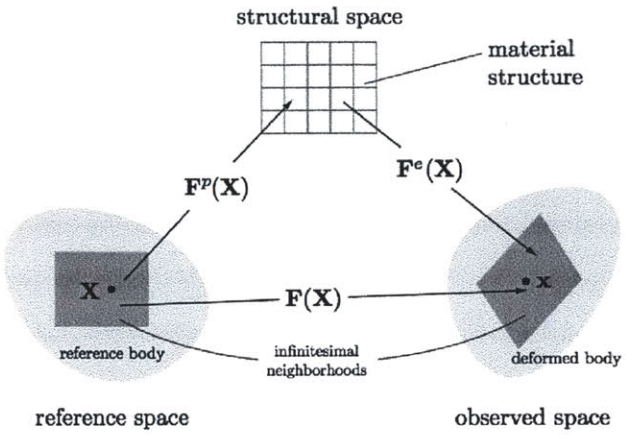

Figure 2-15: Graphical representation of the multiplicative decomposition of the deformation gradient $\mathbf{F}$ into a plastic contribution and an elastic contribution. Image reproduced from Gurtin et al. [93]

2.3.3 Using LAOS to probe EVP behavior

In this thesis, we plan to use LAOS to probe EVP behavior in several different complex fluids. As a rheometric tool, LAOS is especially appropriate here, because it probes nonlinear mechanical behavior, and plastic behavior is of an inherently nonlinear nature. If the direction of deformation in Fig. 2-14 is continually reversed in a cyclical manner, one would essentially be conducting a LAOS test. LAOS typically imposes a sinusoidal shear strain on the material of the following form:

$$\gamma = \gamma_0 \sin \omega t \tag{2.11}$$

For small enough amplitudes γ_0, the resulting periodic shear stress waveform takes the following form [29]:

$$\sigma(t) = G'(\omega)\gamma_0 \sin \omega t + G''(\omega)\gamma_0 \cos \omega t \tag{2.12}$$

Thus, for small amplitude oscillatory shear (SAOS), one can compute the linear viscoelastic moduli $G'(\omega)$ and $G''(\omega)$ as a function of frequency by measuring the periodic stress $\sigma(t)$ [29]. For larger imposed values of the strain amplitude γ_0, the periodic stress can be expressed in terms of a Fourier series [103]:

$$\sigma(t;\gamma_0,\omega) = \sum_{n \text{ odd}} \{G'_n(\omega,\gamma_0)\gamma_0 \sin n\omega t + G''_n(\omega,\gamma_0)\gamma_0 \cos n\omega t\} \tag{2.13}$$

In recent years, there have been many developments in both the analytical framework of Large Amplitude Oscillatory Shear (LAOS), as well as in its applications to the study of complex fluids. On the theoretical side, there are still issues to be addressed concerning the most appropriate way to capture and represent material data, and for these reasons LAOS remains an active area of research [103]. From a practical standpoint, the utility of LAOS as an experimental methodology is that it allows both linear and nonlinear behavior of an unknown material to be probed within a single test protocol. Moreover, the ability to independently modify the frequency ω and strain amplitude γ_0 of the oscillations enables the mapping of an entire phase space (commonly termed the Pipkin space [171]) and provides a "rheological fingerprint" of the material behavior.

One important use of LAOS measurements is that they can be applied towards the rational development and validation of constitutive models that predict nonlinear material behavior. There have already been several examples in the rheology literature of studies focused on using LAOS to determine model parameters and test the predictive performance of constitutive models [84, 220, 38, 154, 83, 92]. Similarly, in the solid mechanics and plasticity community, experiments very similar to LAOS are frequently used to probe material behavior. Solid mechanicians will often use cyclic stress/strain loading curves (although these are often performed in tension and compression, and not in shear) in order to determine whether or not a material exhibits a particular type of behavior. One of the earliest examples of this is the study of the Bauschinger effect [22], in which it was shown that under cyclic tension/compression metals exhibited a progressive decrease in their yield strength (this is graphically illustrated in Fig. 2-16). The Bauschinger effect is but one example of a behavior that can only be observed and quantified under cyclic loading conditions, there are numerous other phenomena that can be observed at large strains which drive the need for development of nonlinear constitutive models [93].

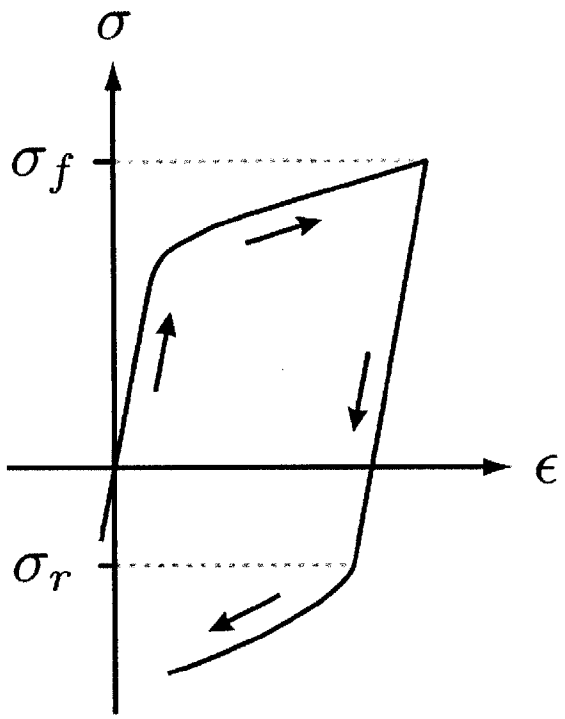

Figure 2-16: Graphical illustration of the Bauschinger effect on a set of stress-strain axes, reproduced from [93]. The magnitude of the yield stress upon reversal of the loading, σ_r, is smaller than the initial yield stress within the material, as well as the hardened value of the yield stress, σ_f.

Recent developments in LAOS have primarily been focused on carrying out experiments in a strain-controlled fashion, i.e. a sinusoidal strain of amplitude γ_0 and frequency ω is imposed and in turn the periodic nonlinear stress output is measured (as outlined in Eq. 2.11- 2.13). It is then possible to extract information about the material from this periodic stress waveform. This is typically accomplished through the use of Fourier analysis [212, 211]. Ewoldt. et al. [71] developed an ontological framework that extends the stress decomposition ideas of Cho et al. [50] and allows one to physically interpret the higher harmonics in these periodic stress waveforms in terms of orthogonal basis functions. These basis functions purport to describe physical processes in the material such as strain-hardening or shear-thinning. For compactness we refer to this as the *LAOStrain* framework. The LAOStrain framework additively decomposes the periodic stress waveform in Eq. 2.13 into an elastic

component σ' and a viscous component σ''. These two components are given as follows:

$$\sigma'(t;\gamma_0,\omega) = \sum_{n \text{ odd}} G'_n(\omega,\gamma_0)\gamma_0 \sin n\omega t \tag{2.14}$$

$$\sigma''(t;\gamma_0,\omega) = \sum_{n \text{ odd}} G''_n(\omega,\gamma_0)\gamma_0 \cos n\omega t \tag{2.15}$$

The insight provided by Ewoldt et al. was that σ' and σ'', which are single valued functions of the strain and rate of strain respectively, can be represented as series of orthogonal Chebyshev polynomials T_n:

$$\sigma'(x) = \gamma_0 \sum_{n \text{ odd}} e_n(\omega,\gamma_0)T_n(x) \tag{2.16}$$

$$\sigma''(y) = \dot{\gamma}_0 \sum_{n \text{ odd}} v_n(\omega,\gamma_0)T_n(y) \tag{2.17}$$

Where $x = \gamma/\gamma_0$ is the scaled strain and $y = \dot{\gamma}/\dot{\gamma}_0$ is the scaled strain rate. The e_n are the elastic Chebyshev coefficients and the v_n are the viscous Chebyshev coefficients. Ewoldt and coworkers then used geometric arguments to show that the $n = 3$ Chebyshev coefficients can be related to intracycle nonlinearities (as opposed to inter-cycle nonlinearities) that are exhibited by the material. A plot from the work by Ewoldt et al. reproduced in Fig. 2-17 below illustrates this by showing the single valued decomposed stresses σ' and σ''. The Chebyshev coefficients e_3 and v_3 can then describe the convexity or concavity of these single-valued decomposed stresses (which can, under certain circumstances, be related to intra-cycle shear thinning/thickening or strain softening/stiffening).

Both Ewoldt [69] and Laüger [118] developed the corresponding framework for carrying out LAOS tests in a stress-controlled manner (or *LAOStress* for short). They extended some of the definitions of Ewoldt et al. [71], but it has not yet been made clear why one may prefer to carry out LAOS experiments in a stress-controlled fashion. Laüger et al. [118] demonstrate that, at large deformations, a given material can behave substantially differently under the two different cyclic loading histories.

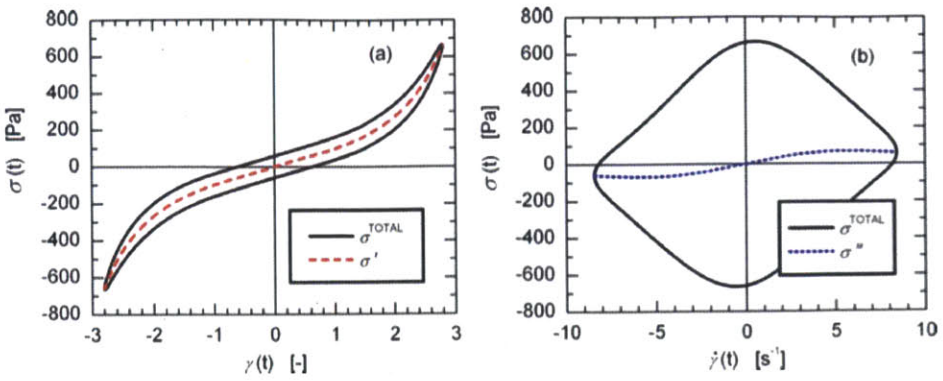

Figure 2-17: Elastic projection, or stress-strain curve (on the left) and viscous projection (on the right) of a sample of snail pedal mucus undergoing large amplitude oscillatory shear. The single valued elastic stress σ' of Eq. 2.14 is indicated as a red dotted line, while the viscous stress σ'' of Eq. 2.15 is indicated as a blue dotted line.

Thus, different aspects of the material behavior in the nonlinear regime may be probed using the two methods. Elegant arguments such as the ones presented by Plazek [172] on the physical interpretation of compliances vs. moduli in the linear regime suggest that there are equally important considerations to be evaluated in LAOS.

LAOStrain has already been utilized as a method to study complex fluids that exhibit EVP behavior [70, 73, 98, 182, 181]. Ewoldt et al. measured and characterized the EVP behavior of xantham gum solutions and a drilling mud. Interestingly, the cyclic stress-strain response from the work by Ewoldt et al. (reproduced here in Fig. 2-18) exhibits some of the hallmarks of a strain decomposable material illustrated in Figs. 2-14 and 2-16. Specifically, a Bauschinger-like decrease in the yield strength is observed as the direction of loading is reversed, and a transition from elastic to plastic behavior is observed in the initial deformation stages.

Recently a series of papers by Rogers and coworkers [182, 183, 179] described the response of soft yielding materials (specifically a colloidal star polymer) to LAOS as a *sequence of physical processes*. The authors introduced the concept of a "Cage Modulus" - a measure that captures elastic behavior during a particular part of the LAOS cycle. They show that under strain-controlled conditions this modulus cannot be evaluated in terms of the higher harmonics in the Fourier transform of the stress signal. This suggests that there may be benefits towards taking a stress-controlled

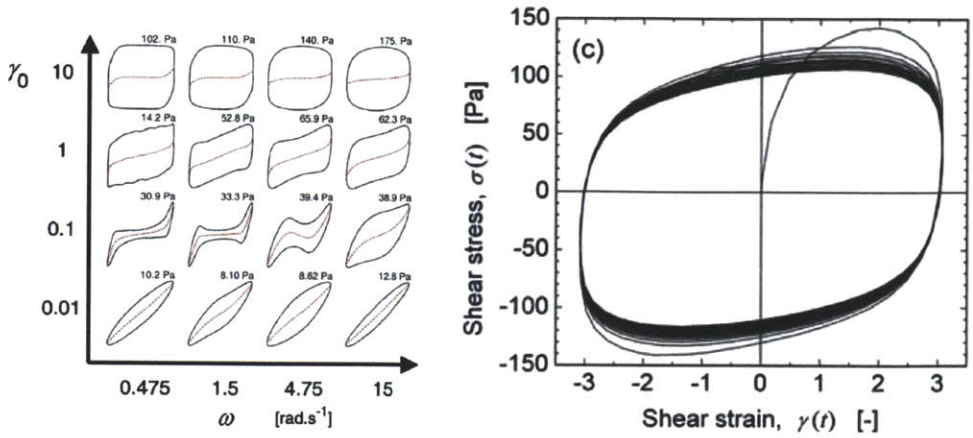

Figure 2-18: Pipkin diagram of a drilling mud from Ewoldt et al. [73] (left) and stress-strain, or Lissajous curve, of a xantham gum (right).

approach towards LAOS, because LAOStress will provide a different set of moduli which may be more closely connected to the physical concept of the "Cage Modulus" discussed by Rogers and coworkers [182, 181]. Comparatively little work has been done in using LAOStress to evaluate these types of nonlinear measures and distinguish between the predictions of different constitutive models for EVP materials.

One of the central contributions of this thesis will be to apply the technique of LAOStress to develop a constitutive model for Carbopol, which is a canonical EVP material studied by many rheologists [168]. A critical component of the work will be the application of the plasticity modeling framework outlined in Sec. 2.3.2 to build the constitutive relationships. The particular constitutive model will go beyond the GNF type characterization used by Barnes [18]. It will effectively link the small strain elastic behavior with large strain visco-plasticity in a continuous, and mathematically robust manner. Chaps. 6 and 7 will discuss this in detail.

2.4 Thixotropy

Thixotropy is the general feature of a material to exhibit a continuous and reversible time-dependent change (usually a decrease) in measurements of viscosity at a particular shear rate. [142, 17, 143]. These time-dependent changes in viscosity are due to a gradual change in the microstructure of the material resulting from the applica-

tion of shear. This mechanism is referred to as shear rejuvenation [53]. Thixotropic materials exhibit a second mechanism, known as aging, which describes the ability of the material to rebuild its initial structure under the absence of shear (hence the reversibility of the initial time-dependent change). The aging phenomenon is typically assumed to result from a slow internal, thermally driven rearrangement of the material's microconstituents [17].

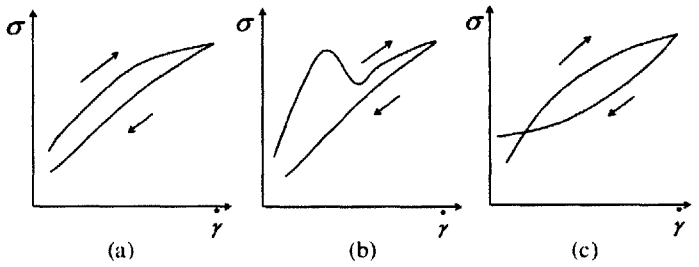

Figure 2-19: Figure reproduced from Mewis & Wagner [143] showing the effect of thixotropy on the flowcurve (or plot of stress σ vs. shear rate $\dot{\gamma}$). Hysteresis loops are observed as the shear rate is increased and decreased, due to the competing effects of aging and shear rejuvenation.

EVP materials (or yield stress fluids) frequently exhibit thixotropic behavior. Møller et al. [147] recently proposed that thixotropy can be used as a distinguishing behavior that separates "ideal" yield stress fluids from "non-ideal" yield stress fluids. The classification used by Møller et al. is more than likely an oversimplification [64, 63]. However it does point towards the need to develop a better understanding of the interrelation of thixotropy with yield-like phenomena in complex fluids.

Perhaps one of the biggest challenges associated with the study of thixotropy is the development of a canonical constitutive model that can capture all of the general rheological features associated with thixotropic EVP materials. There is a substantial body of literature which has worked towards developing such a model [44, 51, 57, 199, 173, 219, 152, 58]. Many of these different proposed models exhibit differences which range from subtle to substantial. However, one common characteristic shared by most of these models is the use of an internal structural parameter (frequently, but not always, denoted as λ) to describe some aspect of the material structure. The material structure can build up or break down over time due to the application of

shear, so the evolution equation for the structure parameter $\lambda(t)$ therefore typically contains an aging term, and a shear rejuvenation term. This parameter is then related to rheological parameters in the fluid, such as the yield stress, viscosity, or modulus. Perhaps the simplest version of such a rheological model is the toy λ-model that was used by Coussot et al. [53] as well as Møller et al. [147].

$$\frac{d\lambda}{dt} = \frac{1}{\tau} - a|\dot{\gamma}|\lambda \tag{2.18}$$

$$\eta = f(\lambda) \tag{2.19}$$

Where $f(\lambda)$ is typically an increasing function of λ. This set of two equations accounts for an increase in λ under zero shear due to aging (the $1/\tau$ term) as well as a decrease in λ due to the mechanism of shear rejuvenation (the $a|\dot{\gamma}|\lambda$ term). The λ parameter is purported to describe some aspect of the material microstructure, and as the fluid structures its viscosity will increase through the dependency in Eq. 2.19. Although this inelastic model is able to capture some of the qualitative features that thixotropic EVP materials exhibit (such as the viscosity bifurcation) its simplicity bars it from being used for quantitative predictions of thixotropic EVP behavior (e.g., it does not predict viscoelasticity).

Waxy crude oils are a good example of a thixotropic EVP material. Researchers have therefore been well aware of the thixotropic nature of waxy crude oils for quite some time now [142, 43]. There have been many detailed studies of the rheology of these fluids, and in many instances an emphasis is placed on sample preparation protocol being a necessary component to ensure repeatable rheological data. [210, 202, 204, 132]. The effect of sample preparation is illustrated in Fig. 2-20, reproduced from [209], where cooling rate, in addition to shear history, is also shown to have an effect on the rheology of a waxy crude oil. The nature of the "thermal beneficiation" [164] and cooling process used to form a gelled waxy crude oil thus plays an important role in unambiguously determining the rheology of the gel. This beneficiation process typically involves heating the fluid to a temperature much higher than T_{wa} and shearing it for a designated amount of time. The fluid can then be cooled to

below the gelation temperature at a prescribed cooling rate.

However, one of the issues presented when measuring the rheology of these fluids is the fact that sample composition varies across different crudes (asphaltene content, wax content [195]). Combined with the thixotropic behavior of these fluids, this makes reproducible rheological data difficult to obtain, and quantitative comparisons with model predictions even more difficult. As a result, there are few studies showing a thorough comparison of rheology of crude oils to predicted response from constitutive models. Some of the models employed are also rather simplified, e.g. the Houska model used by some workers [44, 163] does not account for material elasticity, and the Pedersen model [164] which is also used by Ehsan and Mowla [82] assumes a generalized Newtonian fluid with temperature dependency. A broader approach, both in

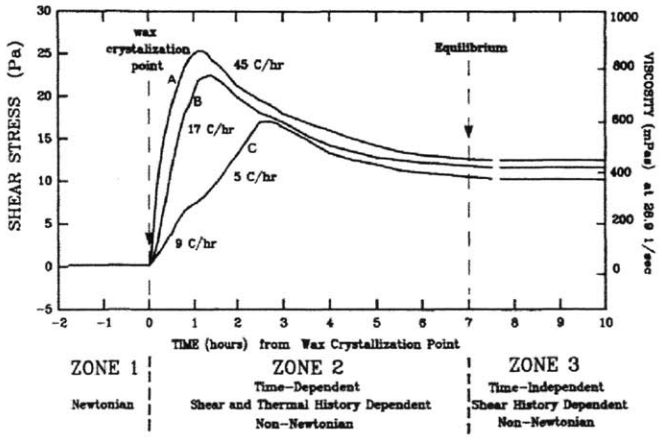

Figure 2-20: Figure reproduced from Wardhaugh and Boger [209] illustrating the effect of cooling rate on the rheology of a waxy crude oil. A steady shear rate of $\dot{\gamma} = 28.9\ s^{-1}$ is applied, and the fluid is cooled to below its wax appearance temperature at a number of different cooling rates. The peak in the stress corresponds to the point where the cooling has stopped, and the viscosity in the material subsequently decays over a long period of time. The nature of these curves is highly dependent on the applied shear rate $\dot{\gamma}$.

terms of experiments and modeling, is therefore required. This will be the focus of Chap. 8, where we will revisit the model waxy crude oil studied in Chap. 5. The work by Coussot et al. [51] and Mujumdar et al. [152] propose several different rheological experiments, among them startup of steady shear and large amplitude oscillatory shear (LAOStrain) as potential ways to validate constitutive models. Combined with

a detailed preparation protocol for our model fluid, we will implement these rheological flows as tools to evaluate a constitutive model in Chap. 8. By verifying our model across a wide range of these flows, further experimental validation can be given to future numerical studies which may use these models (such as the work by Wachs et al. [206] or Chang et al. [46]).

From the point of view of constitutive modeling, the main goal of this thesis is to broaden the scope of the thixotropy literature as a whole by introducing ideas from plasticity that have not yet been widely used in the rheology literature. The connection between thixotropic yield stress fluids and plasticity is not a hard one to make. The term "yield stress fluid" describes nothing more than a yielding material with rate-dependent plastic flow above the critical stress. This behavior is so generic that it is even exhibited by metals at elevated temperatures [93, 120]. Thixotropy, on the other hand, bears striking similarities to the hardening mechanisms that are used in plasticity, which often utilize an internal structure variable similar to λ [93]. The approach used to describe hardening is typically cast into a different form than that given in Eq. 2.18-2.19. Rather than relating the viscosity of the fluid η to some structural parameter, hardening mechanisms specify a relationship between some generalized stress on the material $\bar{\sigma}$ and a generalized plastic flow rate $\dot{\bar{\gamma}}^p$ (these generalized positive-valued scalars are usually the magnitude of the tensor valued stress and strain rate). For rate-independent hardening, the simplest hardening rule that can be proposed is a linear one, where the stress in the material post-yield increases linearly with the plastic strain $\bar{\gamma}^p$

$$\bar{\sigma} = \sigma_y + k_h \bar{\gamma}^p \tag{2.20}$$

Where σ_y is an initial yield stress in the material, and k_h is a hardening coefficient with units of stress. Note that this equation only applies once the material begins to yield, i.e. once $\sigma > \sigma_y$. This hardening rule is rate-independent because the increase in stress does not depend on the rate at which the material is deformed (it only depends on the magnitude of the deformation). For this rate independent hardening

rule, the plastic strain $\bar{\gamma}^p$ serves as the evolving internal variable and performs a function similar to the λ parameter in Eq. 2.18. For rate-dependent hardening, one could specify a simple relationship between the stress $\bar{\sigma}$ and the plastic strain rate $\dot{\bar{\gamma}}^p$:

$$\dot{\bar{\gamma}}^p = \frac{\bar{\sigma} - S}{k} \qquad \text{if } \bar{\sigma} > S,\ \dot{\bar{\gamma}}^p = 0 \text{ otherwise} \tag{2.21}$$

$$S = \sigma_y + k_h \lambda \tag{2.22}$$

$$\frac{d\lambda}{dt} = f(\lambda, \dot{\bar{\gamma}}^p) \tag{2.23}$$

Where S is a transient yield strength, and k is a plastic viscosity coefficient. This hardening is now rate-dependent due to the presence of the equation relating the rate of plastic strain to the stress. The transient yield strength S is also related to λ, which is the internal variable for which we specify an evolution equation in Eq. 2.23. The simplest evolution equation would be $d\lambda/dt = \dot{\bar{\gamma}}^p$, in which case our internal variable again reduces to the plastic strain $\bar{\gamma}^p$. Note how Eq. 2.21-2.23 can be cast into the same form of Coussot's λ-type model in Eq. 2.18-2.19 by rewriting Eq. 2.21 as an equation for viscosity, $\eta = \bar{\sigma}/\dot{\bar{\gamma}}^p$. The only distinction between these two cases would then be that Eqs. 2.21-2.23 would give a shear-thinning fluid for constant values of λ, while Eqs. 2.18-2.19 give a Newtonian fluid for constant values of λ.

Together with equations for the generalized stresses and strains, the plasticity approach also requires some specification of the *direction* of the stress and strain, since the generalized scalars do not carry that information with them. The typical assumption is that plastic strain rate is *codirectional* with the stress, allowing one to arrive at the full tensorial form of the constitutive laws [93]. These constitutive laws will then likely require the use of the Kroner decomposition discussed in Sec. 2.3.2.

While some previous work has only hinted at these plasticity mechanisms to model simple and thixotropic EVP materials [65], a central contribution of this thesis will be to actually implement these mechanisms to predict the behavior of a thixotropic EVP material. The specific thixotropic EVP material that will be studied here is a model waxy crude oil. Chapter 8 describes this work in further detail.

Chapter 3

Rheo-PIV and Flow Visualization

The development of appropriate experimental techniques for carrying out flow visualization is central to our discussion of shear heterogeneities in complex fluids. In this chapter, we detail the development of the "RheoPIV" fixture, which uses particle image velocimetry in order to extract the in-situ velocity field of a fluid undergoing shear in a rheometer. Two versions of this RheoPIV device are developed and used - we will refer to them as RheoPIV v1 and RheoPIV v2. Both of these fixtures are mounted onto a TA Instruments ARG2 stress controlled rheometer.

3.1 RheoPIV v1

A schematic diagram for the first iteration of the RheoPIV fixture is shown in Fig. 3.1. The design of the system is similar to those implemented by Tapadia and Wang to study flow of entangled polymer melts [197, 198] and Meeker et al. for the study of soft pastes [138, 139]. A CCD camera (MatrixVision BlueFox) fitted with a macroscopic imaging zoom lens (Edmund Optics Techspec VZM 600i) is positioned orthogonally to the sample interface such that the imaging plane of the lens/camera is located a few millimeters into the sample away from the fluid meniscus. The upper (rotating) geometry of the rheometer is a 50mm diameter quartz plate, which allows illumination of the sample using a collimated laser beam to form a focused imaging plane in the sample. The laser is a focusable 10mW Edmund optics laser diode, with a wavelength

of 635 nm. The samples are typically seeded with reflective titanium dioxide seed particles from TSI Inc. of average size 3μm, allowing for the local velocity field across the rheometer gap to be measured. The typical seeding density is 0.005% by weight. Fig. 3.1 shows how the lower shearing surface is attached to a raised Peltier configuration (TA instruments 531052) and this allows several different bottom geometries to be used interchangeably, such as a cone or a flat plate. For most tests, precision-machined, black-anodized cones of radius $R = 25$mm, angle $\Theta_0 = 4°$ and truncation 111 μm are used (although in some cases 2° cones are also used). The surface roughness of these cones can also be modified by applying adhesive-backed sandpaper. Roughened surfaces will be utilized throughout this thesis in order to suppress wall slip in certain circumstances.

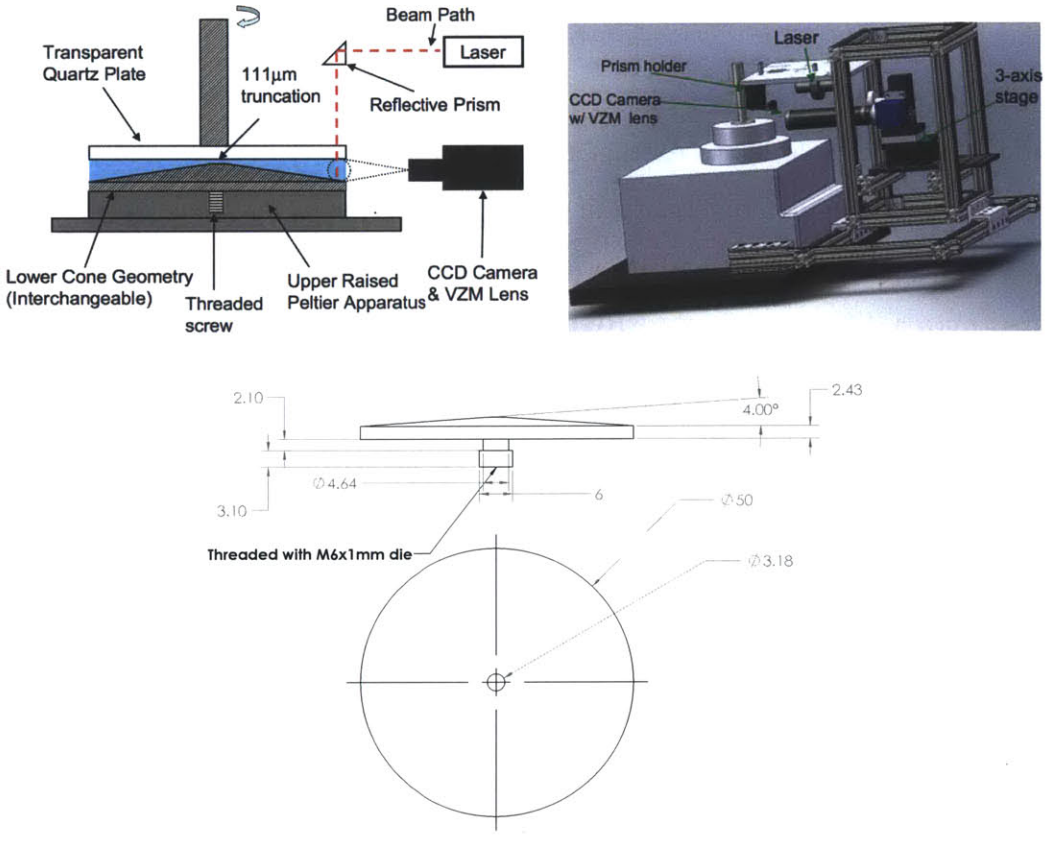

Figure 3-1: Schematic diagram (upper left) and 3D model (upper right, rendered in Solidworks) of the RheoPIV v1 apparatus. The lower image is an engineering drawing of a 25 mm lower cone geometry (dimensions in millimeters).

The light sheet is aligned tangentially to the direction of flow of the fluid, and

approximately 2 mm into the fluid from the edge of the geometry. For a spherical (r, θ, ϕ) coordinate system oriented with its center at the cone tip and the lower cone surface being described by $\theta = \pi/2 - \Theta_0$ (and flow only occurring in the ϕ direction), this corresponds to a laser light sheet tangent to the sphere at $r = R_i = 23$ mm. The laser light sheet illuminates seed particles at different positions along the vertical (shear) direction ($y \simeq R_i(\theta - \pi/2 + \Theta_0)$), so by observing the movement of these particles in the flow direction ϕ (or $x \simeq R_i\phi$) it is possible to determine the velocity profile within the fluid.

The velocity field within the fluid is determined using digital PIV - the particular software package that is used is Digiflow (http://www.dalzielresearch.com/digiflow). Digiflow applies a cross correlation algorithm to a pair of images separated by a time $\frac{1}{F}$, where F is the frame rate that the CCD camera acquires images at (for our system $F = 60$ fps typically). The two subsequent images are divided into interrogation windows of size 16×16 pixels, and the 2D cross correlation function between the two successive frames in each interrogation window is computed. The point at which the cross correlation function is a maximum corresponds to the average displacement of fluid elements within the interrogation window between the two exposures. The 2D velocity field is formed from the ensemble of these displacements obtained from each interrogation window. Because the lateral width of the laser light sheet ($\Delta x \sim 2$ mm) and its thickness (~ 0.25 mm) are both small compared to the value of R_i, the flow can be assumed to be translationally invariant along the x direction. This approximation essentially takes a small enough arc segment on the surface of a sphere (and any movement of particles on this surface) and describes it using a rectangular coordinate system (x, y) with $x \simeq R_i\phi$ and $y \simeq R_i(\theta - \pi/2 + \Theta_0)$. The resulting time resolved velocity field is thus a full two dimensional vector field of the form $\mathbf{v} = [v_x(x, y), v_y(x, y)]$. Combined with the fact that there is, on average, no flow in the y direction, this allows for each 2D velocity field to be averaged along the direction of flow (x) to produce a single velocity profile per image pair, $v_x(y)$.

In order to demonstrate the accuracy of the setup, Fig. 3-2 shows a comparison of the measured velocity profile $v_x(y)$ with the theoretical profile expected for the low

viscosity Newtonian mineral oil under a steady imposed shear rate of $\dot{\gamma} = 0.535\text{s}^{-1}$. The control system of the rheometer imposes a steady shearing velocity at the upper surface, and the magnitude of this velocity is shown at the top of the profile in Fig. 3-2 and annotated as V_w. The theoretical shear rate and velocity profile are then specified to be $v_x(y) = V_w \frac{y}{H} = \dot{\gamma} y$. As can be seen from 3-2, the slope of the measured velocity profile is equal to the average shear rate within the gap and this agrees with the imposed shear rate that is set by the rheometer. The inset in Fig. 3-2 gives the probability distribution of the velocity values over 180 frames and at the position $y = 0.7$mm from the lower plate (corresponding to $N = 4860$ observations). The distribution is Gaussian in nature, with a standard deviation, $\sigma = 0.0187$ mm/s, which is 5% of the mean value. The distribution of velocity measurements is similar at other positions within the gap and the standard deviation was found to vary between 0.014 and 0.023 mm/s. For the velocity in the vertical direction, $v_y(x, y)$, measurements give $v_y = -0.011 \pm 0.04$mm/s. For all of the experiments in this thesis involving velocity measurements, the magnitude of vertical velocities v_y will be much smaller than the magnitude of horizontal velocities v_x. So, in general, v_x and v will be used interchangeably.

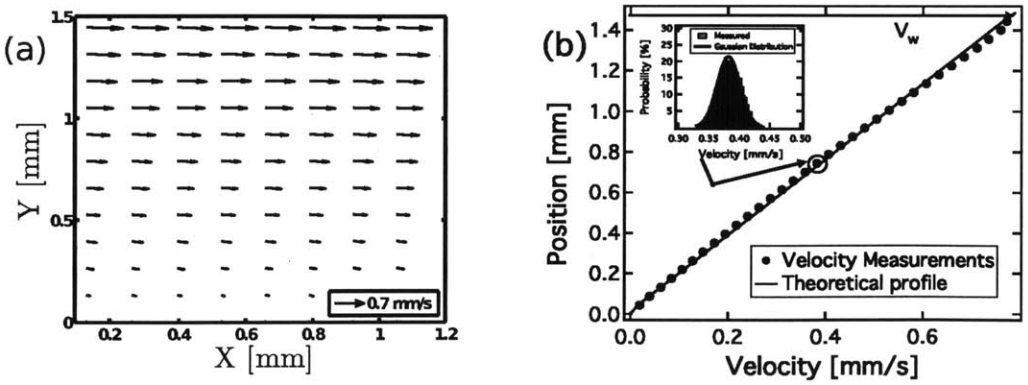

Figure 3-2: (a) 2D velocity field, and (b) averaged velocity profile, v_x of a 0.01% wt. seeded light mineral oil undergoing steady shear, $\dot{\gamma} = 0.535s^{-1}$. Inset shows the distribution of velocity vectors at a position $y = 0.7$ mm from the bottom plate.

3.1.1 Meniscus effects

One important design feature of RheoPIV v1 is the use of concentric upper plates and lower cones of the same radius (typically $R = 25$ mm). This results in the air-fluid meniscus pinning to the upper and lower edge of these geometries. Therefore a nominally flat air-fluid interface is obtained, which is desirable for this RheoPIV device. The camera focuses on the imaging plane through this air fluid meniscus, and any perturbations in the shape of this meniscus can potentially result in artifacts appearing in the measured velocity field. In Fig. 3-3, we compare the shape of the fluid meniscus for an upper and lower geometry of the same radius (b), and for a lower geometry which has a much larger radius (a). The particular fluid that the gap is filled with is a heavy mineral oil.

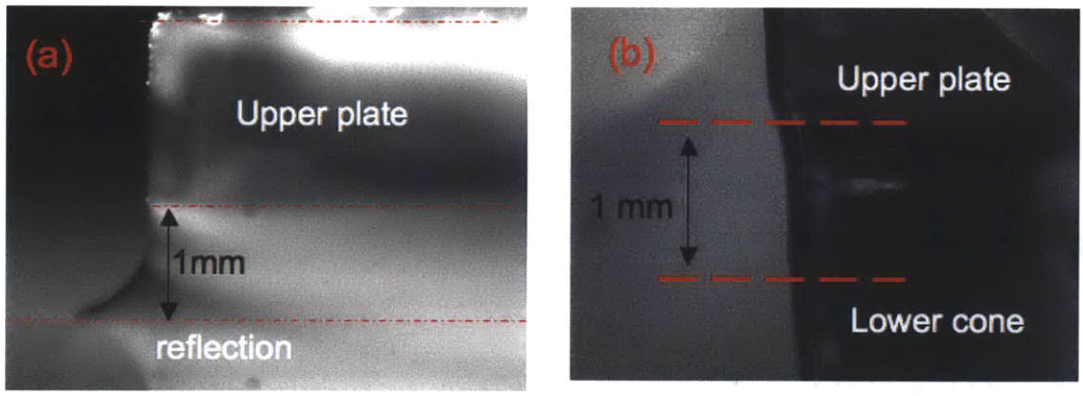

Figure 3-3: Shape of air-fluid meniscus for an upper and lower geometry with matched radii (b), and a lower geometry with a much larger radius (a). The sample loaded into the gap is a Newtonian mineral oil. As is apparent from (a), wetting on the lower plate results in a curved meniscus. In (b), the meniscus remains pinned to the lower plate, and is therefore flat.

As Fig. 3-3 shows, when the lower geometry is much larger than the upper geometry, the fluid is able to wet a large portion of this lower surface, causing a substantial amount of curvature in the meniscus. However, when the two geometries have the same radius (shown in (b)), the meniscus remains generally flat. The conditions in Fig. 3-3 (b) are much more favorable for carrying out flow visualization measurements - in (a) the different indices of refraction of the fluid and air will result in a distortion

(specifically a magnification) of the imaging plane. The raised Peltier plate therefore plays an important role, because it allows for interchangeable lower geometries to be used that have a radius equal to the radius of the upper plate.

Although the raised Peltier configuration helps with pinning the fluid meniscus under static conditions, the imposition of large rotation rates of the geometries (or large shear rates) can result in a deformation of the meniscus when the fluid in the gap is non-Newtonian. These types of edge instabilities have been observed in a number of different fluids [110, 104, 196], and are often thought to be the result of normal stress differences arising in the material [116]. There has been some work carried out towards predicting the shape of these air-fluid interfaces for viscoelastic fluids [157, 193]. In principle, if one could *a priori* determine the shape of the meniscus, ray-tracing could be used in order to understand the effect that this varying shape may have on the measurement of the tracer particle positions. However the manifestation of these instabilities often depends on so many parameters that it is difficult to predict how these types of irregularities in the meniscus may effect flow field visualization. For these reasons, we discuss the design of RheoPIV v2 in the next section, which bypasses these issues with an alternative design.

3.2 RheoPIV v2

3.2.1 Image distortion due to optical aberrations

The goal of designing and constructing RheoPIV v2 was to avoid the issues associated with an irregularly shaped meniscus. One possible way to accomplish this was suggested by Tapadia and Wang [197], who proposed imaging the flow through the upper transparent plate. This approach is illustrated schematically in Fig. 3-4.

S.Q. Wang's group has developed a number of experimental techniques to measure shear heterogeneities in complex fluids [198, 33, 34, 123, 208], however there are few mentions in their work about the detailed implementation of the "Scheme B" illustrated in Fig. 3-4. This scheme was therefore tested in the lab, and it was found

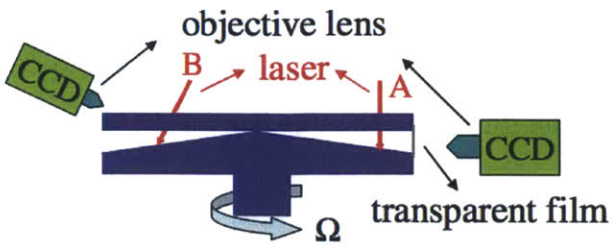

Figure 3-4: Figure reproduced from Tapadia and Wang [197] showing two alternative imaging schemes for particle tracking velocimetry in a cone-plate rheometer. Imaging scheme B tracks the flow through the upper transparent plate, instead of through the sample edge (which Tapadia and Wang covered with a transparent film).

that tracer particles would appear far blurrier if the camera axis was aligned at a non-perpendicular angle to the upper transparent plate. This distortion and blurriness is caused by refraction which occurs as light passes through a medium with a high index of refraction (the upper quartz plate) to air which has a lower index of refraction. The effect of this distortion can be illustrated by carrying out ray tracing on the light rays which the tracer particles reflect and enter into the camera aperture. This is illustrated in Fig. 3-5.

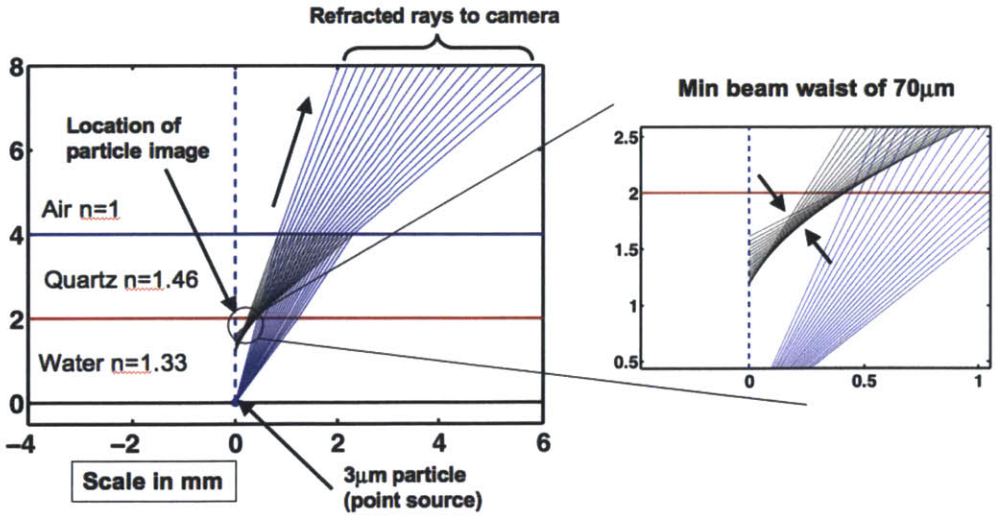

Figure 3-5: Ray tracing of light from a point source to the camera with a numerical aperture (NA) of 0.1.

In Fig. 3-5, light is assumed to leave the particle (3 μm in size, but modeled as a point source) that is located at the bottom of the 2mm thick layer of water (with

index of refraction $n_w = 1.33$). This 2mm thick layer of water is covered with a 2mm thick quartz plate ($n_q = 1.46$). As the light is transmitted from the water to the quartz, and then from the quartz to the air, it refracts twice, obeying Snell's law:

$$\frac{\sin\theta_1}{\sin\theta_2} = \frac{n_2}{n_1} \tag{3.1}$$

where θ_1 and θ_2 are the angles of incidence of the light rays and n_1 and n_2 are the indices of refraction of the different media. The numerical aperture of the objective lens (estimated as $NA \simeq 0.1$) is used to determine the fan angle of light rays which enter into the aperture. The imaging axis of the camera is also assumed to be at a 30° angle to the normal of the quartz plate.

The refracted rays can be traced back (shown as black lines in the figure) to determine the point at which the image of the particle appears. The particle image appears much closer to the water/quartz interface, and this will result in the imaging plane shrinking. More importantly, however, is that the refraction will also cause the particle point source to appear substantially larger. This can be determined by measuring the minimum beam waist, which is approximately 70 μm, or a factor of 20 larger than the actual particle size. Fig. 3-6 compares the visual quality of the particle images using "Scheme B", and using the original RheoPIV v1 apparatus. The particle images appear much sharper when RheoPIV v1 is used. The combined effect of the image plane shrinking as well as a smearing out of the particle images therefore makes "Scheme B" impractical for RheoPIV measurements.

3.2.2 Beveled plate design

In order to circumvent these issues, RheoPIV v2 was designed in order to avoid imaging through the sample meniscus, while at the same time avoiding the optical aberrations that were discussed in Sec. 3.2.1. This was accomplished by machining a custom upper plate geometry, with a bevel in its upper edge to serve as an imaging window. Fig. 3-7 shows a 3-dimensional solid model (rendered in Solidworks), a schematic diagram, as well as a photograph of the machined upper plate geometry

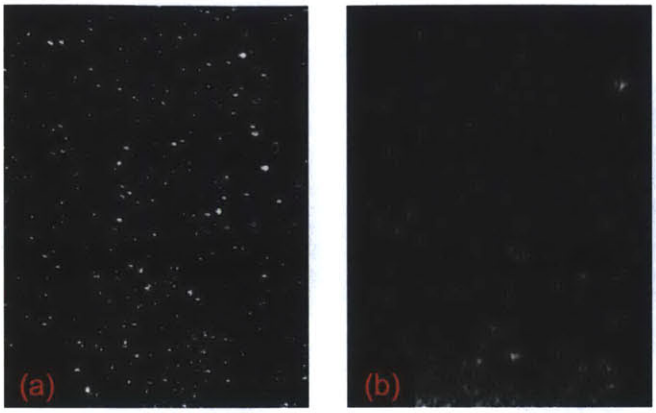

Figure 3-6: Comparison of images obtained of a heavy mineral oil seeded with 3 μm TiO_2 particles using RheoPIV v1 (a) and using the "Scheme B" proposed by Tapadia and Wang. Vertical image scale in both cases is approximately 1.75 mm. For (b), the camera imaging axis is inclined at a 30° angle to the normal of the quartz plate

with the bevel.

For simplicity, the beveled geometry was machined out of acrylic (with an index of refraction of 1.49, which is very close to that of quartz glass). It has an outer diameter of 50 mm, so that it can be used with the same lower geometries that are utilized with RheoPIV v1 (either a 2 or 4 degree black anodized lower cone machined from aluminum). An engineering drawing of the beveled geometry with dimensions annotated is given in Fig. 3-8.

The apparatus shown in Fig. 3-7 (c) allows for the location of the laser light sheet R_i as well as the angle of the reflective mirror θ_m to be tuned. For the experiments in this thesis that used RheoPIV v2, the value of R_i was kept constant at 20 mm, while θ_m was held constant at 45° (creating a vertical laser light sheet). It is possible to decrease θ_m so that the plane of illuminated particles is parallel to the camera focal plane, however this was not necessary because the camera/lens assembly that was used had a high enough focal depth, and all of the particles across the gap were sufficiently in focus. A velocity calibration profile of a heavy mineral oil undergoing steady shear of $\dot{\gamma} = 0.5\ s^{-1}$ in a 50 mm diameter, $\phi = 4°$ cone-plate geometry is shown in Fig. 3-9. The profile is averaged from 100 frames of video taken over a course of 3 seconds. It shows excellent agreement with the linear, theoretical profile predicted for a Newtonian fluid.

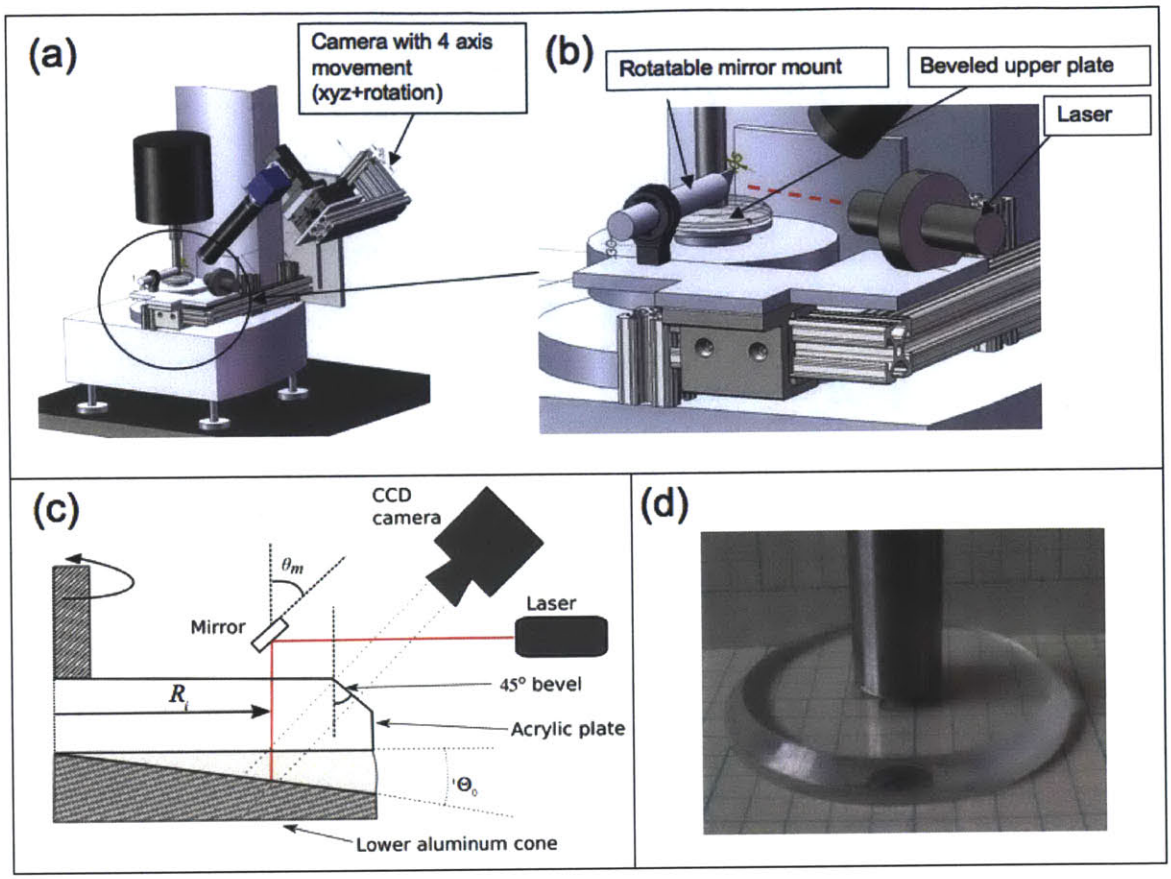

Figure 3-7: Solidworks rendering of RheoPIV v2 in (a), with an expanded view of the geometry/laser area in (b). In (c) a simplified schematic diagram is given, and in (d) a photograph of the beveled geometry (glued to a steel shaft) is shown.

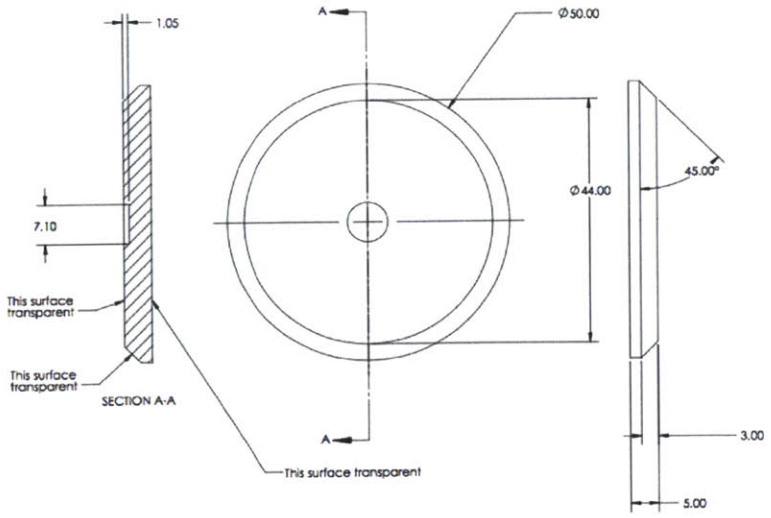

Figure 3-8: Engineering drawing of the acrylic beveled upper plate geometry. All dimensions are in millimeters.

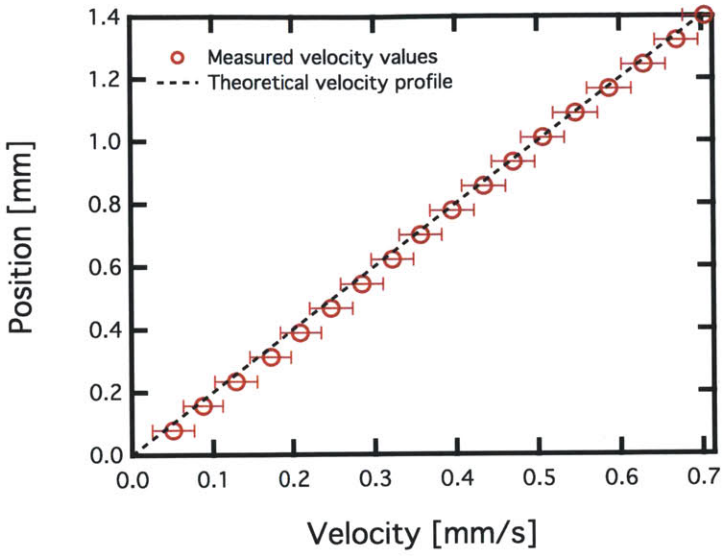

Figure 3-9: Calibration velocity profile for a Newtonian mineral oil under an applied shear rate of $\dot{\gamma} = 0.5\ s^{-1}$ obtained with RheoPIV v2. The Newtonian mineral oil has an index of refraction of 1.47, which is very close to the index of refraction for acrylic. The error bars on the velocity measurement correspond to one standard deviation of the measured velocity at each position across the gap. These standard deviations range between 0.024 and 0.027 mm/s, and are thus comparable to standard deviations from the measurements with RheoPIV v1 given in Fig. 3-2.

The flat beveled edge effectively avoids image distortion which arises from refraction of light across the irregularly shaped air-fluid meniscus. It also avoids the optical aberrations that were discussed in Sec. 3.2.1 by placing the camera axis perpendicular to the acrylic/air interface. Note that the camera axis angle can be varied by varying the orientation of the articulating arm that the camera is mounted to (shown in Fig. 3-7 (a)). This allows for geometries with different bevel angles to be used - for our purposes however only a 45° bevel was used.

The velocity profile obtained in Fig. 3-9 is for a Newtonian fluid with an index of refraction sufficiently matched to the value of n_a for acrylic. This is favorable for measurements with RheoPIV v2, because it eliminates refraction of light rays as they pass from the fluid into the solid acrylic geometry. The refraction may result in similar optical aberrations to those discussed in Sec. 3.2.1, provided the values of the refractive indices in the two media are sufficiently different. For these reasons, RheoPIV v2 is only utilized in Chap. 8, where the fluid under question is a model waxy

crude oil with an index of refraction equal to 1.47. For water based fluids (for example wormlike micellar solutions) where the index of refraction is closer to 1.33, there is some loss in image quality. However the image quality is still markedly improved compared to Fig. 3-6 (b). If the refraction which occurs between the air and quartz in Fig. 3-5 is eliminated, then the beam waist reduces by a factor of 5 to approximately 14 μm, resulting in PIV measurements still being possible. Imaging flow through the beveled surface is therefore generally favorable over imaging through the air-fluid interface at the edge. However, v2 of the RheoPIV fixture has the capability of imaging the flow through the air-fluid interface, by repositioning the camera using the articulating arm that is mounted to the back of the rheometer.

Chapter 4

Rheo-PIV of Shear Banding Wormlike Micellar Solutions

4.1 Wormlike Micelles - A commonly studied shear banding material

This chapter will present a detailed examination of the shear banding phenomenon in a commonly studied wormlike-micellar solution. We recall that some recent studies have suggested that both wall slip [33, 122, 76] and unsteady secondary flows [74, 75] play an important role in the shear banding behavior of wormlike micellar solutions. The work in this chapter will therefore be a careful reassessment of the nonlinear rheological response of a model wormlike micellar solution in a cone and plate geometry, taking recent developments concerning wall slip and secondary flow into account. These results will both test the abilities of the RheoPIV device described in Chap. 3, but will also provide new insight into the transient shear banding behavior of surfactant solutions.

To probe the progressive onset of rheometrical limitations systematically, we will use oscillatory shearing deformations of progressively increasing amplitude. We will also provide a detailed discussion of some of the experimental issues encountered when carrying out velocimetric measurements on wormlike micellar systems - including a

discussion of the effect of secondary flows on PIV imaging, an experimental method used to delay the onset of wall slip, and the consequences of employing a rigid bounding surface at the edge of the cone–plate geometry to improve image quality. After accounting for these experimental difficulties, we show that the high spatial and temporal resolution of the Rheo-PIV system described in Chap. 3, enables us to observe in detail the local deformation behavior and corresponding stress evolution in a micellar solution. This behavior is observed at the onset of shear-banding under both steady and oscillatory shearing deformations.

The shear banded velocity profiles that will be presented here for a cone–plate device are similar to the 3-banded profiles observed by Britton and Callaghan [36], and are well described by a sigmoidal function - this is distinctly different from the 2-banded profiles that have been observed for flow of wormlike micelle solutions in cylindrical Couette cells [185]. Large amplitude oscillatory shear (LAOS) will be used to progressively deform the material deeper into the nonlinear regime and probe the onset of shear-banding behavior in the absence of substantial secondary flows and wall slip. We will also use the LAOS framework developed in previous work [50, 71, 73] to connect local kinematic measurements with nonlinearities in the bulk rheology, and show that the onset of shear banded velocity profiles closely coincides with the growth of nonlinearities in the bulk viscoelastic response. Similar behavior has recently been explored using some of the microstructural constitutive models that have been proposed for describing the rheology of shear banding systems [2, 220], providing a unique opportunity in the future for comparing experimental data with theoretical predictions.

4.2 Experimental

4.2.1 Micellar Fluid - CPyCl

In this chapter we will focus on a single canonical wormlike micellar fluid. The particular system studied is a solution consisting of 100mM cetylpyridinium chloride

(CPyCl) (Alfa Aesar) and 60mM sodium salicylate (NaSal) (Alfa Aeser) in de-ionized water. The system was seeded with 0.001 wt. % Titanium Dioxide particles (average size 3 μm, density 4200 kg/m^3 from TSI Inc.) for the purpose of the PIV measurements. These small particles result in a seeding (or number) density of particles that is high enough to carry out PIV measurements, however the low volume fraction of the particles ($\phi_v \simeq 2 \times 10^{-5}$) means that the particles do not significantly affect the rheology of the fluid. All measurements of the rheology of the CPyCl fluid in this chapter (rheometry and combined Rheo-PIV) were carried out on a TA instruments ARG2 stress controlled rheometer equipped with a 50mm diameter, 4° cone and plate geometry (quartz plate and aluminum cone) and with the temperature controlled to 25°C. Furthermore, all of the RheoPIV measurements are all carried out with the first iteration of the device (RheoPIV v1) which is discussed in Chap. 3. The particular test fluid differs from some of the fluids used in other shear banding studies (e.g. those by Salmon et. al. [185] and Lettinga et. al. [122]) because it is not prepared in brine and does not contain any added sodium chloride. However, an identical fluid composition (i.e. one without salt) has been used in a wide range of previous studies that have covered topics from bulk rheology [176], to microfluidic rheometry and steady channel flow [156] to shear banding in cone–plate geometries [36]. In Fig. 4-1 we summarize the shear rheology of the fluid (measured at 25°C) and show that it is well described by a single mode Maxwell model for low frequencies $\omega \leq 1/\lambda$, for which the viscoelastic moduli G' and G'' are given by the following expressions:

$$G'(\omega) = \frac{\eta_0 \lambda \omega^2}{1 + (\lambda\omega)^2} \quad ; \quad G''(\omega) = \frac{\eta_0 \omega}{1 + (\lambda\omega)^2} \tag{4.1}$$

For the data in Fig. 4-1 the fitting parameters are $\lambda = 1.45$s, $\eta_0 = 39$ Pa.s and $G_0 = 27$ Pa). In addition to this, the steady shear viscosity exhibits a strong shear thinning behavior and a clear stress plateau for rates larger than ~ 0.3 s^{-1}. In Fig. 4-1, the predicted shear stress obtained by using the Cox-Merz rule is also plotted. The Cox-Merz rule is an empirical relation that predicts that the magnitude of the complex viscosity is equal to the shear viscosity at corresponding values of frequency

and shear rate [29]:

$$\eta(\dot{\gamma}) = |\eta^*(\omega)|\Big|_{\omega=\dot{\gamma}} \tag{4.2}$$

From the Cox-Merz rule and the relationship between complex modulus and complex viscosity ($\eta^* = G^*/i\omega$) a prediction of the shear stress under steady shear can be obtained from oscillatory data. As can be seen in Fig. 4-1, there is a progressive deviation of this predicted shear stress from the measured value for shear rates larger than $\sim 0.3\ s^{-1}$ - this is in agreement with the observations made in previous studies [170]. In Fig. 4-1 we also indicate the points on the flowcurve where the strain rate amplitude of each of the oscillatory tests in Sec. 4.3 lies. This helps to illustrate the fact that the progressive increase in the strain amplitude under oscillatory shear can be interpreted, at least qualitatively, as a ramping up along the flowcurve into the stress plateau region, where shear banding is expected to occur. Additional bulk rheological measurements of an identical test fluid (eg. measurements of the normal stress data N_1) are provided in a recent study by Ober et. al.[156].

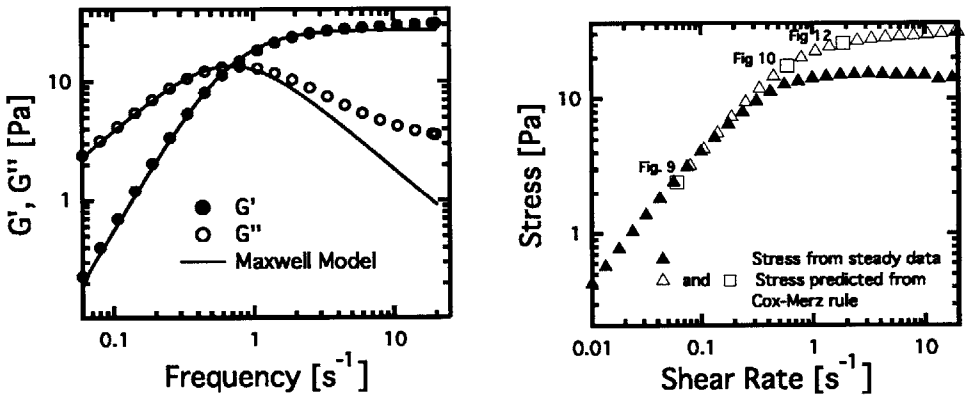

Figure 4-1: Linear viscoelastic moduli of the CPyCl test fluid (top) measured at a strain amplitude $\gamma_0 = 0.1$. The data is fit to a single mode Maxwell model for low frequencies ($\omega < 2$ rad.s^{-1}), with fitting parameters $\lambda = 1.45$s, $\eta_0 = 39$ Pa.s and $G_0 = 27$ Pa. In the lower plot, the steady flowcurve of the CPyCl system is given. The onset of pronounced shear thinning occurs around $0.3\ s^{-1}$. The hollow symbols correspond to the shear stress predicted from the dynamic data using the Cox-Merz rule [29]. Hollow squares correspond to behavior at strain rates equal to the amplitudes used in Figures 4-9, 4-10, 4-12

Controlling oscillatory strain with a stress controlled rheometer One important experimental aspect of the LAOS tests done in this chapter is the use of a stress controlled rheometer to impose an oscillatory strain on the CPyCl test fluid. While the ARG2 can control the strain on the sample through the use of a feedback loop, for some very non-linear fluids (e.g. yield stress fluids) controlled stress instruments may fail to impose a perfectly sinusoidal deformation, resulting in higher harmonic contributions to the periodic deformation [118]. For all of the LAOS experiments in this chapter, the power spectrum of the raw displacement signal from the ARG2 rheometer $\gamma(t)$ was analyzed to determine the relative magnitude of the next highest harmonic contribution to the strain field. For these experiments, the strength of the second highest harmonic contribution ($\omega_3 = 3\omega_1$) was at least 5 orders of magnitude lower than the primary forcing frequency even during shear banding.

4.2.2 Modifications to RheoPIV v1

We will introduce two optional features of the Rheo–PIV system (v1) that will be used to facilitate the measurement of the local velocity field within the CPyCl system. The first is the use of a removable plano-concave lens with radius $R = 25$ mm which can be placed up against the edge of the cone and plate geometry, as shown in the right image of Fig. 4-2.

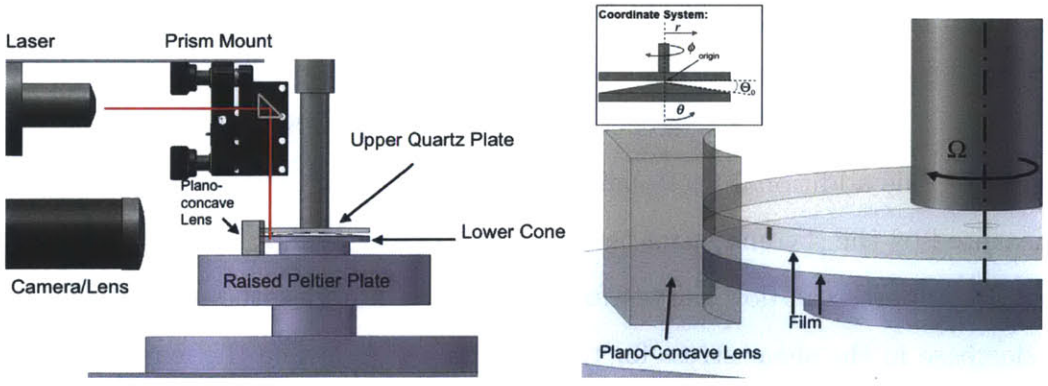

Figure 4-2: Schematic diagram (left) of the Rheo–PIV v1 system with added plano-concave lens. 3D model (right) showing how a plano-concave lens can be placed up against the edge of the cone and plate geometry. In addition it is shown how the transparent film is placed on the upper plate and lower cone.

The purpose of this lens is to provide a planar outer-facing surface through which the camera can image the field of view containing the illuminated seed particles. A flat front face prevents distortion of the image of the seed particles under flow, because rays reflected from the seed particles towards the CCD camera travel through the air-solid and solid-liquid interface at a direction normal to these interfaces. As discussed in Chap. 3, when the surface is not flat, refraction of the optical rays due to differences in the indices of refraction of the different media result in a distortion of the apparent location of the seed particles (thus making it difficult to determine the actual velocity profile within the fluid). When measuring local velocity fields within a Newtonian fluid, this plano-concave lens is typically not required. The upper and lower geometries have the same diameter, resulting in a pinning of the meniscus at the top and bottom edges and an almost flat meniscus profile. However, for viscoelastic fluids like CPyCl, edge instabilities may arise, which will result in an irregularly shaped meniscus even when it is pinned at the upper and lower edges [110, 104, 196]. Previous workers have recognized this and used circular bounding films to prevent these edge irregularities [197]. However, the effects of such bounding films can markedly change the local material response [196] and should therefore be avoided if possible. The plano-concave lens used in this work serves a similar purpose to a circular bounding film, but it does not surround the entire sample. This has the effect of lowering the incremental frictional torque that is imposed on the rotating fixture by such a surface. Nonetheless, there is still a measurable additional frictional force that is present when this lens is in place, due to the change in boundary conditions at the edge of the geometry and possible secondary flows induced near the rigid wall. This additional frictional force registers as an increase in the shear stress as measured by the rheometer for the CPyCl/NaSal system at a particular shear rate. Fig. 4-3 compares the flow curves for the fluid with and without the lens in place. The decrease in the shear stress for the final data point when the lens is in place is a result of the fluid being ejected from the gap, which is delayed to higher shear rates when the lens is not in place.

The second feature of the Rheo–PIV system that is used extensively in this work is

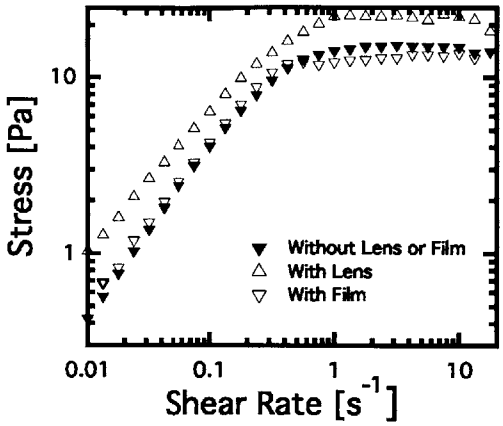

Figure 4-3: Comparison of the flowcurve of the CPyCl system measured using different configurations. Filled symbols are without the lens or film. Hollow symbols are either with the lens, or with the film, but not both. The presence of the lens results in an additional frictional torque being applied to the rotating quartz geometry, which leads to an increase in the apparent shear stress measured by the instrument.

a transparent adhesive polymer film (SS-45 screen protector manufactured by Vivitar) which can be placed on either (or both) the upper or lower geometry, such that the fluid is in contact with this film instead of the polished quartz upper plate or the machined aluminum lower conical fixture. When affixed to the upper quartz geometry, the film has the effect of increasing the roughness of the upper surface, as well as making the surface slightly more hydrophobic. Table 4.1 compares the contact angle of a sessile drop of CPyCl on the quartz surface with and without the adhesive plastic film, as well as the measured surface roughness. As we show below, a result of this modified surface is that slip effects which are often observed for CPyCl solutions at high shear rates (such as those seen by Lettinga and Manneville [122]) can be suppressed to a substantial degree. The effect of surface roughness and hydrophobicity on inhibition of slip is not surprising, and these effects have been documented in previous studies [135]. Unlike the lens, this film does not have a considerable effect on the flowcurve shown in Fig. 4-3.

Fig. 4-4 (a) presents data from calibration experiments which demonstrate the linearity of the velocity profiles obtained by the Rheo–PIV system over a wide range of shear rates spanning those used in this work, for a Newtonian fluid (seeded heavy

Table 4.1: Comparison of surface roughness and equilibrium contact angle of CPyCl test fluid for the aluminum cone and the quartz plate with, and without, the transparent adhesive film. The roughness is measured using a Mitutoyo Surftest SJ-210 profilometer and the contact angle is measured with a Ramé Hart Model 590 contact angle goniometer. Surface roughness measures are R_a (arithmetic average of roughness values), R_q (root mean squared roughness) and R_z (maximum roughness).

Material	Aluminum Cone	Quartz Plate	Quartz + Film
Roughness			
R_a (μm)	0.28±0.04	0.014±0.001	0.045±0.007
R_q (μm)	0.35±0.06	0.018±0.001	0.067±0.01
R_z (μm)	1.8±0.5	0.115±0.006	0.5±0.09
Contact Angle	42±3°	27.3±1.4°	43±3°

mineral oil with a viscosity of 0.1 Pa.s and a density of 880 kg/m^3). The velocity profiles are averaged over approximately 450 frames of video (i.e. 7.5 seconds of flow) and plotted in the form of y/H vs v/V_w, where y is the position across the gap ($y \simeq R_i(\theta - \pi/2 + \Theta_0)$), $H \simeq R_i\Theta_0$ is the gap height at the position $r = R_i$ ($H = 1.6$ mm) and V_w is the velocity of the top surface given by $V_w = \Omega R_i = \dot{\gamma}H$. In addition to this, Fig. 4-4 (b) shows a comparison of the velocity profile measured for a Newtonian fluid undergoing a shear rate of $\dot{\gamma} = \Omega/\Theta_0 = 0.5$ s^{-1} when the upper and lower geometries are covered with the adhesive film and left uncovered. As expected, the presence of the film does not alter the velocity profile. The inset in Fig. 4-4 (b) gives the probability distribution of the measured velocity values at a height of 0.75 mm from the lower cone. The standard deviation of the velocity measured at that location is 0.02 mm/s, which is approximately 5% of the measured velocity (determined from $\sim$ 14000 PIV correlation measurements).

The experimental velocity measurements at a fixed spatial position show a well-define average velocity with a Gaussian distribution that arises primarily from small mechanical vibrations in the frame which holds the camera/lens assembly. This results in small random and uncorrelated relative displacements of the camera and rheometer, which are interpreted as small nonzero velocities in the flow by the PIV analysis (these velocities will be on the order of 0.02 mm/s, as given by the measurement of the

standard deviation). However, averaging flow profiles over several frames (typically 5 or more) removes any small instantaneous bias that may result from the vibrations. While these vibrations do not have an effect on the time averaged velocity profiles, we can still see some small systematic deviations of the time averaged velocity profile from the predicted linear velocity profile in Fig. 4-4. These deviations are chiefly a result of the air-fluid interface at the outer sample edge which is not perfectly flat. Despite the fact that the interface is pinned at the upper and lower plates, small variations in sample volume always result in a slightly curved air-fluid interface. While these slight variations in sample volume are impossible to eliminate entirely, inspecting the shape of the interface by eye is typically sufficient to ensure that reliable velocity profiles are obtained by the Rheo-PIV apparatus.

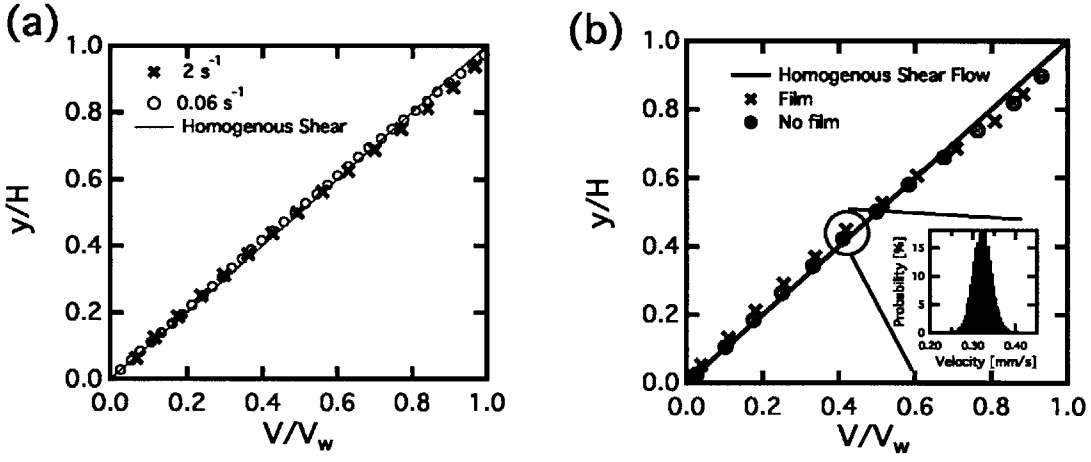

Figure 4-4: Scaled velocity profile of a viscous Newtonian fluid undergoing steady shear at two different shear rates in (a), indicating linearity of the profiles. In (b), the velocity profile within the same Newtonian fluid at a fixed shear rate ($\dot{\gamma} = 0.5\ s^{-1}$) is compared for when the upper and lower plates are covered with the transparent adhesive film. The inset in (b) shows the probability distribution of the measured velocity values at a height of 0.75 mm from the lower cone.

4.3 Results

4.3.1 Steady Shear Rate banding of CPyCl

It is well known that wormlike micellar solutions exhibit shear banding under steady shear flow. Many workers have observed this behavior directly using a variety of velocimetric techniques and under a number of different flow configurations [122, 185, 124, 36, 39, 33]. Britton and Callaghan [36, 37] showed, using NMR velocimetry, that a CPyCl:NaSal 100:60 mM system (identical to the one used in this work) exhibited a three-banded velocity profile, in which a high shear rate band is observed in the middle of the gap, connected to two lower shear rate regions near the upper and lower surfaces. Due to the fact that Britton and Callaghan [36, 37] worked with a fluid identical to that dealt with in this work (with similar values of the measured relaxation time and critical shear rate), and a similar flow configuration (4°/24 mm diameter and 7°/16 mm diameter ceramic cone and plate with an outer containment jacket at the edge), we expect that the velocity profiles observed here should be similar to those observed by Britton and Callaghan. Fig. 4-5 shows the velocity field within the CPyCl solution observed using the Rheo-PIV system at a number of different imposed shear rates. As the figure shows, the velocity profiles evolve from a linear response to 3-banded profiles as the shear rate is incremented slowly from 0.1 s^{-1} to 0.75 s^{-1} and into the stress plateau region. The 3-banded profile in Fig. 4-5 at a shear rate of $0.75s^{-1}$ is characterized by a high shear rate region near the middle of the gap, and lower shear rate regions near the upper and lower surfaces. The behavior at the high shear rates is thus consistent with the 3-banded profiles observed by Britton and Callaghan. However, Britton and Callaghan generally measured their shear banded profiles at even higher shear rates well into the stress plateau region (their use of an outer containment jacket allowed for this by preventing sample from being ejected from the gap). They therefore did not probe the behavior of the fluid in this transition region at lower shear rates. During the transition from linear to 3-banded profiles (for imposed shear rates of $\dot{\gamma} = 0.3$ s^{-1} and $\dot{\gamma} = 0.45$ s^{-1}) the material exhibits an intermediate behavior in which the flow profile appears to have

two developing shear bands instead of three clearly distinct bands. This is in contrast to some shear banding scenarios which have been observed in other geometries (such as those observed by Salmon et. al. [185] in Couette flow) where the shear rate in the highly sheared band remains constant and the interface between the low and high shear rate regions moves as the apparent shear rate is increased.

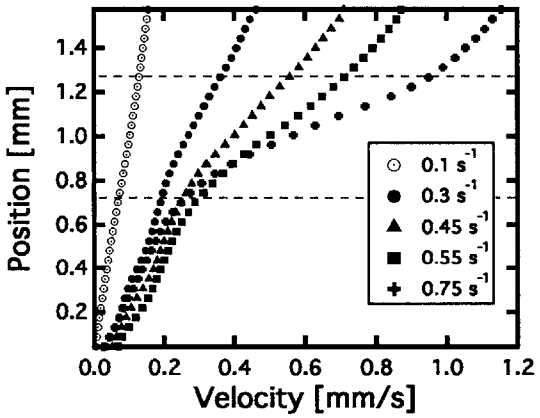

Figure 4-5: Series of steady state velocity profiles observed in the CPyCl test fluid as the shear rate is changed incrementally from 0.1 s^{-1} to 0.75 s^{-1}. At the lowest shear rate the profile is clearly linear, but develops into a 3-banded profile with a region experiencing a higher shear rate near the center of the gap. The dashed grey lines indicate the location of this high shear rate region.

The data presented in Fig. 4-5 was obtained without the plano-concave lens in place, and with the upper and lower geometries being covered by the transparent film. The transparent film was used because it was observed that it generally prevents slip from occurring at the upper plate at moderate shear rates. Fig. 4-6 shows a comparison of the velocity profiles observed in the CPyCl system at the identical steady shear rate of 0.75 s^{-1} in the 4° cone and plate geometry with and without the use of the lens and film.

Fig. 4-6 demonstrates the exquisite sensitivity of Rheo-PIV observations to the imposed boundary conditions. The measured velocity profiles are different in all four cases; The profiles (c-d) show that when the lens is not used, the additional presence of the film on the upper plate prevents wall slip from occurring at that surface. The presence of this wall slip results in a lower shear rate within the bulk of the fluid,

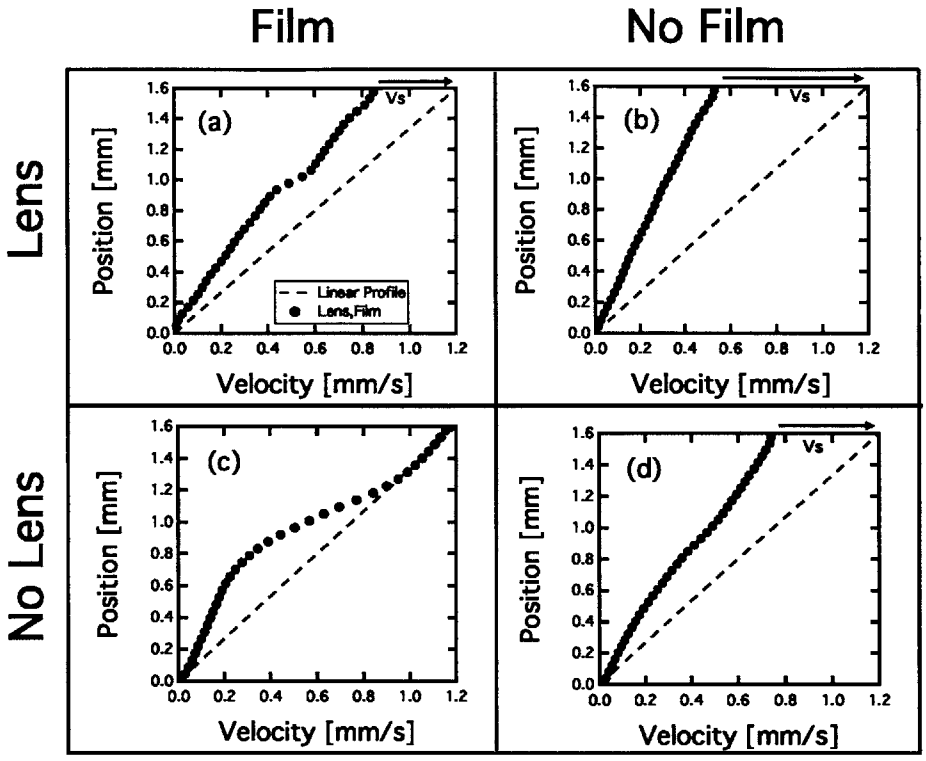

Figure 4-6: Steady state velocity profiles measured at $\dot{\gamma} = 0.75\ s^{-1}$ under different configurations of the Rheo–PIV system. When the plano-concave lens is not used, the film clearly eliminates slip at this shear rate. When the lens is used, the film is less effective and the banded behavior exhibited by the fluid is different - a narrower band appears near the midgap.

causing the velocity profile to appear similar to the profiles observed in Fig. 4-5 for shear rates lower than 0.75 s^{-1}. This suggests that when the plano-concave lens is not used, the transparent film eliminates wall slip and facilitates the formation of the centrally located high shear rate band. However, when the lens is used, as in (a-b), a rather different behavior is observed. Now, the addition of the transparent film only reduces the degree of slip that is present, and does not completely eliminate it. In addition to this, the appearance of the shear banded velocity profile for the case when the lens is used (Fig. 4-6 (a)) is now markedly different to the banded profile shown in Fig. 4-5 for $\dot{\gamma} = 0.75\ s^{-1}$. The banded profile is now characterized by a highly localized high shear rate band in the center (only 2 or 3 data points in width) which more closely resembles a discontinuity in the velocity, as opposed

to the more gradual variation in the shear rate across the gap that is observed in Fig. 4-5. In general, these narrow bands, resembling discontinuities in the velocity profile, have only been observed when the plano-concave lens is used as a bounding surface. However, this behavior is mostly erratic and difficult to predict - the bands can be observed in different positions across the gap for the same imposed shear rates, and in other instances a larger degree of wall slip may occur on the upper surface resulting in a less pronounced high shear rate band. Two high shear rate bands have also been observed at some of the larger shear rates. One possible explanation for this irreproducible behavior is that the presence of the lens may result in an earlier onset of secondary flow within the region of the fluid near the lens, due to the altered boundary condition at the bounding surface.

In order to avoid any potential artifacts that may arise from this plano-concave lens, and also in order to avoid artifacts in our bulk rheological data (Fig. 4-3), we henceforth utilize the configuration shown in the lower left corner of Fig. 4-6 for the rest of our experimental data, i.e. an adhesive film attached to both upper and lower fixures and no lens at the outer edge. This results in reproducible and self consistent behavior as shown in Fig. 4-5. Furthermore, in Fig. 4-7 we show that at the range of shear rates probed in Fig. 4-5, no irregularities in the fluid meniscus at the edge of the cone-plate geometry are observed. This shows that a plano-concave lens or any other bounding film is in fact not required in this CPyCl fluid for velocimetric measurements at these shear rates.

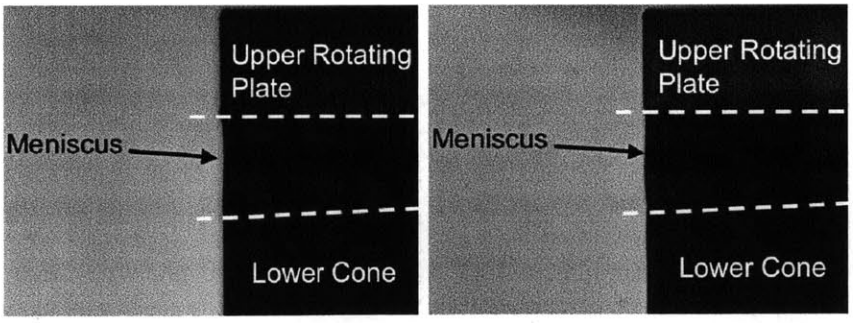

Figure 4-7: Photographic images of fluid meniscus for CPyCl undergoing a shear rate of $\dot{\gamma} = 0.1\ s^{-1}$ (left) and $\dot{\gamma} = 0.75\ s^{-1}$ (right). In both cases, the meniscus remains flat and unperturbed.

4.3.2 Onset of Secondary Flow

The velocimetric data presented in figures 4-5 and 4-6 are only given for shear rates as high as 0.75 s^{-1}. At much larger shear rates, the local shear banded behavior of the fluid becomes much more difficult to observe for several reasons. Firstly, the likelihood of a severe edge irregularity in the meniscus arising is much greater. As discussed in Chap. 3, this results in larger errors in the measured velocity values. While the use of the plano-concave lens (or any other type of bounding film) to impose a planar imaging surface may avoid the issue of these edge irregularities, it still affects the bulk measured stress (Fig. 4-3) as well as the flow kinematics by altering boundary conditions near the edge resulting in the erratic behavior that was discussed in Sec. 4.3.1. Another difficulty that is faced at very large shear rates (typically exceeding 3 s^{-1}, or Weissenberg numbers $\mathrm{Wi} \equiv \lambda\dot{\gamma} \geq 4.4$) is that at the given magnification of the camera/lens, the displacement of seed particles between frames becomes large enough such that the cross-correlation algorithm is unable to resolve the displacement value. This may be avoided by using a lower lens magnification, however lower magnifications result in a concomitant loss of spatial resolution for the velocity profiles. As a result of these difficulties, we choose to restrict our regime of study of the CPyCl solution to shear rates generally lower than 2 s^{-1} (or $\mathrm{Wi} \leq 2.9$), where secondary flows are less likely to occur and experimental artifacts will not play an important role in our measurements (particularly for the LAOS experiments which follow in Sec. 4.3.4).

To verify that there are not any appreciable secondary flows at these lower shear rates, we used an alternative imaging method to observe flow of the CPyCl solution under steady shear in the cone–plate geometry. Specifically, a small amount of Kalliroscope AQ-RF rheoscopic fluid (http://www.kalliroscope.com/) was added to the micellar solution. This rheoscopic fluid contains a high concentration of plate–like mica seed particles. Flow alignment of these seed particles allows for macroscopic flow in the CPyCl solution to be visualized and for qualitative changes with increasing shear rate to be observed. These seed particles have been used previously to

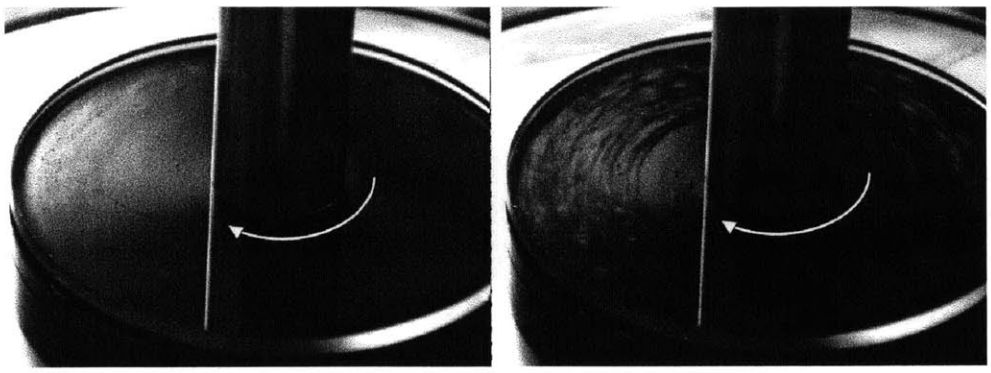

Figure 4-8: aImages taken during steady shear at $\dot{\gamma} = 2\ s^{-1}$ (with Reynolds number $\mathrm{Re} \equiv \frac{\rho\dot{\gamma}R_i^2\Theta_0^2}{\eta} = 0.001$ and Weissenberg number $\mathrm{Wi} = 2.9$) on the left, and $\dot{\gamma} = 5\ s^{-1}$ ($\mathrm{Re} = 0.006$, $\mathrm{Wi} = 7.3$) on the right. The distortions seen near the outer edge for the higher shear rate case are a result of the onset of secondary flow. The distortions begin appearing near the outer edge at a critical Weissenberg number $\mathrm{Wi} \simeq 6$, and grow towards the center over time. The timescale for the distortions to fill the gap is much greater than the relaxation time λ.

observe secondary flows in other viscoelastic fluids [137, 74]. The sample is placed in the cone–plate geometry (with upper transparent quartz plate) and illuminated from above using a white light source. A black anodized lower cone is utilized to enhance contrast of the seed particles and a camera with a telecentric zoom lens is used to observe the evolution of flow induced structures in the fluid. Fig. 4-8 shows two images obtained from the imaging system during steady shear of the CPyCl solution at two different shear rates. At the low shear rate ($2\ s^{-1}$) the fluid appears homogenous with no patterns emerging during the purely tangential flow. However at the higher shear rate ($5\ s^{-1}$) radial and tangential striations in the flow field are clearly seen, as evidenced by the regions of varying contrast in the fluid further away from the center. By observing the evolution of these structures during start-up of steady shear at these higher shear rates, it is apparent that the regions of varying contrast begin to form near the rim of the sample, grow in time and propagate radially towards the center. Corresponding measurements of the total torque exerted on the fixture show the growth of temporal fluctuations [215, 170]. This suggests that a three-dimensional unsteady secondary flow first develops near the outer edge where the sample meniscus is located, and propagates towards the center. The images in

Fig. 4-8 are not intended to provide quantitative detail about the exact nature of the viscoelastic secondary flow that develops in this micellar fluid (i.e. direction, magnitude), however they do show what regions of the fluid are first afflicted, and can be used as a guideline to understand at what shear rates one might expect 2D velocimetric data from Rheo-PIV to begin to show artifacts that arise from significant secondary flow.

4.3.3 The Linear Viscoelastic Regime - SAOS

The ability of the Rheo–PIV setup to provide time resolved images of the local flow behavior makes it well suited for studying the behavior of complex fluids under oscillatory flow. Combined measurements of the bulk rheology and local velocity field within the CPyCl solution were therefore first obtained for small amplitude oscillatory deformations and moderate frequencies to ensure that the expected linear behavior of the fluid is recovered. For this particular experiment, the fluid is loaded into the 4° cone and plate geometry (covered with the transparent film, without the lens in place) and an oscillatory strain $\gamma = \gamma_0 \sin \omega_d t$ is imposed on the sample with $\omega_d = 0.63$ rad.s^{-1} and $\gamma_0 = 0.1$. The resulting Deborah and Weissenberg numbers for this experiment defined as $\mathrm{De} \equiv \lambda\omega_d$ and $\mathrm{Wi} \equiv \lambda\omega_d\gamma_0$ are therefore equal to 0.91 and 0.09 respectively. The imaging system was set up to record images at a frame rate of $F = 60$ frames per second. At this particular frame rate, the system is able to resolve a velocity profile within the fluid every 0.017 seconds - allowing for approximately 600 velocity measurements to be made within each period of oscillation, and providing sufficient data to resolve temporal changes in the velocity field within the fluid. Fig. 4-9 gives the combined bulk rheology (stress and strain determined from torque and angular velocity of the instrument) as well as the locally measured velocity within the fluid. In Fig. 4-9 (a) a series of velocity profiles are plotted over the course of one half period. Each velocity profile is averaged over 20 frames (both spatially for each frame, in the direction of flow, and temporally by averaging over the 20 individual frames) and plotted every 20 frames (corresponding to a 0.33 second interval). This makes individual profiles more easily discernible and minimizes random fluctuations

due to small mechanical vibrations in the system. The variation in velocity across the gap is clearly linear, with no slip occurring at the bottom surface. In Fig. 4-9 (b) a comparison of the velocity of the top plate determined using two different methods is shown. The continuous line corresponds to the angular velocity of the rotating fixture $V_w = \omega_d R_i \cos\omega_d t$ imposed by the rheometer. The individual points (crosshairs) are data that correspond to the velocity measured in the fluid (using the PIV system) in the row of 16×16 correlation windows closest to the top plate. The comparison shows that these two velocities agree over the course of one full period of oscillation, indicating that there is no wall slip occurring at the upper surface.

The third plot shown in Fig. 4-9 (c) is a Lissajous curve of the bulk stress–strain response of the fluid to the oscillatory deformation (averaged over five periods of oscillation). The data is analyzed using the MITlaos software package [71] in order to extract the decomposed elastic stress [50, 71] as well as the higher order Fourier/Chebyschev coefficients that describe the periodic stress response (which were discussed in Chap. 2). By computing the magnitude of the ratio of the third order coefficients to the first order coefficients (e_3/e_1 and v_3/v_1) it is possible to determine the extent of nonlinearity in the material response. From the low values $e_3/e_1 = -8 \times 10^{-4}$ and $v_3/v_1 = 9 \times 10^{-4}$ and the ellipsoidal nature of the Lissajous curve it is clear that the material is exhibiting primarily a linear response at this strain amplitude and frequency. Additional details pertaining to the higher-harmonics of the stress response are provided in the form of a power spectrum in Fig. 4-9 (d). The power spectrum is illustrated by plotting the magnitude of both the imaginary and real parts of the Fourier transform $\breve{\sigma}(\omega)$ of the stress response $\sigma(t)$ against the frequency index ω/ω_d (where $\omega_d = 0.63$ s^{-1} is the driving frequency). The imaginary part of the Fourier transform $\breve{\sigma}_i(\omega)$ corresponds to the component of the stress which is in-phase with the strain $\gamma = \gamma_0 \sin\omega_d t$ and the magnitude of the local peaks $\breve{\sigma}_i(n\omega_d)$ are directly related to the elastic Chebyshev coefficients e_n (see [71] for these relations). On the other hand, the real part of the Fourier transform $\breve{\sigma}_r(\omega)$ corresponds to the out of phase component of the stress and the peaks at $\breve{\sigma}_r(n\omega_d)$ are related to the viscous

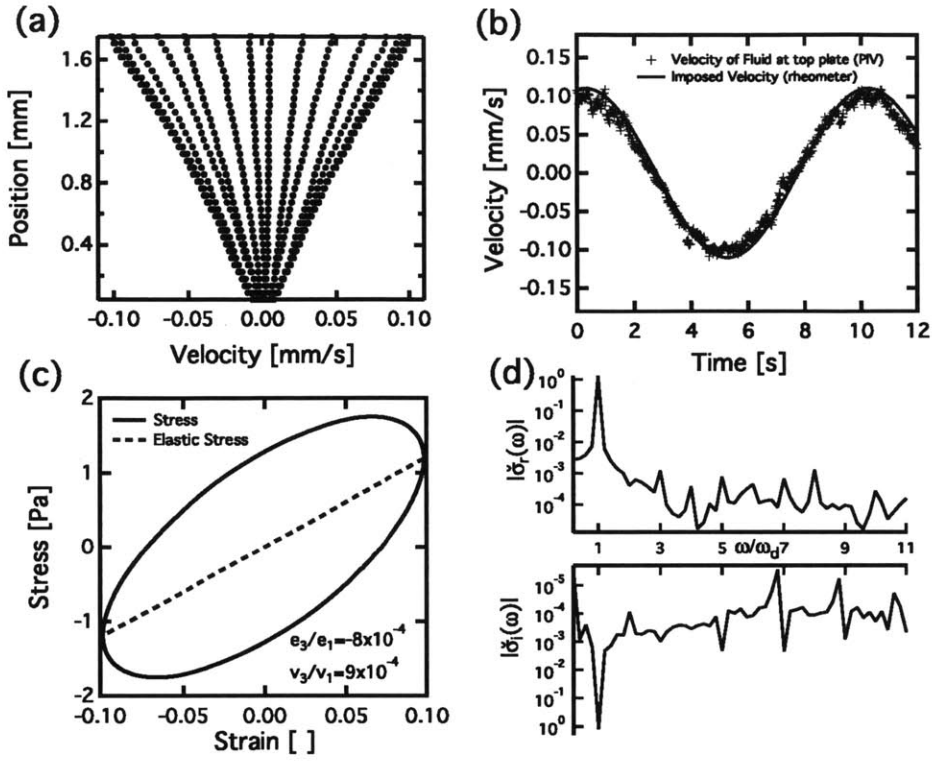

Figure 4-9: Local and global rheological response of the CPyCl fluid under oscillatory shear with $\gamma_0 = 0.1$ and $\omega_d = 0.63$ rad.s^{-1} (De = 0.91, Wi = 0.09). In (a), the evolution of the local velocity field is shown over one half of a period with 15 velocity profiles evenly spaced every 0.33 seconds. In (b) the velocity of the fluid at the top plate (determined using PIV) is compared with the imposed velocity of the upper rotating surface - their agreement indicates no slip is occuring. In (c) the bulk stress and strain are plotted in the form of a Lissajous curve, and in (d) the power spectrum of the stress is provided by plotting the real and imaginary parts of the discrete Fourier transform of the stress, $\breve{\sigma}(\omega)$.

Chebyshev coefficients v_n. The spectral resolution of the data shown in Fig. 4-9 (d) is determined by the number of cycles recorded (5 cycles resulting in a resolution of $\Delta\omega = \omega_d/5$) while the maximum frequency component resolvable $\omega_{\max}$ is determined by the rate of sampling of the stress signal ($\omega_{\max} = \pi f = 188$ s^{-1} from a sampling rate of $f = 60$ Hz). The data however is only plotted up to $\omega/\omega_d = 11$ because the higher frequency components are primarily from background noise in the measured stress signal. The prominent peak for $\omega/\omega_d = 1$ and the very small magnitude of the higher harmonics in Fig. 4-9 (d) ($\omega/\omega_d < 0.005$ for all d) reinforces the fact that for

$\gamma_0 = 0.1$ the wormlike micellar fluid is within the linear regime of deformation.

4.3.4 Large Amplitude Regime - LAOS

Measurements of the form shown in Sec. 4.3.3 illustrate the expected linear response of the CPyCl solution at small strain amplitudes ($\gamma_0 \ll 1$). In this section, the strain amplitude is increased to $\gamma_0 = 1$ (keeping the imposed frequency constant at $\omega_d = 0.63$ rad.s^{-1}) and the evolution in the velocity field within the fluid is measured. Fig. 4-10 (a) shows the evolution of the velocity field within the fluid over one half period of oscillation. The profiles are plotted in the same manner as in Fig. 4-9 (a), i.e. every 20 frames and as averages over 20 frames. While this manner of plotting profiles does not technically show the true instantaneous velocity profile, the 20 frame averages were compared with single frame profiles and the two showed good agreement. Thus, error bars indicating the standard deviation of the velocity measurements (omitted in the plot) are typically the same size as the hollow symbols. At this larger strain amplitude, there is clear evidence of an inhomogenous banded flow with the velocity profile beginning to develop characteristics similar to those observed in Fig. 4-5 for steady shear flow at high shear rates. Due to the self-similarity of the velocity profiles observed during the oscillatory flow, each profile is fitted to the following functional form:

$$v(y) = V_w \left[s\left(\frac{y}{H}\right) + \frac{(1-s)}{2}\left(1 + \tanh\left(b\frac{(y-y_b)}{H}\right)\right)\right], \tag{4.3}$$

where y is the position across the gap, $y_b(t)$ is the position of the middle of the centrally located high shear rate band, and $b(t)$ is a measure of the band sharpness. For the case of large values of $b > 1$ (i.e. a sufficiently sharp band), $V_w(t)$ can be thought of as the velocity of the fluid at the upper wall at each point in time, and the parameter s can be thought of as a ratio of two shear rates, $\frac{\dot{\gamma}_0}{\dot{\gamma}_a}$, where $\dot{\gamma}_0$ is the "background" shear rate of the low shear rate regions near the top and bottom surfaces, and $\dot{\gamma}_a \equiv \frac{V_w}{H}$ is the apparent or nominal shear rate (V_w is the velocity at the wall and H is the gap height). This functional form has 4 parameters that are

determined using a non-linear least squares minimization technique to fit to each profile of Fig. 4-10 - these parameters are $V_w(t)$, $b(t)$, $y_b(t)$ and $s(t)$ (or $\dot{\gamma}_0(t)$). Fig. 4-10 (a) shows an excellent agreement between the measured velocity values and the sigmoidal fit. The excellent fit to the functional form in Eq. 4.3 (a continuous function) suggests that the shear rate within the fluid varies continuously across the gap - this differs from observations made of banding under steady shear in Couette cells (see the work by Salmon et. al. [185] or Ballesta et. al. [15]), however the work by Britton and Callaghan [36, 37] did show that in cone-plate geometries, continuously varying shear rates were observed.

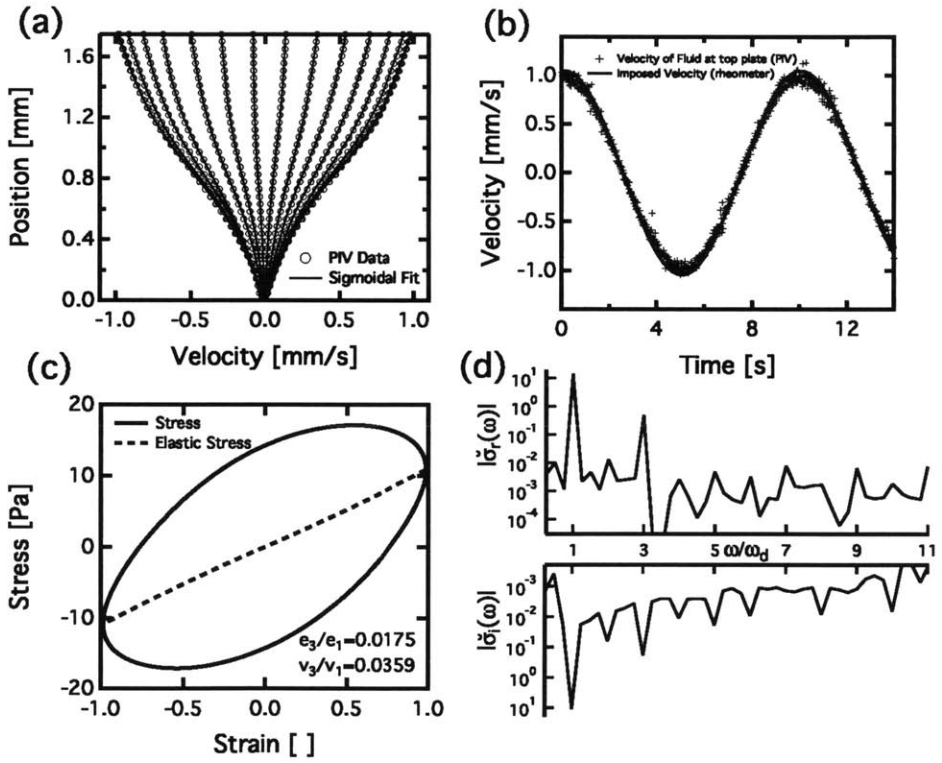

Figure 4-10: Local and global rheological response within the CPyCl fluid under oscillatory shear with with $\gamma_0 = 1$ and $\omega_d = 0.63$ rad.s^{-1} (De = 0.91, Wi = 0.91). Shear banded profiles are now clearly seen in (a), and are fit to the sigmoidal function of Eq. 4.3. The bulk response in (c) and power spectrum in (d) indicate that the material is beginning to exhibit nonlinear behavior.

In addition to this spatially-banded structure, there is also good agreement between the measured velocity in the fluid adjacent to the top wall, and the oscillating

velocity of the top plate, as seen in Fig. 4-10 (b). Once again, this indicates that there is no wall slip occuring at the top surface, and that the transparent film is effective at preventing slip for this particular oscillatory experiment.

Fig. 4-10 (c) shows the Lissajous curve of the material stress-strain response for these particular oscillatory strain conditions. Qualitatively the curve looks very similar to that of Fig. 4-9 (c), however the larger values of the ratios $e_3/e_1 = 0.0175$ and $v_3/v_1 = 0.0359$ compared to the values for $\gamma_0 = 0.1$ indicate that the material is beginning to experience deformations in the non-linear regime. One interesting aspect of this set of data is how low the values of e_3/e_1 and v_3/v_1 are even though the material starts exhibiting a distinctly shear banded velocity profile. This suggests that for this particular fluid, relying on direct velocimetric measurements - and not on measurements of higher harmonics in the stress response - is a more sensitive probe of the onset of shear banding under LAOS.

In order to study any possible dynamic behavior of the shear bands, we tracked the middle position of the high shear rate band over one complete oscillation by plotting the value of the fitting parameter $y_b(t)$ (which corresponds to the location of the center of the high shear rate band) and the band sharpness $b(t)$ over the course of one period of oscillation. This data is shown in Fig. 4-11 and indicates that the values of y_b and b remain relatively constant over time. The center of the high shear rate band remains located near the middle of the sample at $\langle y_b \rangle = 0.8$ mm, while the value of $b(t)$ also remains constant with an average value of $\langle b \rangle = 3.78$. One interesting result is that the centrally located band is resolved for almost all points in time over the course of the oscillation. The only time period where the fitting technique cannot accurately locate the band is at the points of maximum strain (i.e. at the dashed vertical lines in Fig. 4-11). At these points the velocity within the fluid is almost zero everywhere (the imposed sinusoidal oscillation has reached maximum displacement) and so the fitting function of Eq. 4.3 is under-constrained.

The LAOS behavior of the micellar fluid was also probed at an even larger strain amplitude $\gamma_0 = 3$, and once again local velocimetric data was compared with bulk measurements from the rheometer. Fig. 4-12 (a) shows a more pronounced banding

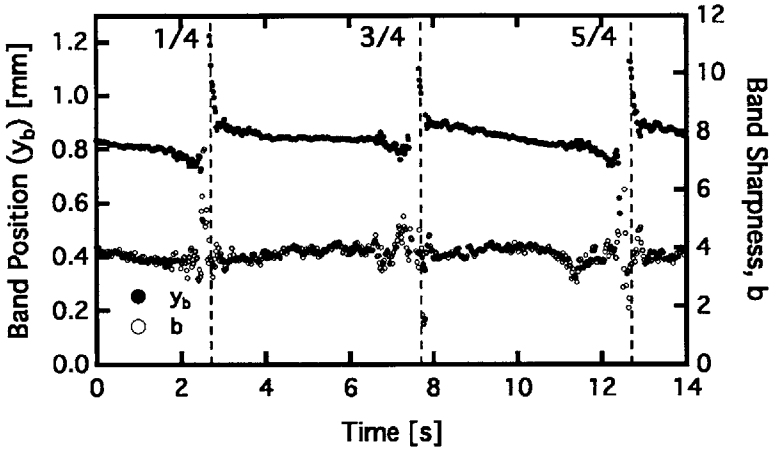

Figure 4-11: Value of the fitting parameters y_b (band position) and b (band sharpness) during one period of oscillation ($T = 2\pi/\omega_d = 9.97$s) for the velocimetric data given in Fig. 4-10. Dashed vertical lines indicate times where the fluid has undergone 1/4, 3/4 and 5/4 of a period.

behavior in the set of velocity profiles measured during one half period. This data is also fit to the sigmoidal function described in Eq. 4.3 and the agreement between the fit and the measured data is excellent. Fig. 4-12 (b) again indicates that there is no observable wall slip occurring on the upper surface. The Lissajous curve presented in Fig. 4-12 (c) shows that the bulk stress-strain data of the fluid now exhibits a clearly nonlinear response. The values of e_3/e_1 and v_3/v_1 are now much larger than they were for the case in which γ_0=1. The positive value of e_3/e_1 can be attributed towards an intra-cycle strain stiffening in this material [71, 73]. It is the appearance and growth of these higher harmonics that lead to the progressive deviation of the shear stress magnitude measured in steady and oscillatory shear and the failure of the Cox-Merz rule (see Fig. 4-1).

One interesting aspect of Fig. 4-12 (d) is the appearance of a more enhanced even harmonic at $\omega = 2\omega_d$ in the imaginary part of the discrete Fourier transform of the stress response. This suggests that there may be a small amount of wall slip occurring in the system [94, 14] however the fact that this harmonic is still relatively weak (a factor of 4 weaker than the intensity of the third harmonic at $\omega = 3\omega_d$) means that any wall slip that may be occurring is difficult to discern in figures 4-12 (a) and (b)

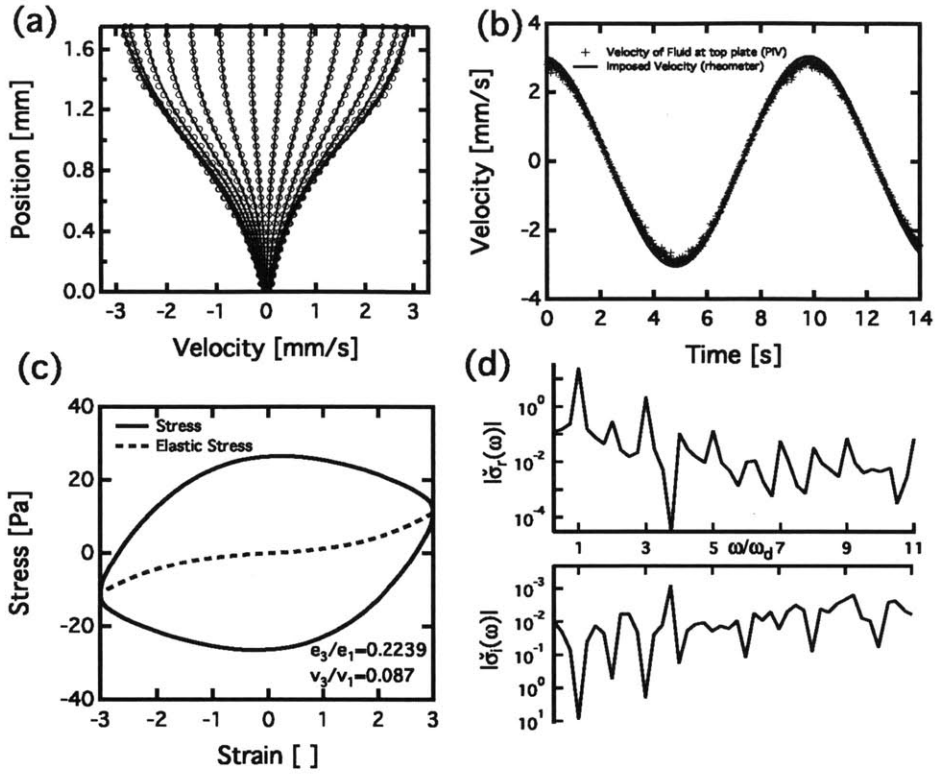

Figure 4-12: Local and global rheological response within the CPyCl fluid under oscillatory shear with $\gamma_0 = 3$ and $\omega_d = 0.63$ rad.s^{-1} (De = 0.91, Wi = 2.73). The banded velocity profiles in (a) are now even more pronounced, and the Lissajous curve shown in (c) is clearly no longer elliptical, indicating that the material response is no longer linearly viscoelastic.

and does not significantly affect the material response.

In Fig. 4-13 we plot the temporal evolution of the fitting parameters y_b and b for the velocimetric data shown in Fig. 4-12. For this instance the average values $\langle y_b \rangle = 0.96$ mm and $\langle b \rangle = 4.30$ are larger than they were for the case in which $\gamma_0 = 1$ - this gives the appearance of a sharper band. The generally higher value of b agrees with what is observed under steady shear as the imposed shear rate is ramped up. Specifically, for the velocity profiles plotted in Fig. 4-5, as the value of $\dot{\gamma}$ is ramped up from 0.45 s^{-1} to 0.55 s^{-1} and 0.75 s^{-1} the fit of Eq. 4.3 to the velocity profiles yields respective values for b of 2.9, 3.2 and 3.7. Thus, more sharply banded profiles are observed at higher imposed shear rates.

The local temporal behavior of $y_b(t)$ and $b(t)$ indicates that there are more pro-

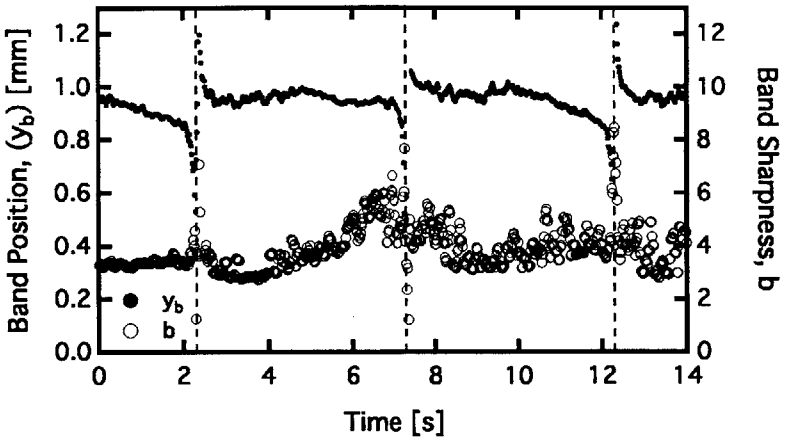

Figure 4-13: Value of the fitting parameters y_b and b during one period ($T = 2\pi/\omega_d = 9.97$s) of oscillation for the velocimetric data given in Fig. 4-12.

nounced fluctuations occurring at this larger amplitude. However, the fluctuations in $y_b(t)$ are still small (on the order of 50 μm) and do not suggest that there is considerable intra or inter-cycle shift of the band position. A drift in the value of y_b of approximately 100 μm can be seen for 0 s $\leq t \leq$ 2 s and 10 s $\leq t \leq$ 12 s (before the sharp discontinuities at 2.2 and 12.2 seconds). However it is difficult to unambiguously determine the origin of this periodic fluctuation. One possible source of this drift is slight irregularities in the air-sample interface which arise at points in the cycle when the sample has undergone a maximum deformation. These irregularities distort the image, resulting in an apparent shift of the band position. An alternative source for these fluctuations is the type of dynamic band motion predicted in some theoretical studies [220]. These fluctuations might be expected to grow as the imposed strain amplitude is increased. However, with RheoPIV v1, observing these dynamics at larger strain amplitudes is difficult due to even more pronounced interface irregularities. The design of RheoPIV v2 provides a potential opportunity for probing these dynamics at larger strain amplitudes, however we have restricted our focus in this chapter to the transition regime and leave this as a possible future endeavor.

While the data from this particular oscillatory test shows little variation in the value of y_b, equivalent Rheo-PIV tests done with the plano-concave lens result in

profiles in which there is a sharper or narrower band near the midgap that moves vertically across the gap during the oscillation. An example of such a test is shown in Fig. 4-14, where an oscillatory deformation with a strain amplitude of $\gamma_0 = 300\%$ is imposed at a frequency of 0.63 rad/s. In Fig. 4-14 (a) and (b), the band near the midgap appears much narrower, and the plot of the band position in (b) and (c) shows a clear variation (y_b/H varies from 0.4 to 0.25). This data, when compared with the data shown in Figs. 4-5 (a-c) and 4-12, emphasizes the fact that the presence of the lens or a rigid outer boundary results in a markedly different type of flow behavior. Specifically, sharper shear bands are observed (compare Fig. 4-14 (a) with Fig. 4-12 (a)), and y_b fluctuates more over the course of an oscillation.

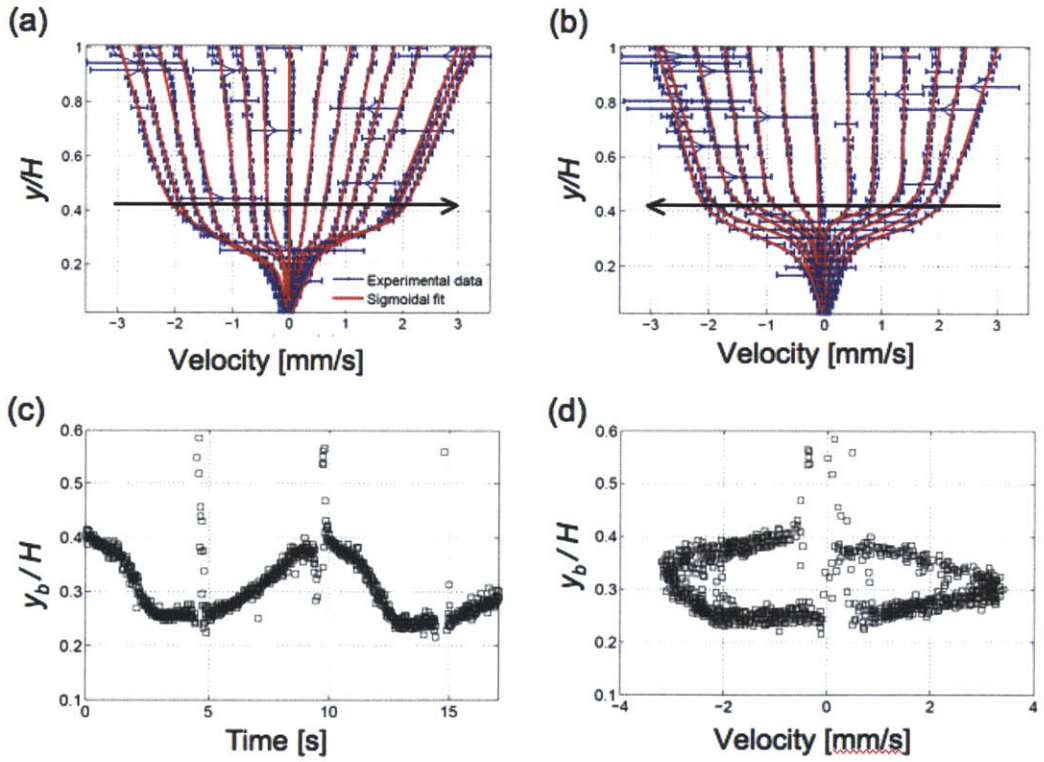

Figure 4-14: Velocity profiles for the CPyCl fluid undergoing an oscillatory deformation with $\gamma_0 = 300\%$ and $\omega = 0.63$ rad/s (De = 0.91, Wi = 2.73), with the plano-concave lens in use (as well as the film). In (a), velocity profiles for half a period of oscillation are shown, while in (b) profiles for the second half are shown. Movement of the band position can clearly be discerned in (c) and (d).

4.4 Summary

We have measured the local velocity fields within a wormlike micellar fluid (CPyCl:NaSal 100:60mM) under both steady and oscillatory shear using particle image velocimetry. This set of experiments has served as a test of the capabilities of the first iteration (v1) of the RheoPIV device discussed in Chap. 3. We have used this opportunity to investigate the use of different experimental techniques that can be used to mitigate wall slip effects that are endemic to Rheo-PIV experiments with complex fluids, and some of the effects that edge irregularities in the cone-plate rheometer can have on the PIV measurements. Specifically, the use of a plano-concave optical lens placed at the geometry edge to improve image quality was discussed, and it was shown that the change in the boundary condition at the edge due to this rigid no-slip surface can result in a considerable qualitative change in the velocity profile observed within the fluid (both in oscillatory and steady shear). Additional flow visualization in the flow-vorticity plane was used to determine the critical shear rates beyond which secondary flows become substantial, and these imaging results were used to select test conditions for which there is minimal secondary flow occurring that might corrupt the PIV measurements.

The RheoPIV device was shown to have a high spatial resolution (~ 20 μm) and high temporal resolution (maximum frame rate of 60 s^{-1}) - it was therefore possible to analyze the evolving velocity profiles within the fluid under oscillatory shear in the transition region as the fluid begins to experience large amplitude deformations and exhibits non-linear rheological behavior. The time periodic velocity field has been characterized for a CPyCl/NaSal micellar fluid under large amplitude oscillations and the velocity profiles exhibit a characteristic 3-banded structure that is well described by the sigmoidal function given in Eq. 4.3. The evolution of increasingly banded profiles is directly correlated with the bulk nonlinear response and pronounced shear banding is shown to occur even for small values of the nonlinearity indices e_3/e_1 and v_3/v_1. These results suggest that, at least for this particular class of wormlike micellar fluid, direct velocimetric measurements are a more sensitive method of determining

onset of shear banding under LAOS, compared to measurements of higher harmonics in the bulk stress signal. For the strain amplitudes tested, the location of the shear band (measured using the fitting parameter y_b) was shown to remain relatively constant during the oscillatory flow. More detailed studies of dynamical changes in the interface position at higher strain amplitudes would likely require the use of v2 of the RheoPIV device which was discussed in Chap. 3. Although we have discussed the design of this device, we leave its use to further study the shear banding phenomenon in surfactant solutions as an avenue for possible future work. For the time being, we note that the combination of localized velocimetric measurements and bulk rheological measurements that were provided in this chapter have given detailed insight into the spatio-temporal dynamics of complex fluids under simple viscometric flows. By using LAOS as the imposed forcing procedure we have been able to document the progressive evolution of the shear-banded structure and associated nonlinear rheological response in a model wormlike micelle solution. Such data can be compared in the future with the predictions of rheological constitutive equations.

In the chapter that follows, we will use the RheoPIV device to next focus on shear heterogeneities in a model waxy crude oil. While the model waxy crude oil will initially be introduced in the context of shear heterogeneities, in Chap. 8 we will revisit the same model fluid in order to study the phenomenon of thixotropy.

Chapter 5

Rheo-PIV of a Yielding in a Model Waxy Crude Oil

5.1 Introduction

We will begin our study of shear heterogeneities in waxy crude oils by first formulating and characterizing a model waxy crude oil. This model crude oil will exhibit the key rheological features associated with real waxy crude oils. We will then connect bulk rheological behavior of the yielding transition that is observed in this model waxy crude oil with local measurements of deformation and wall slip effects. The goal will be to understand what may affect the modes of yielding that can occur in a waxy crude oil gel. The RheoPIV apparatus (v1) (described in Sec. 3.1) will be used to connect local velocity/deformation measurements to changes in the microscale structure of the gelled oil. The model fluid will be used to observe and quantify the dynamical processes accompanying yielding behavior in a wax-oil gel and the changes induced by modifications of the wall boundary conditions. The structural evolution will be studied through a combined approach of measuring the transient bulk rheological behavior, while simultaneously observing spatial and temporal variations in localized velocity fields for a wax-oil gel under an imposed stress or strain rate. We will see that observations of the local velocity fields within the wax/oil system under both imposed stresses and imposed shear rates show that roughened walls inhibit interfacial

slip. Furthermore under a steady imposed shear rate, this inhibition of slip at the wall can result in a larger stress required to achieve steady flow and consequently more power being dissipated into the material. The larger rate of energy dissipation occurs alongside a much faster break down of the fluid structure - an observation that will be verified through a dimensionless scalar metric based on the localized flow measurements.

While this will conclude our discussion on shear heterogeneities, an identical model fluid will be used in Chap. 8 to understand thixotropic behavior in waxy crude oils. Our study of the nature of shear heterogeneities in this chapter will therefore be useful in Chap. 8, as it will allow us to design experimental flows with some *a priori* knowledge of whether or not viscometric assumptions apply.

5.2 Experimental

5.2.1 Chemical Composition of the Model Wax-Oil System

A model waxy oil was created that consisted of two components. The first (majority) component is a mineral oil used to form the continuous or matrix phase (Both a 'light' and 'heavy' version were used; Sigma Aldrich 330779 and 330760 respectively). The second component is a paraffin wax (Sigma Aldrich 327212) with a melting point specified by the manufacturer to be between 58°C and 62°C. The composition of the light mineral oil and wax was examined through the use of Gas Chromatography, or GC. GC spectra for the particular fluids that are used here are shown in Fig. 5-1. From these GC spectra, the wax appears to contain a higher per-weight percentage of larger n-paraffins compared to the mineral oils. Furthermore, the wax contains only about 60%Wt. n-paraffins, while the rest of the wax consists of iso- and cyclo-paraffins. The GC spectrum of the heavy mineral oil is similar to that of the light oil, with a slight shift in the carbon number distribution towards the heavier ends. This results in the heavy oil generally having a slightly higher viscosity than the light oil, although both fluids are Newtonian.

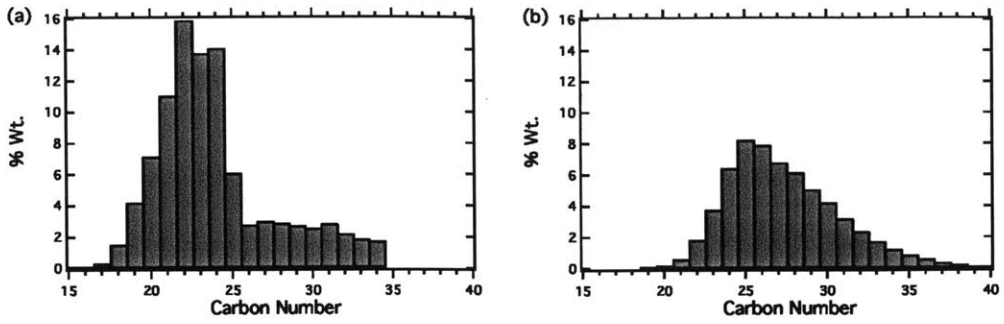

Figure 5-1: Distribution weight percentage composition of n-paraffin carbon number for the light mineral oil (a) and paraffin wax (b)

5.2.2 Thermorheological Behavior of the Wax Oil System

The bulk thermorheological behavior of both the individual model fluid components, and the combined wax-oil system was studied using a TA Instruments AR-G2 stress controlled rheometer. A cone-plate geometry was utilized in order to ensure a uniform imposed strain field throughout the bulk of each sample and the upper and lower geometry surfaces were also roughened by using sandpaper with a root mean squared (rms) roughness $R_q = 30\mu$m in order to avoid slip effects. Thermal control of the samples was achieved by using a lower plate equipped with a Peltier controller. The viscosity of the two mineral oils and the wax were measured as a function of their temperature (at a fixed shear stress, $\sigma = 2.8$Pa). The two mineral oils are Newtonian and exhibit increases in viscosity as temperature is decreased which can be modeled through the use of a simple Arrhenius equation, [29]

$$\eta = \eta_a e^{\frac{\Delta H}{R}\left(\frac{1}{T}-\frac{1}{T_0}\right)}, \tag{5.1}$$

Here η_a is the viscosity of the fluid at the temperature T_0, while ΔH is the activation energy for flow. Values of these parameters for the light oil are reported in 5.1 and the good agreement between the rheology of the model fit and the data is shown in Fig. 5-2. Unlike the mineral oil, the paraffin wax shown in Fig. 5-2 exhibits a much sharper increase in viscosity as it approaches its freezing temperature; it does not solidify immediately but rather exhibits a continuous (and large) change in viscosity

over a drop in temperature of a few degrees. This arises from the formation of the wax crystallites which consist of a range of n-paraffin components, each tending to crystallize at slightly different temperatures. As a result of this very localized transition from a Newtonian oil to a soft glassy solid-like material the thermorheological variations of the wax are modeled using a VFT (Vogel-Fulcher-Tammann) model, [117]

$$\eta = \eta_v e^{\frac{B}{T-T_\infty}}, \tag{5.2}$$

where η_v is the viscosity scale for the wax at very large temperatures, T_∞ is the temperature at which the viscosity of the wax diverges to infinity (which roughly corresponds to the melting temperature of the wax). The parameter B determines how fast the viscosity increases as the temperature of the wax is lowered. At very high temperatures, i.e. $T \gg T_\infty$, the VFT model approaches Arrhenius like behavior with the parameter equivalency $B = \frac{\Delta H}{R}$.

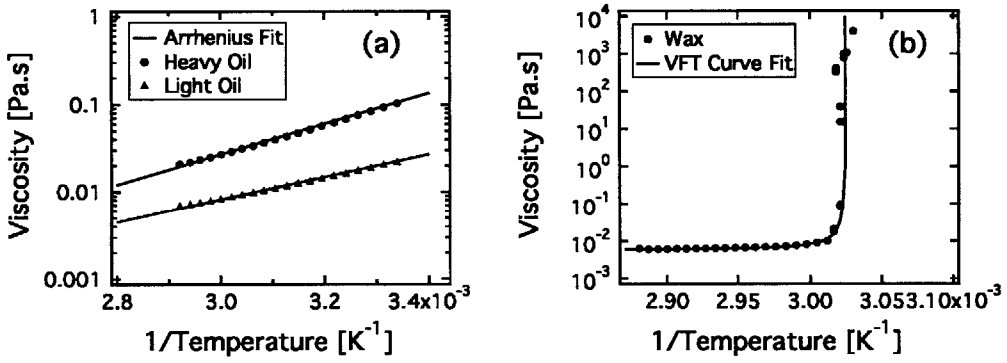

Figure 5-2: Temperature dependence of the viscosity for (a) the light and heavy mineral oil and (b) the paraffin wax. For the wax VFT fit, $B = 0.5$K, $T_\infty = 330.4$K and $\eta_v = 0.0056$ Pa.s. For the light oil $\eta_a = 0.0082$ Pa.s , $\frac{\Delta H}{R} = 2890$ K and for the heavy oil $\eta_a = 0.027$ Pa.s, $\frac{\Delta H}{R} = 3970$ K

The combined model wax-oil system consists of both the mineral oil and wax components (typically mineral oil with 5 or 10 wt.% wax). Thus, the model wax-oil system exhibits thermorheological behavior intermediate to the Arrhenius and VFT behavior of the oil and wax respectively. The dependence of viscosity on temperature for a

range of wax-oil systems is shown in Fig. 5-3. The viscosity of the wax-oil mixtures follows an Arrhenius like behavior for temperatures above a certain value, and below this critical value their viscosity increases at a rate more rapidly than that predicted by the Arrhenius relation (but a slower rate than that predicted by the VFT equation for the pure wax). The temperature at which this marked change in behavior occurs is identified as the rheologically-relevant value of the wax appearance temperature, T_{wa}. By determining T_{wa} rheometrically rather than visually through turbidity data, we identify conditions at which wax precipitates first begin to dynamically impact the wax-oil system and lead to the super-Arrhenius behavior characteristic of a fragile liquid [12]. Values of T_{wa} for the range of model wax-oil systems shown in Fig. 5-3 are given in Table 5.1.

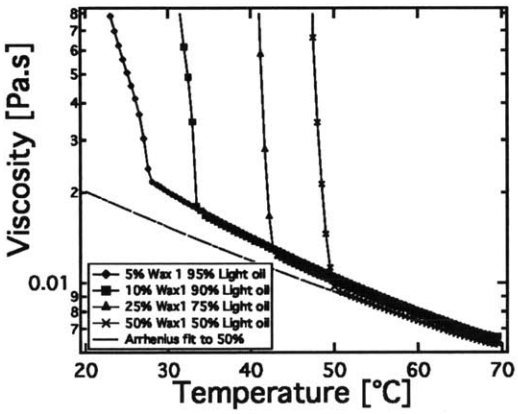

Figure 5-3: Temperature dependence of the steady shear viscosity at $\sigma_0 = 3$ Pa for several mixtures of wax in light oil containing different wt.% of wax. The broken straight line is an Arrhenius fit to the high temperature data for 50 wt.% wax at $T > T_{wa}$.

The non-Newtonian rheological behavior exhibited by these fluids below T_{wa} is due to the formation of a percolated network of wax precipitates. It is possible to directly observe these precipitates in the model wax-oil systems by placing a sample between crossed polarizers and illuminating the sample using monochromatic light under an optical microscope. Under these conditions, the structural anisotropy of the crystals gives rise to birefringence in the sample. Fig. 5-4 shows an image taken using such a setup. The discotic wax precipitates can be seen as bright rod or needle-shaped

	T_{wa} [K]	η_a [Pa.s]	$\frac{\Delta H}{R}$ [K]
Light Oil	N/A	0.0082	2890
5% Wax	302	0.0082	2877
10% Wax	306.5	0.0080	2845
25% Wax	316	0.0077	2717
50% Wax	324	0.0074	2443

Table 5.1: Thermorheological parameters for various wax-in-light oil mixtures. For the Arrhenius fit in each case, T_0 is taken as 60°C.

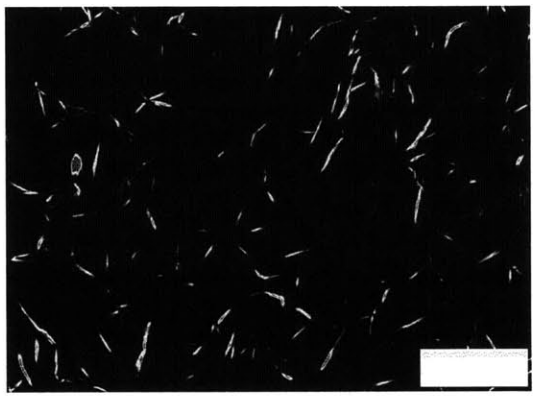

Figure 5-4: Birefringent microscope image showing the shape and size of wax crystallites formed in a 10% wax/light oil system under static conditions at 25°C ($T/T_{wa} = 0.987$). The scale bar on the bottom right has a length of 80μm.

objects due to being observed edge on in the 2 dimensional plane. The shape and size of these precipitates is consistent with observations reported previously in the literature for other wax-containing oils. [203, 162]

5.2.3 Modifications to RheoPIV v1

For flow visualization tests RheoPIV v1 was utilized. Precision-machined cones of radius $R = 25$mm, angle $\Theta_0 = 4°$ and truncation 111 μm were used - the surface roughness of the cone could also be modified by applying adhesive-backed sandpaper. Specifically, the solid surfaces were either covered with an adhesive backed sandpaper with rms roughness, $R_q = 30\mu$m, or were left uncovered having an rms roughness $R_q = 0.6\mu$m. The value of R_q was measured using a Zygo interferometer. Specifically, for n measurements of the vertical distance of a surface from its mean line (y_i), R_q is

given by:

$$R_q = \sqrt{\frac{1}{n}\sum_{i=1}^{n} y_i^2} \tag{5.3}$$

5.3 Results

5.3.1 Bulk Yielding

One defining characteristic of waxy crude oils is their EVP behavior - i.e. they possess a yield stress below their wax appearance temperature.[204] As would be expected for a model system, the wax-oil mixture described above also exhibits a yield stress, with a magnitude that depends on temperature (shown in Fig. 5-5). Experimental data from Visintin [204] demonstrated that the modulus of a crude oil gel (as parametrized by the viscoelastic moduli $G'(\omega)$ and $G''(\omega)$) below the wax appearance temperature can change depending on thermal history of the sample. Thus, to prevent any variability in the strength of the gelled system due to cooling rate differences, all systems were presheared at an elevated temperature $T = T_{wa} + 20°\text{C}$ for 10 minutes at a shear rate of 50 s^{-1} and then cooled at a rate of 1°C/min under quiescent conditions (i.e. zero applied shear rate). A subsequent "holding time" of 10mins was then applied at the desired test temperature before each experiment. This particular sequence of steps is akin to the "thermal beneficiation" and cooling procedures described by Pedersen and is essential for obtaining repeatable measurements in these thermorheologically complex systems. [164]. In addition to this, slip effects were avoided at the wall by carrying out the measurements using roughened upper and lower fixtures that ensure the no slip boundary condition is satisfied.

The data in Fig. 5-5 shows the variation in the measured viscosity with applied shear stress, for the 5% wax-oil systems at a range of temperatures below $T_{wa} = 30.5°\text{C}$. In order to measure the very large (but finite) values of viscosity a creep test is carried out (in which a fixed stress is imposed) and the steady state viscosity is calculated 5 minutes after the imposition of stress from the measured rate of creep

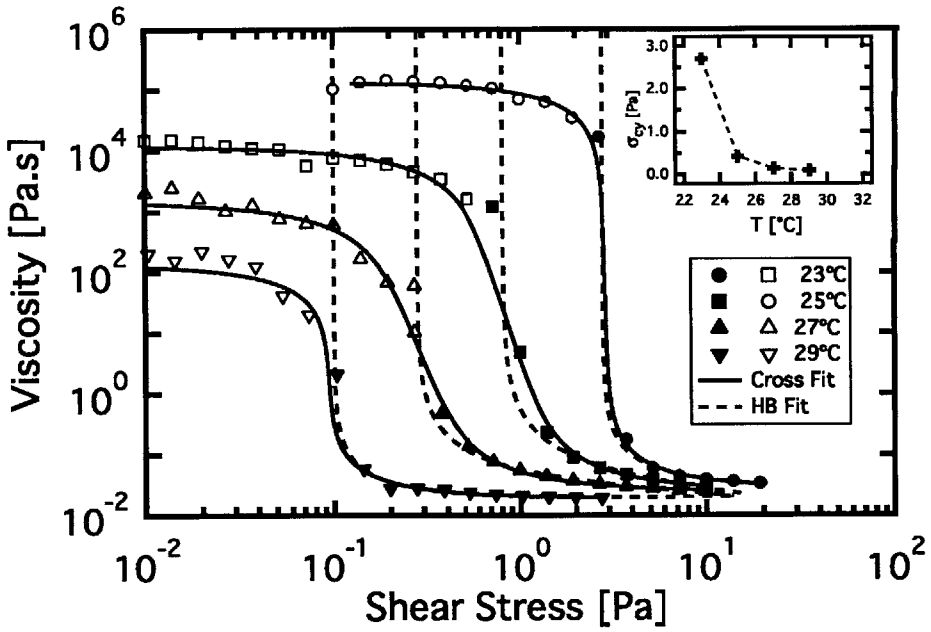

Figure 5-5: Flow curves for the 5% wax-light oil system at a range of temperatures below T_{wa}. Each set of points is fit to the Cross model for viscosity, which is given in Eq. 5.4, and the Herschel Bulkley (HB) model, given in Eq. 5.5. The hollow and filled symbols are used to distinguish the set of points used for the Cross fit (uses both hollow and filled) and the HB fit (uses only filled). The inset shows the variation of yield stress (σ_{cy} based on the estimate from the Cross model) with temperature.

$\dot{\gamma} = \frac{d\gamma}{dt}$ and the imposed stress. It is apparent that there exists a narrow range of stress values over which the viscosity of the fluid drops rapidly by several orders of magnitudes. This stress increases with decreasing temperature, and the drop in viscosity becomes more sudden at lower temperatures. Each data set is fitted to the Cross model:

$$\eta = \eta_\infty + \frac{\eta_0 - \eta_\infty}{1 + \left(\frac{|\dot{\gamma}|}{\dot{\gamma}^*}\right)^m}, \tag{5.4}$$

where η_0 and η_∞ are the limiting values of viscosity at low and high shear rates, respectively, the term $\dot{\gamma}^*$ is a critical shear rate associated with the sudden onset of shear thinning, and m is a parameter which controls the rate of thinning. The Cross model describes viscosity as a function of shear rate; however the data shown

in Fig. 5-5 is best represented with stress as the independent variable. Therefore, it is useful to understand that the critical stress or apparent yield stress predicted by the Cross Model is $\sigma_{cy} \sim \eta_0 \dot{\gamma}^*$ (provided $\eta_0 \gg \eta_\infty$). The Cross model is successful at capturing simultaneously high and low shear stress behavior. Previous work has also utilized similar Generalized Newtonian fluid models in order to describe the flow behavior of waxy crude oils - specifically Visintin et. al. [204] used the RBC model (similar to the Cross model but with stress as the independent parameter instead of shear rate) to model yielding behavior of waxy crude with a finite low shear viscosity

Alternatively, if interest is limited to the flow curve beyond the point of yield, then the data in Fig. 5-5 can also be fit to the Herschel-Bulkley model for high values of the stress (filled symbols corresponding to $\sigma > \sigma_{cy}$):

$$\eta = \begin{cases} \frac{\sigma_y + K|\dot{\gamma}|^n}{|\dot{\gamma}|} & \text{for } \sigma > \sigma_y \\ \infty & \text{for } \sigma \leq \sigma_y \end{cases} \tag{5.5}$$

The Herschel Bulkley model gives an independent estimate of the yield stress through the parameter σ_y. This value can be compared with the estimate of σ_{cy} obtained from the Cross model. The parameters used to fit each set of data in Fig.5-5 to the Cross model, as well as the resulting estimate of σ_{cy}, are given in Table 5.2. For comparison, the value of the yield stress obtained from the Herschel Bulkley model, σ_y, is also provided in Table 5.2.

Previous work that has studied low shear rate viscosity plateaus in yield stress fluids has shown that the value of the low shear stress viscosity (η_0 for our case) depends on measurement time. [147, 146] For this reason, the value of η_0 that is determined from the Cross model fit is a lower bound of the steady zero shear rate viscosity because the measurement points were restricted to a time period of 5 minutes. As a constitutive law, the Cross model is incomplete because it cannot predict the nature of this transient flow for stresses below σ_{cy}. In Chaps 6-8, we will discuss the development of a more sophisticated constitutive framework that can capture this dependency. For now, however, we point towards the fact that there is good agreement between σ_{cy} and σ_y (to within a factor of 2). This indicates that σ_{cy} is

Table 5.2: Parameters for the Cross model fit to model waxy crude oil data in Fig. 5-5. Table includes value of yield stress parameter (σ_y) for the Herschel Bulkley fitting.

	η_0 [Pa.s]	η_∞ [Pa.s]	$\dot{\gamma}^*$ [s^{-1}]	m [ ]	σ_{cy} [Pa]	σ_y [Pa]
23°C	1.35×10^5	2.80×10^{-2}	2.08×10^{-5}	1	2.81	2.80
25°C	1.08×10^4	3.06×10^{-2}	6.04×10^{-5}	0.97	0.6505	0.811
27°C	1.63×10^3	2.56×10^{-2}	9.80×10^{-5}	0.92	0.159	0.278
29°C	2.41×10^2	1.83×10^{-2}	3.04×10^{-4}	0.97	7.32×10^{-2}	0.103

still a physically relevant parameter - namely it is the critical stress value at which the material exhibits a very pronounced shear thinning behavior.

The data shown in Fig. 5-5 is representative of the bulk rheological behavior within the sample, and is not dependent on any type of interfacial slip interaction which might occur between the fluid and the solid surface of the cone-plate geometry. The no-slip boundary condition is ensured by using roughened upper and lower fixtures. Direct observations of the flow field using the Rheo-PIV system (as described above) show that this roughened geometry consistently prevents slip from occurring. Similar measurements can also be made with other yielding systems such as clay dispersions [85, 86] and microgel pastes [138, 139].

One important point related to the data in Fig. 5-5 that bears mentioning is that these viscosity measurements are highly dependent on the shear history of the sample. One must keep in mind that the fluid is cooled to below T_{wa} under quiescent conditions before it is yielded. This results in a generally strong wax-oil gel, because the gel network of wax crystallites was not perturbed while being formed. However, if we cool the gel under shear, the wax oil gel is weaker, with a lower yield stress. Throughout this chapter, we will restrict our focus to the former case, i.e. that of a "strong gel". However in Chap. 8, we will study the rheology (in particular the thixotropic behavior) of a fluid in the latter case, which we will refer to as a "slurry state". Furthermore, because we are starting flow of this "strong gel" from a quiescent (i.e. zero shear) state, we will generally be focusing on *static* yielding phenomena [45, 46]. These phenomena are strongly coupled to the nature of the initial structure within the fluid. This initial structure is actually unable to be fully recovered unless the sample undergoes another heating and cooling step (under quiescent conditions).

Observations of the viscosity-stress dependence of the wax oil system after the fluid has gone through this static yield point (and σ_{cy} has been exceeded) have confirmed this behavior. The irreversibility inherent in the material can be demonstrated by measuring the viscosity of the sample at incrementally higher values of shear stress (starting from stresses below the yield stress following the thermal beneficiation and cooling step). Eventually, when the yield stress $\sigma_{cy}(T_{wa})$ is exceeded, the viscosity of the material drops drastically as the gel structure is disrupted. If the imposed shear stress is then lowered incrementally, the measured viscosity at stresses below the yield stress $\sigma < \sigma_{cy}$ is observed to be lower by factors of 10-100 than it was in the pre-yielded state. This type of extreme time dependent behavior is illustrated in Fig. 5-6; a 5% model wax in light oil system was beneficiated and cooled to 23°C at a rate of 1°C/minute and subsequently held for 10 minutes at 23°C. A series of creep steps was applied to the system, and the strain was measured over this period of time. The instantaneous viscosity of the sample is determined by computing the instantaneous strain rate $\dot{\gamma} = \Omega(t)R/\Theta_0$ at each point in time from the measured angular rotation rate $\Omega(t)$ of the fixture, and then dividing the applied stress by this instantaneous strain rate.

The sample initially creeps under an applied stress of 0.7 Pa for the first 15 minutes, followed by a creep step of 7 Pa for the next 15 minutes. Subsequently the stress is lowered again to 0.7 Pa for the next hour of the test. The stress of 0.7 Pa is below the yield stress of the 5% system at 23°C ($\sigma/\sigma_{cy} = 0.26$). Thus, during the first 15 minutes of the experiment the system is in its pre-yielded state and creeps elastoplastically. When the larger 7 Pa stress is applied ($\sigma/\sigma_{cy} = 2.6$), the percolated network of crystallites yields and the viscosity drops by a factor of 10^6 to a value of $\eta \sim 0.05$ Pa.s. During the third stress step at ($\sigma/\sigma_{cy} = 0.26$), the viscosity recovers partially but it does not increase to the value initially exhibited in the pre-yielded state. Furthermore, even though the viscosity is measured over a period of 1 hour, it does not show enough of an increase to return to its pre-yielded state. Thus, whatever aging the system now exhibits, it is not sufficient for the fluid to return to its initial "strong gel" state with a high static yield stress.

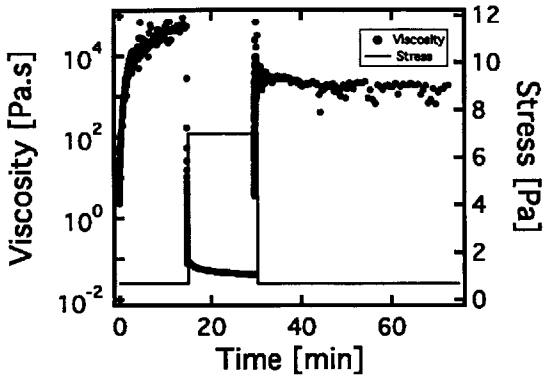

Figure 5-6: Irreversible aspects of yielding demonstrated by a viscosity vs. time plot for a 5% wax in light oil system at 23°C ($\sigma_{cy} = 2.7$ Pa). in this particular experiment, three stress steps are imposed as indicated on the righthand ordinate axis: an initial step below the yield stress ($\sigma/\sigma_{cy} = 0.26$), a second step above it ($\sigma/\sigma_{cy} = 2.6$) and a third step again below the yield stress ($\sigma/\sigma_{cy} = 0.26$). The sample does not restructure and the viscosity does not recover back to the pre-yielded value during the third step even over timescales of several hours.

The irreversible yielding of an initially gelled wax-oil system can be understood by considering the forces which might drive a rearrangement of the wax microstructure. An analogy can be made between waxy crude oils and colloidal gels of anisotropic particles [204]. It is then possible to write an equation that estimates the time scale that is required for Brownian forces to cause sufficient rotational diffusion of the wax crystallites to rearrange into a percolated network characteristic of the pre-yielded "strong gel" state. This time scale can be estimated using the following expression [117]:

$$\tau = \frac{a^3 \mu}{k_b T} , \tag{5.6}$$

In Eq. 5.6, μ is the viscosity of the continuous phase (mineral oil $\eta_0 \sim 0.1$ Pa.s), T is the absolute temperature of the wax-oil gel, and a is the characteristic hydrodynamic size of the wax crystallites. As can be seen, this timescale is a strong function of the characteristic size of the particles a. In the initial, pre-yielded state, the wax precipitates may actually form large aggregates with high values of a. After the "strong gel" yields, these aggregates may break down. While short time scales may

be enough for individual wax crystals to cause some aging, the prohibitively large size of these initial aggregates does not allow the wax microstructure to re-establish the pre-yielded state through the action of Brownian motion alone. Instead, it needs more complex rejuvenation strategies to ensure repeatable initial pre-yielded conditions (such as the thermal beneficiation and cooling procedure used in the present study).

5.3.2 Dependency of yielding on surface properties

As noted above, the rheological behavior described so far has assumed that the no slip boundary condition holds for the model wax-oil system under flow. This was ensured by using roughened upper and lower geometries (with roughness $R_q = 30\mu$m) for all rheological measurements. When the wax-oil system is placed in contact with smoother test fixtures the apparent bulk rheological behavior changes drastically due to the presence of slip.

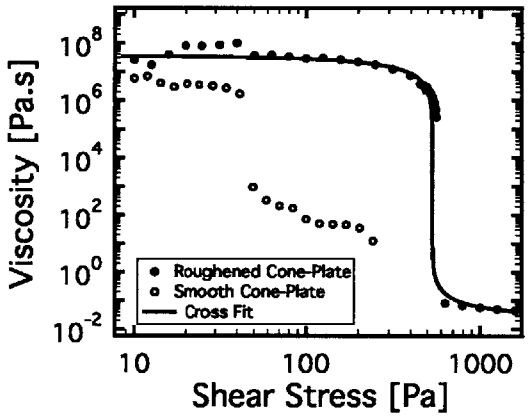

Figure 5-7: Viscosity-stress curve for a 10% wax in light oil system at 23°C ($T/T_{wa} = 0.980$) measured using a cone and plate geometry with roughened surfaces ($R_q = 30\mu$m) and a cone and plate geometry with smooth surfaces ($R_q = 0.6\mu$m).

One artifact of this slip presents itself in plots of the apparent viscosity for a 10% model wax-oil system experiencing steady shearing against each surface as shown in Fig. 5-7. At high stresses, i.e. $\sigma \gtrsim 300$Pa, steady state can not be attained with the smooth surface under imposed stress conditions due to the instrument exceeding its maximum shear rate. However the data in the two cases can still be compared for

lower stresses, i.e. values of $\sigma < \sigma_{cy}$. For these values of stress the measured viscosity for the sample in contact with the smooth geometry is much lower than expected. A decrease in the apparent viscosity for values of $\sigma < \sigma_{cy}$ is also observed for the 5% system, however this effect is less pronounced due to the weaker gel structure in the 5% system.

Barnes [16] shows a similar type of behavior for a printing ink, explaining that the lower viscosity in the case of the smooth surfaces is the result of slip at the fluid-solid boundary. In order to show that the discrepancy between the data in Fig. 5-7 is a result of interfacial slip, the Rheo-PIV system is used in conjunction with lower cone surfaces of different roughness. Specifically, a sequence of creep tests was carried out on a wax-oil system cooled to below T_{wa}, in which the imposed stress is incrementally stepped (in a logarithmic fashion) from a value below the yield stress to a value above it. For each of the creep steps, the imposed stress is held for a period of 60s, the macroscopic strain is recorded and a video recording (at 18 frames per second) was acquired for later PIV analysis to determine the local flow field within the sample. This sequence of creep tests was carried out for the wax-oil system in contact with a roughened lower geometry (again achieved using adhesive backed sandpaper), and for a smooth lower geometry. In both cases (and all other cases where the Rheo-PIV system is used to measure the velocity field) the upper geometry was a smooth quartz glass plate ($R_q = 0.02\mu$m), which is necessary to allow a path for the laser beam. In this experiment, a 5% wax-oil model fluid was used at a higher test temperature (27°C ; $T/T_{wa} = 0.993$), such that turbidity induced by the crystallites was still small. The conditions of this experiment differ from those of Fig. 5-7 in several ways. Specifically, a lower wax content system is used at a higher temperature, and roughness on only the bottom surface is varied, while the upper surface is kept smooth. However, changes in the apparent strain with roughness can still be compared with the localized velocity measurements - these comparisons will show whether or not the changes are a result of varying degrees of slip occurring on the lower surface.

The bulk rheological data from this particular experiment is shown in Fig. 5-8 in the form of the torsional strain $\gamma(t)$ response measured at each imposed stress σ_0. It

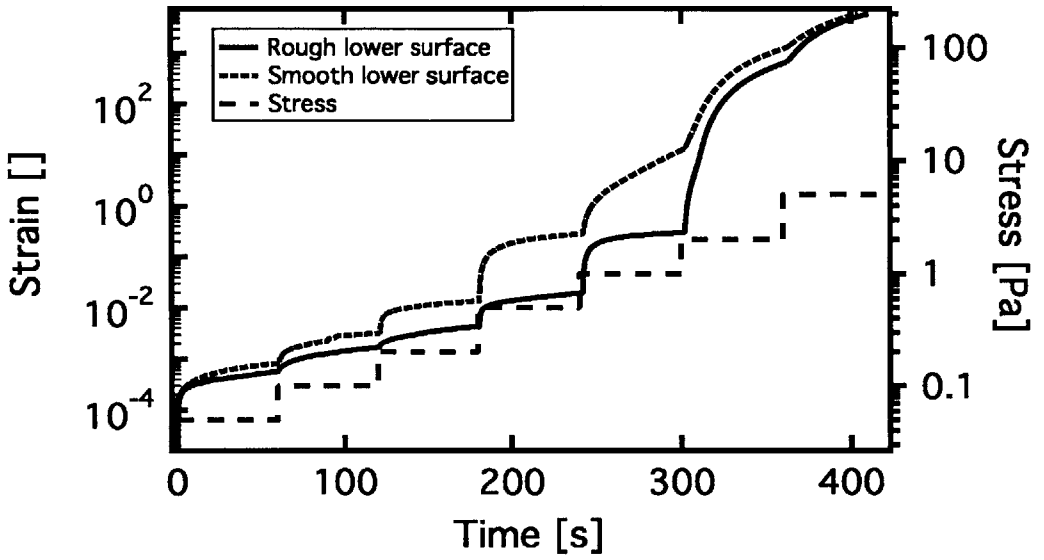

Figure 5-8: Sequence of creep tests used to restart flow of the 5% wax in light oil system.

is apparent that the waxy oil exhibits much larger straining displacements and larger strain rates when it is in contact with a smooth lower surface. Hence, the apparent viscosity computed by the rheometer using the definition $\eta \equiv \sigma_0/\dot{\gamma}(t)$ is generally lower. This behavior is consistent with the bulk rheological data shown in Fig. 5-7. The important role of interfacial slip can be quantified through the analysis of the corresponding time-resolved PIV data corresponding to the creep tests in Fig. 5-8. For each step in stress applied, the time period over which the material experiences substantial deformation is studied, such that it is possible to register a large enough displacement of the seed particles using the imaging system (typically a displacement of ≥ 1 pixel between frames is required). For the sample in contact with the smooth lower fixture, this time period occurs beginning at the 240s mark, when the imposed stress is $\sigma = 1$ Pa. On the other hand, for the roughened case the velocimetry system only registers a displacement large enough when the imposed stress reaches $\sigma = 2$ Pa. Representative velocity profiles are shown on the left in Fig. 5-9 for the wax-oil system during each of these steps. These velocity profiles show that the mechanism through which the material yields is markedly different in both cases. In the case of

the roughened lower surface, the no slip condition is enforced at the lower plate, and flow occurs primarily through the mechanism of a non-zero shear rate in the bulk and a large slip velocity at the upper (smooth) surface. The instantaneous wall velocity $V_w = \Omega(t)R$ for each profile is indicated in the legend.

The full velocity profiles at these three instants in time after the imposition of the stress $\sigma_0 = 2$ Pa are shown to the left in Fig 10 (a) - these profiles show a positive, time-increasing average shear rate within the bulk in addition to pronounced slip. Furthermore, spatial variations in the shear rate $\dot{\gamma}(y)$ indicate that the material is experiencing higher shear rates near the upper surface. Distinctly shear-banded profiles (i.e. profiles with a discontinuity in shear rate, such as those observed in other yielding systems [149, 64]) are not apparent, however the shear rate does show considerable spatial variations across the gap. Specifically, for the velocity profile at $t = 308.5$s, the shear rate varies by a factor of 3 across the gap.

When the no slip boundary condition is relaxed on the lower plate (by using a smoother surface) the velocity profile appears to be plug-like. This is characterized by large slip velocities at the upper and lower surfaces ($v_s = 0.15$mm/s at the lower surface and $v_s = 0.05$mm/s at the upper surface) as well as a low average shear rate within the bulk ($\dot{\gamma}_{\text{bulk}} \simeq 0\text{s}^{-1}$). The critical role of wall roughness in mediating the importance of interfacial slip is not surprising for this model system, and similar effects have been observed in a wide variety of systems, including emulsions [90], microgels, [55] pastes [138, 26] and micellar fluids [122].

The velocity profiles presented in Fig. 5-9 are averaged over one frame of video, however the total number of frames for each creep test totals over 1000. As a result, it is possible to use a larger sequence of frames to determine the velocity profile within the gap over a larger period of the creep test. In order to illustrate the evolution of the velocity field compactly, the profiles are represented in the form of a space-time diagram. These diagrams allow one to easily discern the evolution of the velocity profile within the rheometer gap over a long period of time, and have been used previously in the literature to understand time-evolving velocity fields. [85, 23] For a space time diagram of steady homogenous shear flow with $v_x(y,t) = \dot{\gamma}y$, the

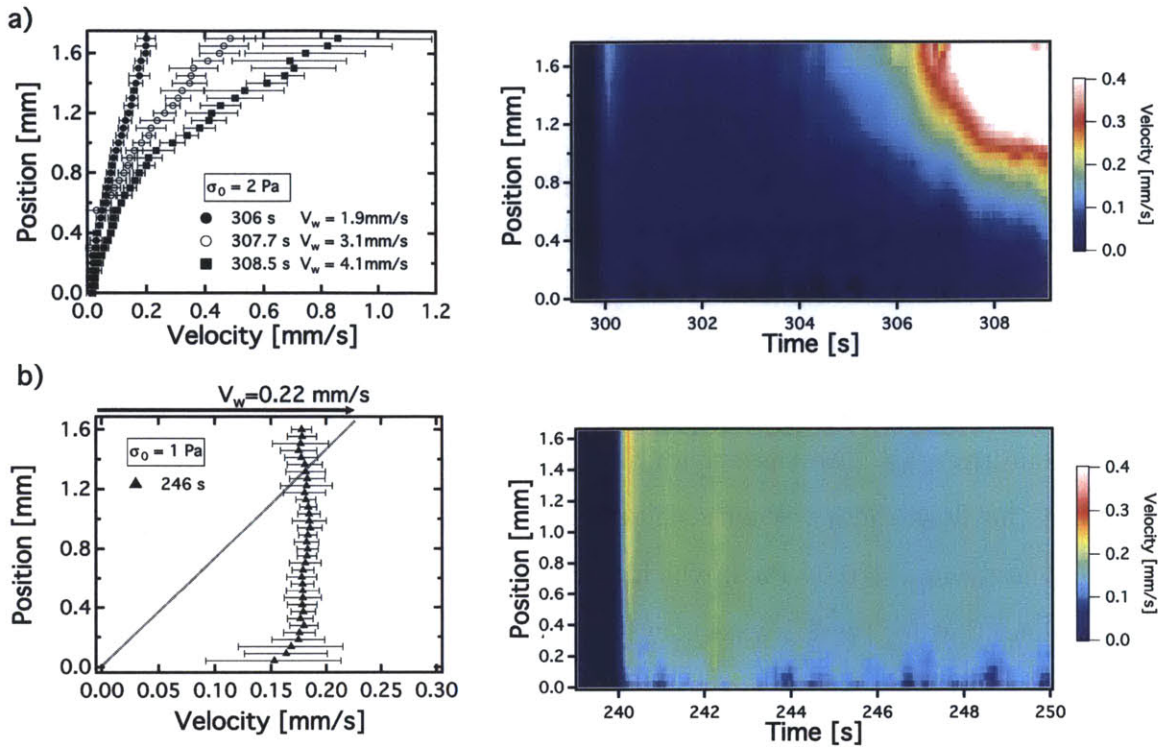

Figure 5-9: The space-time diagrams $v_x(y,t)$ indicating evolution of the velocity profile within the wax-oil system for creep tests shown in Fig. 5-8. In (a) the lower fixture surface is roughened ($R_q = 30\mu$m), in (b) the lower surface fixture is smooth ($R_q = 0.6\mu$m). Three representative instantaneous velocity profiles are shown on the left at $t = 306$, 307.7, 308.5 s for (a) and $t = 246$s for (b). The upper wall velocity, $V_w(t)$ is also shown in the legend for each profile.

diagram should appear as a uniform gradient vertically. Fig. 5-9 shows spatiotemporal diagrams for the roughened creep test beginning at 300 s ($\sigma_0 = 2$ Pa), and the smooth creep test beginning at 240 s ($\sigma_0 = 1$ Pa).

The spatiotemporal diagrams reinforce the slip phenomena indicated by the instantaneous velocity profiles in Fig. 5-9. The smooth lower surface allows for substantial slip to occur, resulting in an apparent flow of the material at a lower stress. Due to the occurrence of slip on the upper and lower surfaces the velocity field within the bulk of the wax-oil is uniform plug-like and accompanied by slip at both surfaces.

The data in Fig. 5-9 verify that the wax-oil system can flow at lower shear stresses through the mechanism of slip on the solid surface. However, this behavior does not preclude bulk yielding at higher shear stresses. In fact, when the velocimetric data

from the 2 Pa creep step (beginning at 300 s) for the smooth surface case is analyzed (data not shown), the shear rate within the bulk of the sample grows to be non zero. Interfacial slip still occurs, however the flow of the material is due to a combined effect of both wall slip and shearing in the bulk. Eventually, at high enough shear stresses ($\sigma_0 \geq 5$Pa), the creep curves shown in Fig. 5-9 for the two different test configurations converge, indicating that at high shear stresses the contribution of slip to the total deformation is negligible, and the microstructure in the bulk material has broken down enough in both instances such that they are able to deform homogeneously throughout the gap. At these high shear stresses, surface characteristics have no effect on the flow. The viscosity value which is measured at these high stresses is approximately $\eta_{app} = 0.04$ Pa.s, which is consistent with values measured directly in steady shear flow for the 5% wax-oil system at a temperature of 27°C ($T/T_{wa} = 0.993$) with $\sigma \gg \sigma_{cy}$ in Fig. 5-5.

Fig. 5-9 illustrates the time varying behavior of the velocity field within the material under a constant stress. Instead of imposing a constant stress on the material, it is also possible to impose a constant strain rate on the material and simultaneously observe the velocity field within the sample. Constant shear rate experiments are a more common methodology used in probing crude oil rheology, and many constitutive models are fitted to experimental data from steady shear rate tests [164, 82]. Under such conditions, one can discern whether or not velocity profiles such as the ones shown in Fig. 5-9 are stable over a longer period of time. To probe the constant shear rate rheology, the 5% wax-oil system was cooled to a temperature of 27°C (i.e. to the strong gel state), and after beneficiation and cooling an imposed shear rate of $\dot{\gamma} = 0.3\text{s}^{-1}$ was applied to the material for a period of 10 minutes (in this test the smooth cone-and-plate geometry was used). The evolution in the bulk stress $\sigma(t)$ in the material was measured during this 10 minute period, as well as the local velocity field $\mathbf{v} = [v_x(x,y), v_y(x,y)]$ within the sample. The lefthand plot in Fig. 5-10 shows the bulk stress in the material calculated by the rheometer following start up of steady shear flow; the stress passes through a peak value after approximately 20 seconds. It subsequently relaxes monotonically toward a lower equilibrium value ($\sigma \simeq 0.35$ Pa).

The bulk averaged rheological behavior appears smooth, however the space-time plot in Fig. 5-10 shows the time varying behavior of the local velocity field in the sample which fluctuates considerably over the course of the 10 minute test period.

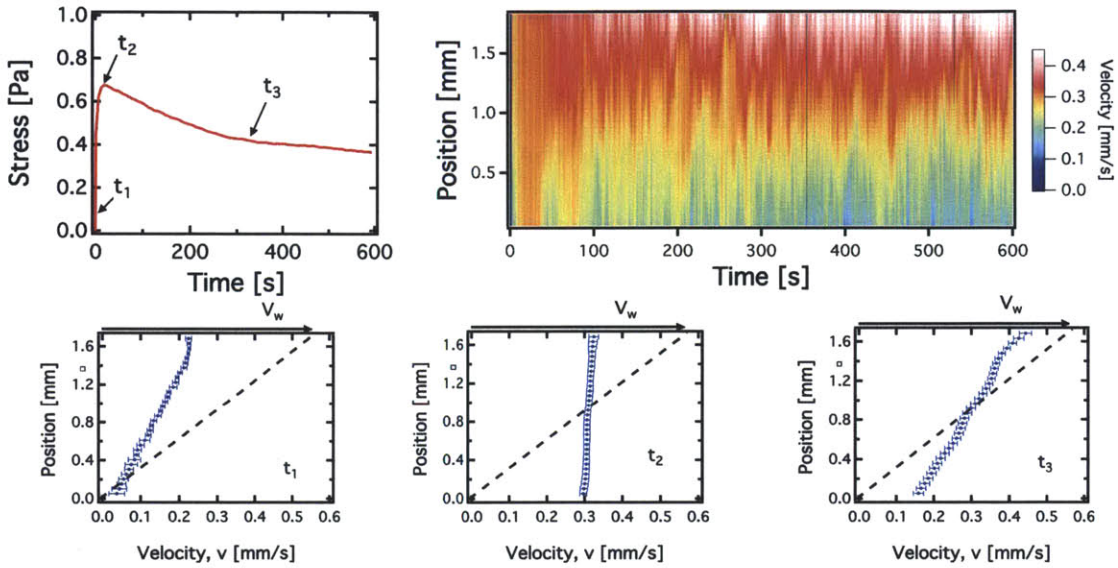

Figure 5-10: Bulk rheology (a) and local velocity field (b) for the 5% wax in light oil system undergoing a shear rate of 0.3s^{-1} at 27°C ($T/T_{wa} = 0.993$). The velocity profiles at the bottom, starting from the left are at (c) $t_1 = 1$s; (d) $t_2 = 20$s; (e) $t_3 = 300$ s.

At the bottom of Fig. 5-10, velocity profiles at three different points in time are plotted in order illustrate the three different stages of flow exhibited by the wax-oil gel. The first profile is measured at the $t = 1$s mark on the time axis of the space time plot in Fig. 5-10 (this corresponds to 1 second after the shear rate of 0.3s^{-1} is imposed). The velocity profile at $t_1 = 1$s is clearly linear - indicating that the material is exhibiting a uniform strain rate within its bulk, albeit with substantial slip occurring on the top surface. The second profile is measured at the 20 second mark. At this point, the profile appears to be almost perfectly plug-like. There is essentially zero strain rate within the bulk, with a slip velocity at both the top and bottom surfaces (these slip velocities are roughly equal, with a relationship between the slip velocity v_s and upper wall velocity v_w of $v_s \simeq v_w/2$). This plug-like profile is not stable in time, because the third velocity profile (which is plotted at $t_3 = 300$s) shows that the material exhibits a non-zero shear rate within its bulk. However

there is still slip occurring at the upper and lower surfaces. These slip velocities are roughly equal, so it is simple to calculate the true shear rate (averaged across the gap) experienced by the fluid from the Mooney expression[216]:

$$\dot{\gamma}_{\text{true}} = \dot{\gamma}_{\text{app}} \left(1 - \frac{2v_s}{v_w} \right) , \tag{5.7}$$

Applying this formula to the profile at the 300 second mark, the value of the true shear rate is $\dot{\gamma}_{\text{true}} = 0.17\text{s}^{-1}$.

Both the slip velocity and the shear rate within the bulk fluctuate continuously over the duration of the experiment and these fluctuations are highlighted in the space time plot. As a result of these fluctuations, the transition from the second to the third stage of flow is neither fast nor smooth - there are periods of time when the shear rate within the bulk, and the slip velocity, rapidly vary. These stick-slip fluctuations indicate that the material is spatially heterogenous in the flow direction, consisting of localized regions in the bulk which are fluid-like and experience higher shear rates, and other regions where the sample is locally rigid and experiences little or no deformation. Furthermore, despite the lack of distinctly banded velocity profiles that have often been observed in some other systems [149, 64, 197], there is still clearly heterogeneity of the material across the gap. This is illustrated by the variations in the shear rate $\dot{\gamma}(y)$ with the position (shown in Fig. 5-10 (e)). To explore the heterogenous structuring in further detail we use a microscope-based optical imaging and shearing apparatus (Linkam CSS450 Shear Cell) consisting of two parallel, concentric, transparent plates between which a fluid sample is placed. One of the plates is connected to a motor and imposes a torsional deformation identical to what it would experience in a parallel plate rheometer. The Linkam shear cell allows for optical access through the plates, such that the local fluid microstructure can be imaged using a high magnification microscope objective.

By placing the Linkam cell between crossed polarizers, the mesoscale structure and movement of individual wax precipitates can be observed more clearly under flow than using the Rheo-PIV system. However, instead of observing the deformation

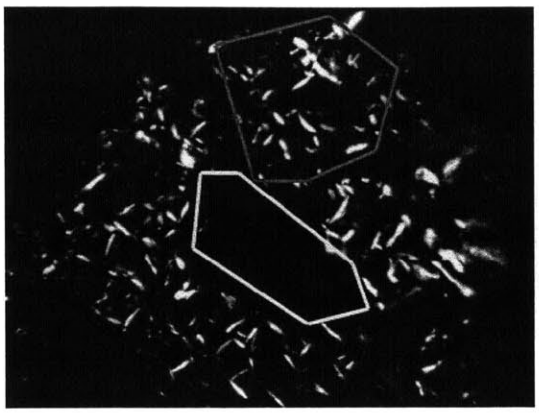

Figure 5-11: 10% wax in light oil system experiencing steady shear of $\dot{\gamma} \sim 0.1\text{s}^{-1}$ at temperature of 25°C ($T/T_{wa} = 0.964$) in the Linkam cell. To image the fluid an Edmund Optics Techspec VZM 600i lens was used in conjunction with a CCD camera. Vertical image size is roughly 1 millimeter. See supporting information for movie.

of the fluid in the 1-2 (flow-gradient) plane the Linkam acquires images in the 1-3 (flow-vorticity) plane.

In Fig. 5-11 we show an image of a 10% wax-oil system experiencing steady shear in the Linkam cell at a shear rate of $\dot{\gamma} = 0.1\text{s}^{-1}$ and identify two specific regions of the image encircled by bounding boxes. The region encircled by the lighter box is dark with no birefringence, and thus contains no precipitates within it; in this region the wax/oil mixture behaves as a Newtonian fluid. On the other hand the other region is a solid fragment (consisting of multiple wax crystallites) which flows essentially as a rigid body i.e. it does not deform over time (but it does translate linearly and rotate). The arrangement of these crystallite fragments is random, however under steady shearing they progressively break down and the average size decreases with time. During a pipeline restart operation one would thus expect local domains characteristic of plug-like flow profiles (resulting from the large fragments) to decrease over time as the stresses which cause the shearing deformation in the material steadily reduce the size of the fragments. This is consistent with the observations for the 5% wax-oil system under a steady apparent shear rate (Fig. 5-10). Specifically, an initial plug-like flow profile is observed at the 20 second mark, however at the 600 second mark the flow observed more closely resembles a linear profile (with some wall slip

still present however).

The process whereby these solid fragments break down is analogous to "shear melting" which has been observed in other yielding systems [68]. More specifically, the behavior observed in the model wax-oil system is similar to the process of fragmentation and erosion that Gibaud and coauthors describe in their work on another yielding fluid (a Laponite suspension) [86]. Gibaud et. al. utilized a dimensionless metric based on frequency of observed plug like velocity profiles to quantify how much erosion had been experienced by an initially gelled fluid. Motivated by this analysis, a dimensionless measure Φ was developed in order to quantify the degree of erosion in the wax-oil mixture under a steady shear rate. This metric is shown schematically in Fig. 5-12 and corresponds to a dimensionless and normalized measure of the area between the actual measured velocity $v_x(y)$ at each time t and an ideal linear velocity profile ($v_x = \dot{\gamma} y$). This measure can be evaluated from the following integral:

$$\Phi = \frac{1}{\dot{\gamma} H^2/4} \int_0^H \left| (v_x(y) - \dot{\gamma} y) - \left(\int_0^H v_x(y) dy - \dot{\gamma} H/2 \right) \right| dy \tag{5.8}$$

Where the first term in brackets in the integrand represents the difference between the local velocity $v_x(y)$ and the expected viscometric value $\dot{\gamma} y$, while the second term represents the difference between the average measured velocity and the average velocity for viscometric flow on the centerline at $y = H/2$. For any velocity profile Φ will vary between 0 and 1. These two limits correspond to the case of the linear velocity profile expected in Couette flow ($\Phi = 0$ and $v_x(y) = \dot{\gamma} y$, as shown in subfigure (a) in Fig. 5-12) and the case of a plug like flow profile ($\Phi = 1$ and $v_x(y) = V_p$ where V_p is the velocity of the plug, as shown in subfigure (c) in Fig. 5-12). When $\Phi \simeq 1$ and the fluid is experiencing plug like flow, the wax-oil gel consists of one fragment, or a few very large fragments, that slip along the top and bottom surfaces. A value of Φ approaching zero indicates that the gelled fragments have broken up and become smaller. Although Φ cannot provide a measure of the size of gel fragments, changes in its value do correspond to higher or lower degrees of fragmentation, and thus indicate whether or not the gel fragments have decreased or increased in size over time.

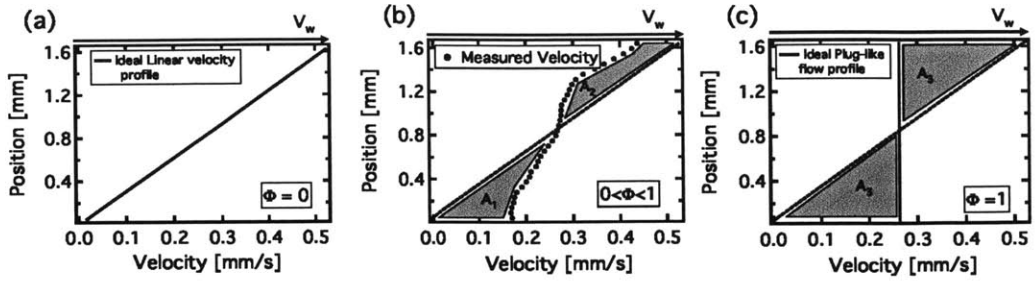

Figure 5-12: Schematic diagram indicating the parameter Φ. For the velocity profile (b) in the middle figure, Φ is given by $\frac{A1+A2}{2(A3)}$.

The computed evolution of $\Phi(t)$ for the data in Fig. 5-10 is shown in Fig. 5-13. There are large local fluctuations over short time intervals; however, the long term decay of $\Phi(t)$ is evidence of the progressive erosion of the structure and reflects the role of applied deformation on the increasing structural homogeneity of the wax-oil sample. We also note that there is an initial time period ($0 \leq t \leq 20$s) where Φ increases from zero to a maximum. This occurs due to the fact that the sample initially experiences a uniform elastic straining within the bulk and then slips to develop a plug like flow profile after 20 seconds. The point at which Φ reaches a maximum and the plug like flow profile is established corresponds to the time t_2 in Fig. 5-10 and coincides with passing through a local maximum in the measured stress acting on the sample. At t_2, the maximum strain has been accumulated in the fluid and from thereon flow occurs through a combination of wall slip and a local fracturing behavior as indicated by the decreasing value of Φ. During this period the applied stress on the material decreases (as shown in Fig. 5-10) as the microstructure is progressively eroded. The short term fluctuations in $\Phi(t)$ can be attributed to the spatial heterogeneity of the sample. The Rheo-PIV imaging system only observes a small portion of the entire sample (corresponding to 1mm field of view along the circumference). From the known circumference of the fixture ($\sim$ 160mm) and the imposed rotation rate it is straightforward to calculate that it takes 300 seconds to make one full revolution at an imposed shear rate of 0.3s^{-1}. This time period is half of the duration of the entire experiment.

In order to observe the long term behavior of the fluid (and illustrate the steady

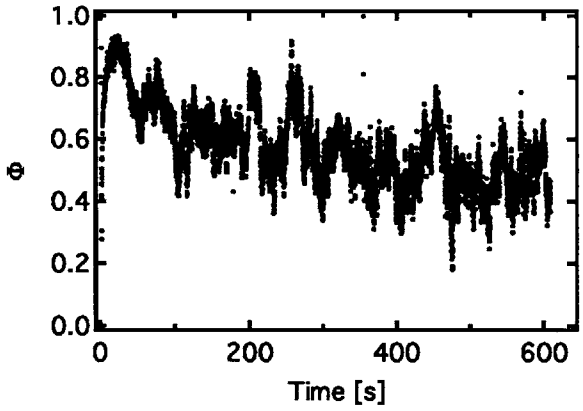

Figure 5-13: Evolution in the flow heterogeneity and erosion in the structure under steady shearing for the space-time data given in Fig. 5-10 ($\dot{\gamma} = 0.3\text{s}^{-1}$ and $T/T_{wa} = 0.993$).

state reached by the system under steady shearing conditions), data for the parameter Φ is shown in Fig. 5-14 for the same system as in Fig. 5-13 (5% wax/oil mixture at 27°C) undergoing a larger steady shear rate ($\dot{\gamma} = 1.5\text{s}^{-1}$) for a longer period of time (1600 s). For this case, the same surface conditions are used as in in Fig. 5-13. Fig. 5-14 presents a locally averaged value of Φ over 0.5 second intervals (31 frames per interval) at each data point. The result of this temporal averaging is to smooth out the short-term fluctuations in $\Phi(t)$ and to reveal the long time asymptotic behavior. At long times, a steady state is reached by the system, corresponding to a value of $\Phi \simeq 0$ and a viscosity which has decreased to a constant value. At this state, the fragments in the wax oil mixture have become very small, and the velocity profile within the fluid is nearly linear, with close to zero slip velocity at the upper and lower surfaces.

In Fig. 5-10, Fig. 5-13 and Fig. 5-14 we have considered evolution of flow profiles for the model wax-oil within a cone plate geometry with a smooth machined aluminum lower surface. We have also demonstrated that the type of surface that the gelled wax/oil is in contact with can have a considerable effect on the behavior of the flow profile (Fig. 5-8). To further explore the role of roughness two experiments were conducted in which a steady shear rate ($\dot{\gamma} = 0.1s^{-1}$) was imposed on a gelled wax-oil system beneficiated and cooled to 27°C ($T/T_{wa} = 0.993$). For the first experiment,

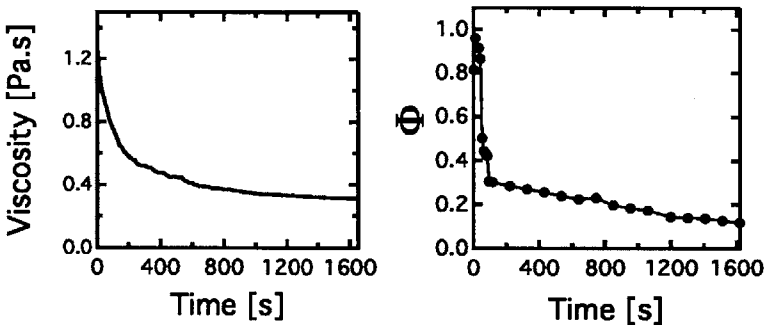

Figure 5-14: Evolution of viscosity and Φ for a 5% wax in oil system under a steady shear rate of $\dot{\gamma} = 1.5\text{s}^{-1}$.

the wax-oil gel was sheared between a smooth upper and lower geometry (as in Fig. 5-10). For the second experiment, the sample was sheared between a roughened lower geometry (root mean square roughness $R_q = 30\mu$m) and the smooth upper geometry (this configuration is identical to the experiment with the roughened lower surface shown in Fig. 5-9). The bulk rheological data from these experiments is shown in Fig. 5-15. In both instances, the stress within the material reaches a maximum value and then decreases gradually over time. The peak stress for the wax-oil gel in contact with the roughened lower geometry, $\sigma_{\text{max,r}} = 0.89$ Pa is significantly larger than the peak stress for the wax-oil gel in contact with the smooth lower geometry, $\sigma_{\text{max,s}} = 0.41$ Pa. Furthermore the stress within the wax-oil gel is always lower when the sample is in contact with the smooth geometry. This behavior is consistent with the data presented in Fig. 5-9 and Fig. 5-7. At the end of each test the stress in both experiments is still decreasing and has not yet reached a steady state. From the rheological measurements shown in Fig. 5-8 at high stress ($\sigma \gg \sigma_{cy}$), it is expected that the two steady state stress values should ultimately approach the same value at long times, coinciding with a value of $\Phi \simeq 0$ where the structure of the material has broken down completely.

The evolution of local velocity fields for both experiments are represented in the space time plots shown in Fig. 5-16 together with the temporal evolution of the erosion parameter $\Phi(t)$. These space time plots show the same characteristic three-

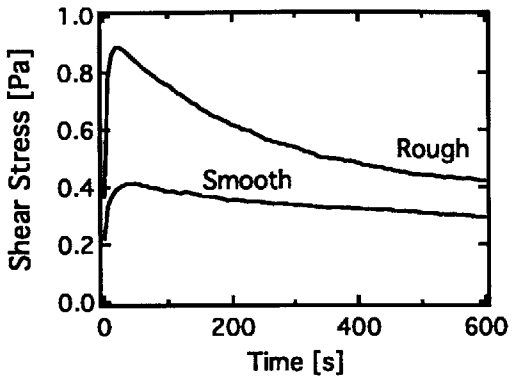

Figure 5-15: Comparison of stress vs time for a 5% wax-oil system at 27°C ($T/T_{wa} = 0.993$) undergoing steady shear of $\dot{\gamma} = 0.1\text{s}^{-1}$ with a roughened lower surface($R_q = 30\mu\text{m}$) and with a smooth lower ($R_q = 0.6\mu\text{m}$) surface.

stage behavior documented at the higher shear rate presented in Fig. 5-10. There is an initial stage where the material is strained uniformly (linear growth in the stress and the velocity profile) followed by a period during which the material flows in a plug-like manner. The third stage is characterized by fluctuating velocity profiles that are intermediate between perfectly linear shearing profiles and plug like slip profiles. This stage corresponds to progressive break down of the gelled fragments. Despite their qualitative similarity, there is an important distinction between the two cases shown in Fig. 5-16. When the sample is in contact with the roughened bottom surface, slip along this surface is inhibited: as a result, the bulk of the fluid moves with a velocity V_p close to zero, and the deformation in the material is primarily a result of bulk deformation coupled with fluctuating slip on the top surface. The inhibition of slip at the bottom surface continues for all times as can be discerned from the lower space time plot in Fig. 5-16 (c).

The long term fluctuations in the space time plots and the slow decay in the measured shear stress (Fig. 5-15) are reflected in the evolution of the dimensionless erosion parameter $\Phi(t)$ (Fig. 5-16 (b) and (d)). For both experiments, the value of Φ initially increases to a value very close to unity (indicating perfect plug like flow in both cases just after the stress maxima shown in Fig. 5-15). Over the rest of the 10 minute period, Φ decreases in a time-fluctuating manner. This fluctuating behavior

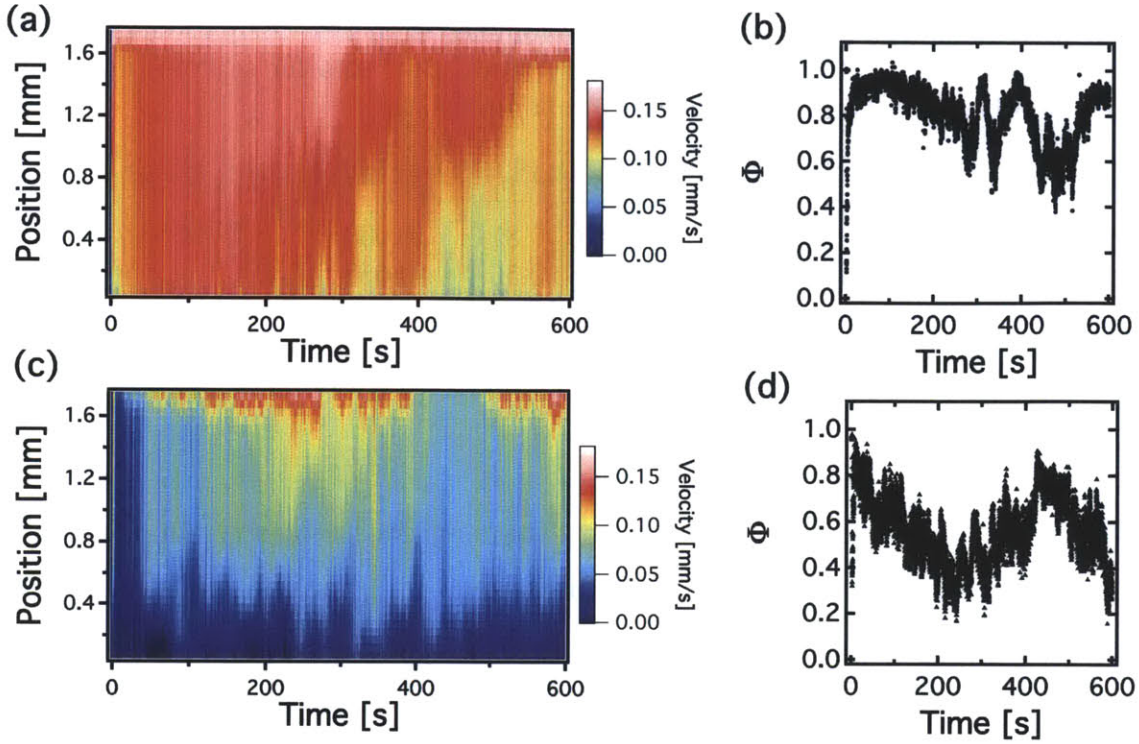

Figure 5-16: Local velocity field in the form of space-time plots for the 5% wax-oil system undergoing a shear rate of 0.1s^{-1} at 27°C ($T/T_{wa} = 0.993$) in contact with (a) a smooth lower surface ($R_q = 0.6\mu$m) and in contact with (b) a rough lower surface ($R_q = 30\mu$m). Evolution of Φ given on right hand side of plots ((b) for the smooth lower surface and (d) for the rough lower surface).

of Φ is due to the localized nature of the Rheo-PIV measurements. As mentioned previously, flow is observed within an imaging window that is small compared to the total size of the sample. At any given instant in time the Rheo-PIV system therefore observes the local (as opposed to the average bulk) flow behavior of the sample. For this reason, it is instructive to consider the time averaged value of Φ for each experiment. These values are reported in Table 5.3 in conjunction with the mean energy dissipation rate per unit volume for each experiment which is defined as

$$\langle \dot{E} \rangle \equiv \frac{1}{t} \int_0^t \dot{E} dt' = \frac{1}{t} \int_0^t \sigma(t) \dot{\gamma} dt' \ . \tag{5.9}$$

As Table 5.3 shows, for the same imposed shear rate, the average value of Φ is

Table 5.3: Time averaged values of Φ and volumetric energy dissipation rate $\dot{E}$ for experiments at a steady shear rate of $0.1s^{-1}$ and $0.3s^{-1}$ and for samples in contact with smooth ($R_q = 0.6\mu m$) or rough ($R_q = 30\mu m$) plates

Experiment		$\langle\Phi\rangle$	$\langle\dot{E}\rangle$ [J/m^{3}s]
$\dot{\gamma} = 0.1s^{-1}$	smooth	0.81	0.034
$\dot{\gamma} = 0.1s^{-1}$	rough	0.56	0.058
$\dot{\gamma} = 0.3s^{-1}$	smooth	0.58	0.14
$\dot{\gamma} = 0.3s^{-1}$	rough	0.53	0.16

lower when the material is in contact with the roughened geometry. In addition to this, an increase in the imposed shear rate results in a lower average value of Φ. The roles that the imposed shear rate and surface roughness have on the value of the erosion parameter can be understood by considering the energy dissipated into the material. It is clear from Table 5.3 that for the higher shear rate experiments ($\dot{\gamma} = 0.3s^{-1}$) there is a higher rate of energy dissipation into the sample. The higher volumetric rate of energy dissipation results in a lower average value of Φ, since the increased energy dissipated into the system results in greater fracturing and erosion of the solid gelled fragments. Using rougher surfaces also results in a larger rate of energy dissipation (at a particular shear rate), so the value of Φ decreases faster when the sample is sheared between rough surfaces. This is consistent with the bulk rheological data shown in Fig. 5-7 and Fig. 5-8, which show that smooth shearing surfaces allow slip, which in turn enables the material to flow at lower stresses for a given shear rate and therefore dissipate less energy.

5.4 Conclusions

In this chapter, we have used measurements of the local velocity and deformation fields within a model waxy crude oil to probe local evolution in the microstructural deformation and the wall slip of the sample while under an imposed stress or strain. The model wax-oil systems that have been developed in this chapter exhibit a temperature- and

composition-dependent rheology similar to real waxy crude oil. When the mixture is cooled below the wax appearance temperature T_{wa} using a careful thermal beneficiation procedure, a percolated network of wax crystallites form that cause the fluid to exhibit a yield stress, σ_{cy}. At stresses below the yield point $\sigma < \sigma_{cy}$ the material is an elastoplastic gel and for high stresses $\sigma > \sigma_{cy}$ it behaves as a strongly shear thinning viscoplastic liquid. The yielding transition for this preparation protocol is irreversible for the most part – the sample spanning structure formed by the precipitated discotic crystallites is disrupted under a large imposed stress but the jammed microstructure is unable to reform without a subsequent thermal beneficiation and cooling step.

The characteristics of the yielding transition in the wax-oil gel were shown to depend on the nature of the solid surface it is placed in contact with. Smooth surfaces with a lower root mean square roughness R_q promote interfacial slip and this can result in measurements of higher apparent shear rates and a lower apparent viscosity at the same imposed stress. The RheoPIV system can also be used to study the erosion in the local microstructure for a gelled system under controlled deformation rate conditions. When a steady shear rate is imposed, the wax-oil gel is initially strained to a critical yield strain and reaches a maximum stress; beyond this point the gel undergoes fluctuating periods of wall slip and structural erosion which results in initially large gelled fragments breaking down into progressively smaller fragments. The rate of erosion can be changed by modifying the characteristics of the bounding surface. Roughened surfaces lead to increased energy dissipation rates, which assist in a more rapid erosion of the gel structure. The combination of time-resolved rheometry and PIV analysis provides new insight into the complex yielding mechanisms experienced by the percolated crystallite structures formed in waxy crude oils. These observations may even ultimately have an impact on pipeline restart strategies or systematic design and selection of pipe wall surface finishes.

In this chapter we have only employed very simple generalized Newtonian fluid (GNF) constitutive laws to predict the rheology of these model crude oils. These types of models are unable to capture the rich transient yielding behavior exhibited by these fluids, or the viscoelastic properties of the gelled solid. They are also not an

appropriate framework for predicting any of the shear heterogeneities that these fluids exhibit. Therefore, in the next two chapters, we will begin a study of EVP behavior in the context of constitutive modeling. We will start with a simpler case, by first utilizing a model EVP fluid which exhibits little thixotropy (a Carbopol microgel). We will use LAOStress to describe its constitutive response, and then use a framework from plasticity theory in order to develop an appropriate constitutive relation. Then, in Chap. 8, we will revisit the model waxy crude oil, and use the framework developed in Chap. 6 to develop a fully thixotropic constitutive law for this EVP material.

Chapter 6

Describing and Prescribing the Constitutive Behavior of Elasto-Viscoplastic Materials

6.1 Introduction

We will begin our study of the second complex phenomenon in this thesis (EVP behavior) by first introducing a LAOStress framework, and then applying it to gels and soft solid materials that can undergo yield-like transitions. We will show that the nonlinear measures extracted from this framework can be used to rationally guide the development of a constitutive model that predicts the behavior of such materials, and help evaluate the relevant material parameters in a systematic fashion. This chapter will be primarily focused on studying EVP materials, which are commonly distinguished from other complex fluids by a critical strain or stress beyond which the material transitions from a predominantly solid-like to a more liquid-like behavior [217, 65]. For many of these soft materials, the canonical Herschel-Bulkley model (which incorporates a yield stress parameter) is often successful at capturing the steady state viscoplastic flow behavior at sufficiently large stresses and shear rates [138, 55, 15, 168]. The Herschel-Bulkley model will therefore form a basis for the

development of our constitutive model. EVP materials are also known to exhibit a number of additional complexities in their response. One of these is wall slip [16] and many studies have focused on understanding the nature of this slip and how it relates to the microstructure of the material [86, 15, 139]. Thixotropy is another frequently encountered complexity which some EVP materials may exhibit [17, 53, 148]. Recently, the presence of thixotropy has been promulgated as a distinguishing behavior which separates a subclass of "ideal" EVP materials (or simple yield stress fluids) from other classes of yielding materials [147]. In this Chapter we will focus on a simple yield stress fluid known as Carbopol. This soft solid has been studied extensively in recent years and is a canonical example of an "ideal" or simple yield stress fluid that exhibits little to no thixotropy (see [168] for a good review, as well as [147, 146, 55]). The lack of thixotropy in these microgels has made them ideal candidates for rheological studies. Measures will also be taken to prevent slip from occurring in the material used here.

The Carbopol microgel will be used to contrast the LAOStress material measures with those of the strain-controlled framework (LAOStrain), and we will discuss the differing physical interpretations provided by these two sets of measures. Guided by the stress-controlled LAOS measurements, we develop two constitutive models that predict the rheological behavior of these soft solid materials. These rheological equations of state capture a distinct sequence of processes under large amplitude deformation, consistent with that described by [182]: in particular, under oscillatory stress loading, the response involves an initial elastic straining, followed by viscoplastic flow, and a subsequent elastic unloading when the applied stress is decreased. The second, more complex, constitutive model discussed here is also capable of exhibiting a viscosity bifurcation at a critical stress [53]. Below this critical stress the model exhibits an unbounded power-law–like growth in the viscosity over time, whereas at constant applied stresses above this critical value, it converges to the familiar Herschel-Bulkley steady state flow curve that is commonly seen for these types of materials. This nonlinear rheological behavior can be described in terms of a constitutive process known as kinematic hardening, which is discussed in detail in Sec. 6.4.4. These

models are both formulated using a decomposition of strain - an approach commonly taken in the continuum mechanics and plasticity literature [93]. Thus, an added benefit of using these models is that they can easily be generalized to frame invariant 3D tensorial form using the multiplicative Kroner decomposition of the deformation gradient, $\mathbf{F}(\mathbf{x}, t)$ [114, 93].

6.2 Experimental

6.2.1 Materials

The material used for this study is a 0.5 % wt. Carbopol microgel (Carbopol 901 variant manufactured by Lubrizol). This class of microgel has been used extensively in many other studies [178, 168] and it has been demonstrated to behave as an "ideal" yield stress fluid in the sense that it is not strongly thixotropic [147]. The steady state flow behavior of Carbopol microgels is well predicted by the power-law Herschel-Bulkley flow rule [55, 160, 64] provided that wall-slip is eliminated, and is relatively easy to measure due to the lack of thixotropy exhibited by Carbopol. For these reasons, Carbopol microgels serve as useful model fluids for exploring and quantifying the LAOStress framework. The microstructure of these gels consists of highly swollen and compressed spherical-shaped blobs (of characteristic dimension ~ 5 μm) which, at high concentrations, provide the material with its yield stress [111, 41, 168, 127].

6.2.2 Rheometry

All strain-controlled oscillatory measurements were carried out on an ARES strain-controlled rheometer (TA Instruments), while stress-controlled oscillatory measurements were carried out using an ARG2 rheometer (TA Instruments). Cone and plate geometries were used in all cases to impose uniform strain fields within the sample. Carbopol microgels are well known to experience wall slip when subjected to steady shearing deformations [178, 55, 21] so for repeatable measurements of true material response it is essential to minimize wall slip. Roughened test fixtures (created us-

ing adhesive-backed sandpaper with controlled grit size) are therefore used on both rheometers. These surfaces have a root mean squared roughness $R_q \sim 30$ μm, which is on the same order, but slightly larger than the characteristic length scale of the swollen microgel structure (5 μm). The effectiveness of this roughening was verified using two techniques: first, it was observed that the roughened surfaces led to increased values of the measured yield stress in the fluid (Barnes [16] showed that this indicates a change in the degree of slip in the material); secondly, it was possible to obtain direct velocimetric measurements of the flow field within the microgel undergoing steady shearing using the Rheo-PIV apparatus discussed in Chap. 3. These velocimetric measurements show that when the gel is in contact with the roughened surfaces, wall slip is effectively eliminated.

One issue that arises when controlling an oscillatory deformation on a sample with a stress-controlled rheometer is the potential impact that the instrument rotational inertia may have on the measurements [207, 126, 118]. For most single head rheometers (such as the ARG2) the total torque signal measured by the rheometer can be additively decomposed into two components; the sample torque and the 'inertia torque'. For progressively larger torque amplitudes and oscillation frequencies, the inertial contributions to the torque may then increase and become large enough to dominate the total torque signal. Therefore, all stress-controlled oscillatory shear experiments were carried out at sufficiently small frequencies and stress amplitudes such that instrument inertia did not significantly affect the total torque signal. Section A.1 of the appendix discusses these effects in detail.

6.3 Theory

6.3.1 Stress vs. Strain Decomposition for a Yielding Material

We first motivate our discussion of the stress-controlled LAOS framework by providing an illustrative example of experimental data. In Fig. 6-1 below, we show the response

of the Carbopol microgel to a sinusoidally imposed strain, $\gamma = \gamma_0 \sin \omega t$ when the strain amplitude γ_0 is small (linear region) and when γ_0 is large (nonlinear region).

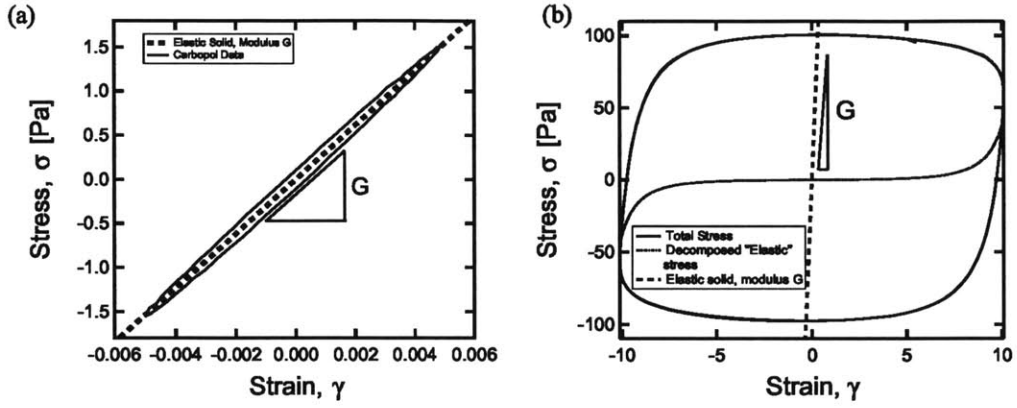

Figure 6-1: Comparison of Carbopol response to small and large amplitude oscillatory deformations. Data was collected in controlled strain mode, at a frequency of $\omega = 0.5$ rad/s.

As can be seen in Fig. 6-1 (a), for small amplitudes ($\gamma_0 = 0.5\%$) the response of the Carbopol microgel to the cyclic strain loading is primarily elastic (with elastic modulus $G = 300$ Pa indicated on the plot) and little dissipation due to the low value of $G'' = 12$ Pa. At the large strain amplitude ($\gamma_0 = 1000\%$), the response of the material is qualitatively different. The shape of the cyclic stress-strain loading curve is closer to a rectangle than an ellipse. This is representative of the response expected for an elasto-viscoplastic material as discussed previously by Ewoldt et. al. [73], Hess and Aksel [98] and Rogers and coauthors [182]. Using the LAOStrain framework, the total shear stress $\sigma(t)$ (which is a periodic signal containing multiple higher harmonic components) can be decomposed into two contributions, an "elastic" stress σ' which is a single-valued function of $x = \gamma/\gamma_0$ (the scaled strain), and a "viscous" stress σ'' which is a single-valued function of $y = \dot{\gamma}/\dot{\gamma}_0$ (the scaled strain rate). The decomposition defined by Cho et. al. [50] and used by Ewoldt and coauthors [71] therefore is:

$$\sigma' \equiv \frac{\sigma(\gamma, \dot{\gamma}) - \sigma(-\gamma, \dot{\gamma})}{2}$$
$$\sigma'' \equiv \frac{\sigma(\gamma, \dot{\gamma}) - \sigma(\gamma, -\dot{\gamma})}{2} \tag{6.1}$$

The fact that the "elastic" stress σ' and the "viscous" stress σ'' are single-valued functions of strain and strain rate respectively allows one to fit various functional forms to the two stresses. These functional forms (such as the orthogonal Chebyshev polynomials used by Ewoldt et. al. [71]) can be used to understand the type of intra-cycle nonlinearities exhibited by the material. While this decomposition is mathematically sound, the physical interpretation of the decomposition may vary from material to material [183]. In particular, in Fig. 6-1 (b), we see that the decomposed "elastic" stress for Carbopol is apparently very low for strain values $-7 \leq \gamma \leq 7$. This is at odds with what is known about the linear, elastic behavior of the gel at low strain amplitudes. The dashed line showing the stress-strain curve for an elastic solid with modulus $G = 300$ Pa further emphasizes this discrepancy. What is apparent is that the zero strain modulus characterizing the decomposed "elastic" stress-strain curve is much smaller (by several orders of magnitude in fact) than the actual shear modulus G of the Carbopol measured in the small deformation limit. This contradictory behavior is difficult to interpret, especially if one wishes to understand the behavior of the material in terms of a sequence of physical processes, as argued by Rogers et. al. [182, 183]. It would also be confusing to use polynomial fitting coefficients of the decomposed σ' curve to extract information about the elastic behavior of the Carbopol for oscillatory deformations when γ_0 is large. Indeed, Rogers et. al. [183] showed that one could interpret the LAOS response of the the Elastic Bingham model studied by Yoshimura and Prud'Homme [217] (in which a linear elastic behavior is present) as exhibiting strain stiffening - an inherently nonlinear elastic behavior. We can identify a similar apparent trend in the Carbopol microgel from the upturned shape of the decomposed elastic stress-strain curve shown in Fig. 6-1 (b) at large strains.

To better understand the behavior of the Carbopol system at these large strain

amplitudes, we first consider a simple elastic-perfectly plastic constitutive model [120]. This model approximately captures the behavior of the material in Fig. 6-1. A critical feature of the model is the additive decomposition of the shear strain γ into elastic and plastic components:

$$\gamma = \gamma^e + \gamma^p \tag{6.2}$$

Where the elastic strain γ^e is related through the shear stress σ as follows:

$$\sigma = G\gamma^e \tag{6.3}$$

The plastic strain rate, $\dot{\gamma}^p$ is assumed to be zero for stresses below a critical yield stress $|\sigma| < \sigma_y$ (i.e. there is no plastic flow below the yield stress). When the stress in the material reaches the yield stress σ_y, the material yields, resulting in the stress saturating and plastic flow occurring in the same direction as the stress. For this simple model the plastic flow is rate independent - i.e. the stress is constant for all values of the plastic strain rate $\dot{\gamma}^p$. The constitutive model can be thought of as an elastic element in series with a yielding element, with elastic strain increasing linearly with the stress, and plastic strain only accumulating for values of $|\sigma| = \sigma_y$, the yield stress. The rate-independent plasticity behavior is somewhat poorly defined (for example, the behavior of this model is not defined for applied stresses of $|\sigma| > \sigma_y$) however rate-independent flow can be realized through the following limit of a power-law flow rule:

$$\frac{\sigma}{\sigma_y} = \lim_{m \to 0} \left(\frac{\dot{\gamma}^p}{\dot{\gamma}^p_{\text{ref}}} \right)^m \tag{6.4}$$

The response of such a model to an oscillatory deformation $\gamma = \gamma_0 \sin \omega t$ is shown in Fig. 6-2. Beginning from the left hand point (s) on the cyclic curve at zero stress, the material first undergoes an elastic deformation. The stress then saturates at σ_y, and rate-independent plastic flow begins to occur. When the direction of straining is reversed, elastic unloading occurs and the stress begins to drop below σ_y.

This model successfully captures the idea that under an increase in the imposed strain $\gamma(t)$, the material will undergo a sequence of physical processes. These pro-

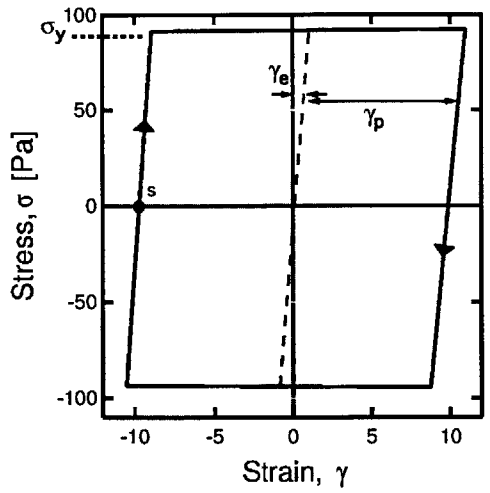

Figure 6-2: Response of a simple elasto-plastic model to oscillatory shear strain $\gamma = \gamma_0 \sin \omega t$. The yield stress corresponds to the location of the plateau in the cyclic curve with a value of $\sigma_y = 90$ Pa.

cesses are specifically those of elastic loading, rate independent plastic flow, and elastic unloading. The decomposition of the strain γ into elastic (γ^e) and plastic (γ^p) components means that the elastic stress-strain curve (which is just a plot of σ vs. γ^e) can be overlaid on the cyclic loading curve (shown as a dashed line on Fig. 6-2).

Symmetry arguments similar to those made by Cho et. al. [50] can be used to extract an apparent elastic strain $\gamma'(\sigma)$ (with a functional dependency on the imposed stress σ) from the measured total strain field $\gamma(t)$ using the following definition:

$$\gamma'(\sigma) = \frac{\gamma(t_1) + \gamma(t_2)}{2} \quad \text{where } \sigma(t_1) = \sigma(t_2) \tag{6.5}$$

For this particular constitutive model, the apparent elastic strain $\gamma'(\sigma)$ determined from the strain decomposition of Eq. 6.5 (which assumes nothing about the underlying nature of the constitutive model) is exactly equal to $\gamma^e(\sigma)$ of the constitutive model given in Eq. 6.2. More generally, from the shape of the Lissajous curves shown in Figs. 6-1, 6-2, it is clear that this decomposition more faithfully captures the elastic nature of the material response at small stresses. One cannot prove that the identity $\gamma^e(\sigma) \equiv \gamma'$ holds for all constitutive models. However these decomposed strain curves strongly suggest that, at least for yield-like elasto-viscoplastic materials, it is more de-

sirable to decompose the strain into individual elastic and plastic components, rather than the stress. The decomposed strains can then be fit to a particular functional form. For example, the decomposed elastic strain $\gamma^e(\sigma) = \gamma'(\sigma)$ in Fig. 6-2 can be easily fit to a linear function, with slope equal to the elastic modulus G from Eq. 6.3.

We apply this strain decomposition to the Carbopol data presented in Fig. 6-1 to obtain the apparent elastic strain $\gamma'(\sigma)$ of the material. The resulting strain decomposition is shown in Fig. 6-3; clearly when we compare this elastic stress-strain curve to that of Fig. 6-1 (b), we see that the variation in the apparent elastic strain $\gamma'(\sigma)$ in Fig. 6-3 is in much closer agreement with the stress-strain curve of the linear elastic solid (dashed line with modulus G) at low stresses. Given what is known separately about the behavior of the Carbopol at low stresses from Fig. 6-1 (a) (i.e. it can be roughly approximated as an elastic solid with modulus G), the elastic stress-strain curve $\gamma'(\sigma)$ obtained in Fig. 6-3 is thus a better indicator of how the material behaves elastically over the course of the loading cycle.

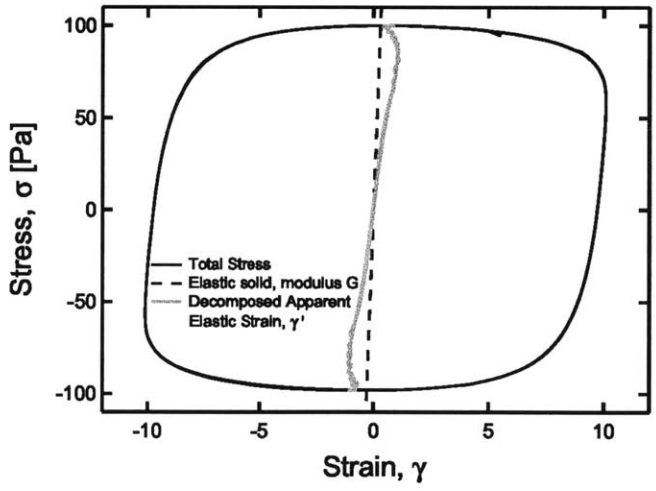

Figure 6-3: Decomposed apparent elastic strain γ' of the Carbopol gel as defined through Eq. 6.5 during a strain-controlled LAOS test with $\gamma_0 = 10$. The slope of this decomposed curve is in better agreement, especially at small strains, with the shear modulus of a linear elastic solid with modulus G shown by the dashed line.

There are, however, several disadvantages of carrying out this strain decomposition when the total strain $\gamma(t)$ is the input to the system ($\gamma = \gamma_0 \sin \omega t$). First, there is no

guarantee that the time-resolved decomposed strain signal γ' is "linear", i.e. it will likely contain multiple higher harmonics. Second, some materials are known to exhibit stress overshoots under LAOS [72], resulting in the possibility of there being more than two points in a cycle at which the stress has the same value. These overshoots would limit the use of the definition given in Eq. 6.5. For these reasons, we describe a framework in the next section that allows stress-controlled experiments to be carried out, with total shear stress as the input ($\sigma = \sigma_0 \cos \omega t$) and with the measured shear strain γ (the output) being decomposable into elastic and plastic components. This provides a linear input into the system, and eliminates the possibility of having to deal with overshoots in the output, as strain overshoots do not occur under stress-controlled conditions in the absence of instrument inertia or fluid inertia effects.

6.3.2 Stress-controlled LAOS framework for analysis of experimental data

The framework used in this paper is similar to that used by Ewoldt [69] and Lauger and Stettin [118] with some slight changes in convention. We also provide complementary definitions of the analogous Chebyshev coefficients to those used by Randy et. al. [71] for the strain-controlled case. We begin by noting that we impose a sinusoidal stress on the material:

$$\sigma(t) = \sigma_0 \cos \omega t \tag{6.6}$$

The resulting strain $\gamma(t; \sigma_0, \omega)$ can then be decomposed into a Fourier series as follows:

$$\gamma(t; \sigma_0, \omega) = \sum_{n \text{ odd}} \{J'_n(\omega, \sigma_0)\sigma_0 \cos n\omega t + J''_n(\omega, \sigma_0)\sigma_0 \sin n\omega t\} \tag{6.7}$$

We consider responses in which only odd harmonics are present. This was also the approach taken by Ewoldt et. al. [69, 71]. Even harmonics may arise during transient responses [14] or due to the presence of dynamic wall slip [91]; however we will not consider these types of phenomena in this work. If desired, it is straightforward to

define the coefficients for even values of n using the formalism we describe. We also neglect any constant strain offsets (corresponding to the $n = 0$ term in Eq. 6.7) that may arise in the response of the material due to initial nonlinear transients in the startup of the imposed oscillatory shear stress. These offsets depend on the specific material and the amplitude of the imposed stress, but in the present framework we will only consider the long time periodic oscillating state with these offsets removed. Furthermore, the convention of using a cosine wave for the imposed stress is adopted, because it simplifies the expressions used to determine Chebyshev fitting coefficients.

Based on the fact that there are only odd harmonics present in the strain signal represented in Eq. 6.7, we can then decompose our strain into an apparent elastic strain, γ', and an apparent plastic strain, γ'':

$$\gamma'(t) = \sigma_0 \sum_{n \text{ odd}} J_n'(\omega, \sigma_0) \cos n\omega t \tag{6.8}$$

$$\gamma''(t) = \sigma_0 \sum_{n \text{ odd}} J_n''(\omega, \sigma_0) \sin n\omega t \tag{6.9}$$

The strain decomposition is based on the idea that we desire an apparent elastic strain, γ', such that over one cycle of oscillation γ' is a single-valued function of σ. We also desire an apparent plastic strain, γ'', such that its time derivative, the *apparent plastic strain rate* $\dot{\gamma}''$, is a single-valued function of σ. The convention of naming γ' an *elastic* strain and naming γ'' a *plastic* strain then follows because elastic strain typically depends on imposed stress only, and plastic strain rate typically depends on stress only. It can be shown that the decomposition represented by Eqns. 6.8 and 6.9 is unique, in the sense that no other linear decomposition of γ satisfies the properties of γ' being a single-valued function of σ and $\dot{\gamma}''$ being a single-valued function of σ (see Appendix A.2). However we also emphasize that for a general class of constitutive models in which strain is decomposable into elastic and plastic components (denoted γ^e and γ^p respectively), the strain decomposition represented by Eqns. 6.8 and 6.9 into apparent elastic and plastic contributions (γ' and γ'') will not necessarily yield the true elastic and plastic strains γ^e and γ^p defined through the constitutive model. In the previous section we saw that the true and apparent strains coincided for a simple

elasto-plastic constitutive model, however in Sec. 6.4.4 we will discuss an example of a constitutive model in which γ^e and γ^p differ from γ' and γ''. For these reasons we use the modifier "apparent" to distinguish between the experimentally-measurable strains and the constitutive counterparts.

Having defined γ' and γ'', we can follow the reasoning of Ewoldt and coauthors [71] and represent these single-valued functions of stress as a series of orthogonal Chebyshev polynomials $T_n(x)$, where x is the scaled stress, $x = \sigma(t)/\sigma_0$.

$$\gamma'(t) = \sigma_0 \sum_{n \text{ odd}} J'_n(\omega, \sigma_0) \cos n\omega t = \sigma_0 \sum_{n \text{ odd}} \underbrace{J'_n(\omega, \sigma_0)}_{c_n} T_n(x) \tag{6.10}$$

$$\dot{\gamma}''(t) = \sigma_0 \sum_{n \text{ odd}} n\omega J_n(\omega, \sigma_0)'' \cos n\omega t = \sigma_0 \sum_{n \text{ odd}} \underbrace{n\omega J''_n(\omega, \sigma_0)}_{f_n} T_n(x) \tag{6.11}$$

The above representation follows from the identity $T_n(\cos\theta) = \cos n\theta$. The resulting material coefficients in Eqns. 6.10 and 6.11 have units consistent with compliances $c_n(\omega, \sigma_0)$ $[\text{Pa}]^{-1}$ and fluidities $f_n(\omega, \sigma_0)$ $[\text{Pa.s}]^{-1}$, respectively. Due to the convexity of the 3rd Chebyshev polynomial, positive values of c_3 (i.e. increasing compliance) result in stress softening of the apparent elastic stress-strain curve. Positive values of f_3 (i.e. increasing fluidity) result in stress-thinning of the apparent plastic strain-rate vs. shear stress curve. Conversely, negative values of c_3 imply stress-stiffening of the elastic material, while negative values of f_3 imply stress-thickening. In general, interpretations of these 3rd order Chebyshev coefficients are only meaningful in the case when they are the leading order of nonlinearity. Furthermore, a number of researchers [113, 73, 182] have shown that in the limit of a perfectly plastic response, a $1/n$ dependency is observed in the magnitude of the Fourier harmonics. Therefore, in the case of yielding materials, the Chebyshev coefficients with order $n \geq 5$ can still play a significant role in determining the material response to LAOS. As a consequence, we will generally refrain from using the individual Chebyshev coefficients f_n and c_n to characterize material response, due to some of the concerns discussed by Rogers and Lettinga [183]. Instead, we define a set of general nonlinear measures that characterize the material response to LAOStress at a particular temporal point

within a sequence of cyclic deformations. These definitions are identical to those given by Ewoldt [69] and Lauger and Stettin [118]; however, the use of a cosine in Eq. 6.6 [69] instead of a sine [118] results in a slightly different expression for these measures in terms of the compliances J'_n and J''_n. Here the measures are also related to the LAOStress Chebyshev framework as well. The first of these measures is the minimum-stress elastic compliance, denoted here as J'_M, which is defined and related to the compliance coefficients J'_n or c_n as follows:

$$J'_M \equiv \left.\frac{d\gamma}{d\sigma}\right|_{\sigma=0} = \sum_{n \text{ odd}} (-1)^{(n-1)/2} n J'_n = \sum_{n \text{ odd}} (-1)^{(n-1)/2} n c_n \tag{6.12}$$

In Fig. 6-4 we illustrate the difference between the nonlinear measure J'_M for LAOStress and the complementary measure G'_M for LAOStrain. G'_M is the minimum-strain elastic modulus which Ewoldt et. al. [71] defined as follows:

$$G'_M = \left.\frac{d\sigma}{d\gamma}\right|_{\gamma=0} \tag{6.13}$$

In each figure, we show two sets of data - one Lissajous-Bowditch curve is measured for the Carbopol system undergoing LAOStress ($\sigma = \sigma_0 \cos \omega t$), and the other Lissajous-Bowditch curve of the same material under LAOStrain ($\gamma = \gamma_0 \sin \omega t$). In the linear viscoelastic regime shown in Fig. 6-4 (a) the material response is indistinguishable in LAOStress or LAOStrain loading, as expected. In Fig. 6-4 (b) the values of γ_0 and σ_0 were chosen such that the two experiments would result in approximately the same maximum stress and strain. It can be seen that the qualitative shape of the Lissajous curves is remarkably similar in both cases, even though the two experimental protocols are different. Specifically, in each curve we can identify an identical sequence of processes that the material undergoes; corresponding to elastic loading, followed by plastic flow and then elastic unloading. We see that the minimum stress elastic compliance J'_M measures the instantaneous compliance when the instantaneous imposed stress passes through zero, while G'_M measures the instantaneous modulus when the instantaneous imposed strain passes through zero. The critical difference between the two measures becomes apparent in their location on the Lissajous curve.

We see that J'_M probes behavior in the elastic region of the curve (at stresses below the critical stress), while G'_M probes the behavior in the plastic flow region of the curve at stresses greater than the critical stress. The compliance J'_M is therefore a better indicator of the intracycle elastic behavior of the material in the unyielded region, and one of the main benefits of the stress-controlled LAOS framework is that J'_M can be evaluated using the individual compliance coefficients J'_n obtained from the Fourier-Chebyshev spectrum (Eq. 6.12). This definition of J'_M corresponds to the reciprocal of the "Cage Modulus" defined and used by Rogers et. al. [182], although they based their definition of "Cage Modulus" on a strain-controlled experiment. The measure J'_M can, of course, be numerically evaluated for both stress and strain-controlled experiments, and from Fig. 6-4 (b) the two appear to have similar values (they are in fact within 7% of each other), however in the general nonlinear case they will not be equal due to the different loading history of the experiments.

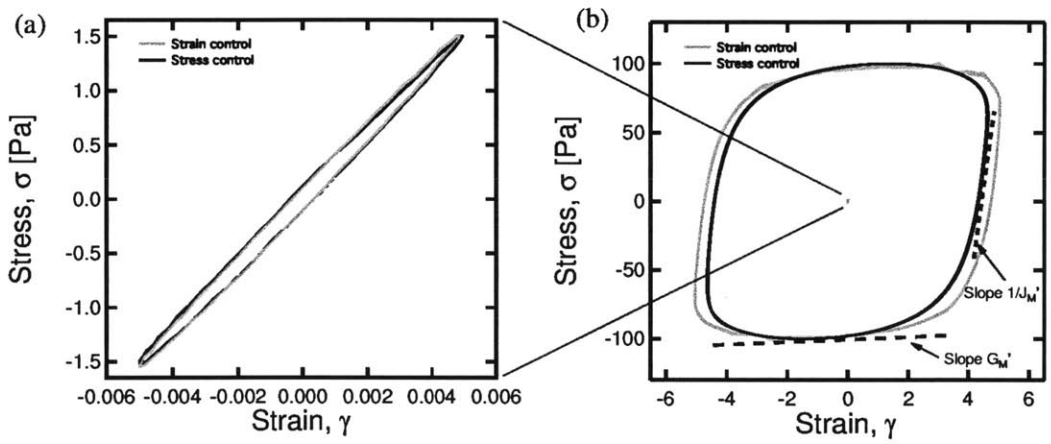

Figure 6-4: (b) graphical comparison in the nonlinear (yielded) regime of the complementary measures G'_M and J'_M evaluated for LAOStress (with $\sigma_0 = 100$ Pa) and LAOStrain (with $\gamma_0 = 5$) data from Carbopol at a frequency of $\omega = 0.5$ rad/s. A comparison (a) in the linear viscoelastic regime of the Lissajous curves obtained in LAOStress and LAOStrain oscillatory tests.

These results suggest an alternative interpretation for the measure G'_M for yielding materials. Under a controlled oscillatory strain, G'_M is evaluated at zero instantaneous strain. However, the choice of this zero strain point is somewhat arbitrary, due to

the fact that for a yielding material, irreversible viscoplastic flow is the dominant mechanism of deformation. Therefore, G'_M fails at describing the elastic behavior of the material. As is observed in Fig. 6-4, G'_M decreases dramatically past the yielding point, suggesting that in this material some type of strain softening may be occuring. However, care must be taken in using this interpretation to develop a constitutive model since, in general, descriptive rheological material functions are not necessarily prescriptive constitutive model parameters. In the upcoming sections we will discuss a model which captures this behavior by implementing a yielding element in series with a linear elastic element, and the decrease in the material function G'_M being caused by the onset of plastic flow in the material.

Another complementary nonlinear measure that can be defined is the elastic compliance J'_L at large stresses, which is related to the compliances J'_n and c_n as follows:

$$J'_L \equiv \left.\frac{\gamma}{\sigma}\right|_{\sigma=\sigma_0} = \sum_{n \text{ odd}} J'_n = \sum_{n \text{ odd}} c_n \tag{6.14}$$

Both J'_L and J'_M are nonlinear elastic measures in the sense that they describe local intracycle elastic behavior in a nonlinear soft solid material or yield stress fluid. If desired, a third nonlinear measure can be defined: $J'_K = d\gamma'/d\sigma|_{\sigma=\sigma_0}$. This is analogous to the measure G'_k introduced by Ewoldt et. al. [71]. In addition to these measures, a relative ratio of the change in compliance within a large amplitude cycle can be defined:

$$R \equiv \frac{J'_L - J'_M}{J'_L} = \frac{4c_3 - 4c_5 + 8c_7 - 8c_9 + ...}{c_1 + c_2 + c_3 + ...} \tag{6.15}$$

When $R > 1$, the material exhibits pronounced nonlinearities in the form of an apparent softening.

Corresponding nonlinear viscous measures can also be defined for LAOStress. These are based on the measured fluidities instead of compliances. The first of these is ϕ'_M, which is the minimum stress fluidity and is defined as follows:

$$\phi'_M \equiv \left.\frac{d\dot{\gamma}}{d\sigma}\right|_{\sigma=0} = \sum_{n \text{ odd}} (-1)^{(n-1)/2} n^2 \omega J''_n = \sum_{n \text{ odd}} (-1)^{(n-1)/2} n f_n \tag{6.16}$$

Table 6.1: Comparison of the nonlinear measures appropriate for stress-controlled LAOS with the analogous nonlinear measures for strain-controlled LAOS.

	LAOStrain		LAOStress		Interpretation in LAOStress
Elastic measures	$G'_L = \frac{\sigma}{\gamma}\Big\|_{\gamma=\gamma_0}$	$\longrightarrow$	$J'_L = \frac{\gamma}{\sigma}\Big\|_{\sigma=\sigma_0}$		Large stress elastic compliance
	$G'_M = \frac{d\sigma}{d\gamma}\Big\|_{\gamma=0}$		$J'_M = \frac{d\gamma}{d\sigma}\Big\|_{\sigma=0}$		Zero stress elastic compliance
	e_n		$c_n = J'_n$		Chebyshev compliance coefficients $c_3 > 0$ stress softening $c_3 < 0$ stress stiffening
Viscous measures	$\eta'_L = \frac{\sigma}{\dot{\gamma}}\Big\|_{\dot{\gamma}=\dot{\gamma}_0}$	$\longrightarrow$	$\phi'_L = \frac{\dot{\gamma}}{\sigma}\Big\|_{\sigma=\sigma_0}$		Large stress fluidity
	$\eta'_M = \frac{d\sigma}{d\dot{\gamma}}\Big\|_{\dot{\gamma}=0}$		$\phi'_M = \frac{d\dot{\gamma}}{d\sigma}\Big\|_{\sigma=0}$		Zero stress fluidity
	v_n		$f_n = n\omega J''_n$		Chebyshev fluidity coefficients $f_3 > 0$ stress thinning $f_3 < 0$ stress thickening

The second is ϕ'_L, which is the fluidity at large stress and has the following definition:

$$\phi'_L \equiv \frac{\dot{\gamma}}{\sigma}\bigg|_{\sigma=\sigma_0} = \sum_{n\ \text{odd}} n\omega J''_n = \sum_{n\ \text{odd}} f_n \tag{6.17}$$

The nonlinear measures are summarized in the Table 6.1, and are contrasted with the analogous nonlinear measures defined for LAOStrain.

One important issue that bears mentioning is the interrelation between the measures defined under stress and strain-controlled oscillatory conditions. It is well known that in the linear regime of deformation, the dynamic compliances J' and J'' can be interrelated to the dynamic moduli G' and G'' (they are complex conjugates, but are not directly reciprocally related [77]). One of the important aspects of the nonlinear relations defined in Table 6.1 is that because there is no general interrelation between the stress-dependent nonlinear compliances J'_n and nonlinear moduli G'_n for the strain-controlled case, there is no general interrelation between nonlinear measures such as J'_M and G'_M. These measures are therefore complements, but not conjugates. Furthermore, the nonlinear LAOStress measures such as J'_M can actually be defined under either LAOStress or LAOStrain conditions, since their definitions are not based

on a particular Fourier decomposition or mode of forcing. However they will not necessary yield the same value in both cases (see Fig. 6-4). Care must therefore be taken when reporting and interpreting different measures of nonlinear rheological response, and it is particularly important to keep track of whether these are evaluated under stress or strain-controlled conditions. In this work, whenever LAOStress measures such as J'_M, J'_L, ϕ'_M, and ϕ'_L are referred to, it is implicit that they are evaluated for controlled-stress experiments (i.e. for $\sigma = \sigma_0 \cos \omega t$). Despite this caveat, the experimental data in Fig. 6-4 for the particular case of the Carbopol microgel suggests that the evaluation of J'_M is not particularly sensitive to whether the experiment is done under LAOStress or LAOStrain (only a 7% change in the value is apparent at $\omega = 0.5$ rad/s and at $\sigma_0 = 100$ Pa).

6.4 Results and Discussion

6.4.1 Rheology of an 'ideal' (non-thixotropic) material

We now focus on a detailed illustration of the utility of the stress-controlled LAOS framework described in Sec. 6.3 by applying it to rheological fingerprinting of the Carbopol microgel. Before probing the behavior of the Carbopol system using LAOS, we demonstrate some of the other important aspects of this material's rheology. In Fig. 6-5 we show the steady state flow curve of the microgel in (a), and in (b) the linear viscoelastic moduli of the microgel are plotted as a function of frequency.

The steady flow data in Fig. 6-5 is obtained by imposing a shear rate on the material, and then waiting approximately 3 minutes for the system to attain a steady state. The protocol is then repeated at a lower shear rate, and the shear rate is reduced progressively in steps to $\dot{\gamma}_{\min} = 10^{-3}$ s^{-1}. The data is fitted to the Herschel-Bulkley model, which is given by the following expression:

$$\sigma = \sigma_y + k\dot{\gamma}^m \tag{6.18}$$

The parameters for the fit given in Fig. 6-5 are $\sigma_y = 49$ Pa, $m = 0.45$ and $k = 19$

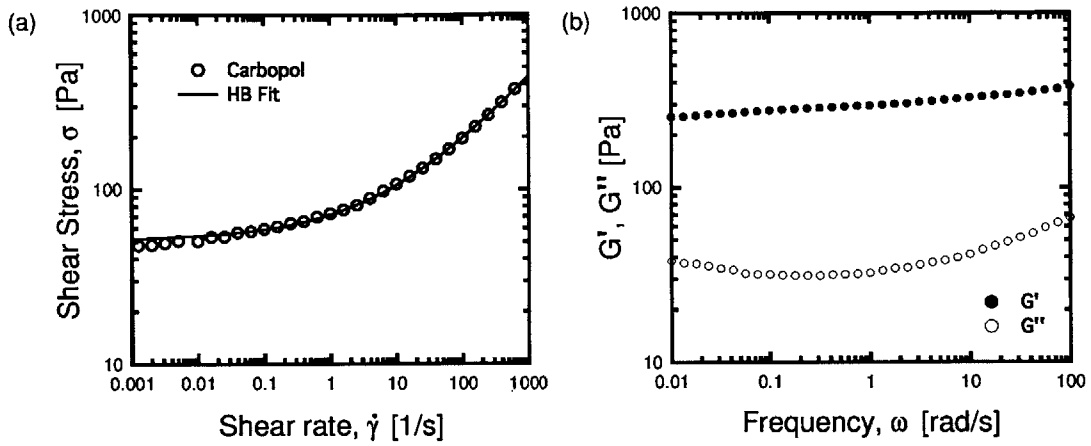

Figure 6-5: Flow curve and linear viscoelastic moduli of the Carbopol microgel using roughened cone and plate fixtures. Linear viscoelastic moduli are obtained with a strain amplitude $\gamma_0 = 4\%$, corresponding to a maximum stress of $\sigma_{\max} \simeq 15$ Pa, which is well below the dynamic yield stress of $\sigma_y \simeq 50$ Pa.

Pa.s^m. The Herschel-Bulkley model is well known to predict the steady state flow behavior of these types of microgels above the yield stress σ_y, and has been used in a large number of previous studies [168, 160, 55]. Fig. 6-5 shows that there is a good agreement between the HB fit and the data, with some deviation at the lower shear rates. The linear viscoelastic moduli show that the Carbopol gel behaves as a viscoelastic solid at low strain amplitudes, with G' generally one order of magnitude larger than G''. Furthermore, there is a very weak power-law dependency of the parameter G' on frequency.

One interesting reported aspect of the rheology of Carbopol gels is the slow creeping flow observed at applied stresses σ which are below the yield stress σ_y. This can be inferred by noting that (with the selected test protocol of 3 minutes shearing at each rate) the data points for the steady state flow curve progressively deviate slightly below the Herschel-Bulkley prediction in Fig. 6-5 as the stress approaches σ_y. This suggests that while the parameter σ_y determined from Fig. 6-5 does correspond, in a limiting sense, to a "steady state" yield stress, the material still creeps viscoplastically below this yield stress. This type of creep has been documented by previous workers [147, 146], who have shown that the measured instantaneous viscosity, $\eta^+(t) \equiv \sigma/\dot{\gamma}(t)$

during creep tests with an applied stress $\sigma < \sigma_y$ continues to increase in time, typically as a power-law with $\eta^+(t) \sim t^n$. The goal of our LAOStress framework is to probe the behavior both above and below the steady state yield stress value σ_y, so it is helpful to understand the nature of this slow viscoplastic creep occurring for stresses $\sigma < \sigma_y \simeq 49$ Pa. We present data from creep tests carried out on the Carbopol microgel in Fig. 6-6 below.

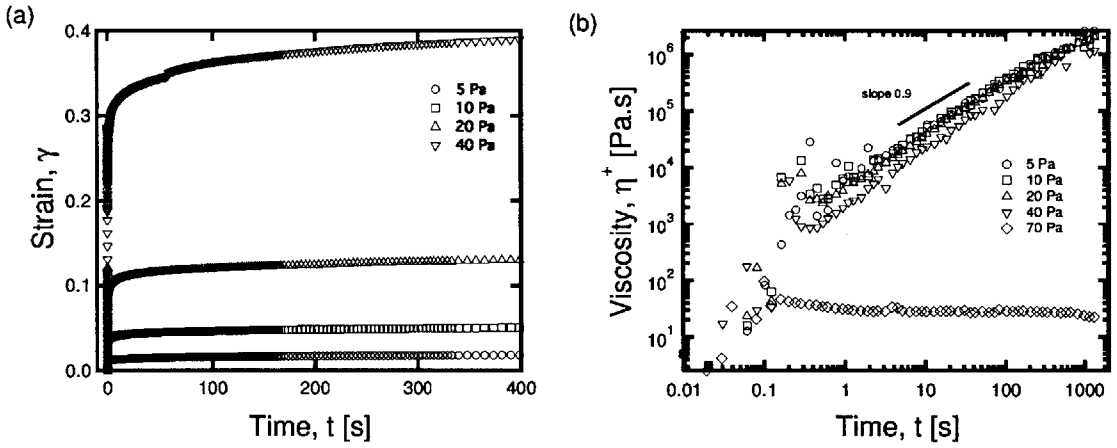

Figure 6-6: Experimental creep data for the Carbopol system at a number of different applied stress values $\sigma < \sigma_y$. In (a) the measured strain $\gamma(t)$ vs. time is plotted, in (b) the instantaneous viscosity $\eta^+(t)$ is plotted vs. time.

The creep curves in Fig. 6-6 (a) are characterized by a rapid initial elastic strain response, followed by a long period of slow creep. In Fig. 6-6 (b) the instantaneous viscosity η^+ as a function of time is plotted on a logarithmic scale - this viscosity is determined by dividing the imposed stress σ by the local slope of the creep curve, i.e. the instantaneous shear rate $\dot{\gamma}(t) \equiv d\gamma/dt$. We see that when the applied stress is below σ_y, the long term creep behavior of this system is characterized by a power-law–like growth of the instantaneous viscosity with time (with viscosity scaling as $\eta^+ \sim t^{0.9}$). By contrast at imposed stresses $\sigma > \sigma_y$ the viscosity rapidly settles to a steady value consistent with the steady flow curve shown in Fig. 6-6 (a). This is similar to what has been observed for the class of fluids that undergo a "viscosity bifurcation" [53], and is identical to the type of behavior observed by Moller et. al. [147] (although with a different value of the power-law exponent). The power-law viscosity bifurcation

at a critical stress is difficult to replicate in constitutive models. For example, the simple Kelvin-Voigt model for viscoelastic solids predicts that under creep loading, the strain will increase as $1 - e^{-t/\tau}$, with τ being a characteristic retardation time. As a result, the instantaneous viscosity $\eta^+(t)$ will increase exponentially in time at any value of the imposed stress. The model developed by Saramito [186] (which incorporates a yielding transition at a critical stress) exhibits the same deficiency as the Kelvin-Voigt model, because it predicts Kelvin-Voigt viscoelastic deformation below the yield stress. What is desired is a constitutive model that predicts a well-defined flow curve at large stresses and a smooth transition to a power-law increase in the instantaneous viscosity $\eta^+(t)$. An example of such a model would be the "Soft Glassy Rheology" (SGR) model introduced by Sollich [194] and refined by Fielding and coworkers [79, 78]. In the forthcoming sections, however, we describe an alternative and relatively simple constitutive model that captures this behavior below a critical stress.

6.4.2 Probing nonlinear behavior using LAOStress

LAOStress experiments provide an ideal test methodology for probing the rheological behavior of the Carbopol microgel above and below the yield stress σ_y. By varying the magnitude of the imposed stress amplitude σ_0, it is possible to observe how the material responds to deformations in the linear elastic regime and the ultimate viscoplastic flow regime. We begin by inspecting the cyclic stress-strain loading curves (or Lissajous-Bowditch curves) of the Carbopol undergoing an imposed oscillatory deformation with $\sigma = \sigma_0 \cos \omega t$ with frequency $\omega = 1$ rad/s. Fig. 6-7 below shows the response of the material at various values of the imposed stress amplitude σ_0:

The Lissajous curves (and all Lissajous curves that follow) are now plotted with the shear stress on the abscissa because the controlled input into the system is shear stress, such that $\sigma = \sigma_0 \cos \omega t$. In Fig. 6-7 (a) we see that the strains accumulated for $\sigma_0 = 200$ Pa are very large due to the irreversible viscoplastic flow which occurs in the material (at $\sigma_0 = 200$ Pa we are well beyond the yield stress σ_y shown in Fig. 6-5). In Fig. 6-7 (b) we expand the ordinate scale to focus on the response for smaller stress

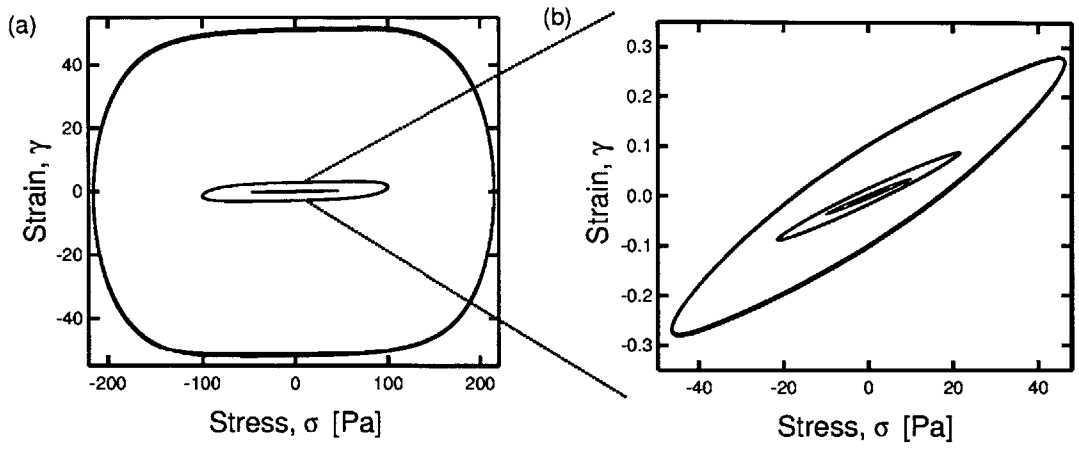

Figure 6-7: LAOS of Carbopol at a number of different stress amplitudes σ_0 and a frequency of 1 rad/s. In (a) the Lissajous curves at the largest stress amplitudes are shown (σ_0 = 200 Pa, 100 Pa), smaller stress amplitude curves are shown on an expanded scale in (b)

amplitudes, and see the beginning of a transition in the shape of the curves that occurs for stress amplitudes approaching $\sigma_y = 49$ Pa. The individual curves for varying stress amplitudes are overlaid on the same plot to illustrate an important point - the value of J'_M , i.e. the instantaneous compliance at zero stress, systematically increases with σ_0, so that the material softens. However this nonlinear material measure does not vary as dramatically as G'_M, which is the analogous LAOStress measure defined in Eq. 6.13.

The full stress-amplitude/frequency dependence of the material response can be compactly illustrated through the use of a Pipkin diagram. However, a drawback to this graphical representation is that each cyclic curve has to be rescaled for clarity. This rescaling is potentially misleading because individual Lissajous curves may then appear to show large relative changes in the shape of their orbit as well as in associated local measures such as the compliance J'_M. However, the Pipkin diagram is helpful for illustrating the fact that the yielding transition in this microgel is a gradual and frequency-independent one, i.e. based on the shape of the Lissajous curves, we cannot easily identify a single stress amplitude at which the material begins to flow. This is due to the dynamic nature of the LAOStress protocol, and the tendency of Carbopol

to exhibit some visco-plastic creep even at the lowest stresses $\sigma_0 \ll \sigma_y$. As we show below, the Pipkin diagram also serves as a tool for comparing the measured response of the Carbopol to the predicted response of constitutive models (i.e. it can serve as a fitting tool).

To demonstrate that the small stress compliance J'_M exhibits a weak dependency on the stress amplitude σ_0 and frequency ω (a behavior that is not immediately apparent from the Pipkin space plot, but is clearly seen from Fig. 6-7), we plot an interpolated contour plot of the minimum stress compliance $J'_M(\sigma_0, \omega)$. This compliance can be evaluated from Eq. 6.12 using the individual compliance coefficients J'_n determined for 5 different frequencies and 8 stress amplitudes. There are only 40 discrete data points for J'_M, so for visual clarity these points are interpolated to a 230×140 grid using the MATLAB command `griddata` with the `cubic` interpolation setting. This contour plot is shown in Fig. 6-9 below, together with a corresponding contour plot of the nonlinear measure J'_L defined in Eq. 6.14.

The contour plots of J'_M and J'_L provide a distinguishing fingerprint of the nonlinear material response. Firstly, we can see that J'_M exhibits a very weak dependency on frequency. It increases as the stress amplitude is increased (i.e. the material softens) and generally seems to reach a maximum at around $\sigma_0 = 100$ Pa, or approximately twice the critical yield stress identified from steady shear. However, the increase is moderate, raising the value of J'_M from 0.0039 Pa^{-1} at $\sigma_0 = 1$ Pa to 0.0063 Pa^{-1} at $\sigma_0 = 100$ Pa. For small imposed stress amplitudes $\sigma_0 \ll \sigma_y$, we see that the large stress compliance J'_L approaches the value of J'_M measured at zero instantaneous stress. This is to be expected because the material behaves primarily as a linear elastic solid for stresses $\sigma_0 \ll \sigma_y$, and in the linear viscoelastic limit $J'_M = J'_L = J'_1$.

Contour plots of the corresponding nonlinear viscous measures, ϕ'_L and ϕ'_M are also plotted to gain further insight into the material response. These nonlinear measures of fluidity are presented in Fig. 6-10 and exhibit a somewhat less complicated dependence on ω and σ_0. In particular, ϕ'_L is completely frequency independent. It is zero for small values of $\sigma_0 \ll \sigma_y$ then exhibits a sudden increase beyond the yield stress σ_y as the material begins to exhibit substantial plastic flow. For this class of materials,

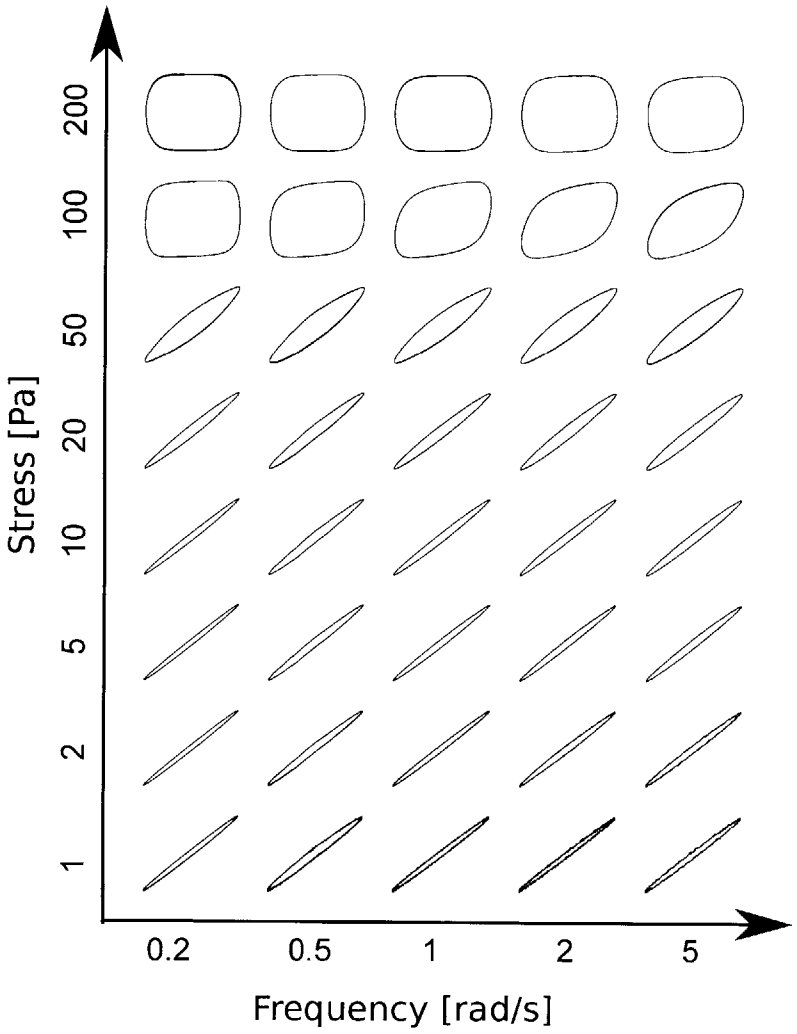

Figure 6-8: Pipkin diagram of Carbopol response to LAOS at a number of different frequencies ω and stress amplitudes σ_0. At low stresses the material response shows little dependency on the frequency ω. A stronger frequency dependence can be seen at the higher stresses.

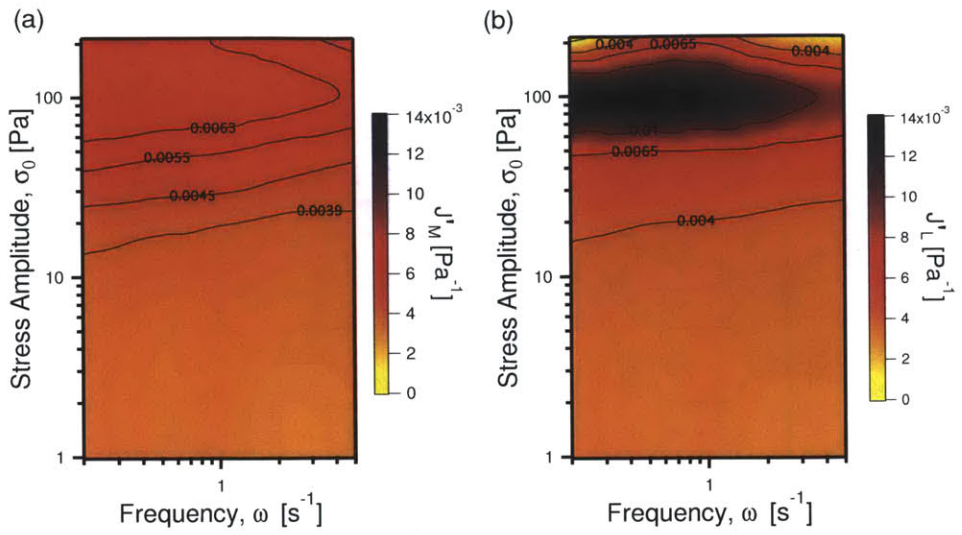

Figure 6-9: Contour plots of the nonlinear compliance measures J'_M and J'_L (see Eq. 6.14 and Eq. 6.12). These measures show a weak frequency dependence, and in general increase as σ_0 is increased, reaching a maximum as the material begins to flow then subsequently decreasing.

the fluidity ϕ'_L therefore serves as a good indicator of the range of imposed stresses beyond which the material yields visco-plastically. Conversely, the fluidity measured at zero stress, ϕ'_M, exhibits a dependency on both ω and σ_0, but its relative changes are small compared to ϕ'_L. This initially unexpected dependency will be discussed in the context of two constitutive models in the upcoming sections.

One of the principal benefits of constructing rheological fingerprints such as the contour plots presented in Figs. 6-9 and 6-10 is that they provide some insight into how to construct a constitutive model that captures the elasto-viscoplastic rheology of the Carbopol gel. A simple initial postulate is to model the Carbopol below the yield stress as an elastic solid with modulus G, with Herschel-Bulkley flow occurring as given in Eq. 6.18 above the yield stress. Such a proposition is initially reasonable, given the observation that both J'_M and J'_L are almost independent of ω and σ_0 below the yield stress. Furthermore, the very sudden transition in the fluidity ϕ'_L measured at large stress amplitudes indicates that there is a distinct difference between the behavior exhibited above and below the critical stress σ_y. A piecewise continuous constitutive model is easy to develop, and is described in the next section. However

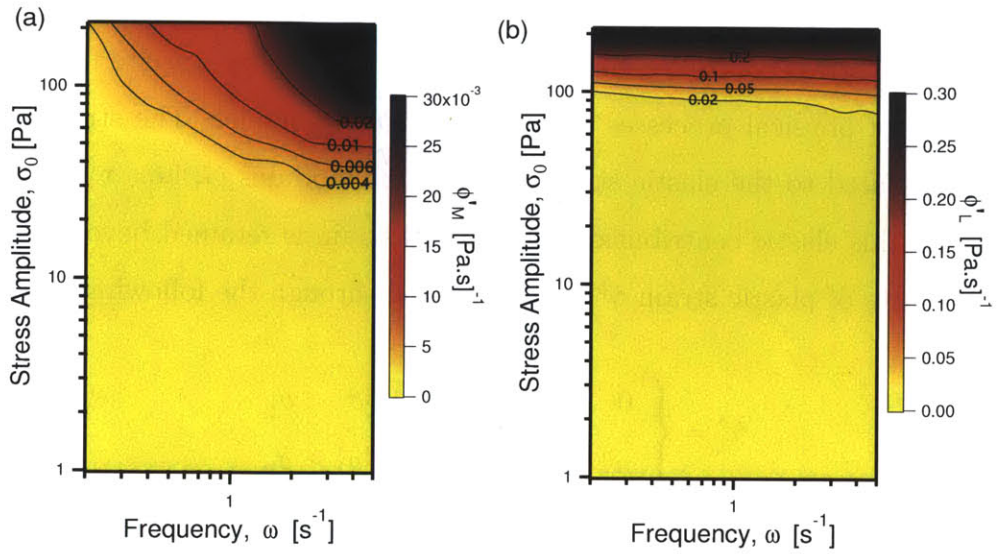

Figure 6-10: Contour plots of the nonlinear fluidity measures ϕ'_M and ϕ'_L. ϕ'_L shows a clear increase as the stress amplitude is increased beyond the yield stress σ_y, indicating onset of yielding. A more complex behavior is exhibited by ϕ'_M, with both stress and frequency dependence.

we will show that there are several aspects of the measured Carbopol behavior that it does not capture. Specifically, it is unable to capture the stress-dependent softening that is observed in the nonlinear material measures J'_M, J'_L below the yield point. After noting these deficiencies, we then modify the constitutive model to capture the elastoplastic creep that is observed experimentally at small stresses. This "kinematic hardening" model captures the variation in the nonlinear compliances J'_M, J'_L, and fluidity ϕ'_M, and enables us to capture more completely the rheological fingerprint of this yielding microgel.

6.4.3 The Elastic Herschel-Bulkley Model

For an elastic Herschel-Bulkley (EHB) material we begin in a manner similar to the approach taken for the elastic-perfectly plastic constitutive model that was discussed in Sec. 6.3.1. The model developed here is discussed in the context of one-dimensional deformations, however a full three-dimensional version of this model is outlined in Sec. 7.1.

First, the total strain is decomposed into elastic and plastic components such that

$\gamma = \gamma^e + \gamma^p$ as in Eq. 6.2. This strain decomposition is an essential component of this model, and the stress-controlled LAOS framework is more appropriate for analyzing the sequence of physical processes envisioned by such a model. The stress σ in the material is related to the elastic strain through the modulus G, i.e. $\sigma = G\gamma^e$ as in Eq. 6.3, and this elastic contribution to the total strain is retained beyond the yield point. The rate of plastic strain $\dot{\gamma}^p$ is then related through the following conditional equation:

$$\dot{\gamma}^p = \begin{cases} 0 & \text{if } |\sigma| < \sigma_y \\ n^p \left(\frac{|\sigma| - \sigma_y}{k}\right)^{1/m} & \text{if } |\sigma| \geq \sigma_y \end{cases} \tag{6.19}$$

Where the material constants σ_y, m and k are the same as those given in the simple Herschel-Bulkley model of Eq. 6.18, and n^p is the direction of stress, i.e. $n^p = \sigma/|\sigma|$. The presence of the directional integer $n^p(= \pm 1)$ forces the plastic strain rate to be co-directional with the imposed shear stress. The only addition to the simple viscoplastic Herschel-Bulkley model of Eq. 6.18 is that elastic behavior has been introduced (and this elastic behavior is present both above and below the yield stress). Compared to the simplest elastic-perfectly plastic material discussed in Section 6.3.1, we have introduced a well-defined rate dependency in the plastic flow rule given by Eq. 6.19. One of the important differences between this particular model and some of the Elastic-Bingham [217] or Elastic Herschel-Bulkley [65] type models used in the rheology literature is that there is no critical strain above which plastic flow begins for this model. The elastic strain γ^e therefore does not saturate for this EHB model. This avoids the problems associated with discontinuities in the stress arising during strain-controlled oscillatory experiments, such as those shown by Yoshimura and Prud'Homme [217]. For stresses below the yield stress value σ_y, the EHB model will show no irreversible deformation or energy dissipation. This dissipation is a result of slow viscoplastic creeping behavior which is clearly exhibited by the Carbopol microgel even below the critical stress.

One way to inspect the overall ability of a model to predict the rheology of the Carbopol gel is to overlay the experimental measurements and predicted response of this model in the Pipkin space represented by Fig. 6-8. The resulting fingerprint

illustrates many different aspects of the microgel's response to deformation, from elastic behavior at low stresses to fully viscoplastic yielding behavior at the higher stresses. In Fig. 6-11 we compare the LAOStress measurements with the response of the EHB model with fitting parameters $\sigma_y = 45$ Pa, $m = 0.43$, $k = 26$ Pa.s^m, $G = 350$ Pa. These parameters are close to those obtained from fitting the steady flow curve in Fig. 6-5 (a), however they have been adjusted slightly to improve the fit of the EHB model to the experimental measurements. The elastic modulus G is also approximately equal to the elastic modulus G' measured in Fig. 6-5 (b).

Fig. 6-11 shows that the EHB model captures the behavior of the Carbopol microgel under LAOS in two limiting regions. Firstly at large stress amplitudes where $\sigma_0 \gg \sigma_y$ (e.g. $\sigma_0 = 200$ Pa). In this region the response of the material is primarily dictated by the Herschel-Bulkley flow rule in Eq. 6.18. The model also fits the data well at very low stresses $\sigma_0 \ll \sigma_y$ (e.g. $\sigma_0 = 1$ Pa). At these low stresses the deformation of the Carbopol gel is close to that of a simple Hookean solid. The primary limitation to this EHB model, however, is that it cannot capture hysteresis in the Lissajous-Bowditch curves for values of $\sigma_0 \leq \sigma_y$. This is because the model assumes perfectly elastic behavior below σ_y. By inspecting Fig. 6-6 or 6-7, we can see that Carbopol gel is far from a perfect linear elastic solid when $\sigma < \sigma_y$.

Plotting the nonlinear compliances J'_M and J'_L at a given frequency as the stress amplitude is incremented provides further insight into the deficiencies of the EHB model in capturing the nonlinear behavior of the Carbopol gel. In Fig. 6-12 we overlay onto the experimental data the values of these nonlinear measures for two models. These are the EHB model which has been discussed in this section (broken line), and the KH model (Kinematic Hardening model; solid line) which will be described in the next section.

It is clear that both the small strain and large strain compliances J'_M and J'_L increase as the stress amplitude σ_0 is increased and the material softens. Both values reach a maximum at a value of $\sigma_0 \simeq 100$ Pa, followed by a subsequent decrease in their value. The EHB model however, predicts an ideal elastic response with $J'_M = J'_L = 1/G = 0.0029$ Pa^{-1}. This can be understood if one considers the nature

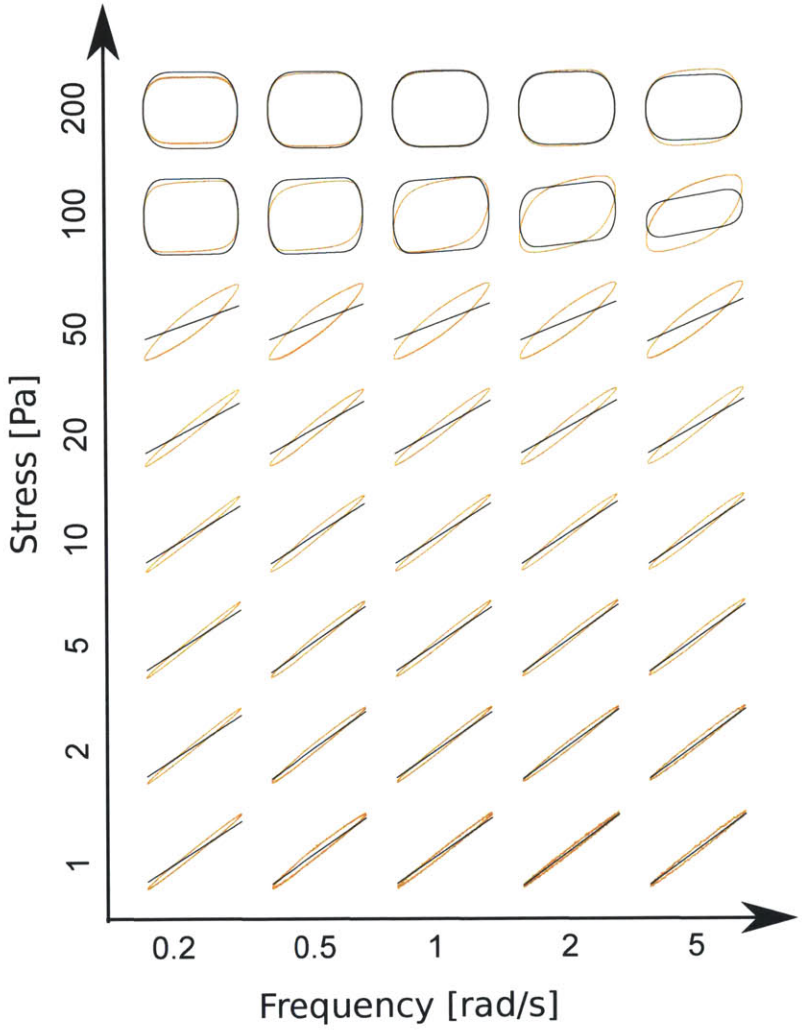

Figure 6-11: Pipkin diagram showing comparison of EHB model (black) with Carbopol data (orange) at a number of different frequencies ω and stress amplitudes σ_0. Shown are individual Lissajous curves of strain $\gamma(t)$ vs. stress $\sigma(t)$. The EHB model fitting parameters are $\sigma_y = 45$ Pa, $k = 26$ Pa.s^m, $G = 350$ Pa, $m = 0.43$.

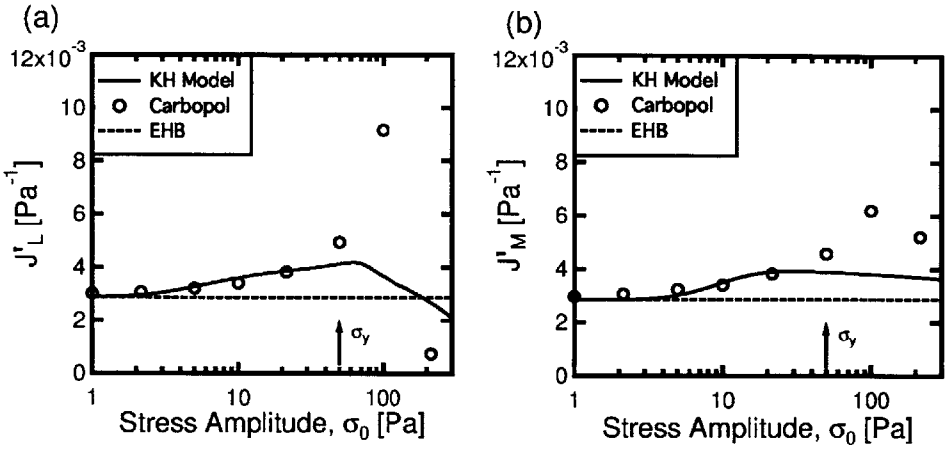

Figure 6-12: Plots of the compliance measures J'_M and J'_L at a frequency of $\omega = 5$ rad/s for a range of stress amplitudes. Carbopol data is contrasted to two models, the Elastic Herschel-Bulkley model (fitting parameters $\sigma_y = 45$ Pa, $k = 26$ Pa.s^m, $G = 350$ Pa, $m = 0.43$) and the Kinematic Hardening model (KH) described in the next section.

of the strain decomposition given in Eq. 6.8 and 6.9. We stated previously in Sec. 6.3 (and show in Appendix A.2) that the strain decomposition in Eq. 6.8 and 6.9 is unique. Therefore, no other decomposition provides an apparent elastic strain γ' that is a single-valued function of σ, and an apparent plastic strain rate $\dot{\gamma}''$ that is a single-valued function of σ. For the EHB model, γ^e is a single-valued function of σ (defined through Eq. 6.3), and Eq. 6.19 is formulated such that $\dot{\gamma}^p$ is also a single-valued function of σ. It follows that when the strain decomposition given in Eq. 6.9 is carried out for the EHB model undergoing a stress-controlled oscillatory deformation, we obtain $\gamma' = \gamma^e$ and $\dot{\gamma}'' = \dot{\gamma}^p$. Thus, for the EHB, model the unique value of elastic strain determined from the experimental strain decomposition of Eq. 6.9 is identical to the elastic strain defined in the constitutive model (Eq. 6.2). The nonlinear measure J'_M can then be determined by combining the definition in Eq. 6.12 with our strain decomposition of Eq. 6.8 and 6.9. Specifically:

$$J'_M = \left.\frac{d\gamma'}{d\sigma}\right|_{\sigma=0} + \left.\frac{d\gamma''}{d\sigma}\right|_{\sigma=0} \tag{6.20}$$

By the chain rule, and the fact that there are only odd harmonics present in the

response of the EHB model, the second term in Eq. 6.20 is zero. Then, because $\gamma' = \gamma^e$, the equation above is rewritten:

$$J'_M = \left.\frac{d\gamma^e}{d\sigma}\right|_{\sigma=0} = \left.\frac{d}{d\sigma}\frac{\sigma}{G}\right|_{\sigma=0} = \frac{1}{G} \tag{6.21}$$

Similar reasoning can be used to show that $J'_L = 1/G$ for all values of ω and σ_0 for the EHB model. In particular:

$$J'_L = \left.\frac{\gamma}{\sigma}\right|_{\sigma=\sigma_0} = \left.\frac{\gamma}{\sigma}\right|_{t=0} \tag{6.22}$$

And because $\gamma'' = \gamma^p$ is zero at $t = 0$ we have:

$$J'_L = \left.\frac{\gamma^e}{\sigma}\right|_{t=0} = \frac{1}{G} \tag{6.23}$$

It is therefore clear that although the EHB model is successful in capturing the behavior of the system at both very low stress amplitudes and very large stress amplitudes, the material response at intermediate stresses is more complex.

Similar arguments about the deficiencies of the EHB model can be made by inspecting plots of the nonlinear viscous measures ϕ'_L and ϕ'_M as shown in Fig. 6-13. The EHB model provides a very good agreement with experimental data for the fluidity measure ϕ'_L - this is because ϕ'_L is a measure of the viscous behavior of the material at large stresses, which is dominated by the Herschel-Bulkley flow rule in Eq. 6.18. However, at small imposed stresses, the EHB model is purely elastic (no dissipation) and predicts that for all values of ω and σ_0, the fluidity ϕ'_M is identically zero. This follows from the definition of ϕ'_M, which samples the material response instantaneously at the point within an oscillatory cycle where the imposed stress is zero. The Carbopol gel, on the other hand, exhibits a progressive increase in ϕ'_M as σ_0 is increased.

To motivate the development of a more advanced constitutive model, we have overlaid on Fig. 6-12 and 6-13 the predicted values of the nonlinear measures J'_L, J'_M, ϕ'_L and ϕ'_M for an alternate constitutive model which incorporates a behavior known

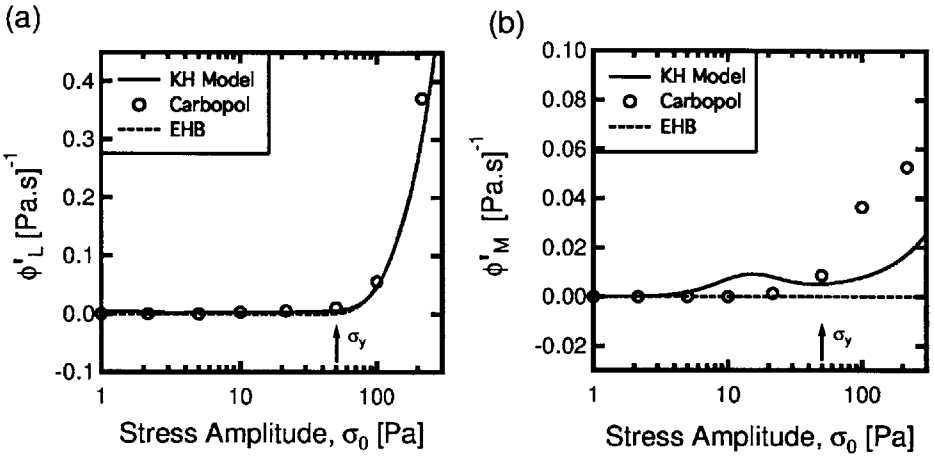

Figure 6-13: Plots of the nonlinear fluidities ϕ'_M and ϕ'_L (note the difference in ordinate scales) at a frequency of $\omega = 5$ rad/s for a range of stress amplitudes. Carbopol data is contrasted to two models, the Elastic Herschel-Bulkley model (fitting parameters $\sigma_y = 45$ Pa, $k = 26$ Pa.s^m, $G = 350$ Pa, $m = 0.43$) and the Kinematic Hardening model (KH) described in the next section.

as kinematic hardening [120]. The nonlinear response of this particular model appears to capture more completely the initial increase and subsequent decrease in the compliances J'_L and J'_M as the stress amplitude σ_0 is increased. In the following section we will show that by incorporating this behavior (which involves the addition of only one more material constant) we can capture the salient features of the Carbopol gel response to LAOStress deformations. This model also removes the somewhat arbitrary discontinuous flow/no flow condition given by Eq. 6.19. This more sophisticated kinematic hardening model also tests the strengths and limitations of the LAOStress strain decomposition in Eqns. 6.8 and 6.9, and illustrates a case in which the one-to-one equivalence between the apparent strains γ' and γ'', and the constitutive model strains, γ^e and γ^p, breaks down.

6.4.4 An Elasto-Plastic Material with Kinematic Hardening (KH Model)

We seek to develop a constitutive model that improves on the ability of the EHB model to capture the rheological fingerprint of the Carbopol gel under LAOS. While

there are many potential ways to accomplish this, there were two main criteria that were used to identify an appropriate model. The first is simplicity, i.e. the desire to introduce as few new additional parameters as possible to the existing EHB model. The second criterion was to build on well-established concepts that already exist in the plasticity literature.

Based on these criteria, the EHB model was modified to account for a behavior known as *kinematic hardening.* Kinematic hardening accounts for movement of the center of location of the yield surface (in stress space) for a given material [120]. For the simple 1-dimensional model which we will deal with here, this implies that the yield stress of the material evolves dynamically with time, as the material is deformed. Kinematic hardening is a concept that is widely used in the plasticity literature, but for the rheologist who is unfamiliar with the topic we recommend one of the many textbooks which have been written on the topics of continuum mechanics or plasticity [120, 112, 93]. For clarity, we have tried to keep the nomenclature in the present work consistent with that used in the plasticity and solid mechanics literature (particularly with that of Gurtin and coauthors [93] and Anand and coauthors [11, 10, 96]). While the case discussed in detail here is a simple 1-dimensional version, in Sec. 7.1 we outline the formulation of a frame-invariant, thermodynamically-consistent version of the constitutive model in 3D tensorial form. The reader can also consult Henann and Anand [96] for a complete version of the model with combined kinematic and isotropic hardening.

As was the case for the EHB model considered in Section 6.4.3, the strain in the KH model admits an additive decomposition; $\gamma = \gamma^e + \gamma^p$ as in Eq. 6.2. We follow the approach of Gurtin et. al. [93]; first a simple form of the free energy of the material is proposed, from which equations for the stress follow. For this particular model, the defining equation for the free energy ψ of the material is as follows:

$$\psi = \frac{1}{2} G \left(\gamma^e\right)^2 + \frac{1}{2} C \left(A\right)^2 \tag{6.24}$$

The free energy contains two terms, the first is an elastic free energy, which depends on

the elastic strain γ^e. This first term would be equivalent for the simpler EHB model, but for the KH model we introduce a second term, a "defect" energy which depends on a dimensionless internal variable A. In the context of polycrystalline metals, this defect energy would be the result of the formation and movement of dislocations in the crystal lattice. For the Carbopol system, the defect energy results from corresponding features relevant to the specific microstructure of the material. Piau [168] described the microstructure of Carbopol gels as consisting of individual swollen polymeric sponges. At a high enough volume fractions, these constituent elements likely become trapped in "cages" that are formed by the neighboring particles. A defect energy may then arise from slip occurring between these particles and a topological rearrangement of their structure [141]. In Eq. 6.24 the variable A is not a strain *per se*, but in the 3-dimensional generalization of this model (which is discussed in Sec. 7.1) it shares some of the properties of a finite strain tensor. In particular it was shown by Henann and Anand [96] that the 3-dimensional tensorial version of this variable, $\mathbf{A}$, is equivalent to an "energetic" plastic left Cauchy-Green tensor (or Finger tensor). The defect variable A evolves as the accumulated plastic strain γ^p in the material varies. The parameter C is a new material constant, termed the back stress modulus [10], which has dimensions of stress.

From the form of the free energy that is specified in Eq. 6.24, the equation for the stress in the material is $\sigma = \frac{\partial \psi}{\partial \gamma^e} = G\gamma^e$ as in Eq. 6.3. While σ is still the stress in the material, and corresponds to the stress that would be measured in an experiment, the presence of the additional term gives rise to a second contribution to the stress, referred to as the back stress, $\sigma_{\text{back}} = \frac{\partial \psi}{\partial A}$:

$$\sigma_{\text{back}} = CA \tag{6.25}$$

The back stress corresponds to the center of the location of the yield surface (in stress space) in the material, and is integral to the development of this model. The fact that the value of the back stress varies with A, allows for time variation in the "effective" stress, $|\sigma - \sigma_{\text{back}}|$ within the material, which determines the plastic flow rate, even

when the imposed stress σ is held constant. The plastic flow rate $\dot{\gamma}^p$ is related to the effective stress through the following equation:

$$\dot{\gamma}^p = n^p|\dot{\gamma}^p| \quad \text{where} \quad n^p = \frac{\sigma - \sigma_{\text{back}}}{|\sigma - \sigma_{\text{back}}|} \qquad \text{(Direction of plastic flow)} \tag{6.26}$$

$$|\dot{\gamma}^p| = \left(\frac{|\sigma - \sigma_{\text{back}}|}{k}\right)^{1/m} \qquad \text{(Magnitude of plastic flow rate)} \tag{6.27}$$

The equation for the plastic flow rate for this particular model is slightly different from that of the EHB model, which is given in Eq. 6.19. The yield stress parameter σ_y has been set to zero in the equation above, and the stress $|\sigma|$ has been replaced by the *effective stress* within the material that is driving plastic flow, $|\sigma - \sigma_{\text{back}}|$. We include the variable n^p again to make it clear that the plastic flow is co-directional with the effective stress, and not with the total applied stress σ. The last important element of this constitutive model is to specify the evolution in the defect energy which involves the plastic flow rate $\dot{\gamma}^p$. The differential equation for the parameter A in a simple one-dimensional form is as follows:

$$\dot{A} = \dot{\gamma}^p - qA|\dot{\gamma}^p| \tag{6.28}$$

This evolution equation accounts for so-called nonlinear kinematic hardening (due to the dependence of $|\dot{\gamma}^p|$ on A in Eq. 6.27) and was first introduced by Armstrong and Frederick [13] to account for the multiaxial Bauschinger effect. As noted above, the Bauschinger effect is the progressive decrease in the yield stress of a material under cyclic loading conditions; the work by Armstrong and Frederick [13] generalized this behavior to multiaxial loading conditions. Eqn. 6.28 is always evaluated with initial conditions of $A(0) = 0$, i.e. the material is in a virgin state with zero defect energy at the start of the deformation. We have also introduced the dimensionless parameter q, as an additional material constant. When compared to the EHB model, we have removed the material constant σ_y and introduced two new constants, q and C. We

have therefore increased the number of material constants in this model relative to the EHB model by one.

It is now clear that with the addition of Eq. 6.28 to the constitutive model (given by Eqns. 6.24, 6.25, 6.26 and 6.27) we can have a dynamic evolution of the back stress σ_{back} as the material is deformed. The implications of this evolution equation for A on the flow behavior can be understood with some simple reasoning. The material always starts out with an initial value of $A(0) = 0$. Then, if we consider the application of a constant stress σ, the material will initially deform elastically, but will also begin to experience some plastic flow due to the fact that the back stress is zero (Eq. 6.25) for the specified initial conditions. As plastic flow occurs, $\dot{A}$ will initially be positive, resulting in growth of the value of A. Eventually the second term in the differential equation in Eq. 6.28 will grow resulting in a reduction in the rate of change of A, until ultimately the material reaches a steady state flow corresponding to $\dot{A} = 0$. Thus, the increase of A with time results in a decrease in the rate of plastic flow $\dot{\gamma}^p$, or an apparent "kinematic hardening" which is exactly what is observed for creep tests of the carbopol system (see the creep curves in Fig. 6-6).

At steady state, the KH model approaches the same form as the EHB model, predicting Herschel-Bulkley flow behavior, which is also exhibited by the Carbopol gel as shown in Fig. 6-5. To show this, we set $\dot{A} = 0$; from Eq. 6.28 it then follows that $qA = \pm 1$ (depending on the direction of the applied stress). Furthermore, from Eq. 6.25 it follows that $\sigma_{\text{back}} = \pm C/q$ at steady state. When we insert this steady state value of σ_{back} into the flow rule of Eq. 6.27, we exactly recover the Herschel-Bulkley flow equation of Eq. 6.18 at steady state, and we identify $C/q = \sigma_y$. The ratio of material constants C/q can therefore be determined by measuring a steady state flow curve such as the one presented in Fig. 6-5.

The KH model thus successfully captures the steady state flow behavior of the carbopol microgel at stress values $\sigma > \sigma_y$. The model also successfully captures the correct creep behavior for imposed stresses below the yield stress. To show this, we plot in Fig. 6-14 the evolution of the apparent viscosity of this particular model, defined as $\eta^+ \equiv \sigma_0/\dot{\gamma}(t)$, for a number of creep tests with different applied stresses

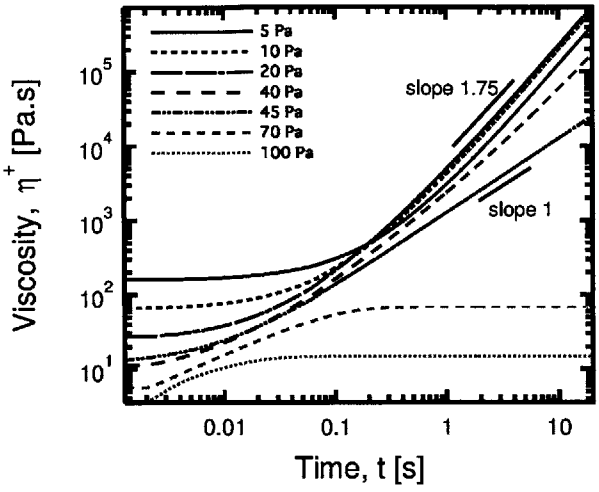

Figure 6-14: Plot showing evolution of the apparent viscosity $\eta^+ \equiv \sigma_0/\dot{\gamma}(t)$ for the KH model at a number of different imposed stresses above and below the value $\sigma_y = C/q = 45$ Pa. Model parameters for the KH model are $C = 540$ Pa, $q = 12$, $k = 26$ Pa.s ^{m}, $G = 350$ Pa, $m = 0.43$.

σ_0. The model was simulated using an Euler forward-time integration scheme, with parameters set as follows: $G = 350$ Pa, $C = 540$ Pa, $q = 12$, $k = 26$ Pa.s^m, $m = 0.43$. These are the same parameters as those used for the EHB fit in Fig. 6-11, however the value $\sigma_y = 45$ Pa is now represented by the ratio C/q leaving only one free parameter to adjust (either the value of q or C). These values are also the same parameters that were used to evaluate the nonlinear compliances J'_L, J'_M, ϕ'_L and ϕ'_M for the kinematic hardening model shown in Fig. 6-12 and 6-13. The numerical values were determined to best capture the overall response of the Carbopol microgel to LAOStress (see details below).

In Fig. 6-14 we show that the KH model predicts creep behavior that is qualitatively similar to that exhibited by the Carbopol microgel shown in Fig. 6-6 (b). For imposed stresses larger than the critical value $\sigma_y = C/q$, the viscosity approaches a steady state rather quickly, and this steady state dependency of viscosity on stress is governed by the Herschel-Bulkley equation given in Eq. 6.18. For values of the stress $\sigma < C/q$, continued power-law growth of the instantaneous viscosity is seen with time. The power-law exponent for this particular set of fitting parameters is

determined to be to 1.75. An asymptotic expansion (derived in the Appendix B) of Eqns. 6.25-6.28 under constant applied stresses $\sigma < \sigma_y$ yields the following scaling:

$$\eta^+ \simeq \eta_c \left(\frac{t}{t_c}\right)^{1/(1-m)} \tag{6.29}$$

This scaling holds for values of the imposed stress below the yield stress C/q, for values of $0 < m < 1$ and for long times. When the imposed stress σ is exactly equal to the yield stress i.e. $\sigma = \sigma_y = C/q$, the constitutive equations predict a linear growth in viscosity with time, with $\eta \sim Ct/m$ (this linear dependency can be identified as the dividing line of slope 1 in Fig. 6-14). The parameters t_c and η_c in Eq. 6.29 represent, respectively, a characteristic time scale and a characteristic viscosity scale for the KH model. They can be determined through the asymptotic expansion to be:

$$t_c = \left(\frac{k}{C}\right)^{1/m} \tag{6.30}$$

$$\eta_c = \sigma \left(\frac{k}{C}\right)^{1/m} \left[\left(1 - \frac{q\sigma}{C}\right)\left(\frac{1-m}{m}\right)\right]^{1/(1-m)} \tag{6.31}$$

This particular model is therefore capable of capturing the power-law like growth in the instantaneous viscosity that we have observed in Carbopol. The slope of 1.75 in Fig. 6-14 is somewhat larger than the slope seen for Carbopol in Fig. 6-6 (b). The parameter m can be modified to model the correct rate of increase of η^+ with time. However for the purposes of fitting the model to LAOS data in the upcoming figures, we found a better agreement when we used the value of m determined from the Herschel-Bulkley fit in Fig. 6-5 (a). This is reasonable because for the LAOS data (where strains are large) it is of primary importance to capture the behavior of the post-yielded flow regime, while small variations in the creeping behavior which occur below the yield stress do not play as important a role in the fitting of the constitutive model parameters.

One interesting consequence of this type of power-law growth or viscosity bifurcation is that the model can then predict a limiting viscosity plateau for $\sigma \leq \sigma_y$ in plots of apparent viscosity vs. imposed shear stress. These types of plateaus have

been documented for Carbopol, and often spark debates as they beg the question as to whether or not a material truly exhibits a yield stress [18, 147]. Fig. 6-15 shows a plot of viscosity vs. shear stress obtained from creep simulations carried out on the kinematic hardening model (with the same fitting parameters as Fig. 6-14) at a number of different imposed stresses. For each stress, the simulation is stopped after a given period of time, and the viscosity is instantaneously sampled. Viscosity plateaus are plotted for a number of different values of the dimensionless time $\hat{t} \equiv t/t_c$. From Fig. 6-15 it is clear that the material exhibits a time dependent plateau in the shear viscosity at stresses $\sigma < C/q$. The magnitude of this viscosity plateau increases as the measurement time is increased and diverges as $\hat{t} \to \infty$. The viscosity measurements at stresses $\sigma > C/q$ however, are insensitive to measurement time and converge to the Herschel-Bulkley equation quickly. Additionally the numerical value of apparent viscosity varies non-monotonically with the applied stress σ at a fixed value of $\hat{t}$. This is due to the non monotonic variation of η_c with σ which is given in Eq. 6.31.

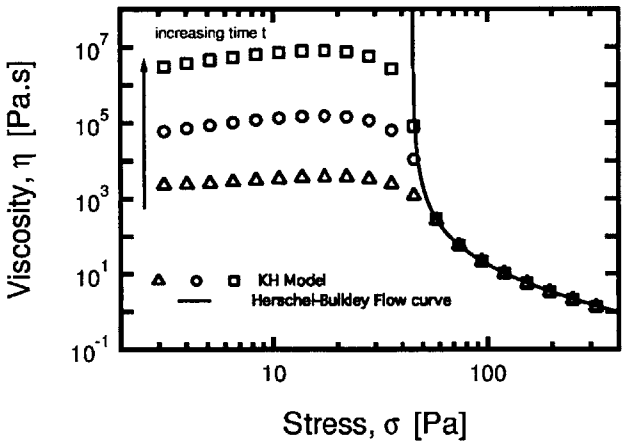

Figure 6-15: Plot showing apparent flowcurve of the viscosity predicted by the KH model after different wait times. Flowcurves are obtained through simulations at a constant imposed stress, the viscosity is sampled at dimensionless times of $\hat{t} = 1.2 \times 10^3$ ($\triangle$), 1.2×10^4 ($\bigcirc$), and 1.2×10^5 ($\square$) after the stress is imposed (corresponding to $t = 1, 10$ and 100 seconds). The overlaid solid line is the Herschel-Bulkley flow curve with the same values of model parameters m, G and k as the KH model, and with $\sigma_y = C/q = 45$ Pa.

We have thus shown that the kinematic hardening model is capable of capturing

several aspects of the rheological behavior of an ideal yield stress fluid such as Carbopol. It is considerably more versatile and realistic than the simpler EHB model, and only introduces one additional material constant. For the KH model, the plastic strain rate $\dot{\gamma}^p$ always varies continuously with the stress, and there are no conditionals on the evolution equations (such as the one in Eq. 6.19) to determine whether or not plastic flow will occur. Furthermore, as a result of the differential equation that defines the evolution in the parameter A, we recover a "viscosity bifurcation" [53] with power-law–like growth in viscosity below a critical stress C/q, and convergence of the viscosity to a steady state value given by Eq. 6.18 above the critical stress C/q. The material can therefore evolve towards two different states, with these states being separated by a "yield stress" determined by the ratio of the parameters C/q.

6.4.5 KH Model under LAOStress

So far, we have only studied the behavior of the kinematic hardening model under constant applied stress conditions. To test how well the model fares at capturing flow behavior of the Carbopol gel under dynamic conditions, i.e. LAOStress, we have overlaid the predicted response of the KH model (black) onto the experimentally-measured response of the Carbopol (orange) on a Pipkin diagram in Fig. 6-16.

From Fig. 6-16, the kinematic hardening model shows considerable improvement over the EHB model in capturing the material response to LAOStress conditions. Both models predict approximately the same behavior at the largest stress amplitude, $\sigma_0 = 200$ Pa, and the agreement between both models and the Carbopol data is excellent for this value of $\sigma_0 \gg \sigma_y$. This is primarily a testament to the effectiveness of the Herschel-Bulkley model in capturing the steady state flow viscosity. However, the kinematic hardening model better predicts the measured behavior at moderate stress values of $\sigma \leq 50$ Pa. This improvement is due to the ability of the KH model to admit plastic flow for imposed stresses below the value C/q, which the EHB model does not account for. We emphasize the fact that the values of the fitting parameters m, k and the ratio C/q are constrained by the fit of the steady shear data in Fig. 6-5 to the Herschel-Bulkley model. Thus, the kinematic hardening model has effectively linked

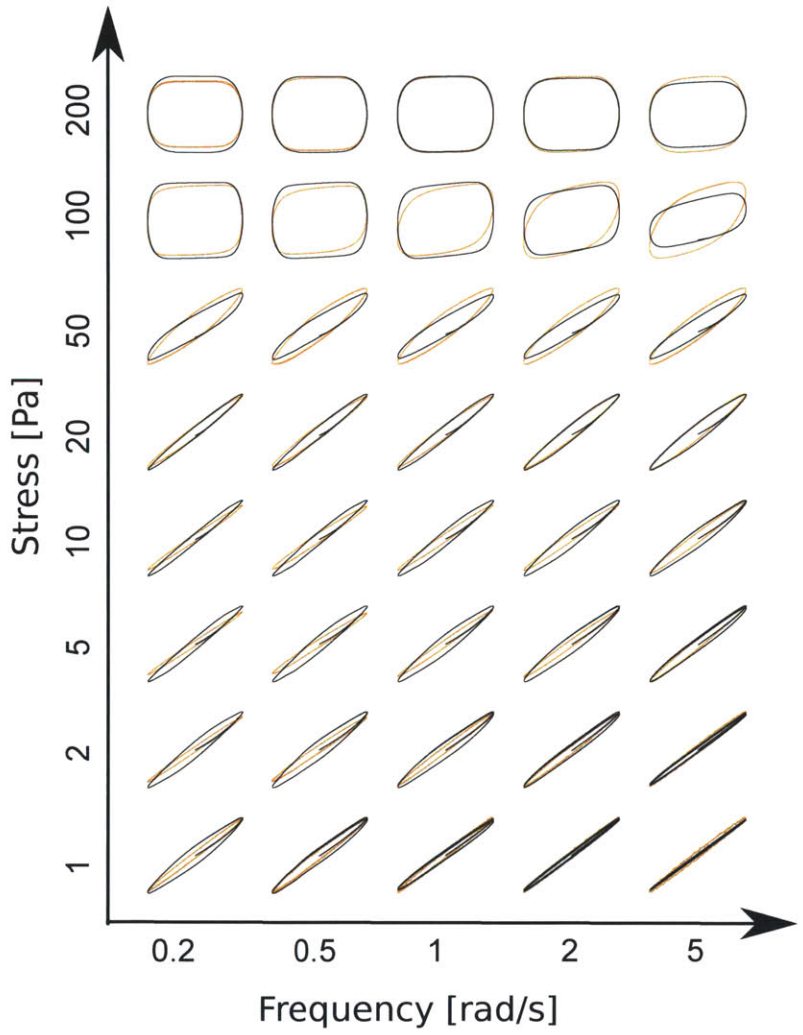

Figure 6-16: Pipkin diagram showing comparison of kinematic hardening model (black) with Carbopol data (orange) at a number of different frequencies ω and stress amplitudes σ_0. The KH model fitting parameters are the same as those used in Figs. 6-12–6-15 and are the same as the EHB fitting parameters in Fig. 6-11 with $\sigma_y = C/q$.

the transient nonlinear behavior under LAOS to steady state flow measurements such as those in Fig. 6-5.

Comparing Fig. 6-16 to Fig. 6-11 also illustrates the fact that the variations in the material measures J'_M and J'_L at all of the tested frequencies are more accurately represented by the KH model. The evolution in the values of J'_M and J'_L for the KH model (plotted in Fig. 6-12) are related to the variation in the elastic and plastic strains defined in the constitutive model, γ^e and γ^p. As a result of the differential equation relating $\dot{\gamma}^p$ to the defect parameter A, $\dot{\gamma}^p$ is no longer a single-valued function of the stress σ. The apparent plastic strain γ'' given by the strain decomposition in Eq. 6.9 is therefore different from γ^p, because the strain rate $\dot{\gamma}''$ given by Eq. 6.9 must be a single-valued function of σ by construction (see Appendix).

Monitoring and quantifying changes in the values of nonlinear measures such as J'_M and J'_L in LAOStress can help in understanding the evolution in internal parameters (like A or the back stress σ_{back} in the KH model). This provides insight into how one might approach more sophisticated constitutive modeling of these kinds of soft materials. To illustrate this, in Fig. 6-17 we present contour plots of the nonlinear material measures $J'_M(\omega, \sigma_0)$ and $J'_L(\omega, \sigma_0)$ for the KH model. These can be contrasted with the contour plots of the measured values of J'_M and J'_L for Carbopol in Fig. 6-9. The general qualitative behavior of the model and the microgel is similar. For example, both model and data exhibit an initial increase and then a subsequent decrease in J'_M as the stress amplitude σ_0 is increased. However, there is a stronger frequency dependence predicted for the KH model - this can be discerned from the slopes of the isocontours. For the large stress compliance J'_L, both model and data show an initial increase to a value larger than that of J'_M, i.e. the material softens (or becomes more compliant) at large stresses. Again, the kinematic hardening model shows a stronger frequency dependence than the measurements, and also the maximum value of J'_L predicted by the kinematic hardening model is smaller than that observed experimentally.

For completeness, we add contour plots of the fluidities ϕ'_L and ϕ'_M for this model so that they can be contrasted with the experimental data. The simpler EHB model

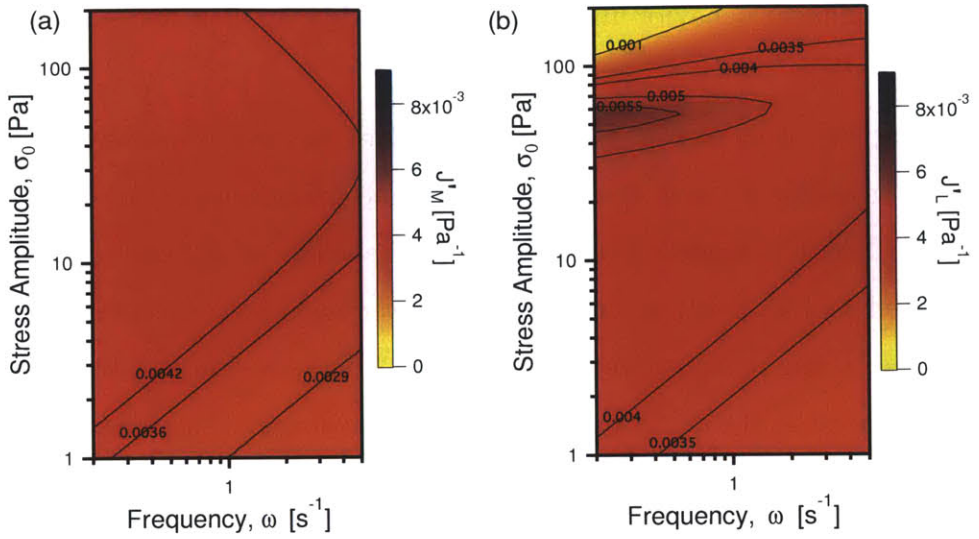

Figure 6-17: Contour plots of the nonlinear material measures J'_M and J'_L for the KH model with the same fitting parameters used in Fig. 6-16. Qualitatively similar features to the contour plots of the Carbopol microgel in Fig. 6-9 can be seen in these contour plots.

was already able to capture the stress-dependent variation of the large strain measure ϕ'_L (which is dominated by viscoplastic flow). Hence, the kinematic hardening model achieves an equally good agreement as the EHB model does with the Carbopol data. The improvement over the EHB model comes primarily from the non-zero values of ϕ'_M when kinematic hardening is added to the constitutive model. Progressively larger values of ϕ'_M at large values of σ_0 and ω are exhibited by the kinematic hardening model. This variation of ϕ'_M is an important aspect of the material response in LAOS. Physically, it can be related to the time-varying nature of the Carbopol gel and its ability to exhibit viscoplastic flow, even at low stresses. The KH model captures this behavior through the dynamic evolution of the back stress $\sigma_{\text{back}}(t)$ with characteristic time scale t_c (Eq. 6.31), and the modified flow rule in Eq. 6.27. These features of the KH model allow the material to exhibit nonzero fluidity at low instantaneous stresses, even though under "steady state" conditions (i.e. creep tests in which we wait extremely long periods of time $t \gg t_c$ to measure an apparent viscosity) we would have $\eta^+ \to \infty$ and fluidity $\phi^+ \to 0$. The simpler EHB model attains this steady state instantaneously, and therefore predicts a constant (zero) value of ϕ'_M.

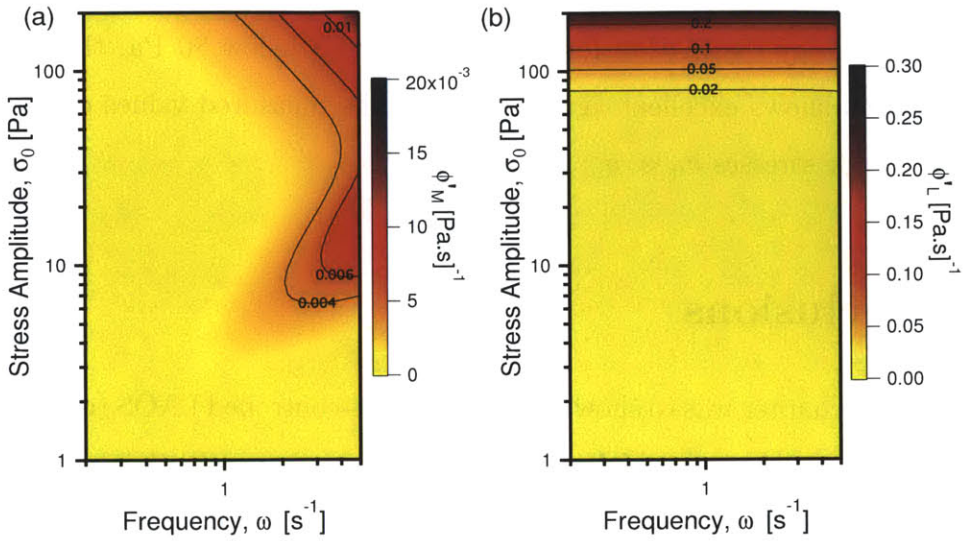

Figure 6-18: Contour plots of the nonlinear measures ϕ'_M and ϕ'_L for the KH model with the same fitting parameters as in Fig. 6-16.

An objective way to document the improved fit of the KH model to the experimental data is by calculating the volumetric energy dissipated into the material per cycle, E_d. This energy can be computed by evaluating the following integral:

$$E_d = \int_0^{2\pi/\omega} \sigma\dot{\gamma} dt = \sigma_0^2 J_1'' \pi \tag{6.32}$$

where the second equality follows due to the orthogonality of the Fourier terms in Eq. 6.7 over the domain $[0, 2\pi/\omega]$. It is well known that, for a sinusoidal forcing, the energy dissipated within the material per cycle only depends on the first viscous Fourier coefficient [80, 107, 73]. Geometrically, this parameter E_d represents the area enclosed within the elastic Lissajous curves shown in Fig. 6-16. This measure provides the starkest contrast between the EHB and KH model fits to the Carbopol data, because for $\sigma < \sigma_y$ the EHB model does not dissipate energy at all - it behaves as an ideal elastic solid. In Fig. 6-19 we evaluate contour plots of $E_d(\omega, \sigma_0)$ and see that the increase in E_d near σ_y for the EHB model is very abrupt. On the other hand, E_d increases more gradually for both the kinematic hardening model and the microgel data. In Fig. 6-19 (d) we compare experimental values of E_d for the Carbopol microgel to predictions of the KH and EHB model with the same fitting coefficients

used in Fig. 6-16 at a constant frequency of $\omega = 5$ rad/s. While the EHB model fails to predict the energy dissipation for stress amplitudes below 80 Pa, the kinematic hardening model shows excellent agreement with the measured values of E_d for the Carbopol even for stresses $\sigma_0 \ll \sigma_y$.

6.5 Conclusions

The focus of this chapter was to show how shear stress-controlled LAOS (or LAOStress) can be used to extract meaningful nonlinear measures that quantify the response of EVP materials to oscillatory deformations. We have seen that in general, these descriptive rheological measures are not identical to prescriptive constitutive model parameters. A further goal has therefore been to show how these material measures can be used to develop and quantitatively assess the performance of constitutive models that can predict yield-like responses of EVP materials. To that end, we have introduced the stress-controlled LAOS framework in Sec. 6.3. This framework is identical to that first used by Ewoldt [69] and Lauger and Stettin [118], and has been extended to include the Chebyshev coefficients c_n and f_n which characterize the nonlinear compliance and fluidity of a material.

We have discussed the implications of a stress vs. strain decomposition of the material response, and how it may be physically more meaningful for EVP materials to adopt the stress-controlled approach in which strain is decomposed into elastic and plastic components. This strain decomposition into "apparent" components γ' and γ'' is intimately related to the concepts of elastic and plastic strains defined for certain classes of constitutive models. However, with more complex constitutive models, the specific relation between these apparent strains and the corresponding parameters (γ^e and γ^p) in a model is not straightforward (i.e they may not be equal to each other).

The Chebyshev compliance and fluidity coefficients have been defined in this work, but we have refrained from using them to quantify material behavior for two reasons. The first reason is due to the potential differences between the experimentally-decomposed strains (i.e. the *descriptive* measures γ' and γ'') and the constitutive

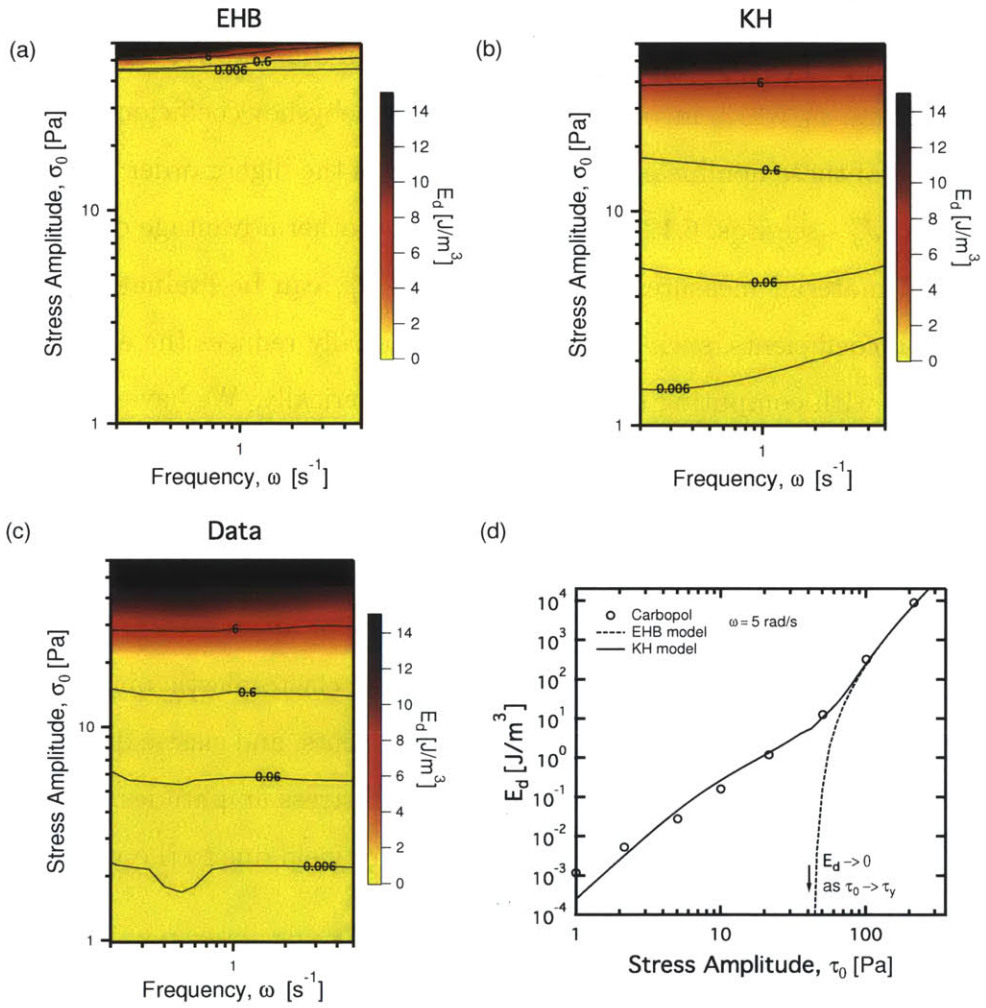

Figure 6-19: Contour plot of the volumetric energy dissipated per cycle (E_d) in (a), the EHB model plotted in Fig. 6-11, in (b), the kinematic hardening model plotted in Fig. 6-16 and in (c), measurements performed with the Carbopol microgel. In (d), a comparison of the predictions of both models is given with LAOStress data for the Carbopol microgel at an imposed frequency of $\omega = 5$ rad/s.

model strain decomposition (*prescriptive* measures γ^e and γ^p), and the implications that this has for prescribing a particular constitutive behavior. Second, we are generally interested in very large nonlinearities in the rheological fingerprint (e.g. yielding) where it has been shown [113, 73, 182] that harmonics higher than $n = 3$ can play a significant role in the material response. As a result we have focused our efforts on measuring and predicting the nonlinear compliances J'_M and J'_L, and the nonlinear fluidities ϕ'_M and ϕ'_L which involve all the Fourier-Chebyshev coefficients. Expressions exist for each of these nonlinear measures in terms of the higher order Fourier compliances J'_n and J''_n - see Eqs. 6.12, 6.14, 6.16, 6.17. Another advantage of this approach is that local material measures, such as J'_M and J'_L, can be evaluated as a sum of the non-local coefficients, such as c_n. This substantially reduces the error that would be associated with computing local derivatives numerically. We have shown that the nonlinear compliance J'_M serves as a better indicator of the intracycle elasticity of the material below the yield stress than the equivalent strain-controlled measure, G'_M, which decreases by orders of magnitude after the material yields. For LAOStress conditions, the value of J'_M remains relatively stable for all stress amplitudes and frequencies. This behavior is consistent with that of an elasto-plastic material, in which strain is decomposed into elastic and plastic components, and elastic deformations occur "in series" with viscoplastic deformations at all stress amplitudes. For Carbopol, the nonlinear fluidity ϕ'_L increases dramatically after yield due to the viscoplastic flow in the material which occurs above the yield stress.

Based on these observations, we have introduced two constitutive models that can be used to capture the behavior of the Carbopol microgel. The first of these models, the Elastic-Herschel-Bulkley model (EHB), is successful at capturing the behavior of the material under LAOS conditions at very large stress amplitudes and also at very small stress amplitudes. However, this model was shown to be deficient from the perspective of the nonlinear measures J'_M, J'_L and ϕ'_M — specifically, it predicts constant values for all of these measures. To improve on this shortcoming, we modified the EHB model to account for *kinematic hardening*. This constitutive process involves the introduction of an evolving internal material parameter (A) which is

defined through a nonlinear differential equation. This internal parameter, known as the back stress, corresponds to the location of the center of the yield surface of the material in stress space. The dynamics introduced through this equation allow the material to exhibit a continuous transition under LAOS from the unyielded to the yielded regime. While the simpler EHB model exhibits a sudden change in behavior for stresses in the vicinity of the yield stress σ_y, the ability of the KH model to evolve over time in a continuous manner prevents this discontinuous change in behavior from occurring. The KH model is able to capture many of the salient features of the Carbopol response. In particular, below the yield stress it predicts a power-law growth in the instantaneous viscosity with time, a behavior which has been documented experimentally [147]. Above the yield stress, the model predicts a steady state flowcurve given by the Herschel-Bulkley constitutive relationship. The corresponding yield stress at which this viscosity bifurcation occurs is easily tunable in the model by altering the ratio of the material constants $C/q = \sigma_y$. The kinematic hardening model also predicts nonzero viscous dissipation within the material at stresses below the yield stress. This is due to the ability of the model to exhibit slow viscoplastic creep at low stresses $\sigma < \sigma_y$.

An important aspect of this modeling approach which remains to be addressed is the connection between these simple 1-dimensional models to more general (3-dimensional) forms. Thus, in the chapter that follows we will introduce and discuss a 3-dimensional tensorial version of the KH model developed here. We will obtain approximate analytical solutions to the stress and rate of deformation tensors for a number of different canonical rheometric flows. This will serve to illustrate the versatility of the KH model in predicting more complex flow scenarios. Subsequently, in Chap. 8, we will build on the framework of the KH model introduced here, in order to account for thixotropic behavior in EVP materials. Thixotropic behavior is observed in many EVP materials, such as the model waxy crude oils studied in Chap. 5. This penultimate chapter will therefore develop an expanded constitutive law, which will serve as a capstone of this thesis.

Chapter 7

3D Form of KH Model - Predictions and Limits

7.1 Formulation of Models

Both the EHB model, and the kinematic hardening model can be generalized to 3-dimensional form, such that the constitutive models are frame invariant and satisfy the first and second laws of thermodynamics. The nomenclature used and the approach taken here is very similar to that taken by Gurtin et. al. [93], so readers who are interested in additional details are advised to consult those works. Lemaitre and Chaboche [120] is also a good general reference for readers interested in various types of kinematic hardening models. This chapter will serve to highlight some of the important concepts of the model; Anand and coauthors [11, 10, 96] discuss more complex versions of the model that is detailed in this chapter. Specifically, the model discussed here does not include isotropic hardening, which is required to describe a change in the size of the material's yield surface. The model here is also not thermo-mechanically coupled as is the case for more general models. Isotropic hardening will be added to the 1-dimensional version of this model in Chap. 8 in order to capture thixotropic effects.

A central component of this generalization is the Kroner decomposition [114], in which the deformation gradient, $\mathbf{F}$, is multiplicatively decomposed into elastic and

plastic components, $\mathbf{F}^e$ and $\mathbf{F}^p$ respectively.

$$\mathbf{F} = \mathbf{F}^e\mathbf{F}^p \tag{7.1}$$

This plays the same role that the additive decomposition of Eq. 6.1 plays for the 1-D case. The polar decomposition of the elastic component of the deformation gradient is as follows:

$$\mathbf{F}^e = \mathbf{R}^e\mathbf{U}^e \tag{7.2}$$

With $\mathbf{R}^e$ representing a rotation and $\mathbf{U}^e$ a stretch. The stretch $\mathbf{U}^e$ has the following spectral representation:

$$\mathbf{U}^e = \sum_{i=1}^{3} \lambda_i^e \mathbf{r}_i^e \otimes \mathbf{r}_i^e \tag{7.3}$$

Where λ_i^e are the principal values and $\mathbf{r}_i^e$ are the principal directions of $\mathbf{U}^e$. From the stretch $\mathbf{U}^e$ we can therefore define the elastic Green-St. Venant strain tensor which is as follows:

$$\mathbf{E}^e = \frac{1}{2}\left(\mathbf{F}^e(\mathbf{F}^e)^\intercal - 1\right) = \frac{1}{2}\left(\mathbf{U}^{e^2} - 1\right) \tag{7.4}$$

In addition to the definition of $\mathbf{E}^e$, we can define the right ($\mathbf{C}^e$) and left ($\mathbf{B}^e$) elastic Cauchy-Green tensors as follows:

$$\mathbf{C}^e = (\mathbf{F}^e)^\intercal\mathbf{F}^e \tag{7.5}$$

$$\mathbf{B}^e = \mathbf{F}^e(\mathbf{F}^e)^\intercal \tag{7.6}$$

The left elastic Cauchy-Green tensor $\mathbf{B}^e$ can also be referred to as a Finger tensor [29, 125].

7.1.1 Elastic Herschel-Bulkley (EHB) Model

For the simpler EHB model, elastic strains are assumed to be small, so the free energy can be written as a function of $\mathbf{E}^e$, and the following specific form is assumed:

$$\Psi = G|\mathbf{E}^e|^2 + \frac{1}{2}\Lambda|\mathrm{tr}\mathbf{E}^e|^2 \tag{7.7}$$

Eq. 7.7 above has introduced the parameter Λ as an additional material parameter which was not needed for the 1 dimensional case of simple shear discussed in Sec. 4.3. It is related to the bulk modulus K through $K = \Lambda + 2G/3$. Eq. 7.7 results in the following form for the second Piola elastic stress $\mathbf{T}^e$:

$$\mathbf{T}^e = 2G\mathbf{E}^e + \Lambda\,(\mathrm{tr}\mathbf{E}^e)\,\mathbf{1} \tag{7.8}$$

Where $\mathbf{T}^e$ is defined as follows:

$$\mathbf{T}^e = J(\mathbf{F}^e)^{-1}\mathbf{T}(\mathbf{F}^e)^{-\mathsf{T}} \tag{7.9}$$

Where $\mathbf{T}$ is the Cauchy stress and $J = \det(\mathbf{F})$. In the elastic free energy form given in Eq. 7.7, it is also possible to replace $\mathbf{E}^e$ with a logarithmic elastic strain (Hencky strain) defined as follows:

$$\mathbf{E}^e_H \equiv \log \mathbf{U}^e = \sum_{i=1}^{3} (\log \lambda^e_i)\mathbf{r}^e_i \otimes \mathbf{r}^e_i \tag{7.10}$$

The Hencky strain can be used to more accurately capture elastic behavior over a large range of elastic strains.

The next step is to formulate a plastic flow law which determines the rate of plastic flow given an applied stress. For the EHB model we will use a rate-dependent plastic flow rule. We begin with the plastic velocity gradient $\mathbf{L}^p$ which is related to $\mathbf{F}^p$ as follows:

$$\mathbf{L}^p = \dot{\mathbf{F}}^p(\mathbf{F}^p)^{-1} \tag{7.11}$$

$\mathbf{L}^p$ can be split into its symmetric and skew components, such that $\mathbf{L}^p = \mathbf{D}^p + \mathbf{W}^p$. One of the assumptions in this model is that of plastic irrotationality, which assumes $\mathbf{W}^p = 0$, i.e. there is no plastic spin. We can then write the plastic stretching $\mathbf{D}^p$ as a product of its magnitude, $d^p = |\mathbf{D}^p|$, and its direction $\mathbf{N}^p = \mathbf{D}^p/d^p$.

$$\mathbf{D}^p = d^p\mathbf{N}^p \tag{7.12}$$

$\mathbf{N}^p$ is the 3D tensor-valued analog of the direction n^p discussed in the 1D version of the model (see Eq. 6.19). To determine $\mathbf{N}^p$, we assume that plastic flow is co-directional with the stress. However, this codirectionality holds for a different projection of the total stress, the deviatoric Mandel stress $\mathbf{M}_0^e$ [93]. Thus:

$$\mathbf{N}^p = \frac{\mathbf{M}_0^e}{|\mathbf{M}_0^e|} \tag{7.13}$$

Where the Mandel stress $\mathbf{M}^e$ is associated with an intermediate "structural" space in the material [93] and is defined as:

$$\mathbf{M}^e = \mathbf{C}^e\mathbf{T}^e \tag{7.14}$$

And its deviatoric part is $\mathbf{M}_0^e = \mathbf{M}^e - \frac{1}{3}(\mathrm{tr}\mathbf{M}^e)\,\mathbf{1}$. We can then define an equivalent plastic strain rate and equivalent shear stress:

$$\dot{\bar{\gamma}}^p = \sqrt{2}d^p \qquad \text{Equivalent plastic strain rate} \tag{7.15}$$

$$\bar{\sigma} = \frac{1}{\sqrt{2}}|\mathbf{M}_0^e| \qquad \text{Equivalent shear stress} \tag{7.16}$$

The presence of the $\sqrt{2}$ factor in Eq. 7.15 arises so that under simple shearing conditions, the equivalent plastic strain $\dot{\bar{\gamma}}^p$ is equal to the plastic strain rate $\dot{\gamma}^p$ discussed for the 1D shear case (the conventional strain rate tensor is in rheology is typically defined as $\underline{\underline{\dot{\gamma}}} = 2\mathbf{D}$). In Eq. 7.16, the $\sqrt{2}$ factor arises as a result of the von-Mises yield criterion - the factor preserves the value of the scalar yield stress σ_y when the 3D model is simulated under simple shearing conditions. The positive, scalar valued parameters $\bar{\sigma}$ and $\dot{\bar{\gamma}}^p$ defined above are related through the familiar Herschel-Bulkley flow equation:

$$\dot{\bar{\gamma}}^p = \begin{cases} 0 & \text{if } \bar{\sigma} < \sigma_y \\ \left(\frac{\bar{\sigma}-\sigma_y}{k}\right)^{1/m} & \text{if } \bar{\sigma} \geq \sigma_y \end{cases} \tag{7.17}$$

Due to the presence of the $\sqrt{2}$ factors in the equivalent plastic strain rates and equivalent shear stress, this Herschel-Bulkley flow equation reduces to the 1D equation with

identical values of the yield stress σ_y and the fitting parameters k and m discussed in Sec. 6.4 when the material is specialized to simple shearing conditions.

7.1.2 Implementing Kinematic Hardening

Kinematic hardening is introduced into the model by modifying the free energy Ψ defined in Eq. 7.7 as follows:

$$\Psi = G|\mathbf{E}^e|^2 + \frac{1}{2}\Lambda|\mathrm{tr}\mathbf{E}^e|^2 + \underbrace{\Psi^p(\mathbf{A})}_{\text{defect energy}} \tag{7.18}$$

The form of the free energy equation above introduces a defect energy, Ψ^p, which depends on the tensor $\mathbf{A}$ (which is the three-dimensional generalization of the parameter A that was discussed in Sec. 6.4.4). $\mathbf{A}$ is symmetric and unimodular (i.e. $\det(\mathbf{A}) = 1$), and has the following spectral representation:

$$\mathbf{A} = \sum_{i=1}^{3} a_i \mathbf{l}_i \otimes \mathbf{l}_i \tag{7.19}$$

Where the $\mathbf{l}_i$ are the principal directions of A. The following simple form of Ψ^p is used to model the defect energy:

$$\Psi^p = \frac{1}{4}C\left[(\log a_1)^2 + (\log a_2)^2 + (\log a_3)^2\right] \tag{7.20}$$

In Eq. 7.20 the back stress modulus C has been introduced, which is a new material parameter. Eqns 7.18 and 7.20 above result in the following equation for the back stress, $\mathbf{M}^e_{\text{back}}$:

$$\mathbf{M}^e_{\text{back}} = C \log \mathbf{A} \tag{7.21}$$

The tensor $\mathbf{A}$ is then defined through the following evolution equation:

$$\dot{\mathbf{A}} = \mathbf{D}^p\mathbf{A} + \mathbf{A}\mathbf{D}^p - q\mathbf{A}(\log \mathbf{A})\dot{\bar{\gamma}}^p \tag{7.22}$$

In this equation we have introduced the new material constant q, which is equivalent

to the dimensionless q parameter discussed for the 1D model in Sec. 4.3. The value of the parameter q determines the dynamic recovery of $\mathbf{A}$. The effective stress driving the plastic flow, $\mathbf{M}^e_{\text{eff}}$, is then given by:

$$\mathbf{M}^e_{\text{eff}} = \mathbf{M}^e_0 - \mathbf{M}^e_{\text{back}} \tag{7.23}$$

With kinematic hardening we assume that the plastic flow $\mathbf{D}^p$ is now codirectional with the effective stress $\mathbf{M}^e_{\text{eff}}$, so for the directional tensor $\mathbf{N}^p = \mathbf{D}^p/d^p$ we now have:

$$\mathbf{N}^p = \frac{\mathbf{M}^e_{\text{eff}}}{|\mathbf{M}^e_{\text{eff}}|} \tag{7.24}$$

The stress driving plastic flow in the EHB model must also be modified, to account for the backstress, so Eq. 7.16 becomes:

$$\bar{\sigma} = \frac{1}{\sqrt{2}}|\mathbf{M}^e_{\text{eff}}| \tag{7.25}$$

Finally, the power-law rate-dependent flow rule is introduced, which gives the relation between $\bar{\sigma}$ and $\dot{\bar{\gamma}}^p$:

$$\dot{\bar{\gamma}}^p = \left(\frac{\bar{\sigma}}{k}\right)^{1/m} \tag{7.26}$$

This particular flow rule has eliminated the conditionality of Eq. 7.17, and thus eliminated the explicit appearance of the yield stress parameter σ_y. The discontinuity in the plastic flow behavior has therefore been "regularized" through the introduction of the evolving tensor $\mathbf{A}$. Regularization of the yield criterion plays an important role in the numerical simulations of these types of constitutive laws [88] - here it has been accomplished without explicitly specifying a finite (but large) constant viscosity below the yield stress.

7.2 3D KH Model under steady flows

A viscometric flow commonly employed by rheologists is a steady shearing deformation, where the velocity gradient $\mathbf{L}$ is given as follows:

$$\mathbf{L} = \begin{bmatrix} 0 & \dot{\gamma} & 0 \\ 0 & 0 & 0 \\ 0 & 0 & 0 \end{bmatrix} \tag{7.27}$$

Rheologists will typically use such flows in order to determine the shear and normal stress components of the Cauchy stress tensor $\mathbf{T}$, and then compare these to predictions from constitutive laws. The 1-dimensional version of the KH model described and simulated in Chap. 6 only accounts for a single scalar shear stress. With the 3-dimensional form of the KH model outlined above, it is now possible to predict the full 3-dimensional form of the Cauchy stress tensor $\mathbf{T}$ for a number of different flow configurations.

It is not immediately apparent how the velocity gradient $\mathbf{L}$ (which is imposed on the material) is related to the plastic stretching tensor $\mathbf{D}^p$. A rheologist will usually measure Cauchy stress $\mathbf{T}$, in terms of the rate of deformation tensor, $\mathbf{D}$, so we are therefore interested in obtaining an analytical relationship of the form $\mathbf{T} = f(\mathbf{D})$ rather than of the form $\mathbf{T} = f(\mathbf{D}^p)$. However, one assumption which can frequently be made for a wide variety of materials is that of *small elastic deformations.* This assumption typically holds when the yield stress C/q is much smaller than the elastic shear modulus G, i.e. the yield strain in shear is $C/(qG) \ll 1$. For an actual EVP material, one can also experimentally verify this criterion of small elastic strains by checking that the ratio $J'_M/\sigma_y \ll 1$ (this would require a LAOStress measurement). If these criteria hold, considerable plastic flow will be occurring at stresses which only cause small elastic deformations. From such an assumption, it follows that the elastic stretch tensor is very close to the identity tensor, i.e. $\mathbf{U}^e \simeq \mathbf{1}$, and therefore $\mathbf{F}^e \simeq \mathbf{R}^e$. The elastic part of the deformation gradient $\mathbf{F}^e$ is now simply a rotation, for which its inverse is its transpose.

By making this assumption, one can then obtain a simplified relation between the stretching tensor $\mathbf{D} = \frac{1}{2}(\mathbf{L} + \mathbf{L}^{\intercal})$ and the plastic stretching tensor $\mathbf{D}^p$ (which the constitutive law specifies in terms of a stress, e.g. see Eq. 7.26). To obtain such an expression, we first note that the velocity gradient $\mathbf{L}$ can be expressed in terms of the plastic velocity gradient $\mathbf{L}^p$ and the elastic velocity gradient $\mathbf{L}^e$ [93]

$$\mathbf{L} = \mathbf{L}^e + \mathbf{F}^e\mathbf{L}^p\mathbf{F}^{e^{-1}} = \mathbf{L}^e + \mathbf{R}^e\mathbf{L}^p\mathbf{R}^{e^{-1}} \tag{7.28}$$

We can then show that the stretching tensor $\mathbf{D}$ is actually equal to the second term on the right hand side in Eq. 7.28. This can be accomplished by simply combining Eq. 7.28 with the expression $\mathbf{D} = \frac{1}{2}(\mathbf{L} + \mathbf{L}^{\intercal})$.

$$\mathbf{D} = \frac{1}{2}(\mathbf{L} + \mathbf{L}^{\intercal}) = \frac{1}{2}((\mathbf{L}^e + \mathbf{F}^e\mathbf{L}^p\mathbf{F}^{e^{-1}}) + (\mathbf{L}^e + \mathbf{F}^e\mathbf{L}^p\mathbf{F}^{e^{-1}})^{\intercal}) \tag{7.29}$$

In Eq. 7.29, we can first show that $\mathbf{L}^e + \mathbf{L}^{e\intercal} = 0$. We note that:

$$\mathbf{L}^e = \dot{\mathbf{F}}^e\mathbf{F}^{e^{-1}} = (\dot{\mathbf{R}}^e\mathbf{U}^e + \mathbf{R}^e\dot{\mathbf{U}}^e)\mathbf{U}^{e^{-1}}\mathbf{R}^{e^{-1}} = \dot{\mathbf{R}}^e\mathbf{R}^{e^{-1}} \tag{7.30}$$

This follows from $\mathbf{U}^e \simeq 1$ for all times, so the rate of change of elastic stretch $\dot{\mathbf{U}}^e$ is zero. Eq. 7.30 implies that $\mathbf{L}^e$ is skew symmetric [93], so its transpose is its negative. Thus $\mathbf{L}^e + \mathbf{L}^{e\intercal} = 0$, so two of the terms in Eq. 7.29 cancel out. We can then show that the remaining two terms simplify to the second term in Eq. 7.28.

$$\mathbf{D} = \frac{1}{2}((\mathbf{F}^e\mathbf{L}^p\mathbf{F}^{e^{-1}}) + (\mathbf{F}^e\mathbf{L}^p\mathbf{F}^{e^{-1}})^{\intercal}) = \mathbf{R}^e\mathbf{L}^p\mathbf{R}^{e^{-1}} \tag{7.31}$$

Where the last equality follows from taking the transpose of the second term, and from noting that $\mathbf{L}^p = \mathbf{D}^p$ (i.e. there is no plastic spin and $\mathbf{L}^p$ is symmetric - this assumption was introduced in Sec. 7.1. and is justified in [93]). We are therefore left with the following simple equation, which relates $\mathbf{D}$ to $\mathbf{D}^p$

$$\mathbf{D} = \mathbf{R}^e\mathbf{D}^p\mathbf{R}^{e^{-1}} \tag{7.32}$$

Our goal is now to use the expression in Eq. 7.32 in order to obtain a functional relationship of the form $\mathbf{T} = f(\mathbf{D})$. To do this, we begin by writing out the flow rule which combines Eq. 7.24 and Eq. 7.26 to obtain a tensorial expression for $\mathbf{D}$ in terms of the deviatoric Mandel stress $\mathbf{M}_0^e$ and the parameter $\mathbf{A}$:

$$\mathbf{D} = \mathbf{R}^e(d^p\mathbf{N}^p)\mathbf{R}^{e^{-1}} = \mathbf{R}^e\left(\frac{1}{\sqrt{2}}\left(\frac{|\mathbf{M}_0^e - C\log\mathbf{A}|}{\sqrt{2}k}\right)^{1/m}\frac{\mathbf{M}_0^e - C\log\mathbf{A}}{|\mathbf{M}_0^e - C\log\mathbf{A}|}\right)\mathbf{R}^{e^{-1}} \tag{7.33}$$

We now have an expression giving $\mathbf{D}$ in terms of the deviatoric Mandel stress $\mathbf{M}_0^e$. This expression can be conveniently simplified to be in terms of the deviatoric Cauchy stress $\mathbf{T}_0$ by noting that:

$$\mathbf{M}_0^e = J\mathbf{R}^{e^{-1}}\mathbf{T}_0\mathbf{R}^e \tag{7.34}$$

Which follows from Eqs. 7.9 and 7.14, and the fact that $\mathbf{M}^e$ is an isotropic function of $\mathbf{U}^e$ (see pg. 563 of [93] for a guided proof of this). We may further restrict our material to be incompressible, so that $J = 1$. We also define a new variable, $\bar{\mathbf{A}}$, which is related to $\mathbf{A}$ as follows:

$$\mathbf{A} = \mathbf{R}^{e^{-1}}\bar{\mathbf{A}}\mathbf{R}^e \tag{7.35}$$

This results in the following expression giving the rate of deformation tensor $\mathbf{D}$ in terms of the deviatoric Cauchy stress $\mathbf{T}_0$ and this new internal parameter $\bar{\mathbf{A}}$.

$$\mathbf{D} = \left(\frac{1}{\sqrt{2}}\left(\frac{|\mathbf{T}_0 - C\log\bar{\mathbf{A}}|}{\sqrt{2}k}\right)^{1/m}\frac{\mathbf{T}_0 - C\log\bar{\mathbf{A}}}{|\mathbf{T}_0 - C\log\bar{\mathbf{A}}|}\right) \tag{7.36}$$

The new parameter $\bar{\mathbf{A}}$ in the equation above can now be thought of as an evolving internal parameter which lies in the space of the deformed body (represented in Fig. 2-15). $\mathbf{A}$, on the other hand, lies in the structural space of the body. As one may expect, the evolution equation for $\bar{\mathbf{A}}$ will now be different from that of $\mathbf{A}$. We can determine the form of this evolution equation by combining Eqs. 7.35, 7.32 and 7.22.

$$\left(\mathbf{R}^{e^{-1}}\bar{\mathbf{A}}\mathbf{R}^e\right)^{\cdot} = \mathbf{R}^{e^{-1}}\left(\mathbf{D}\bar{\mathbf{A}} + \bar{\mathbf{A}}\mathbf{D} - q\sqrt{2}\bar{\mathbf{A}}\log\bar{\mathbf{A}}|\mathbf{D}|\right)\mathbf{R}^e \tag{7.37}$$

By expanding the derivative on the left hand side, and multiplying on the left by $\mathbf{R}^e$ and on the right by $\mathbf{R}^{e^{-1}}$, one arrives at the following evolution equation for $\bar{\mathbf{A}}$:

$$\overset{\circ}{\bar{\mathbf{A}}} = \mathbf{D}\bar{\mathbf{A}} + \bar{\mathbf{A}}\mathbf{D} - q\sqrt{2}\bar{\mathbf{A}}\log\bar{\mathbf{A}}|\mathbf{D}| \tag{7.38}$$

Where $\overset{\circ}{\bar{\mathbf{A}}} = \dot{\bar{\mathbf{A}}} + \bar{\mathbf{A}}\mathbf{W} - \mathbf{W}\bar{\mathbf{A}}$ is the corotational derivative of $\bar{\mathbf{A}}$ [93] (and $\mathbf{W} = \dot{\mathbf{R}}^e\mathbf{R}^{e^{-1}}$ is the spin). Alternatively Eq. 7.38 can be expressed in terms of the upper convected derivative of $\bar{\mathbf{A}}$ which is $\overset{\diamond}{\bar{\mathbf{A}}} = \dot{\bar{\mathbf{A}}} - \bar{\mathbf{A}}\mathbf{L}^{\intercal} - \mathbf{L}\bar{\mathbf{A}}$:

$$\overset{\diamond}{\bar{\mathbf{A}}} = -q\sqrt{2}\bar{\mathbf{A}}\log\bar{\mathbf{A}}|\mathbf{D}| \tag{7.39}$$

This evolution equation now involves a frame-invariant, corotational (or alternatively an upper convected) derivative in order to account for the fact that $\bar{\mathbf{A}}$ lies in the deformed space of the body.

We now have two simple equations (7.39 and 7.36), which analytically describe how the Cauchy stress $\mathbf{T}$ will evolve in the material given a particular deformation rate $\mathbf{D}$. These types of expressions can be used to understand the response of the material in an Eulerian reference frame, which is the basis for many rheological experiments. Note that the only simplification that was made to arrive at these two equations was that of small elastic strains, i.e. $C/(qG) \ll 1$, resulting in $\mathbf{U}^e \simeq \mathbf{1}$.

7.2.1 Analytical expressions for Cauchy stress under steady shear

With Eqs. 7.39 and 7.36 derived, we can now attempt to obtain analytical expressions for the components of the Cauchy stress tensor $\mathbf{T}$ under steady shearing conditions as given in Eq. 7.27. For ease of representation, we rewrite Eq. 7.36 as follows:

$$\mathbf{T}_0 = \sqrt{2}^{m+1}k|\mathbf{D}|^m\mathbf{N} + C\log\bar{\mathbf{A}} \tag{7.40}$$

Where $\mathbf{N}$ is simply the direction of stretching, defined as $\mathbf{N} = \mathbf{D}/|\mathbf{D}|$. In order to arrive at an analytical solution for the steady state values of the components of $\mathbf{T}$ under steady shear, one must set $\dot{\bar{\mathbf{A}}} = 0$ in Eq. 7.39, and then solve for the steady state value of the tensor $\bar{\mathbf{A}}$ from the following equation:

$$\bar{\mathbf{A}}\mathbf{L}^{\intercal} + \mathbf{L}\bar{\mathbf{A}} - q\sqrt{2}\bar{\mathbf{A}}\log\bar{\mathbf{A}}|\mathbf{D}| = 0 \tag{7.41}$$

Note that due to the presence of the $\bar{\mathbf{A}}\log\bar{\mathbf{A}}$ term in this equation, a set of nonlinear coupled equations for the components of $\bar{\mathbf{A}}$ is obtained. A solution to this set of equations has eluded us, however the equations can be linearized and simplified considerably for the case where $q \gg 1$. Note that the initial conditions for imposition of steady shear are $\bar{\mathbf{A}}(t = 0) = \mathbf{1}$. For large values of q, the recovery term $-q\sqrt{2}\bar{\mathbf{A}}\log\bar{\mathbf{A}}|\mathbf{D}|$ grows quickly, resulting in $\bar{\mathbf{A}}$ growing only slightly and thus being very close to $\mathbf{1}$ for all times. We can therefore write $\bar{\mathbf{A}} = \mathbf{1} + \mathbf{B}$, with $|\mathbf{B}| \ll 1$. The Mercator series for the natural logarithm of $\bar{\mathbf{A}}$ is as follows:

$$\log\bar{\mathbf{A}} = \log(1 + \mathbf{B}) = \mathbf{B} - \frac{\mathbf{B}^2}{2} + \frac{\mathbf{B}^3}{3} - \ldots \tag{7.42}$$

Eq. 7.42 above can then be combined with Eq. 7.41. This results in the following expression:

$$2\mathbf{D} + \mathbf{B}\mathbf{L}^{\intercal} + \mathbf{L}\mathbf{B} - q\sqrt{2}|\mathbf{D}|\mathbf{B} = O(\mathbf{B}^2) \tag{7.43}$$

Inserting a steady shear velocity gradient into the equation above, and keeping only terms that are linear in $\mathbf{B}$, gives the following relationship between the components of $\mathbf{B}$

$$\begin{bmatrix} 0 & \dot{\gamma} & 0 \\ \dot{\gamma} & 0 & 0 \\ 0 & 0 & 0 \end{bmatrix} + \begin{bmatrix} 2\dot{\gamma}B_{12} & \dot{\gamma}B_{22} & 0 \\ \dot{\gamma}B_{22} & 0 & 0 \\ 0 & 0 & 0 \end{bmatrix} - q\dot{\gamma}\begin{bmatrix} B_{11} & B_{12} & 0 \\ B_{12} & B_{22} & 0 \\ 0 & 0 & 0 \end{bmatrix} \simeq 0 \tag{7.44}$$

Solving for the components of $\mathbf{B}$ (which form a linear set of equations) gives the following values:

$$\mathbf{B} \simeq \begin{bmatrix} 2/q^2 & 1/q & 0 \\ 1/q & 0 & 0 \\ 0 & 0 & 0 \end{bmatrix} \tag{7.45}$$

Next, using the fact that for $q \gg 1$, $\log \bar{\mathbf{A}} \simeq \mathbf{B}$, we can obtain the components of the deviatoric Cauchy stress tensor:

$$\mathbf{T}_0 \simeq \begin{bmatrix} 2\sigma_y/q & \sigma_y + k\dot{\gamma}^m & 0 \\ \sigma_y + k\dot{\gamma}^m & 0 & 0 \\ 0 & 0 & 0 \end{bmatrix} \tag{7.46}$$

We therefore have that the 1-2 shear component of the deviatoric Cauchy stress is given by $T_{12} \simeq \sigma_y + k\dot{\gamma}^m$, which is to be expected for a Herschel-Bulkley type material with a shear yield stress $\sigma_y = C/q$. Note, however, that the expression for $\mathbf{T}_0$ in Eq. 7.46 is not strictly deviatoric, except in the limit where $q \to \infty$. This is due to the fact that the approximate solution above does not account for order $1/q^2$ terms in the 2-2 entry of $\log \bar{\mathbf{A}}$. This can be amended by taking higher order terms in the expansion of $\log \bar{\mathbf{A}}$. Specifically, if we include order $\mathbf{B}^2$ terms in our expansion, and then solve Eq. 7.41 for the components of $\mathbf{B}$, we obtain the following expressions for the components of $\log \bar{\mathbf{A}} \simeq \mathbf{B} - \mathbf{B}^2/2$:

$$(\log \bar{\mathbf{A}})_{11} \simeq -\frac{q + \sqrt{4+q^2} - \sqrt{2q(4+q^2)(-q+\sqrt{4+q^2})}}{q} \tag{7.47}$$

$$(\log \bar{\mathbf{A}})_{22} \simeq -2 + \frac{\sqrt{2q(4+q^2)(-q+\sqrt{4+q^2})}}{\sqrt{4+q^2}} \tag{7.48}$$

$$(\log \bar{\mathbf{A}})_{12} \simeq \frac{-\sqrt{2q(4+q^2)(-q+\sqrt{4+q^2})} + 2q(4+q^2-q\sqrt{4+q^2})}{2q\sqrt{4+q^2}} \tag{7.49}$$

The expressions above are rather complex, however they can be simplified by expansion through a Taylor series, where terms up to order $1/q$ are kept in the 1-2

entries and terms up to order $1/q^2$ are kept in the 1-1 and 2-2 entries. This yields the following expression for $\log \bar{\mathbf{A}}$:

$$\log \bar{\mathbf{A}} \simeq \begin{bmatrix} 1/q^2 & 1/q & 0 \\ 1/q & -1/q^2 & 0 \\ 0 & 0 & 0 \end{bmatrix} \tag{7.50}$$

From which follows a better approximation for the (now deviatoric) Cauchy stress $\mathbf{T}_0$:

$$\mathbf{T}_0 \simeq \begin{bmatrix} \sigma_y/q & \sigma_y + k\dot{\gamma}^m & 0 \\ \sigma_y + k\dot{\gamma}^m & -\sigma_y/q & 0 \\ 0 & 0 & 0 \end{bmatrix} \tag{7.51}$$

This KH model, therefore, predicts a first normal stress difference given by $N_1 \simeq 2C/q^2 = 2\sigma_y/q$, which is independent of the applied shear rate $\dot{\gamma}$. This is interesting, because these normal stress differences appear to arise even in the absence of any elastic stretches (note that we have set $C/(qG) \ll 1$ to arrive at these expressions). In Chap. 6 we fit the q parameter by observing transients under LAOStress - the presence of a normal stress difference suggests an alternative method for fitting the q parameter.

To confirm the validity of the expression in Eq. 7.51, and also investigate the range of q values over which it holds, we carried out numerical simulations where Eqs. 7.39 and 7.36 were evolved under startup of a very small steady shear rate. The purpose of the small steady shear rate was to verify that the Cauchy stress evolves towards a point where $T_{12} \simeq C/q$ and where $N_1 \simeq 2C/q^2$ (as is given in Eq. 7.51). A shear rate $\dot{\gamma}$ is therefore chosen such that $(C/q) \gg k\dot{\gamma}^m$. Constitutive parameters identical to those used for the fitting of the Carbopol microgel in Chap. 6 were used (i.e. $C/q = \sigma_y = 45$ Pa, $m = 0.43$, $k = 23$ Pa.s^m) with the exception that G was set to infinity. The particular shear rate used was $\dot{\gamma} = 1 \times 10^{-3}$ s^{-1}, or in non-dimensional form, $\dot{\Gamma} \equiv \dot{\gamma}\left(\frac{C}{qk}\right)^{1/m} = 4.8 \times 10^{-3} \ll 1$. These simulations were carried out for a large range of q parameters, and the steady state values of both the dimensionless normal stress and shear stress (N_1/σ_y and T_{12}/σ_y respectively) are plotted below as

a function of the dimensionless parameter q. As the results in Fig. 7-1 show, the approximate solution given by Eq. 7.51 does an excellent job at predicting the values of T_{12} and N_1 for values of q larger than 4. To improve the agreement at smaller values of q, higher order terms could be included in the entries of $\mathbf{T}_0$.

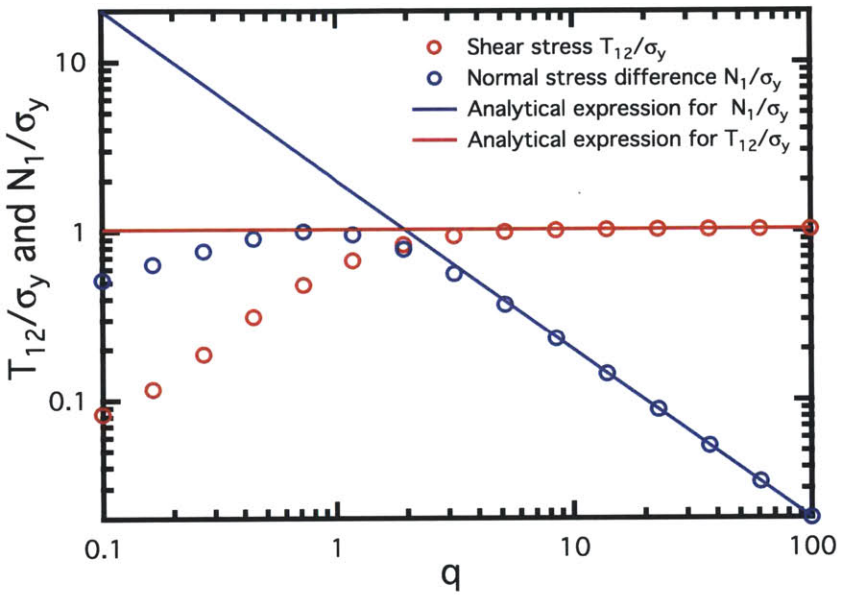

Figure 7-1: Plot of the simulated values (circles) of T_{12}/σ_y and N_1/σ_y for the 3D version of the KH model for a range of values for the q parameter. The solid lines show the prediction of these stresses obtained using the approximate solution in Eq. 7.51.

Increasing the q parameter (while keeping the shear yield stress σ_y constant) has the general effect of decreasing the magnitude of the first normal stress difference N_1. However, the increase in this q parameter has an additional effect, which is related to the dynamics of the evolution equation of $\bar{\mathbf{A}}$. Specifically, larger values of q result in a quicker increase in the recovery term in the evolution equation for $\bar{\mathbf{A}}$. As a result, one would expect the shear and normal stresses to saturate to their steady values much quicker for large values of q. To show this effect graphically, we plot below N_1/σ_y and T_{12}/σ_y vs. strain γ for the simplified 3D KH model (as given in Eq. 7.36 and 7.39) simulated under startup of a steady shear rate of $\dot{\Gamma} = 4.8 \times 10^{-3}$. The same model parameters are used as in Fig. 7-1, and curves are plotted for a number of q values logarithmically spaced from 100 to 5. The effect of q on the evolution of

the stresses is now evident - larger values of q result in smaller strains accumulating before the stresses saturate. The factor $1/q$ can therefore be thought of as a critical strain required for the KH model to fully yield and evolve towards its steady state (i.e. it is very similar to a yield strain). These types of curves provide an alternative method for fitting the parameter q to experimental data.

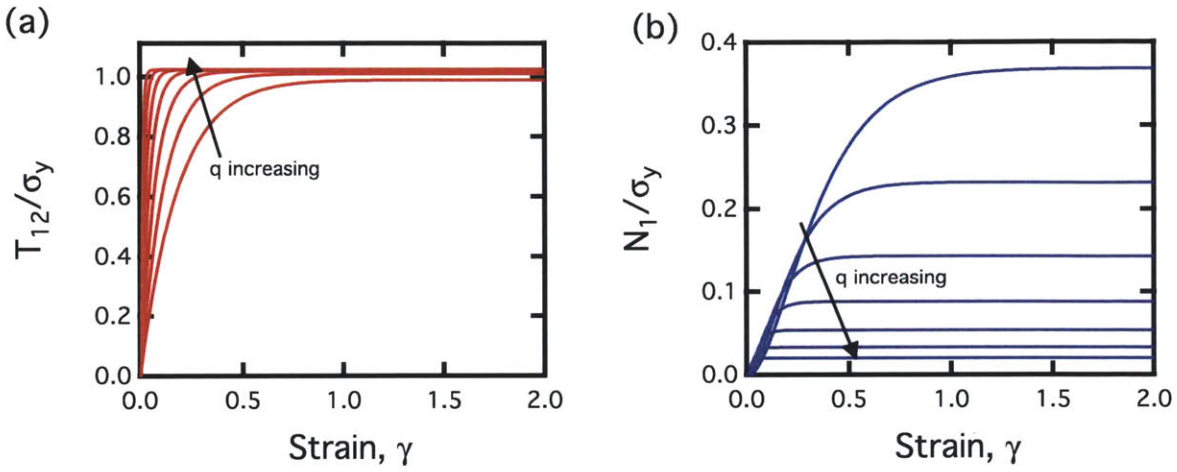

Figure 7-2: Plots of N_1/σ_y and T_{12}/σ_y vs. time for the 3D KH model simulated under startup of a steady shear rate of $\dot{\gamma} = 1 \times 10^{-3}$ s^{-1}. The same model parameters as in Fig. 7-1 are utilized, and curves are plotted for q values logarithmically spaced from $q = 100$ to $q = 5$.

Note that in the limiting case where $q \to \infty$, the normal stress difference approaches zero and the shear stress T_{12} responds immediately to the imposition of a steady shear rate. In this limiting case, the behavior predicted by the KH model is identical to that of a Herschel-Bulkley ($m < 1$) or Bingham like ($m = 1$) model, with a von-Mises yielding criterion to determine if plastic flow will occur (this is identical to the model used by Ovarlez et al. [161]).

The kinematic-hardening behavior has therefore regularized the flow/no flow condition in the Herschel-Bulkley model through the introduction of transient viscoplastic flow which can occur at all levels of stress. This is in contrast to many of the currently used regularization schemes which involve specifying a very large viscosity for stresses below the yield stress σ_y [88]. Data such as that provided in Fig. 6-6 shows that such a specification is unrealistic, because the transient viscosity of the fluid actually varies

in time when a stress is applied below σ_y, i.e. the material creeps before arresting. The zero shear-rate viscosity is therefore not constant. Incidentally, the kinematic-hardening behavior can also allow for partial elastic recoil to occur when the stress is stepped to zero after the material has undergone a creep test. This type of behavior cannot be accounted for in the 3 dimensional Herschel Bulkley type models used by Ovarlez et al. [161] or Martinie et al. [134].

7.2.2 Analytical expressions for Cauchy stress under shear free flows

In this section, we give analytical expressions for the Cauchy stress under two different extensional (or shear-free flows). These expressions will follow from linearizing Eq. 7.41 and will again hold for values of $q \gg 1$. Although these flows are typically difficult to realize in practice [29], computing the form of the stress tensor is useful in order to verify that the model does not result in any unphysical predictions. The KH model predictions can also be compared to some of the 3D Herschel-Bulkley type constitutive laws that are frequently encountered in the literature (e.g. see the work by Martinie et. al. [134]).

Uniaxial Elongational flow

The first flow that we use is elongational flow [29], where the velocity gradient $\mathbf{L}$ takes the following form:

$$\mathbf{L} = \begin{bmatrix} \dot{\epsilon} & 0 & 0 \\ 0 & -\dot{\epsilon}/2 & 0 \\ 0 & 0 & -\dot{\epsilon}/2 \end{bmatrix} \tag{7.52}$$

Following the same procedure outlined in Sec. 7.2.1 (i.e. neglecting order $\mathbf{B}^2$ terms and higher), we can obtain a linear relationship between the components of $\mathbf{B}$ which can be solved:

$$\begin{bmatrix} 2\dot{\epsilon} & 0 & 0 \\ 0 & -\dot{\epsilon} & 0 \\ 0 & 0 & -\dot{\epsilon} \end{bmatrix} + \begin{bmatrix} 2B_{11}\dot{\epsilon} & 0 & 0 \\ 0 & -B_{22}\dot{\epsilon} & 0 \\ 0 & 0 & -B_{33}\dot{\epsilon} \end{bmatrix} - \begin{bmatrix} \sqrt{3}q\dot{\epsilon}B_{11} & 0 & 0 \\ 0 & \sqrt{3}q\dot{\epsilon}B_{22} & 0 \\ 0 & 0 & \sqrt{3}q\dot{\epsilon}B_{33} \end{bmatrix} \simeq 0 \tag{7.53}$$

We solve for these components, and then insert them into Eq. 7.40 (remembering that $\log \bar{\mathbf{A}} \simeq \mathbf{B}$) in order to obtain an expression for the deviatoric Cauchy stress, $\mathbf{T}_0$.

$$\mathbf{T}_0 \simeq \begin{bmatrix} 2(\sqrt{3})^{m-1}k\dot{\epsilon}^m + \frac{2C}{\sqrt{3}q-2} & 0 & 0 \\ 0 & -(\sqrt{3})^{m-1}k\dot{\epsilon}^m - \frac{C}{1+\sqrt{3}q} & 0 \\ 0 & 0 & -(\sqrt{3})^{m-1}k\dot{\epsilon}^m - \frac{C}{1+\sqrt{3}q} \end{bmatrix} \tag{7.54}$$

The diagonal terms in the equation for $\mathbf{T}_0$ above have terms proportional to $\dot{\epsilon}^m$, in addition to constant "yield terms" which contain the coefficients C and q. Using the expressions for the 1-1 and 2-2 components of $\mathbf{T}_0$, we can write an approximate analytical expression for the extensional viscosity:

$$\eta_E \equiv \frac{T_{11} - T_{22}}{\dot{\epsilon}} \simeq \sqrt{3}^{m+1}k\dot{\epsilon}^{m-1} + \frac{3\sqrt{3}\sigma_y}{\dot{\epsilon}(3 - 2/q^2 - \sqrt{3}/q)} \tag{7.55}$$

If we consider the limit where $\dot{\epsilon} \to 0$, and $q \gg 1$, then the T_{11} stress component approaches a value of $2C/\sqrt{3}q$, while the T_{22} and T_{33} stress components approach values of $-C/\sqrt{3}q$. Under these conditions, the material will have just yielded. We can insert the components of the stress tensor in this case into the von-Mises yield criterion in order to determine an equivalent stress

$$\sigma_e = \sqrt{\frac{(T_{11} - T_{22})^2 + (T_{22} - T_{33})^2 + (T_{11} - T_{33})^2 + 6({T_{12}}^2 + {T_{13}}^2 + {T_{23}}^2)}{2}}, \tag{7.56}$$

and we obtain a value of $\sigma_e = \sqrt{3}C/q = \sqrt{3}\sigma_y$. This agrees with the equivalent stress σ_e determined for the simple shear case when $q \gg 1$. The material therefore yields

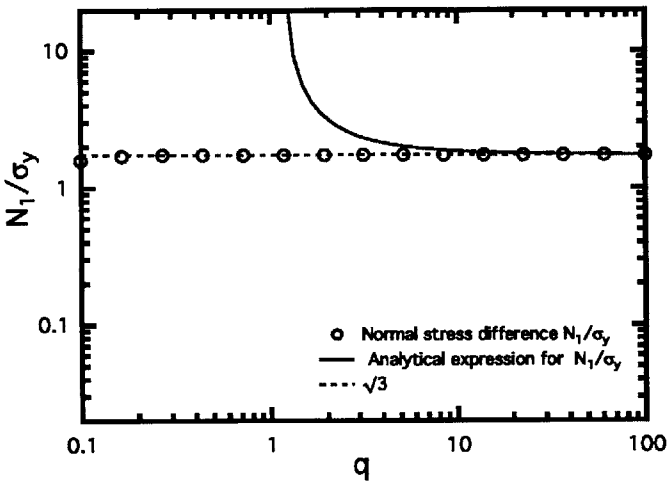

Figure 7-3: Plot of the simulated values (circles) of N_1/σ_y for the 3D version of the KH model for a range of values for the q parameter, under elongational flow. The solid lines show the prediction of these stresses obtained using the approximate solution in Eq. 7.51.

under both shear and extensional deformations when the equivalent stress reaches the same value. This verifies that the material satisfies the von-Mises yield criterion for large values of q. The von-Mises yielding criterion has been experimentally verified for a wide range of EVP materials (e.g. emulsions, physical gels and colloidal gels, among others) [161].

To verify the validity of the approximation in Eq. 7.54, we plot in Fig. 7-3 the steady state, dimensionless normal stress difference ($N_1/\sigma_y = \frac{T_{11}-T_{22}}{\sigma_y}$) against q for a very small dimensionless extensional shear rates ($\dot{\mathcal{E}} \equiv \dot{\epsilon}\left(\frac{C}{qk}\right)^{1/m} = 4.8 \times 10^{-3}$) under uniaxial elongational flow. In Fig. 7-3 we include the analytical approximation from Eq. 7.54 (solid line) as well as the direct numerical results obtained through numerical simulation of Eqs. 7.39 and 7.36 (hollow circles). There is good agreement between the analytical approximation and the numerical results for $q \geq 8$. The numerical results generally predict a value of $N_1 \simeq \sqrt{3}\sigma_y$ for all values of q, so that appears to be a good approximation that holds for even smaller values of q. The analytical approximation, however, diverges at a value of $q = 2/\sqrt{3}$, and then becomes negative for small values of q. While higher order terms of B can be used to obtain a more

accurate approximation for $N_1(\dot{\epsilon})$, the results in Fig. 7-3 suggest that the following expression holds over a large range of q values:

$$N_1(\dot{\epsilon}) \simeq \sqrt{3}^{m+1} k\dot{\epsilon}^m + \sqrt{3}\sigma_y \tag{7.57}$$

Planar elongational flow

Another flow frequently studied by rheologists is planar elongational flow [29], where the velocity gradient $\mathbf{L}$ takes the following form:

$$\mathbf{L} = \begin{bmatrix} \dot{\epsilon} & 0 & 0 \\ 0 & -\dot{\epsilon} & 0 \\ 0 & 0 & 0 \end{bmatrix} \tag{7.58}$$

Combining the above equation with Eq. 7.43 gives the following relationship between the components of the tensor $\mathbf{B}$

$$\begin{bmatrix} 2\dot{\epsilon} & 0 & 0 \\ 0 & -2\dot{\epsilon} & 0 \\ 0 & 0 & 0 \end{bmatrix} + \begin{bmatrix} 2B_{11}\dot{\epsilon} & 0 & 0 \\ 0 & -2B_{22}\dot{\epsilon} & 0 \\ 0 & 0 & 0 \end{bmatrix} - \begin{bmatrix} 2q\dot{\epsilon}B_{11} & 0 & 0 \\ 0 & 2q\dot{\epsilon}B_{22} & 0 \\ 0 & 0 & 0 \end{bmatrix} \simeq 0 \tag{7.59}$$

These can be solved for, and then inserted into Eq. 7.51 in order to obtain the components of the deviatoric Cauchy stress $\mathbf{T}_0$:

$$\mathbf{T}_0 \simeq \begin{bmatrix} k(2\dot{\epsilon})^m + \frac{C}{q-1} & 0 & 0 \\ 0 & -k(2\dot{\epsilon})^m - \frac{C}{q+1} & 0 \\ 0 & 0 & 0 \end{bmatrix} \tag{7.60}$$

For shear flow, elongational flow and planar elongational flow, the results giving the Cauchy stress tensor reduce to that of a Newtonian fluid with shear viscosity k when we set $m = 1$, and the shear yield stress $C/q = \sigma_y = 0$. As a result, the Trouton ratio for elongational flow will also approach $\eta_E/k = 3$ in this limit, and for planar elongational flow the Trouton ratio will approach $\eta_E/k = 4$.

7.2.3 Accounting for elastic deformations - large and small

Small elastic deformations

Our simplifications so far of the equations in Sec. 7.1.2 have resulted in only the plastic part of the deformation gradient, $\mathbf{F}^p$, contributing to the total stretching deformation $\mathbf{D}$ of the material (this has resulted in the parameter G not playing a role in our equations). It is possible to account for *small* contributions to the deformation $\mathbf{D}$ from the elastic part of the deformation gradient, $\mathbf{F}^e$. In Eq. 7.30, we simplified our equations by assuming that $\dot{\mathbf{U}}^e = 0$, however if we account for a nonzero value of $\dot{\mathbf{U}}^e = 0$, then we can rewrite the elastic part of the deformation gradient $\mathbf{L}^e$:

$$\mathbf{L}^e = \underbrace{\dot{\mathbf{R}}^e\mathbf{R}^{e^{-1}}}_{\mathbf{W}^e\text{, a spin}} + \underbrace{\mathbf{R}^e\dot{\mathbf{U}}^e\mathbf{U}^{e^{-1}}\mathbf{R}^{e^{-1}}}_{\mathbf{D}^e\text{, a stretching}} \tag{7.61}$$

Calling the term $\mathbf{R}^e\dot{\mathbf{U}}^e\mathbf{U}^{e^{-1}}\mathbf{R}^{e^{-1}}$ a stretching only applies for small elastic deformations, when the skew part of $\dot{\mathbf{U}}^e\mathbf{U}^{e^{-1}}$ is close to zero (see pg. 90 of [93]). The elastic part of the deformation gradient therefore now has a stretching $\mathbf{D}^e$ in addition to just the spin $\mathbf{W}^e$, which was the only part of $\mathbf{L}^e$ accounted for in our assumptions thus far. Our total deformation $\mathbf{D}^t$ can now be written as a sum of two stretching deformations, $\mathbf{D}$ and $\mathbf{D}^e$:

$$\mathbf{D}^t = \mathbf{D} + \mathbf{D}^e \tag{7.62}$$

Where $\mathbf{D} = \mathbf{R}^e\mathbf{D}^p\mathbf{R}^{e^{-1}}$, as before in Sec. 7.2. The tensor $\mathbf{D}$ follows the same behavior as given in Eqs. 7.39 and 7.36. Therefore, one way to account for the influence of small elastic deformations is to add an additional elastic stretching $\mathbf{D}^e$ onto the plastic part of the stretching, $\mathbf{D} = \mathbf{R}^e\mathbf{D}^p\mathbf{R}^{e^{-1}}$. The additional elastic stretching $\mathbf{D}^e$ can now be related to a time derivative of the Cauchy stress $\mathbf{T}$. In order to show this, we take the time derivative of Eq. 7.8 to obtain the following:

$$\dot{\mathbf{T}}^e = 2G\dot{\mathbf{E}}^e + \Lambda(\mathrm{tr}\dot{\mathbf{E}}^e)\mathbf{1} \tag{7.63}$$

By noting that $\overset{\circ}{\mathbf{T}} = \mathbf{R}^e\dot{\mathbf{T}}^e\mathbf{R}^{e^{-1}}$ (this only holds for small elastic stretches), and also using the identity $\dot{\mathbf{E}}^e = \mathbf{F}^{e\intercal}\mathbf{D}^e\mathbf{F}^e \simeq \mathbf{R}^{e^{-1}}\mathbf{D}^e\mathbf{R}^e$ (see pg. 90 of [93]), we arrive at the following relation:

$$\overset{\circ}{\mathbf{T}} = 2G\mathbf{D}^e + \Lambda\,(\mathrm{tr}\mathbf{D}^e) \tag{7.64}$$

The relation above can also be inverted to give the elastic stretching $\mathbf{D}^e$ in terms of the corotational derivative of the Cauchy stress $\overset{\circ}{\mathbf{T}}$. The equation above thus allows us to account for the additional presence of small elastic stretches in the total deformation of the material.

Large elastic deformations

Obtaining an analytical expression for cases of large elastic stretches (i.e. $\mathbf{U}^e \gg \mathbf{1}$) is much more difficult, because simplifying the relationship between the total stretching tensor and the plastic stretching tensor as $\mathbf{D} = \mathbf{R}^e\mathbf{D}^p\mathbf{R}^{e^{-1}}$ is no longer possible. Thus, converting the tensorial form of the equations in 7.1.2 to an Eulerian reference frame involving $\mathbf{D}$ (or $\mathbf{D}^t$) will not be possible. However, we can still carry out numerical simulations on the set of equations given in Sec. 7.1.2, to investigate what the full 3D form of the KH model predicts when elastic stretches are large.

Startup of steady shear simulations were carried out using Matlab on the form of the equations given in Sec. 7.1.2 at a number of different imposed shear rates. The stress tensor $\mathbf{T}$ was monitored and the simulations were stopped once this tensor approached a steady state value. Plots of the dimensionless shear stress T_{12}/σ_y and the dimensionless first normal stress difference N_1/σ_y against applied dimensionless shear rate $\dot{\Gamma}$ can then be produced. These are given below in Fig. 7-4. The particular fitting coefficients used for this 3D simulation of the full form of the KH model are identical to those used for the fit to the Carbopol microgel in Chap. 6. Specifically: $C/q = \sigma_y = 45$ Pa, $m = 0.43$, $k = 23$ Pa.s^m, $q = 12$, and $G = 350$ Pa. Note that the full 3D form of the KH model in Sec. 7.1.2 also requires specifying the parameter Λ. We set this parameter to have a value of 5000 Pa, so that $C/(q\Lambda) = 0.01 \ll 1$ and the material's elastic behavior approaches that of an incompressible solid . Overlaid

on the values corresponding to this simulated flowcurve in Fig. 7-4, we also plot the analytical prediction for the shear stress from Eq. 7.51 (which assumed $q \gg 1$ and $C/(qG) \ll 1$).

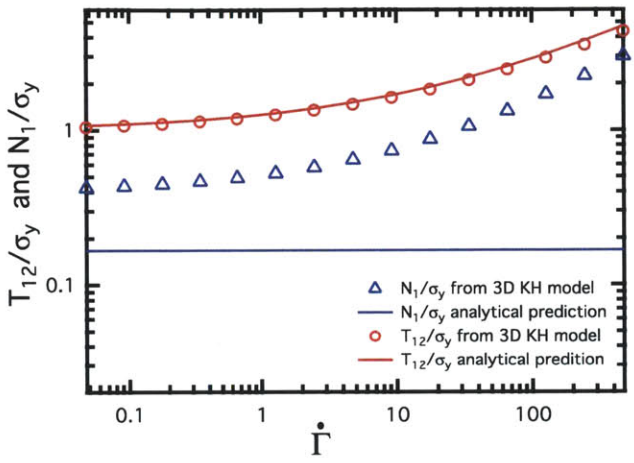

Figure 7-4: Prediction of the steady flowcurve for the 3D form of the KH model given in Sec. 7.1.2. Circles give the predicted dimensionless shear stress and first normal stress difference, while the solid lines are predictions using the analytical approximations in Eq. 7.51.

Note that the analytical expression for the shear stress T_{12} (which is just the 1-D Herschel-Bulkley equation) agrees with the simulated predictions. This is encouraging, because it shows that the 3D form of the KH model is, in fact, a more general form of the 1-D version discussed in Chap. 6. It also implies an equivalency between the parameters fit using the 1-D version of the model, and the parameters of the 3D version. This makes fitting experimental flowcurve data (such as that in Fig. 6-5) to a 3D form of the KH model very easy.

At the lowest shear rates $\dot{\Gamma}$, we can make an *a posteriori* estimate of the order of magnitude of elastic stretches (γ^e). A rough estimate gives $\gamma^e \sim T_{12}/G \sim C/(qG) = 0.13$, which is still well below 1. At the highest shear rates $\dot{\Gamma}$, the analytical expression for T_{12} does appear to slightly overpredict the values obtained from simulations of the full 3D form of the KH model. At these highest shear rates, we estimate the elastic stretches to be $\gamma^e \sim 0.58$, which is beginning to approach a value of 1. Nonetheless, there is only a 7.5% disagreement between the analytical expression for T_{12} and the

simulated value of T_{12} at these shear rates.

From Fig. 7-4 we see that the values of N_1 are under-predicted by the analytical approximation in Eq. 7.51. The analytical expression in Eq. 7.51 is a lower bound on the value of N_1. When there are large elastic deformations ($C/(qG) \gg 1$), a large contribution towards the normal stress difference N_1 will come from nonlinearities arising in the elastic stress-strain relation specified in Eq. 7.8. The particular functional form of N_1 can therefore be tuned by altering the expression which gives the elastic free energy (e.g. linear elastic, neo-Hookean, Mooney-Rivlin solid [117, 93]). This provides additional flexibility within the framework of the KH model to describe the elastic response of real materials.

7.3 Further Discussion

7.3.1 Oldroyd-B vs. KH Model

One interesting observation that can be made about the form of the KH model discussed in Sec. 7.2 is that it is very similar to the Oldroyd-B constitutive model that is frequently used to describe polymer melts and solutions. The Oldroyd-B model is equivalent to an upper convected Jeffrey's model [29], in which the total stress in the material is additively decomposed into a polymeric contribution $\mathbf{T}_p$ and a solvent contribution $\mathbf{T}_s$, as follows:

$$\mathbf{T} = \underbrace{2\eta_1 \mathbf{D}}_{\mathbf{T}_s} + \underbrace{G_1(\hat{\mathbf{A}} - \mathbf{1})}_{\mathbf{T}_p} \tag{7.65}$$

With G_1 a modulus and η_1 a viscosity coefficient. The tensor variable $\hat{\mathbf{A}}$, much like the $\bar{\mathbf{A}}$ tensor used by the KH model in Sec. 7.2, is an internal variable which evolves according to the following differential equation:

$$\overset{\nabla}{\hat{\mathbf{A}}} = \mathbf{L}\hat{\mathbf{A}} + \hat{\mathbf{A}}\mathbf{L}^{\intercal} - \frac{G_1}{\eta_2}(\hat{\mathbf{A}} - \mathbf{1}) \tag{7.66}$$

If we revisit the form of the KH model discussed in Sec. 7.2, we can decompose the deviatoric Cauchy stress in a manner similar to Eq. 7.65, however for the KH model, the polymeric contribution to stress is replaced by the back stress, $\mathbf{T}_{\text{back}}$:

$$\mathbf{T}_0 = \underbrace{\sqrt{2}^{m+1} k |\mathbf{D}|^m \frac{\mathbf{D}}{|\mathbf{D}|}}_{\mathbf{T}_s} + \underbrace{C \log \bar{\mathbf{A}}}_{\mathbf{T}_{\text{back}}} \tag{7.67}$$

Where the tensor $\bar{\mathbf{A}}$ evolves according to the following differential equation:

$$\dot{\bar{\mathbf{A}}} = \mathbf{L}\bar{\mathbf{A}} + \bar{\mathbf{A}}\mathbf{L}^{\intercal} - \sqrt{2}q|\mathbf{D}|\bar{\mathbf{A}} \log \bar{\mathbf{A}} \tag{7.68}$$

Eqs. 7.67-7.68 begin to look even more like the Oldroyd-B model if we set $m = 1$ (i.e. set a Bingham/linear viscous behavior above the yield stress), and consider large values of q. As discussed in Sec. 7.2, when q is large, we can approximate both the $\log \bar{\mathbf{A}}$ terms and the $\bar{\mathbf{A}} \log \bar{\mathbf{A}}$ terms as $(\bar{\mathbf{A}} - \mathbf{1})$. This results in the following expressions for the Cauchy stress, and the evolution equation for $\bar{\mathbf{A}}$:

$$\mathbf{T}_0 = \underbrace{2k\mathbf{D}}_{\mathbf{T}_s} + \underbrace{C(\bar{\mathbf{A}} - \mathbf{1})}_{\mathbf{T}_{\text{back}}} \tag{7.69}$$

$$\dot{\bar{\mathbf{A}}} = \mathbf{L}\bar{\mathbf{A}} + \bar{\mathbf{A}}\mathbf{L}^{\intercal} - \sqrt{2}q|\mathbf{D}|(\bar{\mathbf{A}} - \mathbf{1}) \tag{7.70}$$

Eqs. 7.69 and 7.70 above are exactly identical to the equations for the Oldroyd-B constitutive law, with the exception that the coefficient of the recovery term in Eq. 7.66 has been set to $\sqrt{2}q|\mathbf{D}|$. This is equivalent to making one of the relaxation times in the Oldroyd-B model (λ_1) a function of the magnitude (or second invariant) of the strain rate tensor $|\mathbf{D}|$. This simple modification causes a yielding behavior to arise.

The Oldroyd-B model and KH model are perhaps best illustrated through a diagram of mechanical analog elements. Such a diagram is given in Figs. 7-5 (a) and (b). The mechanical analog element for the KH model is drawn for the limiting case of $m = 1$, $q \gg 1$ and $C/(qG) \ll 1$. When elastic contributions to the deformation

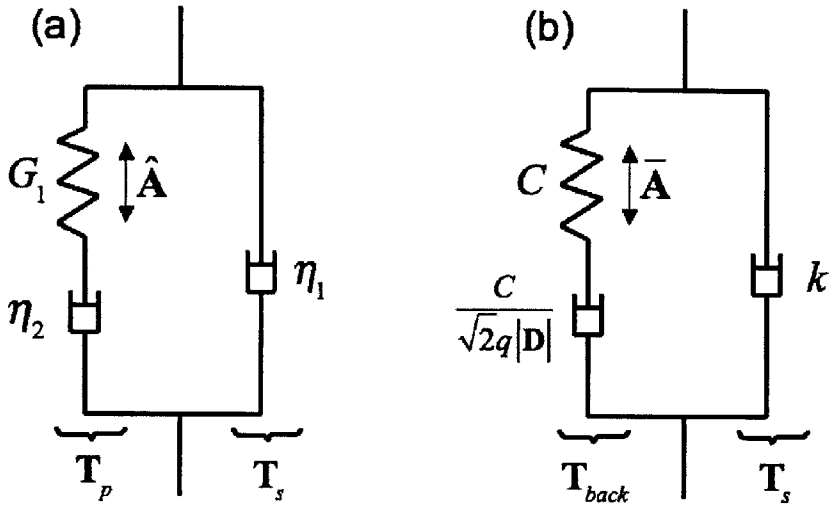

Figure 7-5: Mechanical analog element for the Oldroyd-B model (a) and the KH model (b). The mechanical analog element for the KH model is drawn for the limiting cases of $m = 1$, $q \gg 1$ and $C/(qG) \ll 1$.

are not ignored, it is necessary to include another elastic element in series with this Jeffrey's type element. It is clear that the elements are arranged in a similar fashion for the two models, with two branches resulting in the stress being additively decomposed into two components. For the case of the KH model, however, the polymer contribution to the stress $\mathbf{T}_p$ is referred to as the back stress, $\mathbf{T}_{\text{back}}$. Table 7.1 shows the parameter equivalency between the KH model and the Oldroyd-B model. Again, this equivalency only holds for the KH model when $m = 1$, $q \gg 1$ and $C/(qG) \ll 1$.

The use of modified Jeffrey's-like constitutive laws to describe yielding behaviors is by no means new in the rheology literature. The models used by Coussot et al. [51] Quemada [173], Dullaert and Mewis [67] and Souza Mendez [59] are for the most parts variants of the Jeffrey's like constitutive model (although most of these are cast into 1-dimensional forms). The unique aspect of the KH model is, however, that it requires modifying only one fitting coefficient in the Jeffrey's model, resulting in the constitutive law predicting a yield like behavior. This is much simpler than the modifications made in the other models mentioned here, which must also account for thixotropy. In the following section, we will describe ways to implement thixotropic

Table 7.1: Table showing the parameter equivalency between the KII model and the Oldroyd-B model (KH model is simplified for the limiting case where $m = 1$, $q \gg 1$ and $C/(qG) \ll 1$).

	3DKH (for $m = 1$, $q \gg 1$ and $C/(qG) \ll 1$)	Oldroyd-B
Internal Variable	$\bar{\mathbf{A}}$	$\hat{\mathbf{A}}$
Modulus	C	G_1
Solvent Viscosity	k	η_1
Polymer Viscosity	$\frac{C}{\sqrt{2q\lvert\mathbf{D}\rvert}}$	η_2
Relaxation Time	$\lambda_1 = \frac{1}{\sqrt{2q\lvert\mathbf{D}\rvert}}$	$\lambda_1 = \frac{G_1}{\eta_2}$
Back/Polymer Stress	$\mathbf{T}_{\text{back}}$	$\mathbf{T}_p$

behavior into this KH model, and in Chap. 8 we fit a thixotropic version of the KH model to experimental data for a model waxy crude oil.

7.3.2 Implementing thixotropy

The KH model does not account for thixotropic behavior. As discussed in Chap. 2, thixotropy usually entails an aging and shear rejuvenation behavior. The internal parameter $\mathbf{A}$ in the KH model only evolves under the application of a non-zero shear rate $\dot{\bar{\gamma}}^p$, so the KH model cannot account for aging behavior in a material (which is typically associated with Brownian motion and thermally activated rearrangement of a material's microconstituents, which can occur while the material is not being deformed).

Based on numerous prior studies in the thixotropy literature, there are a number of possible ways to modify the KH model to account for thixotropy [143]. Most of these methods would involve introducing a positive scalar internal variable, λ, which evolves according to a differential equation. This equation must account for both aging and shear rejuvenation. Then, the KH model parameters can be specified as a function of λ. For example, k can be modeled as a function of λ so that it decreases when the material shear rejuvenates, and increases when the material ages. For the

most part, this is the approach taken in the works by Coussot et al. [51] Quemada [173], Dullaert and Mewis [67] and Souza Mendez [59]. The approach that we will take in Chap. 8 will be similar. We will modify the scalar flow rule in Eq. 7.26 in order to account for a scalar yield stress. This scalar yield stress is dependent on the level of structure in the material which is captured by the parameter λ:

$$\dot{\bar{\gamma}}^p = \left(\frac{\bar{\sigma} - \sigma_y}{k}\right)^{1/m} \qquad \text{if } \bar{\sigma} > \sigma_y \text{ , } \dot{\bar{\gamma}}^p = 0 \text{ otherwise} \tag{7.71}$$

$$\sigma_y = \sigma_y(\lambda) \tag{7.72}$$

The equations above allow the material to isotropically harden and soften. This is in contrast to the process of kinematic hardening, where the material may strengthen along the direction of deformation (i.e. in a non-isotropic manner). Constitutive laws which account for both isotropic and kinematic hardening allow for both the size and center of the yield surface (in stress space) to vary. Fig. 7-6 below, reproduced from Muránsky et al. [153], illustrates the difference between these two hardening mechanisms.

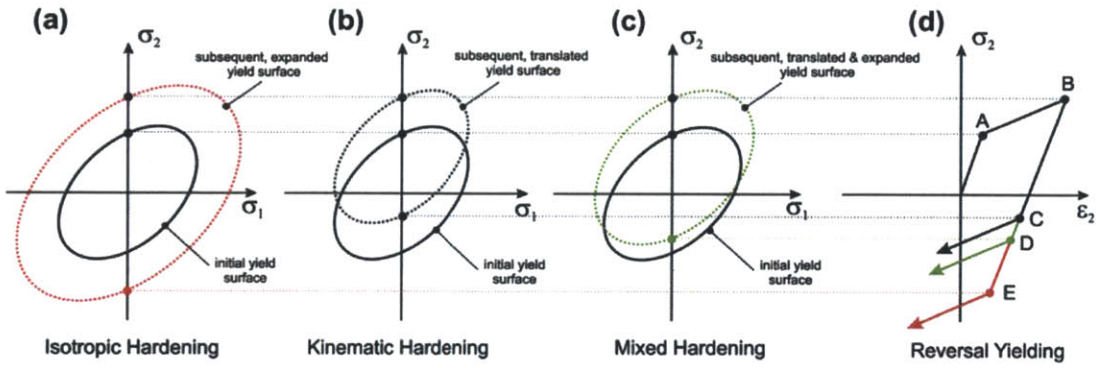

Figure 7-6: Figure reproduced from Muránsky et al. [153] illustrating the difference between the isotropic and kinematic hardening mechanisms. In (a), an Isotropic hardening model shows expansion of the yield surface with plastic strain; In (b) a kinematic hardening model shows translation of the yield surface with plastic strain; In (c) a mixed isotropic-kinematic hardening model shows both the expansion and translation of the yield surface with plastic strain; In (d) are the resulting stress-strain curves showing how the yield stress under load reversal can be different for the different plasticity models.

The importance of thermodynamic admissibility

Although the KH model framework offers flexibility in implementing thixotropic behavior, it is important to emphasize that there are thermodynamic restrictions to the types of modifications that are allowable. Discussions of these restrictions are lacking in the current literature.

Many workers have utilized models which specify a dependency of a modulus (e.g. G) on the structural parameter (e.g. λ) - see for example, Quemada [173], Dullaert and Mewis [67], Souza Mendez [59] and Mujumdar et. al. [152]. This type of a dependency, combined with rheological aging in the material, violates dissipation inequalities which can be derived through the first and second laws. Gurtin et. al. [93] give the following mechanical free energy imbalance for an isothermal material:

$$\dot{\Psi} - \mathbf{T} : \mathbf{D} = -\delta \leq 0 \tag{7.73}$$

Where Ψ is the free energy per unit volume in the material, and $-\delta$ is the overall dissipation in the material per unit volume, which must always be non-positive. We consider a Jeffrey's type viscoelastic model, where we have set the solvent viscosity $\eta_1 = 0$ and the polymer viscosity $\eta_2 = \infty$ (this limit can easily be reached by both the models of Quemada or Souza Mendes), leaving a single elastic element with modulus $G(\lambda)$. For simple 1-D deformations, we would have $\Psi = G(\lambda)\gamma^2/2$, with G an increasing function of λ. Because the aging process in the material causes an increase in λ under a zero shear rate, it is possible for $\dot{\lambda}$ (and $\dot{\Psi}$) to be positive even when $\mathbf{D}$ or $\dot{\gamma}$ are zero. Therefore, the left hand side of Eq. 7.73 will be positive during this aging process, violating the dissipation inequality. Hence, models such as those of Quemada and Souza Mendes clearly violate Eq. 7.73 in (at the very least) the limiting case of when $\eta_1 = 0$ and $\eta_2 = \infty$.

To illustrate how such models may give unphysical predictions, we consider the following sequence of step deformations for this type of "thixoelastic" element with $\sigma = G(\lambda)\gamma$: First, a step in strain of γ_0 is imposed at $t = t_1$. At this initial time, the material is not in its fully aged state with $G(\lambda) = G_1$, a low value. The stress

will increase instantaneously to a value of $\sigma(t_1) = G_1\gamma_0$. The material is then allowed to age (i.e. increase λ) while the strain is held constant, resulting in the modulus increasing to a value $G(\lambda) = G_2$. This results in the stress in the material increasing in order to preserve the equality $\sigma = G(\lambda)\gamma_0$. At some time t_2, we then step the strain back down to zero, which also results in the stress stepping down to zero. The sequence of steps in strain and stress are shown graphically in the figure below:

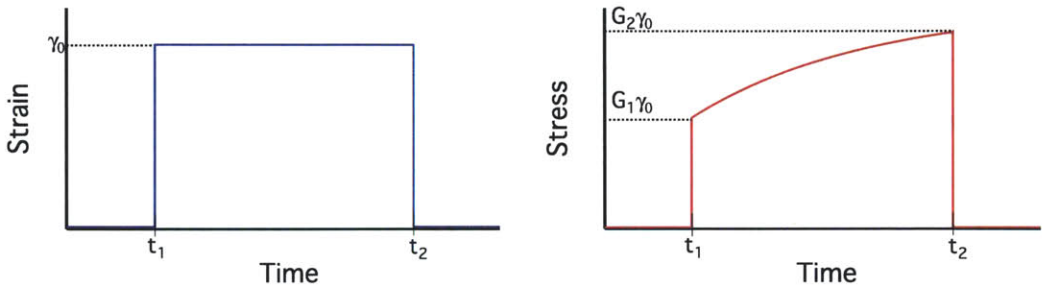

Figure 7-7: Sequence of steps in strain on a "thixoelastic" element with $\sigma = G(\lambda)\gamma$. The aging results in an increase in stress while the strain is held constant. This allows the material to increase the elastic strain energy it has stored, while the extent of its deformation remains constant.

We can then evaluate the mechanical work done on the material W_1 and W_2 for each step in strain through the following integral:

$$W_1 = \int_{t_1^-}^{t_1^+} \sigma(t)\dot{\gamma}(t)dt = \frac{G_1\gamma_0^2}{2} \tag{7.74}$$

$$W_2 = \int_{t_2^-}^{t_2^+} \sigma(t)\dot{\gamma}(t)dt = -\frac{G_2\gamma_0^2}{2} \tag{7.75}$$

Because $G_2 > G_1$, the material has essentially given back more energy than was initially stored at $t = t_1$. The question remains as to where this energy has come from. Clearly a more sophisticated constitutive model is required in order to correctly capture this thixoelastic behavior. Such a model would ideally begin from specifying a form of the free energy in the material Ψ, so as to not violate forms of the dissipation inequality such as that given Eq. 7.73. This form of the free energy must correctly account for the effects that aging has on the material, and may necessarily need to be cast as a thermomechanically coupled model due to the underlying thermal/Brownian

mechanisms which are responsible for the aging process.

7.4 Summary

Here we have developed a fully three-dimensional, frame-invariant, thermodynamically consistent version of the KH model that was discussed in Chap. 6. We have shown that under steady shearing conditions, the predictions of this 3D version of the model agree with those of the simple 1D case, demonstrating an equivalency between the model parameters.

Furthermore, under certain simplifying assumptions (small elastic stretches $\mathbf{U}^e \simeq \mathbf{1}$, and values of $q \gg 1$) we have derived approximate analytical expressions for the components of the deviatoric Cauchy stress tensor $\mathbf{T}_0$ under a number of different canonical flows. These include: steady shearing deformation, uniaxial elongational flow, and planar elongational flow. For steady shearing deformations, the analytical expression for the 1-2 shear component of the Cauchy stress agrees with the simple 1D version of the KH model, but the model also predicts a constant first normal stress difference $N_1 = 2C/(q^2)$. For the elongational flows, the approximate analytical solutions simplify to the Newtonian case (with appropriate values of the Trouton ratio) if we set $m = 1$ and set the yield stress $\sigma_y = C/q \to 0$.

The 3D KH model can be simplified to other constitutive laws under certain limits. Specifically, for the limit $\sigma_y \to 0$, the 3D KH model simplifies to a Newtonian (or power law, depending on the value of m) fluid. In the limit of $q \to \infty$, the 3D KH model simplifies to a 3D Bingham or Herschel Bulkley like viscoplastic fluid (again depending on the value of m) with a von-Mises yielding criterion which determines whether plastic flow will occur or not.

We briefly examined the case where large elastic stretches $\mathbf{U}^e$ arise due to the yield stress σ_y being comparable to the shear modulus G. Under these conditions and viscometric shearing, the shear stress vs. shear rate flowcurve of the 3D KH model agrees with the one-dimensional version of the KH model. However, larger normal stress differences arise due to nonlinearities arising in the elastic stress-strain

relationship (these nonlinearities increase as strain to some power greater than 1). However, the formulation provided here for the 3D KH model is flexible, and the elastic stress-strain relationship (normally specified in the form of a free energy potential) can be modified separately in order to correctly describe the elastic normal stresses of the material. This can be done without losing the ability to predict the steady shear stress vs. shear rate flowcurve data.

This 3D KH model introduced here therefore has several advantages over previously proposed generalizations of the Bingham or Herschel-Bulkley model [161, 134]. First, the flow/no flow criterion is regularized using the evolution equation for $\mathbf{A}$, which lets the material naturally evolve towards a yielded or unyielded state, depending on the level of the stress that develops in the material under an imposed deformation. Consequently, there is no need to track yield surfaces when simulating flow transients of the 3D KH model in more complex geometries. Secondly, the 3D KH model is able to predict transient flow for stresses below the yield stress σ_y (it also predicts a viscosity bifurcation as shown in Chap.6). These types of transients are commonly observed in EVP materials, and a single zero shear rate viscosity parameter is not sufficient to characterize this behavior. Third, and finally, tuning of the elastic behavior in the 3D KH model can be used to capture normal stress differences in EVP materials.

The version of the KH model discussed in this chapter was also compared to the Oldroyd-B constitutive model, a canonical model which is commonly used to describe the behavior of viscoelastic polymers. Under certain limits ($C/(qG) \ll 1$, $m = 1$, $q \gg 1$), the 3D KH model is identical to the Oldroyd-B model, with the exception that the polymer viscosity η_2 is inversely related to the second invariant (or magnitude) of the rate of deformation tensor, $|\mathbf{D}|$.

Although the KH model outlined in this chapter cannot predict thixotropy (the evolution equation for its internal variable $\mathbf{A}$ does not account for aging at rest), we have suggested how thixotropy can be implemented into this framework. We will therefore continue in Chap. 8 with a study of the thixotropic behavior of the model waxy crude oil that was introduced in Chap. 5. We will use the framework for the

KH model in order to develop a new constitutive law to capture the thixotropic, EVP behavior that this model crude oil exhibits. This new constitutive law will introduce isotropic hardening into the current KH model. We will mostly consider a simple, 1D version of the model, however this behavior can also be generalized to a 3D, frame invariant form [96].

Chapter 8

Thixotropy

8.1 Introduction

Having developed a constitutive law to predict the rheology of a non-thixotropic EVP material, we now revisit the model waxy crude oil from Chap. 5. The goal of this chapter will be to utilize detailed experimental measurements of our model crude oil in several different rheological flows to motivate the development of a thixotropic constitutive model. These measurements can then be used to determine appropriate values of the constitutive parameters. This model builds on the kinematic-hardening framework discussed in Chap. 6, but we will be careful to illustrate the links between the model here and other models in the literature that have already been employed to predict thixotropic behavior. The end goal in this chapter is to develop a constitutive model, and framework, which can predict material response in a number of different rheological flows, and will be ultimately useful for numerical simulations of complex flows of waxy crude oils.

8.2 Experimental

8.2.1 Model Fluids & Rheometry

The fluid used here is the same model waxy crude oil that has been introduced in Chap. 5. It is created by combining the heavy mineral oil (Sigma Aldrich 330760) with a paraffin wax (Sigma Aldrich 327212). The components are combined together at a high temperature ($\geq$ 60°C) and stirred in order to dissolve the wax in the oil. The model fluid behaves as a Newtonian liquid in this state, and can then be loaded into the rheometer.

In this chapter, we utilize two different rheometers to probe the response of this fluid to deformations. An ARES rheometer is used for the strain controlled large amplitude oscillatory shear (LAOStrain) measurements. This ARES rheometer is equipped with lower Peltier plate for temperature control of the sample. The upper fixture is a cone with a diameter of 50 mm and an angle of 2°. The upper and lower surfaces are also roughened (root mean squared roughness $R_q \simeq 30$ μm) in order to minimize any wall slip. The second rheometer that is used is an ARG2 stress-controlled rheometer. This rheometer is utilized in two different configurations. The first of these is the standard configuration, which is equipped with a lower Peltier plate for temperature control, and an upper cone (diameter 60 mm and angle of 2°). As in the case for the ARES rheometer, this configuration has roughened upper and lower surfaces, with $R_q \simeq 30$ μm. The second configuration for the ARG2 is the RheoPIV configuration (v2) that was introduced in Chap. 3. This configuration allows for in-situ measurements of the flow field within the fluid to be extracted. This apparatus is described in detail in Sec. 3.2, and utilizes smooth surfaces.

In Fig. 8-1, we illustrate one of the characteristic features of the rheology of these model waxy crude oils - the wax appearance temperature, T_{wa}. Fig. 8-1 presents measurements of the viscosity of the heavy oil, and a 5% and 10% wax in oil mixture at a range of temperatures (obtained using the standard ARG2 configuration). The data in Fig. 8-1 is taken by imposing a shear rate of $\dot{\gamma} = 50$ s^{-1} on the fluid, while lowering the temperature at a rate of 1°C/minute from 55°C to 25°C. As seen in Fig. 8-1, the

mineral oil exhibits an Arrhenius-like exponential dependency of viscosity on temperature. Both the 10% and 5% wax in oil systems also exhibit an Arrhenius-like dependency of viscosity on temperature for large values of T, however they rapidly diverge from this dependency at a temperature known as the wax appearance temperature, T_{wa}. This temperature signifies the point at which wax crystals first begin to precipitate out of the fluid. The morphology of these crystals is typically sheet-like or needle like [109, 202], and the high aspect ratio of the crystallites may result in a mechanical gel forming at low concentrations of precipitated wax [7].

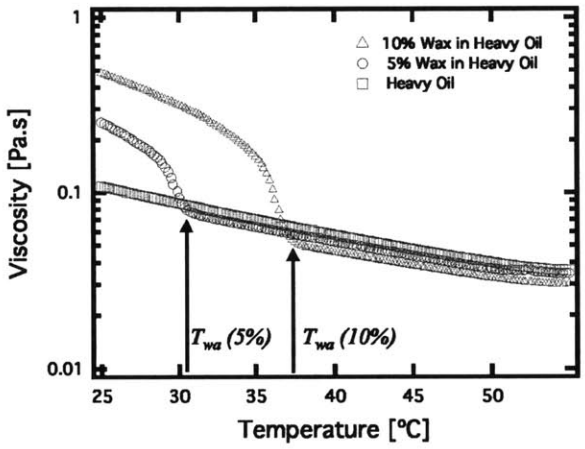

Figure 8-1: Temperature sweep of viscosity for 3 different model fluids, at an imposed shear rate of $\dot{\gamma} = 50\ s^{-1}$. Temperature is ramped at a rate of 1°C/min. The measured value of $\Delta H/R = 3970$ K for the heavy oil's Arrhenius behavior is equal to the value measured in Fig. 5-2

Spatially averaged vs. local stresses and shear rates

For the remainder of this chapter, we will carefully distinguish between spatially averaged measurements of stresses and shear rates, and the local values of the stress and shear rate within the fluid. The model waxy crude oils that we will deal with here are known to exhibit wall slip and other shear localization phenomena (see Chap. 5). When these phenomena present themselves in cone-plate geometries, the stress and shear rate may no longer be uniform along the radial position of the geometry r [168, 184] (see the appendix for a discussion of these affects). We will therefore define

an average stress $\hat{\sigma}$ and average shear rate $\hat{\dot{\gamma}}$ as follows:

$$\hat{\sigma} \equiv \frac{3\mathcal{T}}{2\pi R^3} \tag{8.1}$$

$$\hat{\dot{\gamma}} \equiv \frac{\Omega}{\Theta_0} \tag{8.2}$$

Where $\mathcal{T}$ is the torque that the rheometer imposes on the sample, Ω is the angular rotation rate of the geometry, R is the radial size of the geometry, and Θ_0 is the cone angle. We can also define an average strain accumulated as $\hat{\gamma} \equiv \int_{t_1}^{t_2} \frac{\Omega(t)}{\Theta_0} dt$. Under homogenous shearing with no wall slip, these average quantities reduce to the local true stress σ, the local true shear rate $\dot{\gamma}$ and the local true strain $\hat{\gamma}$. Due to the ubiquity of wall slip and other shear localization events in the fluids here, we will reserve the symbols σ and $\dot{\gamma}$ to refer to the stress and shear rate under homogenous deformations only.

8.2.2 Slurry vs. strong gel scenario - Sample preparation methods

In Chap. 5, we pointed out that an important component of carrying out bulk rheological measurements on a waxy crude oil is the selection of an appropriate sample preparation protocol. This is important because waxy crude oils are extremely sensitive to variations in their thermal and shear history as they are cooled to below their wax appearance temperature [209]. In what follows, we justify the selection of one particular preparation protocol, which provides consistently reproducible rheometric data that can be used for the development of a constitutive model.

One may envision two different scenarios under which a waxy crude oil may be transported through a pipeline. For the first scenario, consider a length of pipeline containing waxy crude at a temperature $T > T_{wa}$, under quiescent (zero flow-rate) conditions. If the temperature of this fluid slowly and uniformly drops to below T_{wa}, then a gel network will form in the material due to the presence of solid wax precipitates. Because the cooling of this fluid occurs under no flow (and a zero shear

rate), the crystallite aggregates may grow to large sizes and the gel structure formed in the crude oil will be strong. As a result, starting the flow in the pipeline after cooling will require large pressure drops, with the possibility that the fluid undergoes an adhesive failure (or wall slip) at the pipe wall [119].

The second scenario involves cooling the waxy crude oil under non-quiescent (flowing) conditions. For such a scenario, the gel structure formed in the oil will be weaker, due to the disruptive effect of shearing the aggregates of wax crystals as they form. Therefore, smaller pressure drops will be required in order to maintain the flow of the fluid through the pipeline, and it will be less likely that the flow occurs through the mechanism of wall slip.

As was discussed in Chap. 5, we refer to the state of the crude oil in the first scenario as a "strong gel" and the state of the material in the second scenario as a "slurry". The strong gel and slurry states of the oil are reproduced in a laboratory scale setup with the model wax-oil and the rheometer by cooling the wax-oil mixture either quiescently (under zero shear) or under a high shear rate ($\hat{\dot{\gamma}} = 50\ s^{-1}$). In, Chap. 5, we focused on the behavior of the wax-oil system in its strong gel state. In this chapter, we will restrict our focus to the rheology of the material in its slurry state.

Fig. 8-2 illustrates some critical differences between the response of a 5% wax-oil mixture in the two different states to a step in steady shear of $\hat{\dot{\gamma}} = 1.2\ s^{-1}$. The response of the model fluid in the slurry state is shown in Fig. 8-2 (a). The model fluid is brought to this state by cooling the sample from 55°C to 27°C at a cooling rate of 1°C/min, under an applied shear rate of $\hat{\dot{\gamma}} = 50\ s^{-1}$. Once the fluid reaches the final temperature of 27°C, the shear rate of $\hat{\dot{\gamma}} = 50\ s^{-1}$ is held for an additional 3 minutes, in order for any thermal transients in the system to die out. After this additional time period of 3 minutes, the shear rate is immediately reduced to $\hat{\dot{\gamma}} = 1.2\ s^{-1}$. This sequence of steps is administered using the ARG2 in its RheoPIV configuration with a 2° lower cone (discussed in Sec. 3.2) so that both spatially averaged rheological measurements of $\hat{\sigma}$ and $\hat{\dot{\gamma}}$, and the local flow field within the sample can be obtained.

The response of the model fluid in its strong gel state is shown in part (b) of

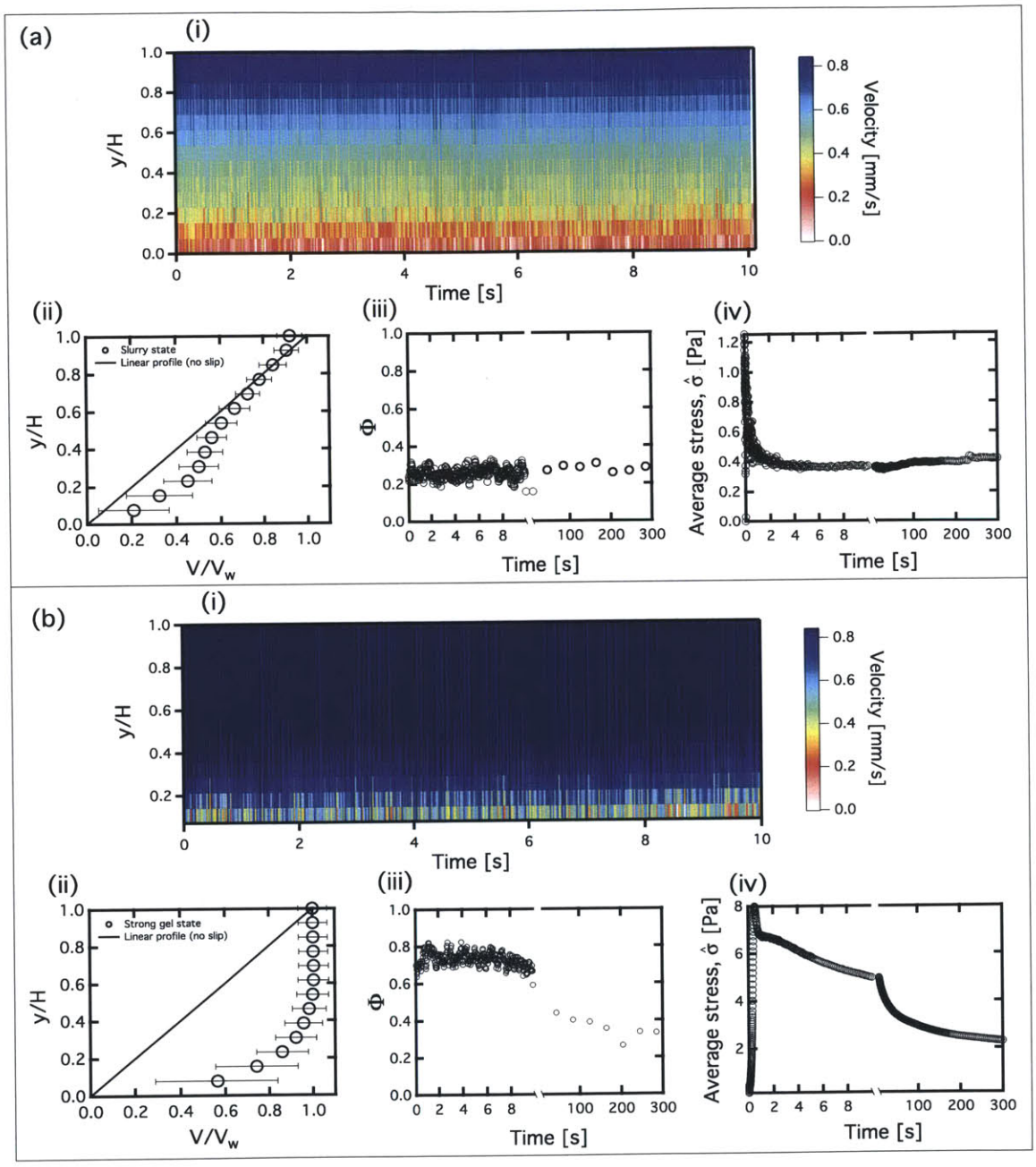

Figure 8-2: Illustrating the difference between the wax-oil system in its "slurry state" (a) and in its "strong gel" state (b). For each of the states, startup of (spatially averaged) steady shear at $\hat{\dot{\gamma}} = 1.2\,\mathrm{s}^{-1}$ is imposed at $t = 0$, and $\hat{\sigma}$ is measured over the course of 300 seconds (iv). In (i), we show spatiotemporal diagrams of the velocity field within the fluid for the first 10 seconds. Plots of the parameter Φ for the entire 5 minutes are given in (iii), while in (ii) we give the average velocity field within the fluid over the 300 seconds. Error bars are equivalent to 2 standard deviations of the velocity measurement at each height.

Fig. 8-2. This state of the fluid is achieved by following the same protocol for the slurry state, however for the cooling step and the subsequent 3 minute holding time, the shear rate is held at $\hat{\dot{\gamma}} = 0\ s^{-1}$. This results in an essentially unperturbed gel network before the shear rate of $\hat{\dot{\gamma}} = 1.2\ s^{-1}$ is imposed.

The use of the RheoPIV configuration allows for both the average stress $\hat{\sigma}$ in the fluid, as well as the local velocity field to be monitored over the course of the 300 second application of the shear rate $\hat{\dot{\gamma}} = 1.2\ s^{-1}$. For the slurry state, the stress $\hat{\sigma}$ shows a constant measured value of 0.4 Pa. The strong gel state shows an initial peak in the stress, followed by a slow decay in the measured value of $\hat{\sigma}$, occurring over the course of several minutes. The velocity field within the fluid in the two states (illustrated through the use of spatiotemporal diagrams for the first 10 seconds, as well as the average velocity profiles in (ii)) is completely different for each case. As would be expected for the strong gel state (where larger stresses are needed to break the gel structure in the bulk of the fluid) the material flows through the mechanism of wall slip at the lower surface, and remains adhered to the upper surface. The velocity profile in this state therefore appears plug-like, in contrast to what is seen for the material in the slurry state. In the slurry state, a velocity profile closer to linear is observed, with a non-zero shear rate in the bulk

In order to characterize the long term evolution of the velocity profiles within the sample in these two states, we utilize the non-dimensional metric Φ which characterizes the nature of the velocity profiles (evaluated using Eq. 5.8). This metric Φ varies from 0, for a perfectly linear velocity profile with $v(y) = \hat{\dot{\gamma}}y$, to 1, for a plug-like profile with velocity $v(y) = V_p$.

A single value of Φ can be determined for each frame of video, so measured values of Φ corresponding to each frame of video are plotted for the first 10 seconds of the experiment. Subsequently, values of Φ which have been averaged over 10 seconds of video are plotted at 30 second intervals (and the time axis on the figure is expanded in this region). The material in the slurry state shows readings of Φ being constant over the entire 300 second duration of the test, and close to zero. Measurements of $\Phi = 0$ are difficult to obtain for wax-oil fluids below T_{wa}, due to some wall slip, and due to the

turbidity of the fluid. The turbidity introduces errors in the velocity measurements that always positively contribute towards Φ. Nevertheless, this behavior can still be compared to the behavior of the material in the strong gel state. In the strong gel state, Φ initially has a value closer to unity, then subsequently decreases over long time scales. This process has been observed and documented already in Chap. 5, and is the result of an erosion process [85] whereby the wax crystal structure breaks down into smaller aggregates and weakens the gel.

The measurements of $\hat{\sigma}$ and Φ in Fig. 8-2 suggest that in the strong gel state, the initial response of the fluid to an imposed shear rate will be dominated by localized failure events at the wall, followed by long transients in the evolution of the (likely heterogenous) microstructure. These circumstances are quite far from the typically assumed uniform distribution of stress and shear rate within a fluid being deformed in a cone and plate rheometer. In order to avoid the impact that these types of complicated yielding scenarios may have on interpreting bulk rheological data, we choose to utilize the slurry preparation protocol for all experiments that follow. As is seen in Fig. 8-2 (a), the 5% wax-oil system in its slurry state exhibits less wall slip, and no prolonged decay in the stress signal due to fluctuating stick-slip events that break down the microstructure. Some deviations of the velocity profile from the linear form for values of $y/H < 0.4$ are observed - these are due to the turbidity of the material decreasing the precision of the velocity measurements deeper into the fluid (and consequently the error bars are much larger for these values of $y/H < 4$). Despite this, bulk rheological data for this slurry state material is comparatively easier to interpret with a continuum mechanics constitutive modeling framework.

To end this section, we graphically emphasize the difference between these two "strong gel" and "slurry" states in Fig. 8-3. Fig. 8-3 contains two bright-field microscopy images of the wax crystal microstructure for a 5% wax-oil mixture at 25°C in its slurry state (a), and strong gel state (b). In these images, the wax crystals show up as dark particles in a light background. These crystals are discotic, but appear needle-like when viewed edge on in the two-dimensional plane. The wax network formed in the slurry state is looser with more vacant (light gray) regions where no

precipitates are present. The strong gel state consists of fewer vacant regions with a tighter network of wax precipitates - this is the underlying reason behind the strong gel exhibiting a higher yield stress than the slurry.

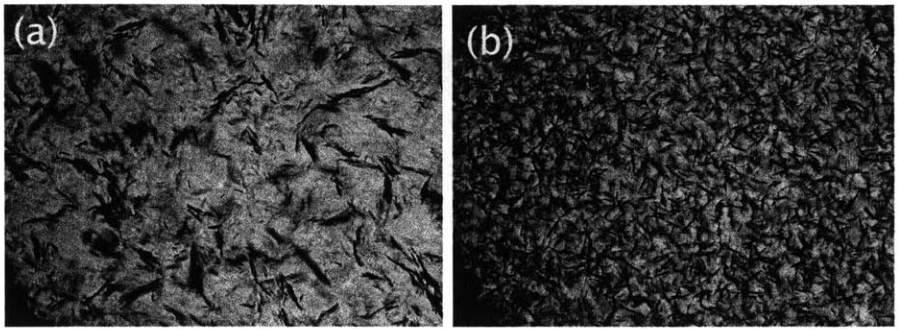

Figure 8-3: Bright field microscopy images of the 5% wax-oil system in the slurry state (a) and strong gel state (b). The horizontal scale of each image is 1 mm, both images are taken at 25°C

We see that in the strong gel state, one large aggregate of wax precipitates exists (a percolated network which spans the whole image in Fig. 8-3 (b)). The size of this aggregate precludes it from reforming under the influence of Brownian motion after the strong gel structure has been broken down. We can use Eq. 5.6 in order to estimate a timescale for rotary diffusion of the aggregate. We will assume that the aggregate spans the entire imaging view ($a = 1$ mm), within a continuous phase (heavy oil) with viscosity $\mu = 0.1$ Pa.s at a temperature $T = 300$ K. Under these conditions, a time scale of $\tau = 2.4 \times 10^{11}$ s is obtained. This timescale is on the order of thousands of years - hence the irreversibility of yielding transitions observed in Chap. 5 which dealt with samples in the strong gel state. However, in the slurry state, we observe individual wax crystals and much smaller aggregates. For a single wax crystal of characteristic size $a = 1$ μm, the timescale τ then reduces to a value of $\tau = 240$ s. There is, of course, a distribution in the size of the wax crystals and aggregates in the slurry state. However, Fig. 8-3 does indicate that the fluid contains wax crystals below 10 μm in size. As a result, one would expect Brownian motion to be sufficient to cause some restructuring of the sample (but not to the point of reaching the strong gel state). As we will see in the upcoming sections, this results

in the slurry state material exhibiting thixotropic behavior.

8.3 Experimental Results and Discussion

For the wax-oil system in the slurry state, we propose three different rheological tests as canonical flows to both probe the material response of the wax-oil mixture, and provide a set of data for fitting constitutive models. In what follows, we describe these three types of rheological flows, and discuss implications of the experimental results for constitutive modeling.

8.3.1 Steady state flowcurve.

For thixotropic systems, steady state flow curves (that is, plots of viscosity vs. shear rate, or shear stress vs. shear rate) are often difficult to obtain [17]. The reason for this is because the measured viscosity frequently depends on the duration of the experiment. However, flowcurves are commonly used in fitting of constitutive models to yielding materials [204, 55]. Souza Mendes and Thompson [59] recently suggested that for these types of fluids, the steady state flowcurve describes the equilibrium locus of the dynamic thixotropic system. For constitutive models which incorporate an evolving structural parameter (commonly denoted as λ in the thixotropy literature [17]), this implies that the steady state flowcurve can be fit to the constitutive model predictions for the special case when $\dot{\lambda} = 0$, which may significantly simplify the fitting procedure.

To provide a set of data for fitting our model, we therefore plot in Fig. 8-4 the measured flowcurves for the heavy mineral oil, and the 5% and 10% wax-oil systems in their slurry state ($T = 27°\mathrm{C}$). These measured flowcurves are obtained by using the ARG2 in its standard configuration. The measurements are carried out by shearing at a given globally averaged rate $\hat{\dot{\gamma}}$, and are determined to have reached a steady state by using a "steady state sensing" option on the ARG2. This option measures the temporally averaged torque $\mathcal{T}$ over successive 30 second periods, and then determines that the measurement has reached a steady state when 3 periods are within 5% of

the same value. As a result, each measurement point requires typically 5 minutes to reach a steady state, and the measurement of the entire flow curve requires 2-3 hours.

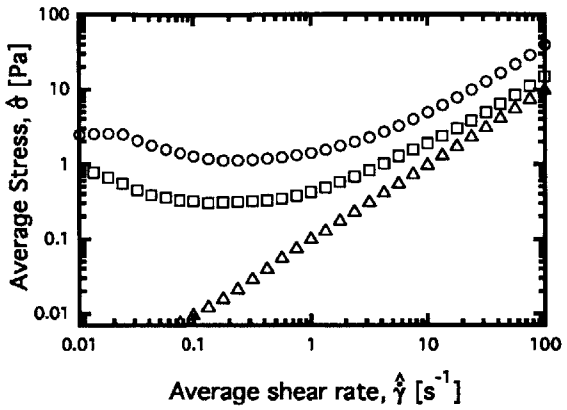

Figure 8-4: Measured flow-curves of the various systems used in this study. (△) Heavy mineral oil, (○) 10% Wax in oil, and (□) 5% Wax in oil.

Several key features can be identified from the flowcurves shown in Fig. 8-4. Firstly, both the 5% and 10% model fluids exhibit Newtonian-like behavior at high shear rates, with the applied stress being linearly proportional to applied shear rate. As expected, the 10% system has a larger steady state viscosity than the 5% system, due to the higher volume fraction of solid precipitates. However, one unusual feature of the flowcurves for the model crude oils is that they exhibit a non-monotonicity, i.e. there is a region at lower shear rates ($\hat{\dot{\gamma}} \leq 0.1\ s^{-1}$) where the stress decreases as the shear rate is increased.

Non-monotonic flowcurves (NMFC's) typically point towards the presence of some type of material instability [116, 169, 89]. Some shear banding fluids, for example wormlike micellar solutions, are often assumed to have an *underlying* non-monotonic flowcurve [24]. This non-monotonic flowcurve cannot be measured, because at imposed shear rates in the decreasing region of the flowcurve, the material splits into two [185] or more [36] coexisting regions with different local shear rates. In this work we refer to this as a "standard shear banding scenario".

Despite this example, there are several examples in the literature of *measured* NMFC's. Dijksman et. al. [61] measured NMFC's in granular media in a number

of different geometries, while Michel et. al. [144] observed these types of flowcurves in fluids with a transient network. In both of these instances, the authors indicate the presence of some type of unstable flow which is manifested in the material. In the case of Michel et. al., they observe "wavy deformations of the sample surface" and "progressive cavitation-like proliferation of bubbles in the bulk". Dijksman et. al. point toward the possibility of a heterogenous stress field within the granular material (for the cone-plate geometry this means a difference between $\hat{\sigma}$ and $\sigma(r,t)$). This differs from the standard shear banding scenario envisioned for wormlike micellar solutions. The standard shear banding scenario assumes stable flow (albeit shear-banded) but an underlying unstable NMFC.

For the materials studied by Michel et. al., Dijksman et. al, and our model crude oil, the NMFC of $\hat{\sigma}$ vs. $\hat{\dot{\gamma}}$ is thus measurable, however it likely precludes the standard shear banding scenario. It instead implies a more complex scenario, in which the assumed homogeneity of both the stress and strain fields in a cone-plate geometry breaks down in a complex manner. As pointed out by Michel et. al., it is possible that at these low values of the imposed shear rate, our material exhibits complex spatiotemporal fluctuations in local values of stress and strain rate. As a result, in general $\hat{\sigma}(t) \neq \sigma(r,t)$ and $\hat{\dot{\gamma}}(t) \neq \dot{\gamma}(r,t)$. These fluctuations would likely correspond to regions where the material exhibits differing levels of structure. One way to physically interpret this type of behavior is as a nonequilibrium phase transition. Boltenhagen et al. [32] and Hu et al. [100] were able to access non-monotonic regions in the flowcurves of low concentration, shear-thickening wormlike micellar solutions, and interpreted this as a shear-induced phase transition. Due to the coexistence of two different phases within the material, Boltenhagen et. al. rationalized a feedback mechanism which allowed for this region of the flowcurve to be accessed. They were also careful in stating that the measurements of shear rate $\hat{\dot{\gamma}}$ and shear stress $\hat{\sigma}$ that are given in flowcurves such as Fig. 8-4 correspond to spatially averaged shear rates and stresses, and not the stress or shear rate within an individual phase. This is important point to bear in mind when interpreting bulk rheological data such as that shown in Fig. 8-4. So, while the data in 8-4 is temporally equilibrated (due to the

steady state sensing on the ARG2), it only represents a spatial average of the locally fluctuating true shear rate and true stress.

RheoPIV in the non-monotonic region of the flowcurve. The ARG2 in its RheoPIV configuration can be used in order to provide experimental evidence for a material instability associated with the NMFC. We use the 5% wax-oil system in its slurry state at a temperature of $T = 27°C$ to demonstrate this (higher wax content systems are too turbid to provide meaningful velocimetric data). The particular set of steps that are taken are first: preshearing the material at $\hat{\dot{\gamma}} = 50\ s^{-1}$ for 5 minutes. Then, a sequence of 3 steps in shear rate is imposed (this point in time is denoted as $t = 0$ s). The first step is at $\hat{\dot{\gamma}} = 0.02\ s^{-1}$ for 30 minutes, followed by a step to $\hat{\dot{\gamma}} = 1.2\ s^{-1}$, and finally a step back to $\hat{\dot{\gamma}} = 0.02\ s^{-1}$. The measured stress and velocity profiles for this test are shown in Fig. 8-5.

Fig. 8-5 (a) illustrates that even though the rheometer imposes an apparent shear rate in the two cases which differs by a factor of 60, the steady measured stress is roughly equal (they differ by less than 12%) for both values of $\hat{\dot{\gamma}}$. This is indicative of the extreme shear thinning exhibited by the model waxy crude oil, and is consistent with the non-monotonicity in the measured flowcurve of Fig. 8-4. Transient responses are also exhibited in the response of the material to the steps in shear rate. At $t = 1600$ s, when the shear rate is stepped to $\hat{\dot{\gamma}} = 1.2\ s^{-1}$, an immediate increase in the stress is observed, followed by a subsequent decrease with the stress reaching a minimum at approximately $t = 1630$ s. Then, a gradual increase (from $t = 1630 - 3000$ s) in the stress is seen towards a steady value of $\hat{\sigma} = 0.71 \pm 0.01$ Pa. At $t = 3410$ s, when the shear rate is switched to $\hat{\dot{\gamma}} = 0.02\ s^{-1}$, the stress initially decreases, followed by a subsequent increase in the stress reaching a maximum (and steady value) at $t = 3440$ s.

These types of transients are consistent with what one would expect from a thixotropic material undergoing cycles of structuring and destructuring [66]. In particular, from $t = 1600$ s to $t = 1630$ s, the material is beginning from a mostly structured state (due to the low value of the shear rate imposed for $t \leq 1600$ s). This

requires a sudden increase in the stress to break the wax structure, until the structure is completely broken and the stress reaches a minimum at $t = 1630$ s . From $t = 3410$ s to $t = 3440$ s the material begins from a destructured state due to the high value of the shear rate imposed previously. It therefore requires a smaller stress to cause flow, but this stress will increase due to a build up in the structure which can occur at the lower shear rates.

From $t = 1630$ s to $t = 3000$ s we also observe the effect of a long-time structuring which results in an increase in the measured viscosity within the fluid $\hat{\eta}(t) \equiv \hat{\sigma}(t)/\hat{\dot{\gamma}}$. The presence of multiple timescales for restructuring of the fluid is not surprising. Fig. 8-3 (a) indicates that for the material in the slurry state, there is a distribution of characteristic sizes of the microstructure. Some wax crystals appear smaller than others, and some form into aggregates of increasing size. The characteristic time for rearrangement of the microstructure is a strong function of the size of these crystals and aggregates ($\tau \sim a^3$) [17, 190]. The evolution of the fluid rheology should therefore reflect this distribution of timescales.

The measurements of $\hat{\sigma}$ in Fig. 8-5 (a) provide clear evidence that the model waxy crude oil is highly thixotropic. However, Fig. 8-5 (a) provides no indication that the flow field within the material is heterogenous or shear-banded. Evidence for a material instability where such flow fields are present is given in Figs. 8-5 (b) and (c). In these two sub-figures we contrast the measured velocity field within the fluid as two different values of $\hat{\dot{\gamma}}$ are imposed. Under an imposed shear rate of $\hat{\dot{\gamma}} = 0.02$ s^{-1}, we observe stochastic fluctuations in the average shear rate across the gap, in the slip velocity at the upper plate, and in the general nature of the velocity profile. From $t = 0 - 100$ s, the velocity profile indicates a region of higher shear rate near the center of the gap. This is reminiscent of the 3-banded velocity profiles which have been observed in wormlike micellar solutions undergoing steady shear in cone-plate geometries [36, 39]. However, this type of velocity profile only appears for a brief period of time. Later velocity profiles (e.g. at times $t = 1150$ s and $t = 1300$ s plotted in Fig. 8-5 (b) (ii)) show a uniform shear rate across the gap with larger slip velocities at the upper and lower plates. The velocity profile plotted for $t = 1300$ s

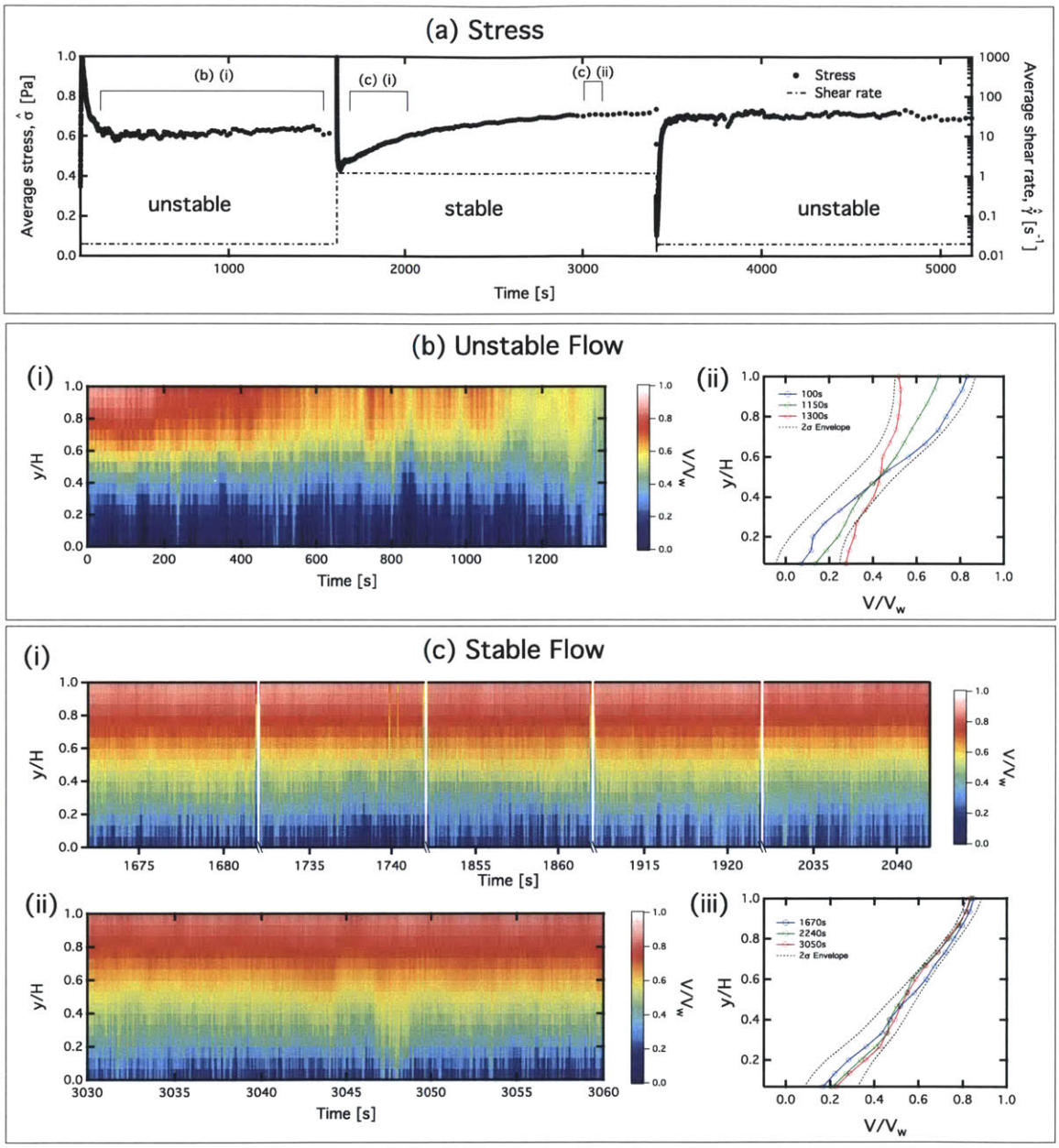

Figure 8-5: Switching between the stable ($\dot{\hat{\gamma}} = 1.2\ \mathrm{s}^{-1}$) and unstable ($\dot{\hat{\gamma}} = 0.02\ \mathrm{s}^{-1}$) regions of the flowcurve in Fig. 8-4 (5% wax-oil mixture). The steady measured stress values are the same for the two different shear rates, however in the unstable region (b), more fluctuations are observed in the velocity profile, as indicated by the 2σ envelop of the profiles. Within the stable region, velocity profiles are sampled at several 10 second intervals (c) (i), and then for a longer 30 second interval (c) (ii) beginning at $t = 3030$ s. Fluctuations in the shear rate across the gap are a factor of 2 lower in this stable region. Measurements are carried out using the RheoPIV configuration of the ARG2 (smooth cone-plate geometry)

is near plug-like ($\Phi = 0.73$) with scaled slip velocities of $(1 - v(y)/V_w) = 0.48$ at the upper surface and $(v(y)/V_w) = 0.28$ at the lower surface.

In order to quantify these fluctuations, we consider a Reynolds averaging [115] of the velocity field $v(y,t)$ such that:

$$v(y,t) = \bar{v}(y) + v'(y,t), \tag{8.3}$$

Where $\bar{v}(y)$ is the average part of the velocity defined as follows:

$$\bar{v}(y) \equiv \frac{1}{t_2 - t_1} \int_{t_1}^{t_2} v(y,t) dt \tag{8.4}$$

and $v'(y,t)$ is the fluctuating part of the velocity. We can define a (dimensionless) time and space averaged shear rate across the gap measured using the RheoPIV device. This shear rate is defined as follows:

$$\tilde{\dot{\gamma}} \equiv \frac{1}{\hat{\dot{\gamma}} H (t_2 - t_1)} \int_{t_1}^{t_2} \int_0^H \frac{dv(y,t)}{dy} dy \; dt = \frac{\bar{v}(H) - \bar{v}(0)}{V_w}, \tag{8.5}$$

To quantify the effect that the fluctuating part of the velocity $v'(y)$ has on the shear rate, we define a standard deviation of the shear rate as follows:

$$\sigma_{\dot{\gamma}} \equiv \sqrt{\frac{1}{t_2 - t_1} \int_{t_1}^{t_2} \left(\tilde{\dot{\gamma}} - \frac{v(H) - v(0)}{V_w} \right)^2 dt} \tag{8.6}$$

$$= \sqrt{\frac{1}{t_2 - t_1} \int_{t_1}^{t_2} \left(\frac{v'(H) - v'(0)}{V_w} \right)^2 dt} \tag{8.7}$$

For the data in Fig. 8-5 (b), the shear rate measured in the gap is $\tilde{\dot{\gamma}} \pm 2\sigma_{\dot{\gamma}}$, where the $\pm$ represents the 95% confidence bound in this average over time, and is indicative of the extent of the fluctuations in the local shear rate $\dot{\gamma}$ over time. In Fig. 8-5 (b), we compute $\tilde{\dot{\gamma}} = 0.59$ and $\sigma_{\dot{\gamma}} = 0.13$

In Fig. 8-5 (c), we show measured profiles for the case when $\hat{\dot{\gamma}} = 1.2$ s^{-1}. At this higher shear rate, it is necessary to acquire images at a higher frame rate due to the increased velocity of the tracer particles. Due to limited digital storage space,

we are limited to sampling the velocity field at several smaller intervals in time. We choose to sample the velocity field for 5 different 10 second intervals from $t = 1670$ s to $t = 2040$ s, which coincides with the region of increasing measured stress. We also sample the velocity for 30 seconds at $t = 3030$ s, where the spatially averaged stress $\hat{\sigma}$ has approached and remains at a constant value. In these regions, the average shear rate across the gap fluctuates considerably less, with $\bar{\dot{\gamma}} = 0.66$ and $\sigma_{\dot{\gamma}} = 0.068$. The 95% confidence bound has been reduced by a factor of 2 compared to the case when $\hat{\dot{\gamma}} = 0.02$ s^{-1}. The velocity field also appears to be linear for all times, with some wall slip occurring at the upper $((1 - \bar{v}(H)/V_w) = 0.14)$ and lower $((\bar{v}(0)/V_w) = 0.21)$ surfaces. The fluctuations in shear rate and slip velocity that are observed in Fig. 8-5 (b) are therefore markedly reduced for the case where the imposed shear rate is $\hat{\dot{\gamma}} = 1.2$ s^{-1}.

In Fig. 8-5 (b) (ii) and (c) (ii) we also include envelopes which account for magnitude of the fluctuations in the velocity $v'(y)$. These envelopes are defined as $\bar{v}(y) \pm 2\sigma_v(y)$, where $\sigma_v(y)$ is the standard deviation of the velocity as a function of height, and is defined as follows:

$$\sigma_v(y) \equiv \sqrt{\frac{1}{t_2 - t_1} \int_{t_1}^{t_2} (v'(y))^2 \, dt} \tag{8.8}$$

In Fig. 8-5 (b) (ii) and (c) (ii), $\sigma_v(y)|_{\hat{\dot{\gamma}}=1.2} < \sigma_v(y)|_{\hat{\dot{\gamma}}=0.02}$ for all values of y, indicating that there are more fluctuations in the velocity when the applied shear rate is $\hat{\dot{\gamma}} = 0.02$ s^{-1}. The difference in the magnitude of these fluctuations is highest near the upper surface ($y = H$), where fluctuations are 4.8 times larger for the case when $\hat{\dot{\gamma}} = 0.02$ s^{-1}. Incidentally, at $y = H$ velocity measurements are most accurate due to sample turbidity affecting the image quality less. After quantifying these fluctuations, we can therefore conclude that Fig 8-5 provides clear evidence of an fluctuating velocity field associated with a material instability in the wax-oil mixture. This unstable flow manifests at low shear rates (which lie in the decreasing region of the NMFC). We also conclude that the unstable flow does not appear when larger shear rates are applied which lie within the stable (increasing) region of the flowcurve.

The material instability which is observed consists of spatial heterogeneities in the local shear rate, both across the gap and along the direction of flow, fluctuations in wall slip, and the occasional appearance of plug like velocity profiles. This is the result of the competition between formation and breakdown of the structure within the sample. The formation of new aggregates is due to Brownian motion [17], while the breakdown of aggregates results from the application of shear. Furthermore, the local stress within the fluid σ is fluctuating, while the global averaged stress $\hat{\sigma}$, remains constant. This type of behavior is generally consistent with what has been observed for other systems that exhibit measurable NMFC's.[169, 144, 61]

8.3.2 Stress overshoots - Startup of steady shear.

The second rheological test that we utilize is the measurement of stress overshoots under startup of steady shear. The purpose of these types of tests is to probe the effect of "aging time" on material response. Aging time is the time that elapses between sample preparation, and imposing the step in shear rate. The sample preparation is typically carried out by shearing the material at a high rate (well within the stable region of the flowcurve in Fig. 8-4) for an extended period of time. Then, during the period of aging, the sample is left unperturbed so that there can be a build up in the material structure. When the step in shear rate occurs, the material will go through a yielding transition which depends on the initial structure, which in turn depends on the aging time. Thus, these types of tests can be used to both quantify the effect that structure has on the rheology of the system, but also to quantify any time scales which may be associated with the formation of this structure.

The particular tests are carried out on the 10% model waxy crude oil prepared to its slurry state at a temperature of 27°C. The ARG2 in its standard configuration is used, which utilizes roughened cone-plate surfaces to eliminate wall slip. We adopt the nomenclature of Fielding et. al. [79] and denote aging/waiting time as t_w. After the sample is prepared, a waiting time of $t_w = 2$ s is applied, and then a step in shear rate to $\dot{\hat{\gamma}} = 2\ s^{-1}$ is imposed for 10 minutes. Following this step, the material is left unperturbed for a waiting time $t_w = 5$ s, and the steady shear step

of $\hat{\dot{\gamma}} = 2\ s^{-1}$ is imposed for 10 minutes. In total, 7 startup tests of steady shear are imposed successively, with the waiting time between these steps being incremented in a logarithmic fashion up to a value of 200 seconds. Thus, for each value of t_w, measurements of the stress $\hat{\sigma}$ are obtained for the 10 minute step in shear rate. The measurements of stress and strain in this section will be indicated as averages ($\hat{\sigma}$ and $\hat{\gamma}$). However, the average strain rate $\hat{\dot{\gamma}}$ here is high enough, and wall slip is suppressed, so deviations of the average values from the local shear rate $\dot{\gamma}$ and local stress σ will be small.

In Fig. 8-6 below we plot the measured response of the average or nominal stress $\hat{\sigma}$ as a function of the spatially averaged strain $\hat{\gamma}$, for seven different values of t_w. Several observations can be made about the evolution of $\hat{\sigma}$. First, an overshoot is seen at applied strains of approximately $\hat{\gamma} = \hat{\dot{\gamma}}\Delta t \simeq 0.3$ dimensionless units. This overshoot increases with t_w, however it appears to saturate after t_w exceeds 20 seconds. The overshoot is clearly the result of structuring within the fluid that occurs over the course of the aging time t_w. A second observation that can be made is the gradual monotonic increase in $\hat{\sigma}$ which occurs over much longer time scales, and over multiple steps in the shear rate. This slower increase in $\hat{\sigma}$ is a manifestation of the same type of thixotropic behavior that is observed in Fig. 8-5 (a), where at an applied shear rate of $1.2\ s^{-1}$ it takes a long time (on the order of tens of minutes) for the value of $\hat{\sigma}(t)$ (and hence $\hat{\eta}(t)$) to stabilize. This is a result of slow structuring within the material, which occurs on time constants that are much larger than the waiting time of $t_w = 20$ s which is approximately required for the peak stress to saturate. This is additional experimental evidence of a distribution of scales associated with restructuring. One moment of this distribution appears to be responsible for an increase in the "steady" measured stress $\hat{\sigma}$ at a given applied deformation rate and another is responsible for an increase in the transiently observed yield peak.

Our constitutive model will primarily focus on predicting the transient yield peak in the stress $\hat{\sigma}(t)$ at intermediate strains $\hat{\gamma} \simeq 0.3$. This is frequently of greater practical relevance than the very long time response of the stress. These yield peaks would likely be responsible for relatively large additional pressure drops being required to

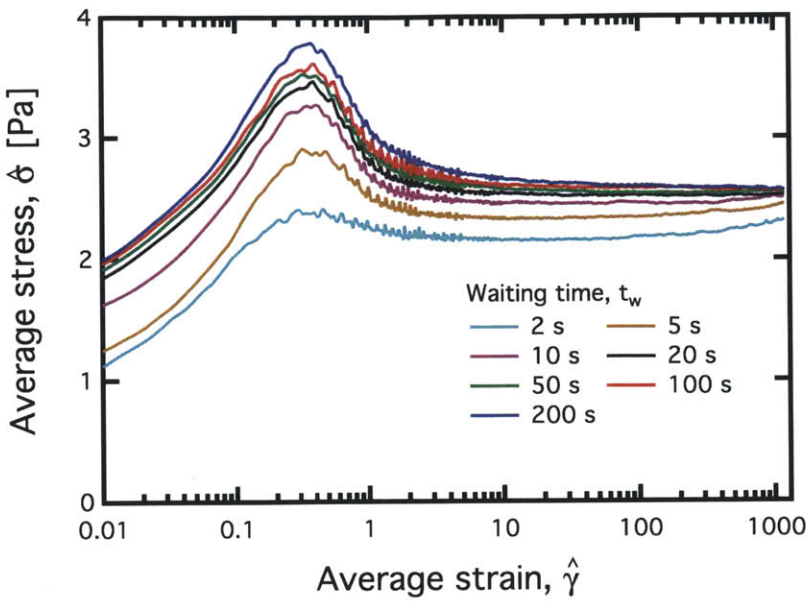

Figure 8-6: Stress overshoots for different waiting times t_w in the 10% model waxy crude oil system. Fluid is prepared to its slurry state at 27° C.

restart a pipeline where flow has ceased for a short period of time. In the work by Fielding et. al.[79], the soft glassy rheology (SGR) model was shown to predict these types of overshoots. In this work, we will take a different approach and use well-established mechanisms from plasticity theory in order to capture and quantitatively predict these stress overshoots. Compared to the SGR model, the model used in this work can be extended to tensorial form, which is more applicable to simulations of complex flow scenarios (e.g. pipe flow). The model used here is written in terms of a set of evolution equations, rather than being in an integral form.

To quantify the magnitude of the yield peak, which will in turn assist in the fitting of the constitutive model, we define our stress overshoot $\Delta\sigma_o$ as the difference between the peak stress during each test and the measured stress 10 seconds after the step in shear rate is imposed. At this level of imposed strain it is clear that short term transients associated with the yield peak have died out. The measured value of $\Delta\sigma_o$ is plotted as function of t_w in Fig. 8-7. In this figure, the saturation of the magnitude of the yield peak is clearly evident, with $\Delta\sigma_o$ approaching an asymptotic value close to 1 Pa.

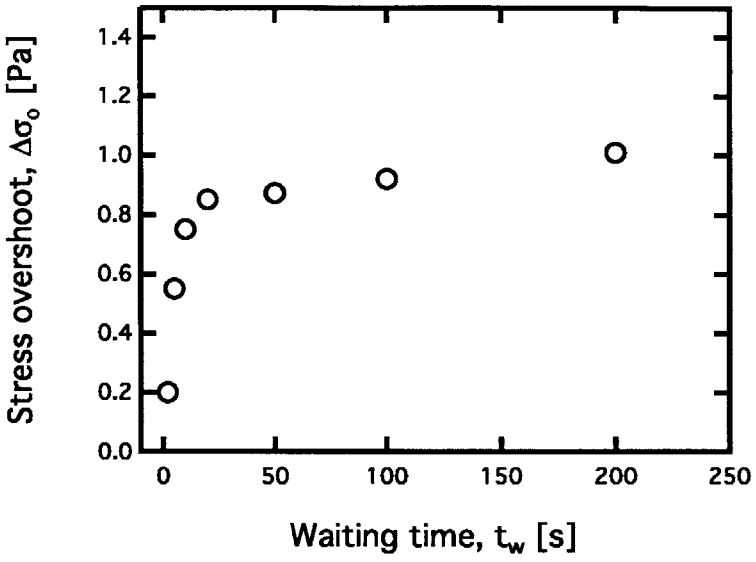

Figure 8-7: Stress overshoot $\Delta\sigma_o$ as a function of t_w extracted from Fig. 8-6.

8.3.3 Large Amplitude Oscillatory shear

The third rheological flow that we use to probe the constitutive response of the material is large amplitude oscillatory shear strain (LAOStrain). We recall that LAOStrain is generally carried out by imposing an oscillatory deformation on the material $\gamma = \gamma_0 \sin \omega t$. In this Chapter we will, strictly speaking, impose an oscillatory *average* strain on the material, $\hat{\gamma} = \gamma_0 \sin \omega t$. Even though we will be suppressing wall slip here, we will utilize the symbols $\hat{\sigma}$, $\hat{\gamma}$ and $\dot{\hat{\gamma}}$ to represent our rheological data. This is to account for the possibility of small fluctuations in the local variables σ, γ and $\dot{\gamma}$. Furthermore, in contrast to Chap. 6, LAOStrain will be utilized here. This is in order to better characterize the material behavior at intermediate strains where the material has just yielded. In EVP materials, LAOStress can cause a sudden increase in strain when σ exceeds σ_y, limiting the range of strains over which tests can be done.

Two independent test parameters can be tuned in these types of flows - the oscillation frequency ω and the strain amplitude γ_0. When the strain amplitude is small enough, the stress in the material $\sigma(t)$ is linear in strain and can be decomposed into in phase and out of phase components as shown in Eq. 2.12. Under these conditions

the storage and loss moduli G' and G'' are both functions of the frequency ω. When the imposed strains are large, most materials exhibit a nonlinear response with a periodic stress that can be expressed in terms of a Fourier series as given in Eq. 2.13. The coefficients $G'_n(\omega, \gamma_0)$ and $G''_n(\omega, \gamma_0)$ are then higher harmonic moduli that will depend on both the frequency of oscillation and the strain amplitude.

In this chapter, we will generally refrain from utilizing any of the defined material measures that exist for LAOStrain. Many such measures exist, however our discussion in Chap. 6 showed that for EVP materials, the description provided by LAOStrain measures may contradict the description provided by the material's constitutive law. For example, our discussions in Sec. 6.3 showed that the LAOStrain "elastic" measure G'_M decreases by several orders of magnitude as the strain amplitude of oscillation is increased for a Carbopol microgel. This suggests that the material exhibits an extreme level of strain softening. However, the KH model prescribes a linear elastic response to the material, and yet is still able to capture the decrease in G'_M. Using the trends of these measures as a basis for forming constitutive laws is misleading.

Another reason for avoiding the use of LAOStrain measures is because they are only defined for periodic stress waveforms. Due to the thixotropic nature of the model crude oil, the stress response to a sinusoidal deformation will in fact contain prolonged transients due to the aging/shear rejuvenation of the fluid which can occur over long timescales. The goal of our model is to predict and quantify these transients, so the LAOStrain measures based on Fourier transform rheology (e.g. those of Ewoldt et al. [71]) will be of no use.

The LAOStrain measurements in this work will therefore be primarily used as a fitting tool in order to guide the development of a model and then to compare the model response to the response of the real fluid. One benefit of using LAOS tests to fit constitutive models is that several key aspects of the rheological behavior of the fluid are exhibited under LAOS. At low values of γ_0, the linear viscoelastic behavior of the fluid is probed. Larger values of γ_0 can then probe the yielding transition exhibited by our model crude oil. It is also possible to observe transients in the LAOS response which result from the inherently thixotropic behavior of these fluids.

Hence, if a constitutive model can predict the response of a material to LAOS, then it can likely predict responses that are time varying and occur over a large range of deformations.

Several researchers have used cyclic stress-strain loading curves, or Lissajous-Bowditch curves, as signatures that are used to fit fluid response to a constitutive model [152, 154]. We represent the response of our model crude oil to LAOS through the use of these Lissajous-Bowditch curves. A series of these curves can be plotted for a number of different strain amplitudes γ_0 and frequencies ω. We carry out a series of LAOS tests on the 10% model crude oil fluid in its slurry state at a temperature of 27°C. These measurements are carried out with the ARES rheometer, with a roughened cone-plate geometry configuration that suppresses wall slip. A series of measurements at progressively larger strain amplitudes γ_0 and at a fixed frequency of $\omega = 1$ rad/s is shown in Fig. 8-8. Between each measurement, a waiting time of $t_w = 100$ s is applied so that the structure associated with the transient yield peaks shown in Fig. 8-6 has enough time to build up. For each measurement at a given strain amplitude, four oscillations are applied.

In Fig. 8-8 (b) we represent the Lissajous curves as 3D trajectories with stress $\hat{\sigma}$ plotted against strain $\hat{\gamma}$, and another orthogonal input variable, the strain rate $\dot{\hat{\gamma}}$. We are primarily interested in the stress-strain projection of these 3D curves, which is shown in Fig. 8-8 (a). The curves in Fig. 8-8 (a) and (b) are only plotted for their stable limit cycle or "alternance state" [83]. This alternance state is reached after multiple cycles of oscillation. In Fig. 8-8 (c), we illustrate the transients which occur before reaching the alternance state by plotting these Lissajous curves on independent (rescaled) axes for each strain amplitude γ_0. In Fig. 8-8 (c), overshoots and prolonged transients are clearly evident in the response of the material.

In Fig. 8-8 (c) we see that at low values of γ_0 the material response is that of a linear viscoelastic solid, with $G' > G''$. This can be distinguished from the elliptical shape of the loading curve, which implies a linear response. As γ_0 is progressively increased, σ_m, which is the maximum stress measured in the fluid (including transients), also increases. However σ_m then saturates at moderate strain amplitudes,

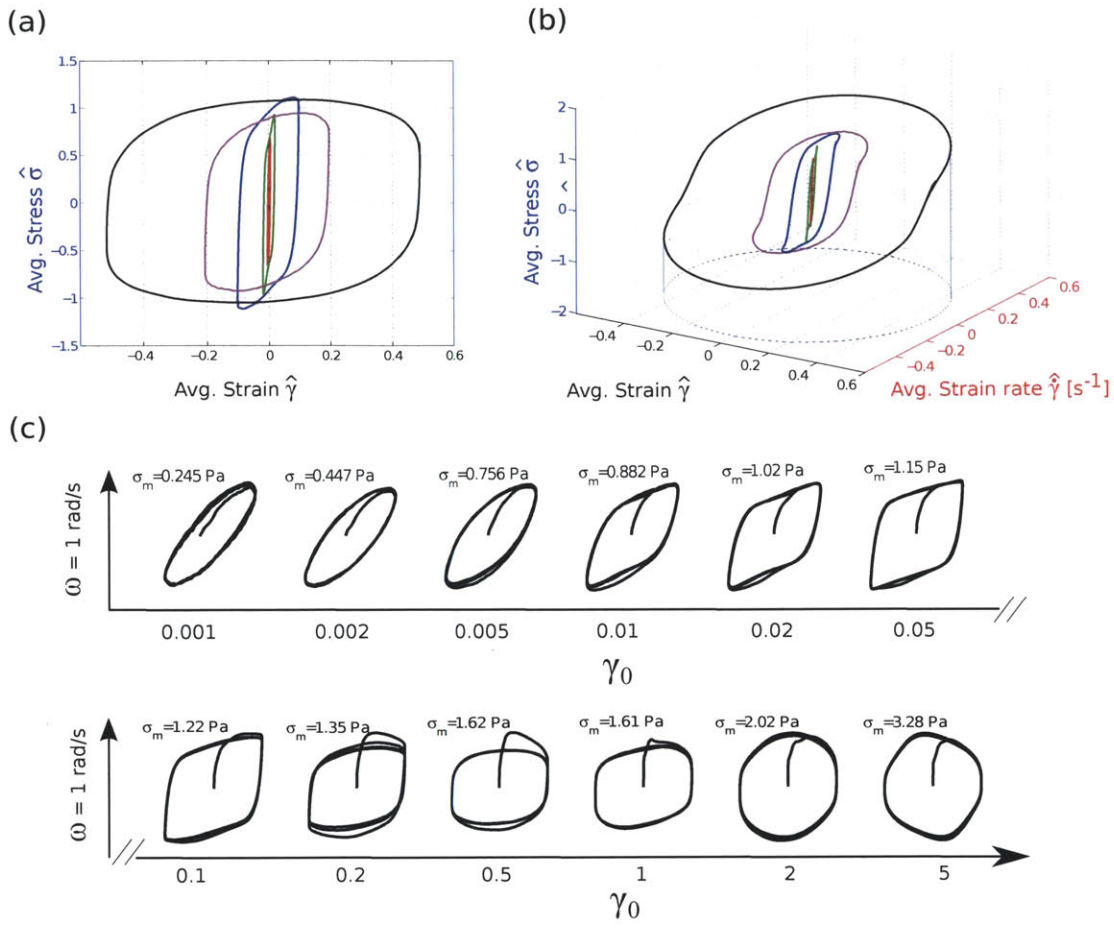

Figure 8-8: LAOS tests on the 10% model crude oil in its slurry state at 27°C. The tests are carried out at a frequency of $\omega = 1$ rad/s, with increasing strain amplitude γ_0. Waiting time between successive tests is $t_w = 100$ s. The full 3D trajectory of the alternance state is shown in (b), with the 2D stress-strain projection in (a). In (c) the transients associated with the startup of oscillations are shown for a large range of γ_0.

a behavior typically associated with a yield-like response. For the moderate strain amplitudes between 5% and 50% the characteristic shape of the cyclic curves also indicates yielding. At these values of γ_0 the material undergoes a sequence of processes which involve elastic loading, followed by saturation of the stress and viscoplastic flow, and then elastic unloading when the direction of straining is reversed. This sequence of events occurs within each cycle (i.e. it occurs on an intra-cycle basis), and is responsible for the transition from elliptical to rhomboidal loading curves [73, 182].

There is also valuable information contained in the material's inter-cycle response,

i.e. in the prolonged transients exhibited, especially for strain amplitudes of $20\% \leq \gamma_0 \leq 100\%$. These transients manifest in the form of an initial stress overshoot which occurs as the material is first strained. This type of stress overshoot is evidence of the same type of transient yield peak that was discussed for the startup of steady experiments in Sec. 8.3.2. It also takes several cycles (on the order of 10 seconds) for the stress to settle into its steady alternance state.

Several key features of Fig. 8-8 can be used to guide the development of the constitutive model (the detailed formulation of which will be given in Sec. 8.4). First, we see no inter-cycle change in the linear viscoelastic behavior between each cycle of loading. This implies that G' and G'' remain constant with time for the material. If both G' and G'' are to be non-constant functions of some structure parameter λ, which in turn depends on t_w, then deformations in the linear regime cannot cause a change in the structure parameter λ. This rules out some of the approaches discussed by Souza Mendes and Thompson [59], who argue for stress being the driving agent for a change in λ as opposed to strain. Both total stress and total strain causing a change in λ would result in G' and G'' exhibiting changes over time as they are probed in a SAOS experiment. However, if we specify a *plastic strain* (see Sec. 2.3.2) as being responsible for changing the structure parameter λ, and this plastic strain only accumulates when the material yields at larger stresses and strains, then we will be able to predict the behavior observed in Fig. 8-8. Thus, a central component of our modeling approach will be to additively decompose strain into plastic and viscoelastic components, with plastic strain only accumulating when the shear stress in the sample is above some critical value. In terms of a mechanical analog representation, this model can be thought of as a viscoelastic element in series with a nonlinear plastic yielding element. The yielding element will then utilize two important concepts from plasticity theory - isotropic hardening and kinematic hardening - in order to capture both the nonlinear intra-cycle behavior of the material, as well as the transient inter-cycle behavior (i.e. the stress overshoot that is associated with thixotropy) that is exhibited under LAOS.

8.4 Constitutive Model

8.4.1 Formulation of the Isotropic-Kinematic hardening (IKH) model

The goal of this section is to develop a constitutive model that quantitatively predicts the salient features of the model crude oil rheology observed under our 3 flows in Sec. 8.3. As discussed in Sec. 8.3.3, a central component of our approach will be to additively decompose the total shear strain in our material into linear viscoelastic (γ^{ve}) and plastic (γ^{p}) components, such that

$$\gamma = \gamma^{ve} + \gamma^{p} \tag{8.9}$$

The purpose of the plastic strain is to only accumulate when the applied stress is above a certain critical value, so for low stresses $\gamma = \gamma^{ve}$ and the response of the material is linear viscoelastic. The linear viscoelastic response at small stresses can be specified in a number of different ways. For example, we can further decompose the viscoelastic strain γ^{ve} into elastic and viscous components, such that $\gamma^{ve} = \gamma^{v} + \gamma^{e}$. This would correspond to specifying a Maxwell-like linear viscoelastic behavior below the yield stress, with $\gamma^{e} = \sigma/G$ and $\dot{\gamma}^{v} = \sigma/\eta$. Alternatively, a Kelvin-Voigt viscoelastic behavior can be specified. There are in fact an infinite number of LVE-type behaviors that can be specified for this constitutive model - we show 3 of them in Fig. 8-9 in the form of mechanical analog elements. The goal of this work is to predict the model crude response to the 3 canonical rheological flows that were discussed in Sec. 8.3. These flows will be predominantly determined by the large strain, nonlinear response of the material - therefore our main focus will be on prescribing the correct behavior to the nonlinear yielding element with strain γ^{p}. As a result, we will not discuss fitting of linear viscoelastic behavior in detail. The reader who is interested in this should feel free to consult any of the classical textbooks on linear viscoelasticity [77, 29] and to replace the linear viscoelastic elements shown in Fig. 8-9 with the element of their choice (and this will not affect the large strain nonlinear behavior).

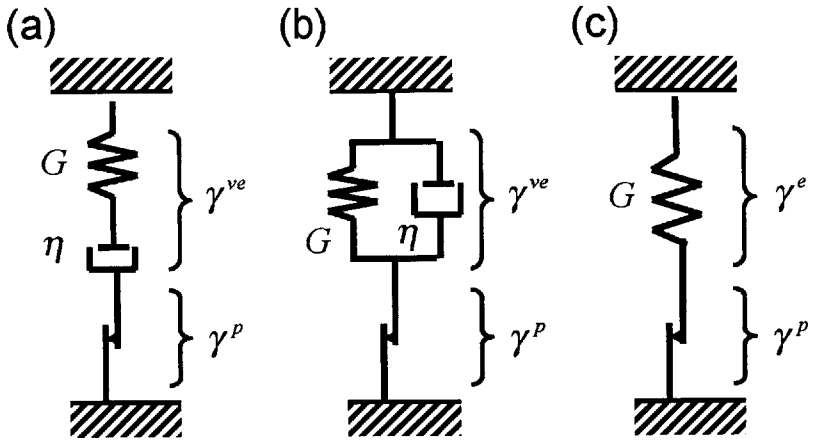

Figure 8-9: Different forms of IKH model. (a) Maxwell IKH model (MIKH) (b) Kelvin IKH model (KIKH) and (c) Elastic IKH model (EIKH)

For most of our cases, we will consider the most canonical form of LVE behavior which is a linear Maxwell-like behavior as shown in Fig. 8-9 (a) with elastic modulus G and viscosity η. We will also make two assumptions about the nature of the linear viscoelastic behavior. First, we observed in Sec. 8.3.3 that under small amplitude oscillatory shear, G' and G'' remain constant in time - i.e. deformations in the linear regime do not affect material structure. We will therefore assume that only the plastic accumulated strain γ^p can drive a restructuring of the fluid. The second, stronger assumption is based on measurements of G' and G'' as a function of t_w. These measurements showed that both G' and G'' are in fact *weak* functions of t_w, with G' only varying by 20% and G'' varying less than that as t_w is changed. We therefore assume that the LVE parameters G and η are constant, and do not depend on material structure. This assumption has been discussed by Quemada [173], and is utilized here to reduce the number of fitting parameters required for this model. However, we will see that the model still quantitatively captures the three flows discussed in Sec. 8.3.

Specifying the plastic strain rate

Having discussed the linear viscoelastic behavior, what now remains is to specify the form of the plastic shear strain γ^p. A first order assumption would be to prescribe

a Bingham-like behavior, where plastic flow only occurs above a critical stress σ_y:

$$\dot{\gamma}^p = \begin{cases} 0 & \text{if } |\sigma| < \sigma_y \\ n^p \left(\frac{|\sigma| - \sigma_y}{k} \right) & \text{if } |\sigma| \geq \sigma_y \end{cases} \tag{8.10}$$

Where $n^p = \sigma/|\sigma|$ is the direction of the applied stress - this is the codirectionality hypothesis, which ensures that plastic deformations always occur in the same direction as the applied stress. The parameter k is a material constant with units of viscosity.

The simple Bingham equation given in Eq. 8.10 may capture some of the most basic features of the flowcurve in Fig. 8-4, however it lacks the ability to predict the correct transient behavior and stress overshoots that were observed in Sec. 8.3. In order to predict these transients, the flow rule in Eq. 8.10 will be modified in order to account for kinematic hardening and isotropic hardening/softening. Kinematic hardening has been already introduced in Chap. 6, and it accounts for a movement of the center of the yield surface, in stress space. Isotropic hardening, on the other hand, accounts for an expansion or contraction of the yield surface, and is frequently used to model the strengthening of polycrystalline metals [120].

These types of hardening mechanisms are commonly used in the plasticity literature, and full 3-dimensional versions of models with combined isotropic and kinematic hardening have been developed [11, 96] that are both frame invariant and thermodynamically consistent. For simplicity we will only develop a 1-dimensional version of the model here. In order to account for these mechanisms, the Bingham equation given in Eq. 8.10 will be modified as follows:

$$\dot{\gamma}^p = \begin{cases} 0 & \text{if } |\sigma_{\text{eff}}| < \sigma_y(\lambda) \\ n^p \left(\frac{|\sigma_{\text{eff}}| - \sigma_y(\lambda)}{k} \right) & \text{if } |\sigma_{\text{eff}}| \geq \sigma_y(\lambda) \end{cases} \tag{8.11}$$

Where the stress σ has been replaced by the effective stress, σ_{eff}, which is defined as follows:

$$\sigma_{\text{eff}} = \sigma - \sigma_{\text{back}} \tag{8.12}$$

Where σ_{back} is the back stress in the material. In addition to the presence of the

back stress in Eqn. 8.11, the yield stress σ_y is also now a function of a structure parameter λ. Furthermore, the direction of plastic strain n^p is now codirectional with the effective stress, so that:

$$n^p = \frac{\sigma_{\text{eff}}}{|\sigma_{\text{eff}}|} \tag{8.13}$$

With the formulation in Eqn. 8.11, the yield surface is now no longer a constant - the center of the yield surface can change through the variation of σ_{back} (kinematic hardening) and the yield surface can contract/expand through the variation of σ_y (isotropic hardening). The variation of two yield parameters (center of yield surface σ_{back} and size of yield surface σ_y) bears some similarity to the Houska model used by Sestak et. al. [188] and Cawkwell and Charles [44], where the yield stress is decomposed into two components. This model is commonly used to predict the rheology of crude oils, however the parallels between the Houska model and isotropic and kinematic hardening mechanisms have not been previously pointed out.

What now remains is to specify how the back stress σ_{back} and the yield stress σ_y vary for a given deformation. We begin with the back stress, and first relate it to an internal variable A which was introduced in Chap. 6

$$\sigma_{\text{back}} = CA \tag{8.14}$$

We see that σ_{back} is linearly related to the internal variable A through the back stress modulus C which has units of stress [10]. We then specify an evolution equation for A which is a more general form of the Armstrong-Frederick equation [13] discussed by Jiang and Kurath [105] that can be used to capture the Bauschinger effect [22].

$$\dot{A} = \dot{\gamma}^p - f(A)|\dot{\gamma}^p| \tag{8.15}$$

When we specify $f(A) = qA$ (with q a dimensionless material constant) then we recover the classical Armstrong-Frederick equation, which is typically used to describe cyclic loading in metals, but was also used to describe the LAOS behavior of Carbopol microgels in Chap. 6. In order to more accurately capture the intra-cycle behavior

under LAOS for this model fluid at a range of strain amplitudes γ_0, we specify a power law function of $f(A)$ which has the following form:

$$f(A) = (q|A|)^{\nu} \text{sign}(A) \tag{8.16}$$

Where both ν and q are material constants. The evolution equation for A in Eq. 8.15 is always evaluated with an initial condition of $A = 0$. If we consider the application of a nonzero plastic strain rate $\dot{\gamma}^p$, then A will initially increase in the direction of γ^p. This results in an increase in the back stress, or a "hardening" of the material in the direction of flow. However, the variable A will eventually saturate due to the second term in Eq. 8.15. The saturation value of A is $\pm 1/q$, with the back stress therefore saturating at $\pm C/q$ (with the sign depending on the direction of the plastic straining $\dot{\gamma}^p$). The value C/q therefore corresponds to the center of the yield surface under steady flowing conditions ($\dot{\gamma}^p \neq 0$) and in the case where σ_y were zero, then C/q would also correspond to the steady state yield stress of the material.

The physical interpretation for the internal variable A is that it is a strain-like variable, which is in turn related to a defect energy that accumulates within the material for nonzero plastic strains γ^p [11, 96] (see Chap 6). The defect energy accumulates because of a rearrangement of the material microstructure, which in our case consists of the interlocking wax crystal network. For 3-dimensional versions of constitutive models that include kinematic hardening, the variable A necessarily takes on a tensorial form, as was seen in Chap. 7 [96].

Next, the variation of the transient yield stress $\sigma_y(\lambda)$ must be specified. We specify a linear relationship between the yield stress σ_y and a dimensionless variable λ

$$\sigma_y = k_3 \lambda \tag{8.17}$$

Where the parameter k_3 is a material constant with units of stress, and λ is an additional evolving internal variable that characterizes the material microstructure.

As is typically done in the thixotropy literature, we can then write a differential equation which determines how λ evolves over time. We use the following frequently

encountered equation [17, 152, 151]

$$\frac{d\lambda}{dt} = k_1 (1 - \lambda) - k_2 \lambda |\dot{\gamma}^p| \tag{8.18}$$

The change in λ is therefore determined by the competition between a build up term (first term in Eq. 8.18) and a breakdown term (second term of Eq. 8.18) of the material structure. The buildup term is assumed to be the result of Brownian motion causing a rearrangement in the wax microstructure, while the breakdown term results from shearing this microstructure. The two new material constants which have been introduced in Eq. 8.18 are k_1 (with units of reciprocal seconds) and k_2 which is dimensionless. The constant k_1 determines the critical waiting time t_w required for a build up of the wax microstructure, while the constant k_2 determines the rate at which the wax microstructure breaks down for a given shear rate. An important distinction of the evolution equation proposed in Eq. 8.18 is that the *plastic* strain rate, and not the total strain rate, is responsible for breaking the material structure. The rationalization for this is that only strains which are considerably large can cause a significant change in the material microstructure. Furthermore, small strains which result in primarily elastic behavior should not perturb the material microstructure, and should not have an effect on the λ parameter (or on the A parameter for that matter). This is an approach that is frequently taken in the plasticity literature [93].

Strictly speaking, Eq. 8.18 allows for both isotropic hardening *and* softening. The isotropic hardening in fact only results from a build up in structure which can occur even under the application of zero shear. This is in contrast to some of the hardening equations that are used in the plasticity literature, where shear can actually cause an increase in the yield stress of the material [11, 10]. For our model crude oil, shear only results in a nonzero softening term (second term in Eq. 8.18) which causes the yield stress to decrease.

In many of the thixotropic models used in the rheology literature, a single variable λ is typically used to characterize the material structure [17]. The model introduced here differs from this approach, and bears more similarities to the approach taken

in plasticity theory [11], due to the introduction of two variables, λ and A. One natural question which then arises is what is the significance of these two variables with respect to the material microstructure, and how do these two variables differ?

Mujumdar et. al. [152] argued that the scalar parameter λ quantifies the ratio of the number of links in a transient network at a particular level of structure, to the number of links in the network when it is fully structured. For our wax microstructure, we can therefore envision λ as being representative of the total number of links per unit volume between the wax particles and aggregates. If we assume that the force required to break such links is always the same, then the yield stress σ_y can be approximated as a linear function of λ. Because the variable λ quantifies a number of links, it will necessarily be a positive scalar parameter, even in a 3-dimensional version of the model. Furthermore, this scalar parameter can only be used to quantify an isotropic resistance to deformations (i.e. a resistance which is the same in all directions of loading).

However, an additional parameter is necessarily required to characterize a non-isotropic resistance, i.e. a strengthening of the material along the direction of deformation. Non-isotropic resistance to deformation is most important when considering oscillatory loading, where the direction of deformation changes (e.g. LAOS), or more complex 3-dimensional deformations. Capturing this non-isotropic resistance is precisely the purpose of the internal variable A and the back stress σ_{back}, which are allowed to take on both negative and positive values for the 1-dimensional case of our model (unlike λ and σ_y which are always positive). Furthermore, a fully 3-dimensional version of this model would generalize A to a tensor valued $\mathbf{A}$, and the back stress σ_{back} to a tensor valued $\mathbf{T}_{\text{back}}$ (which we also call $\mathbf{M}^e_{\text{back}}$ in Chap. 7). Thus, in contrast to the scalar valued λ which only counts the links between wax particles, this tensor valued variable $\mathbf{A}$ additionally characterizes the orientation of the wax microstructure. This aspect of the microstructure will likely be affected by the orientation of the wax sheets observed in Fig. 8-3 (a property which cannot be described by a simple scalar), which will in turn play a role in determining how these particles resist deformation along a certain direction. We therefore argue that the inclusion of both of

these internal variables forms a more complete picture of the material microstructure.

Summary of the IKH model equations and fitting parameters

We end this subsection by summarizing the constitutive model in a concise form, as well as providing a list of the material constants required for fitting. We first have the decomposition of shear strain into linear viscoelastic strain and nonlinear plastic strain

$$\gamma = \gamma^{ve} + \gamma^{p} \tag{8.19}$$

The linear viscoelastic strain can be specified through the introduction of an appropriate LVE constitutive element (Maxwell, Kelvin-Voigt, or simple elastic as shown in Fig. 8-9), while the rate of change of the plastic strain is given by the following:

$$\dot{\gamma}^{p} = \begin{cases} 0 & \text{if } |\sigma - CA| < k_3\lambda \\ \frac{\sigma - CA}{|\sigma - CA|}\left(\frac{|\sigma - CA| - k_3\lambda}{k}\right) & \text{if } |\sigma - CA| \geq k_3\lambda \end{cases} \tag{8.20}$$

Where A and λ are internal variables that vary through the following differential equations:

$$\dot{A} = \dot{\gamma}^{p} - (q|A|)^{\nu}\,\mathrm{sign}(A)|\dot{\gamma}^{p}| \tag{8.21}$$

$$\dot{\lambda} = k_1(1-\lambda) - k_2\lambda|\dot{\gamma}^{p}| \tag{8.22}$$

With the Maxwell model specified as the LVE behavior shown in Fig. 8-9 (a), this model has 9 fitting parameters, which are: G, η, k, k_1, k_2, k_3, C, q, ν. This is only one additional parameter compared to the Houska model, which is commonly used to describe the rheology of crude oils [43].

For the reader interested in more general tensorial forms of this model, the additive strain decomposition for the case of the EIKH model shown in Fig. 8-9 (c) can, in a similar manner as was done in Chap. 7, be generalized to a multiplicative Kroner

decomposition [114] of the deformation gradient $\mathbf{F}$ such that

$$\mathbf{F} = \mathbf{F}^e \mathbf{F}^p \tag{8.23}$$

Where $\mathbf{F}^e$ is the elastic part of the deformation gradient, and $\mathbf{F}^p$ is the plastic part of the deformation gradient. Anand et. al. [11], Henann and Anand [96] and Ames et. al. [10] all give examples of frame invariant forms of constitutive models with both isotropic and kinematic hardening (although their evolution equations for the internal variables differ).

8.4.2 Quantitative predictions

We will now see what aspects of the crude oil rheology the IKH model can predict. We will use the data for the three canonical flows given in Sec. 8.3 for the 10% model waxy crude system in its slurry state at a temperature of 27°C. We first consider the steady state flow curve given in Fig. 8-4. Under steady flowing conditions, our IKH model reduces to the special case where $\dot{\lambda} = 0$ and $\dot{A} = 0$. The relationship between the magnitude of our plastic flow rate $|\dot{\gamma}^p|$ and the magnitude of our stress $|\sigma|$ in Eq. 8.11 becomes the following

$$|\sigma| = k|\dot{\gamma}^p| + \frac{C}{q} + \frac{k_3 k_1}{k_1 + k_2|\dot{\gamma}^p|} \tag{8.24}$$

In the case where we choose the KIKH or EIKH variants of the model, then under steady flowing conditions $\dot{\gamma}^p$ is the only contribution towards the strain rate. Eqn 8.24 therefore gives a functional form of the IKH model which can be fitted to steady state flowcurves such as that in Fig. 8-4. In Fig. 8-10 we show such a fit, and see that the model correctly predicts the important features of the flowcurve. It predicts a Newtonian limit at high shear rates, as well as a decreasing region of the flowcurve which appears at the intermediate shear rates. As the shear rate is taken to zero, the EIKH and KIKH variants predict a constant stress $|\sigma| = C/q + k_3$. The MIKH variant however will predict a high viscosity Newtonian region at lower shear rates

with $\sigma \simeq \eta\dot{\gamma}$ (which the material does not appear to exhibit). These types of high viscosity, Newtonian regions at the low shear rate often appear for thixotropic yield stress fluids, but they are difficult to measure precisely. However, tuning the LVE element in the IKH model allows for flexibility in the model in capturing this type of behavior.

The particular values of the fitting coefficients used in Fig. 8-10 are $C/q = 0.85$ Pa, $k = 0.42$ Pa.s, k_3=1.5 Pa, $k_1/k_2 = 0.033$ s^{-1} and $\eta = 500$ Pa.s. The fitting to the steady state flowcurve only depends on the ratios k_1/k_2 and C/q, and not the actual values of each of these material constants. It also does not depend on G or ν (or η in the case of the EIKH and KIKH variants). It is therefore necessary to fit the model to additional data in order to determine the values of these parameters.

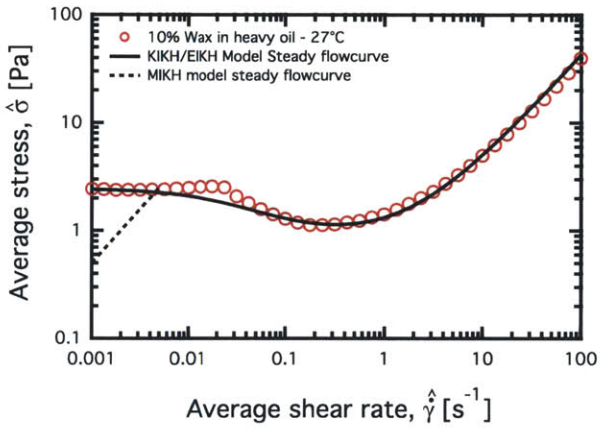

Figure 8-10: Fitting of the IKH model to the flowcurve of Fig. 8-4. Fitting constants are $C/q = 0.85$ Pa, $k = 0.42$ Pa.s, k_3=1.5 Pa, $k_1/k_2 = 0.033$ s^{-1} and $\eta = 500$ Pa.s

Although the simple equation given in 8.24 predicts a non-monotonic dependency of stress σ on shear rate $\dot{\gamma}$, it does so assuming the case of homogenous shear, i.e. a spatially and temporally uniform shear rate within the material. In Sec. 8.3.1 we experimentally indicated that for moderate shear rates (i.e. rates where we observe a decrease in $\hat{\sigma}$ as $\hat{\dot{\gamma}}$ is increased) we may have unstable flow occurring within the material and the shear rate may not be homogenous. Therefore, Eqn. 8.24 should only be assessed as a first order approximation of what the local stress is within the material as a function of the globally applied shear rate. A more realistic prediction

for the stress in Fig. 8-10 would account for these heterogeneities in the flow. One possible way to do this would be by simulating startup of steady shear flow with λ initially being spatially heterogenous across a parallel plate gap, i.e. the material begins with a structure that is not uniform. This is a reasonable assumption, given previous observations that have shown thixotropic yield stress fluids exhibiting an "erosion" behavior that is oft times spatially heterogenous [86]. We will not deeply explore such scenarios in the current work - however in Sec. 8.4.3 we will provide a brief discussion on possible avenues for predicting this complex flow behavior.

We now assess whether the stress overshoots that were measured in Sec. 8.3.2 can be quantitatively predicted by the IKH model using the same values of the fitting parameters used in Fig. 8-10. We also specify values of $G = 250$ Pa, $k_1 = 0.1$ s^{-1}, $C = 70$ Pa and $\nu = 0.25$ (and use the Maxwell variant of the model illustrated in Fig. 8-9)

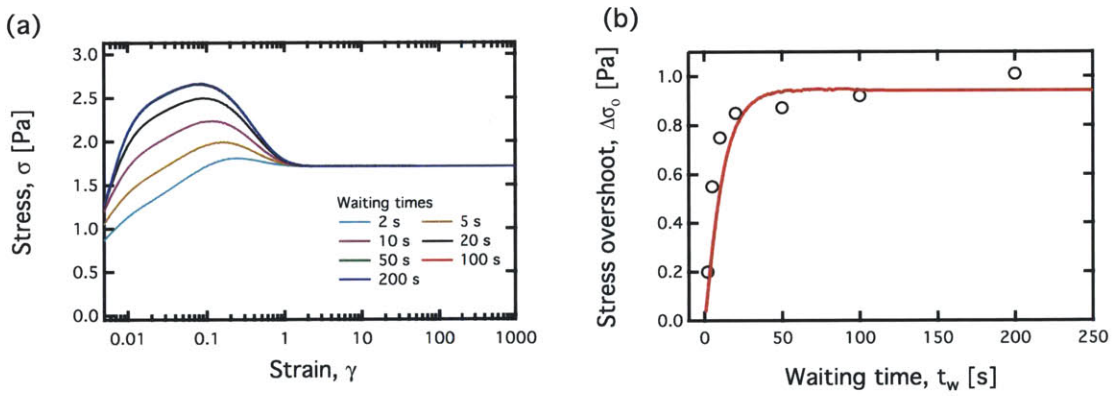

Figure 8-11: Prediction of stress overshoots under startup of steady shear for the IKH model in (a). Shear rate is $\dot{\hat{\gamma}} = 2$ s^{-1}. In (b), we show the predicted stress overshoot (red line) from the IKH model simulated in (a) (fitting parameters are the same for (a) and (b).) The particular model parameters are: $C/q = 0.85$ Pa, $k = 0.42$ Pa.s, k_3=1.5 Pa, $k_1/k_2 = 0.033$ s^{-1}, $G = 250$ Pa, $\eta = 500$ Pa.s, $k_1 = 0.1$ s^{-1}, $C = 70$ Pa, $\nu = 0.25$.

Fig. 8-10 (a) shows that the IKH model does capture several of the qualitative features of the response of the 10% wax oil system to startup of steady shear. Stress overshoots are predicted, and these increase as a function of waiting time t_w due to the fact that λ can increase during the waiting time. We also see that the value of the

stress overshoot saturates beyond waiting times of $t_w \simeq 20$ s. This is in accordance with what is observed within the material.

Fig. 8-10 (b) gives a quantitative comparison between the predicted value of the stress overshoot $\Delta\sigma_o$ with its measured value. The IKH model is able to predict the overshoot saturating at approximately 1 Pa, and it predicts the critical waiting time required for this overshoot to saturate. This critical waiting time is set by the quantity $1/k_1$, which has units of seconds, and essentially sets the timescale required for a buildup in the λ parameter to take place.

The only aspects of the material response that the IKH model does not predict in Fig. 8-11 is the absolute value of the maximum stress that the material experiences, as well as the long term increase in the steady measured stress $\hat{\sigma}(t)$. As we mentioned previously, this long term increase in $\hat{\sigma}(t)$ can be attributed to the presence of longer time scales for restructuring. These would likely be due to the distribution of characteristic length scales in the microstructure. One way the IKH model could be modified to predict this behavior would be by introducing a third internal variable, and making k a function of this variable (this dependency is adopted for some isotropic hardening models [96]). An evolution equation for this third variable that is similar to Eq. 8.18 could be specified, however the associated parameters determining time scales (e.g. k_1) would have to be modified in order to reflect this slow restructuring. Coincidentally, this would also improve the prediction of the value of the maximum stress experienced by the material. For the sake of simplicity however, we choose to focus on predicting the relative stress overshoot $\Delta\sigma_o$, and therefore avoid introducing a third internal variable. The introduction of a third internal variable would also require a subtle distinction in the microstructural interpretation for the λ variable used here. One way to justify this would be to consider rearrangement of the individual wax crystals vs. rearrangement of flocs of crystals. Due to difference in size, one may rearrange slower than the other, and these may have different impacts on the fluid rheology (e.g. one may impact long term steady state viscosity while the other will affect initial yielding transients).

Next we assess the predictive capabilities of the IKH model with respect to the

LAOS response of the model crude oil illustrated in Fig. 8-8. For the LAOS response, we use the same values of the coefficients used for the fits in Figs. 8-11 and 8-10, however we modify the value of k_3 and C/q slightly. Specifically, we set $k_3 = 0.7$ Pa and $C/q = 0.7$ Pa (while keeping C constant at 70 Pa). In Fig. 8-12 (a), we show a fit of the MIKH variant to the LAOS response of the 10% wax oil system in its slurry state at 27° C. The simulated LAOS response of the IKH model always uses the initial conditions of $A = 0$ and $\lambda = 1$. For visual clarity Fig. 8-12 only illustrates the limit cycle, or alternance state of these LAOS tests.

Good agreement is generally seen between the data and the IKH model for the limit cycles observed under LAOS. Both material and model exhibit a transition from linear viscoelastic behavior to nonlinear behavior at strain amplitudes of approximately $\gamma_0 = 0.2\%$. This very small linear range of strains means that at moderate strain amplitudes (say $\gamma_0 = 20\%$), the IKH response is dominated by the behavior of the nonlinear yielding element with strain γ^p.

In Fig. 8-12 (b) we compare the values of the maximum stress σ_m for the experimental data and the IKH model. The maximum stress σ_m is defined as the maximum stress over all cycles of oscillation, so it includes the initial transients (overshoots) that are not shown in the alternance plots of Fig. 8-12 (a). Fig. 8-12 (b) also includes the predicted values of σ_m for a Maxwell LVE model (with $\eta = 500$ Pa.s and $G = 250$ Pa), and a Bingham model (with $k = 0.42$ Pa.s and $\sigma_y = 1.4$ Pa). The MIKH model reduces to the LVE model for small strains, and a Bingham model for large strains, while also having the ability to predict the behavior at intermediate strains.

The IKH model is able to predict the transients that the material undergoes for these LAOS tests. Before each test is carried out at a given amplitude γ_0, a waiting time $t_w = 100$ s is applied, resulting in the material being structured before the oscillatory deformation is imposed. For this reason, the IKH simulation begins with the initial condition $\lambda = 1$, and over the course of several oscillations λ will decrease resulting in a decrease in the size of the Lissajous orbits. Fig. 8-13 shows two representative transient Lissajous curves of the material undergoing an initial 3 cycles of deformation at two different amplitudes, $\gamma_0 = 0.1\%$ and $\gamma_0 = 20\%$.

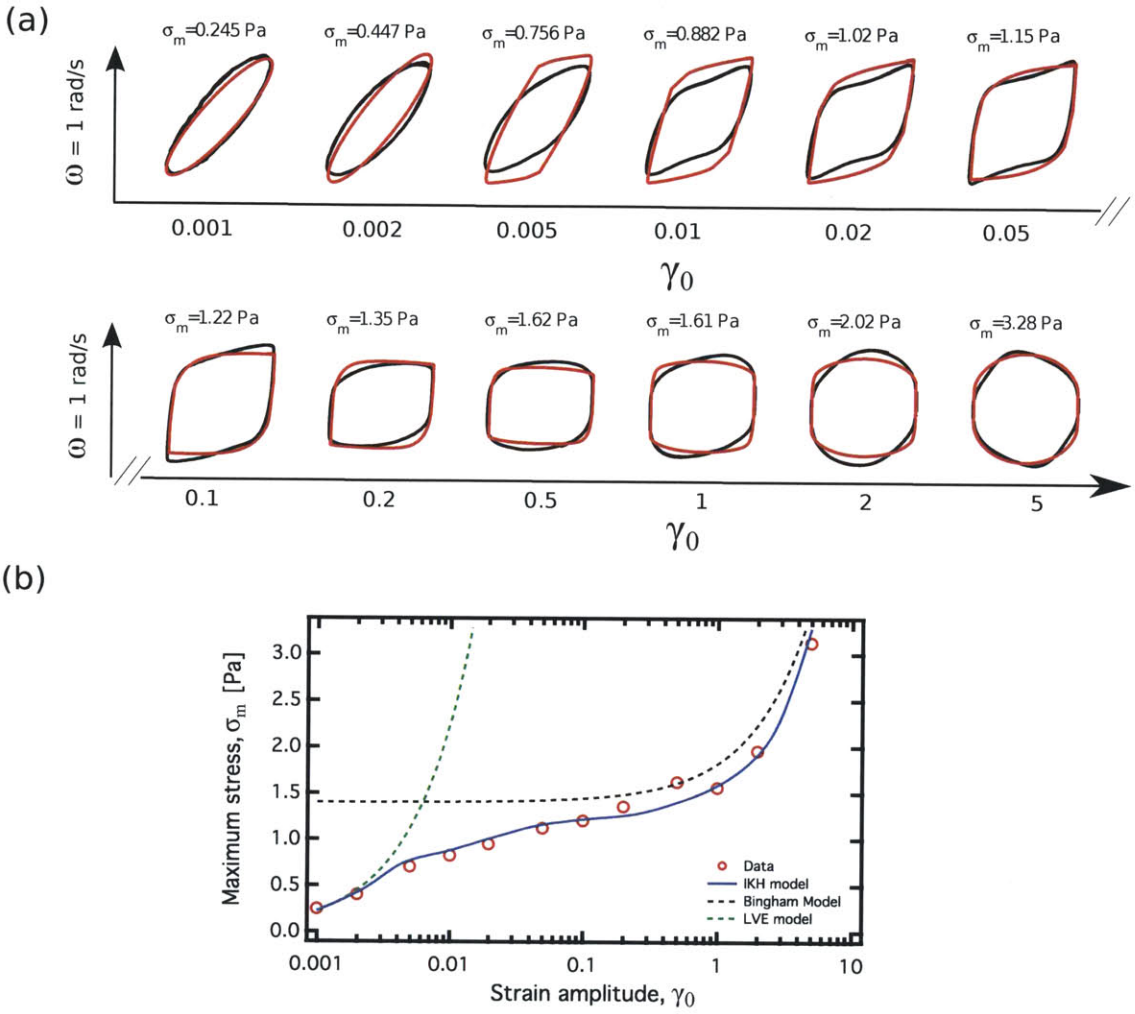

Figure 8-12: Fitting of the alternance state in (a) of LAOS tests shown in Fig. 8-8. Fitting parameters are $C/q = 0.7$ Pa, $k = 0.42$ Pa.s, k_3=0.7 Pa, $k_1/k_2 = 0.033$ s^{-1}, $G = 250$ Pa, $\eta = 500$ Pa.s, $k_1 = 0.1$ s^{-1}, $C = 70$ Pa, $\nu = 0.25$. Red line is IKH model, black line is 10% model crude oil data. In (b) the prediction of σ_m of the IKH model compared to the experimentally measured values of σ_m. The predictions of a Maxwell LVE model and a Bingham model are also shown.

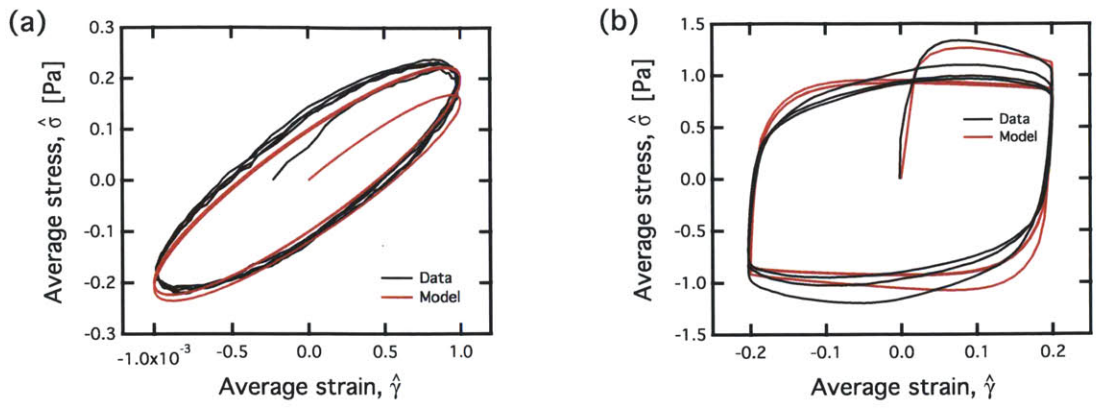

Figure 8-13: Transient LAOS data for the IKH model and the 10% model crude oil at two strain amplitudes, $\gamma_0 = 0.1\%$ (a) and $\gamma_0 = 20\%$ (b). The same fitting coefficients as in Fig. 8-12 are used.

For the small amplitude case in Fig. 8-13 (a), the material requires approximately one half of a cycle of oscillation before the behavior settles into a steady state. Furthermore, no overshoots are observed in the stress when the deformation first begins. This type of behavior is consistent with a standard linear viscoelastic response, where no thixotropy is present. Our model predicts this type of behavior - and this in turn justifies the approach of using γ^p in the evolution equation of 8.18. This approach only allows thixotropic effects to become apparent at larger strain amplitudes when γ^p is no longer zero. We do begin to see these thixotropic effects at the higher strain amplitude in Fig. 8-13 (b), where both a stress overshoot is observed, and multiple cycles of oscillation are required for the material to settle into an alternance state. The IKH model quantitatively predicts the magnitude of this overshoot, and qualitatively predicts the shrinking of the Lissajous orbits over multiple cycles.

The LAOS tests in Fig. 8-12 illustrate the dependency of the material response on the strain amplitude γ_0, however we are also free to tune the frequency of imposed oscillations ω when carrying out these tests. At small strain amplitudes (e.g. $\gamma_0 = 0.1\%$), the variation of ω typically allows for the linear viscoelastic behavior of the material to be probed. However, we will vary frequency at a moderate strain amplitude ($\gamma_0 = 2\%$) in order to illustrate one important aspect of the material's response in the nonlinear regime of deformations.

Fig. 8-14 (a) shows the cyclic Lissajous curves of the first 3 cycles of oscillation for the material undergoing LAOS at 4 frequencies spanning an order of magnitude ($\omega =$ 0.5 rad/s to $\omega = 5$ rad/s). At this moderate strain amplitude, the material response is clearly nonlinear, with some transient behavior occurring over multiple cycles. However, very little dependency of the response is seen on ω. This is indicative of a deformation rate-independent response at moderate strain amplitudes. The predicted model response shown in Fig. 8-14 (b) is able to capture this type of behavior. The reason for this is due to the rate-independent nature of the kinematic hardening behavior prescribed in Eq. 8.15. This equation can be rewritten in terms of increments in A and γ^p as follows:

$$dA = d\gamma^p - f(A)|d\gamma^p| \tag{8.25}$$

The internal parameter A therefore evolves independently of the rate of plastic strain $\dot{\gamma}^p$. For the strain amplitude shown in Fig. 8-14, γ^p becomes much larger than γ^{ve}, and so A evolves in a manner which is mostly independent of the total strain rate $\dot{\gamma}$. The other internal variable, λ, does evolve in a rate-dependent fashion - at the highest frequency, the Lissajous orbits shrink faster due to the accelerated decrease in λ. However, the overall response of the material at this range of frequencies is characterized by rate-independent kinematic hardening - a behavior which is most appropriately described by equations of the Armstrong-Frederick type [13] used in Eq. 8.25.

The IKH model predicts several important features of the material response to the 3 canonical rheological flows outlined in Sec. 8.3. To end this subsection, we will discuss one additional flow, and compare it to the predicted response of the IKH model.

In Fig. 8-4, the particular experimental protocol that was used to measure the flowcurve of the material controlled the applied global (or spatially averaged) deformation rate $\hat{\dot{\gamma}}$ on the material. An alternative way to control the flow in the material would be to ramp the applied average stress $\hat{\sigma}$ on the material at a very slow rate, and measure the corresponding average shear rate at incremental points in time. This

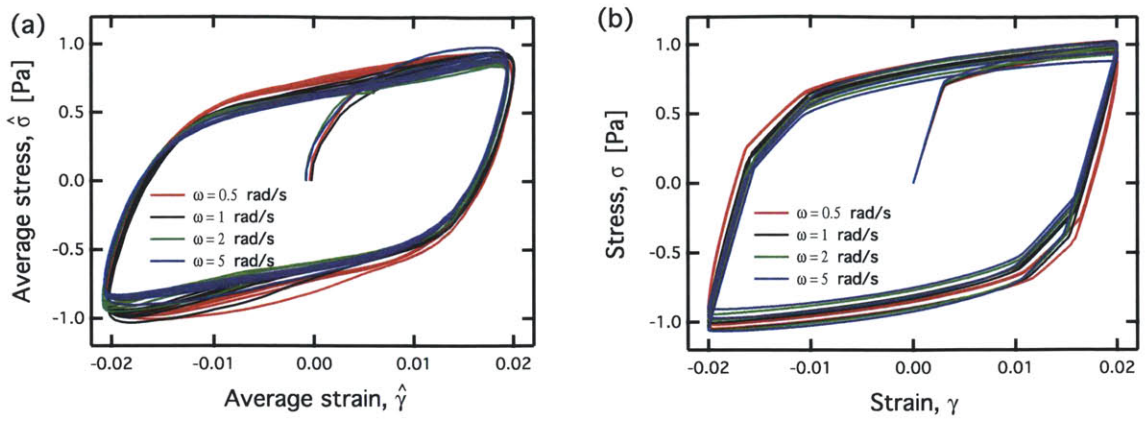

Figure 8-14: Frequency-dependent behavior under LAOS at moderate strain amplitudes ($\gamma_0 = 2\%$) for both the 10% model crude oil (a) and the IKH model (b). The IKH model fitting coefficients are the same as in Figs. 8-12 and 8-13.

"stress ramp" test was carried out on the 10% wax-oil system in its slurry state at 27°C using the ARG2 in its standard configuration. The material is initially brought to its fully structured state by applying a wait time of $t_w = 300s$, and then a stress ramp from 0.1 Pa to 5 Pa is imposed over the course of 2 hours (this results in a constant value of $d\hat{\sigma}/dt = 0.00136$ Pa). Once the stress reaches the maximum value of 5 Pa, the ramp is immediately reversed and brought down to 0.1 Pa at a rate of $d\hat{\sigma}/dt = -0.00136$ Pa. The shear rate within the fluid is sampled at regular intervals over the course of the increasing and decreasing ramps in stress.

In Fig. 8-15, we show the results of this stress ramp, as well as the predicted response of the IKH model to such a stress ramp using the same fitting parameters that were used in Fig. 8-11 and 8-10. For comparison with the applied shear rate measurements, the flowcurve obtained in Fig. 8-4 is also included on this figure. A good agreement is seen between model and data. The IKH model predicts the hysteresis that occurs in the stress ramp experiments. Specifically, a larger stress (asymptotic value of $\sigma = 2.08$ Pa) is required to start the flow from the structured state, and as the stress is decreased, the same shear rates can be sustained at lower values of the applied stress (which approaches an asymptotic value of $\sigma = 1.11$ Pa). This essentially corresponds to different measurements for the static and dynamic yield stress within the material [48], and the nonzero λ parameter in the structured

state is responsible for this difference. Note that while σ approaches the limit of $C/q + k_3$ for the rate-controlled experiment, the asymptotic values of σ determined from the stress ramp experiments are both different from this value. The difference between the static and dynamic yield stress is what is responsible for the "avalanche effect" that is frequently observed in thixotropic yield stress fluids [52].

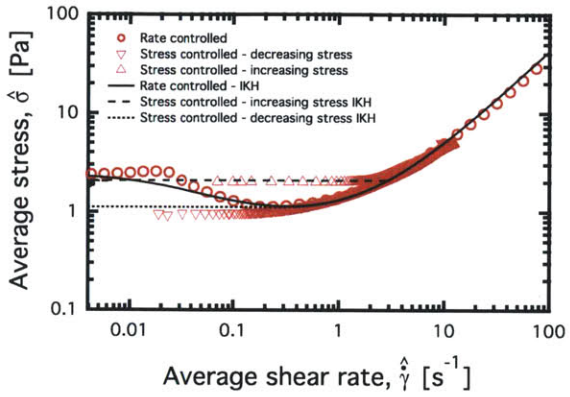

Figure 8-15: Flowcurves of the model crude oil (red data points) and the IKH model (solid and dashed lines) obtained under controlled rate experiments and stress ramp experiments. The data is for the same model system at the same temperature shown in Figs. 8-10–8-14, with the same fitting coefficients as in Fig. 8-10 and 8-11.

We have thus seen that the IKH model is considerably versatile from the perspective of capturing the model crude oil response. It has captured the salient features of the response exhibited by the fluid to a number of different rheological flows. The fitting parameters used were consistent among these flows, so Fig. 8-15 constitutes a true test of the predictive nature of the model.

8.4.3 Further Discussion

To conclude our discussion of the IKH model, we will expand on a few important points related to the limitations of the current version of the model. We will also comment on how this model is related to other constitutive models that are commonly encountered in the literature.

Fitting procedure and Model limitations

We outline a general fitting procedure used to determine values of the model parameters. This procedure is as follows: First fit the parameters k, k_3 and the ratios C/q and k_1/k_2 are determined from the steady state flowcurve in Fig. 8-4. Next SAOS tests can be used to fit the linear viscoelastic behavior (and if this is Maxwell-like, then G and η can be determined). Then, LAOS can be used to determined appropriate values of C, q, ν, k_1 and k_2. Finally, stress overshoot measurements can be used to verify that $1/k_1$ agrees with the critical waiting time required for the saturation of the yield peak. Note, however, that the fitting of the parameters to the steady state flowcurve of Fig. 8-4 may proceed differently for different materials. Specifically, the flow instability that was observed in Sec. 8.3.1 may differ for other materials. For example, a standard shear banding scenario may be observed where the non-monotonic region of the flowcurve is inaccessible. Under such circumstances, the values of k_3, C/q and k_1/k_2 would have to be determined with another method.

The caveat of this fitting procedure points towards an important limitation of how the IKH model was used to predict the steady state flowcurve of the material: Steady state flowcurves of the IKH model were plotted for the case of homogenous shear, so $\hat{\sigma} = \sigma$ and $\hat{\dot{\gamma}} = \dot{\gamma}$. However, at the lowest globally applied shear rates, the flow does not appear to be homogenous. One way to account for this would be to initially specify a heterogenous value of $\lambda(y, t = 0)$, and then allow for the material to evolve under application of a constant global shear rate. The IKH model would predict transient shear banding under such a scenario - regions with initially high values of λ will not deform, but regions with low values of λ will exhibit high shear rates. This shear banding would be extremely sensitive to initial spatial variations of $\lambda(y)$, and would therefore be an interesting topic of future study.

The IKH model can also predict shear banding arising due to spatial variations in the stress field. This type of shear banding can be illustrated by simulating flow of the IKH model in a geometry which has large spatial variations in the stress. For example, the shear stress in a concentric cylinder Taylor-Couette cell will scale

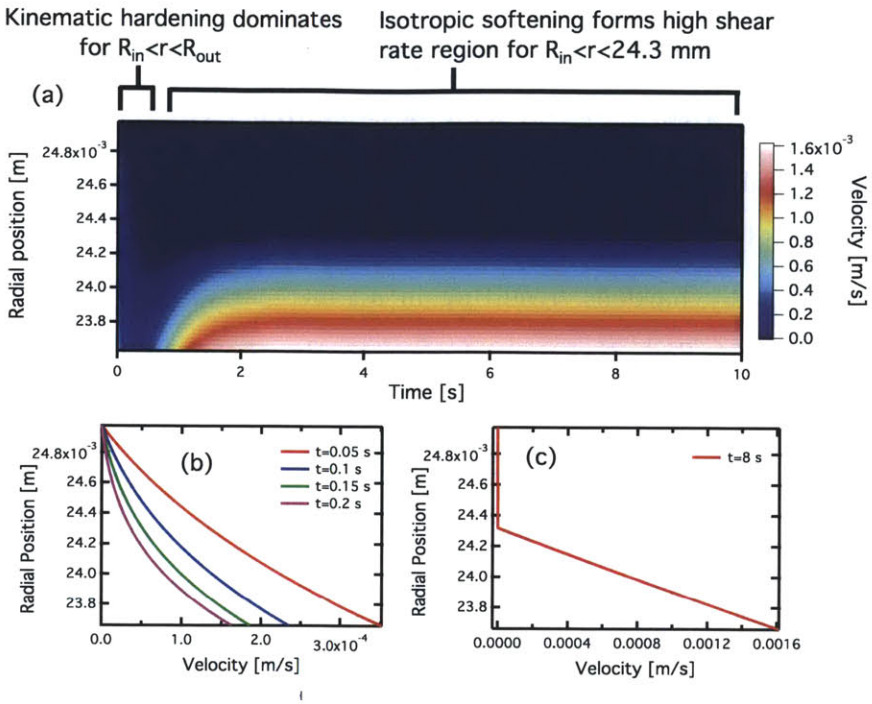

Figure 8-16: Shear banding predicted by the IKH model in a Taylor-Couette concentric cylinder geometry. A steady imposed torque $\mathcal{T}$ is applied, resulting in a steady imposed, heterogenous stress in the material. The material is allowed to evolve from its initial configuration of being fully structured, i.e. $\lambda = 0$. In (a), a space-time profile of the velocity field is shown. In (b) and (c) several velocity profiles are given for different points in time.

as $\sigma \sim \frac{1}{r^2}$, where r is the radial coordinate. The stress will therefore be larger at the inner wall of the geometry where $r = R_{in}$, rather than at the outer wall where $r = R_{out}$. To illustrate this type of banding, we simulate in Fig. 8-16 startup of flow for the IKH model in a Taylor-Couette cell under a steady applied torque $\mathcal{T}$. For the simulations in Fig. 8-16, the inner radius of the cell is $R_{in} = 23.7$ mm and the outer radius is $R_{out} = 25$ mm. The torque is set so as to impose a stress which varies (in a $1/r^2$ fashion) from $\sigma = 1.95$ Pa to $\sigma = 1.75$ Pa. The simulated data in Fig. 8-16 is evaluated for the IKH model with initial spatially uniform values of $\lambda = 1$ and $A = 0$. The fitting coefficients used were $G = 250$ Pa, $\eta = 500$ Pa.s, $k = 0.42$ Pa.s, $k_1 = 0.1$ s^{-1}, $k_2 = 3$, $k_3 = 1.5$ Pa, $C = 70$ Pa, $q = 87.5$ (these are consistent with the fitting values for the real model waxy crude oil).

The data in Fig. 8-16 is shown in the form of a space-time diagram in (a), where

color scale represents the tangential velocity component v_θ, and in the form of velocity profiles plotted for different times in (b) and (c). At time $t = 0$, the step in the torque is imposed and the material starts from its fully structured state with $\lambda = 1$. It initially exhibits a nonzero shear rate across the gap, which decreases over the first 0.5 seconds of the experiment. During this initial deformation stage, the material kinematically hardens, resulting in an increase in A and a strengthening of the material in the flow direction. Consequently, the shear rate across the gap decreases during this time period.

However, beyond the 0.5 second mark, there is an onset of shear banded behavior in the fluid. For the region of the fluid located closest to the wall, i.e. for values of $r < 24.3$ mm, the isotropic softening process (accounted for by the term $-k_2|\dot{\gamma}^p|\lambda$ in Eq. 8.18) begins to dominate over the kinematic hardening process. As a result the value of λ will start to decrease in this region of the fluid, and a high shear rate band forms in the material closest to the inner wall. The material closer to the outer wall exhibits a negligible shear rate at long times. These types of steady shear banded profiles (with one sheared band and one stationary, unsheared band) have been observed in numerous thixotropic yield stress fluids. We therefore see that the IKH model is capable of predicting shear banding due to the presence of spatial variations in the stress.

The IKH model can be improved even further by incorporating nonlocal effects into the constitutive law [89]. These nonlocal effects are typically introduced in the form of a diffusion-like term (i.e. second spatial derivative) in the constitutive equations. In the rheology literature, one example of this would be the introduction of a diffusive term into the Johnson Segalman model [106] in order to account for shear banding behavior [158]. Bocquet et. al. also introduced nonlocal behavior in a constitutive law for soft glassy materials [31]. From the plasticity literature, a potential way to account for nonlocal effects would be to introduce a gradient based theory of plasticity such as that discussed by Aifantis [6, 201].

The other limitation of the IKH model in its current form (which has already been mentioned previously) is the use of the single timescale k_1 for describing the

buildup in the structure of the material. Experimental evidence points towards a slow restructuring of the fluid which results in an increase in the plastic viscosity term k over time. This has been neglected in our model, and k has been set to a constant. However future workers may choose to implement such a dependency in a modified version of the IKH model. This will likely require the introduction of additional fitting parameters, however it can still be interpreted as an isotropic hardening mechanism [96]. To illustrate how this would be done, we carry out a set of numerical simulations of startup of steady shear for an IKH model, but with an additional dependency of k (the plastic viscosity coefficient) on a third internal variable, which we will denote as $\hat{\lambda}$. This third internal variable evolves according to the following differential equation:

$$\dot{\hat{\lambda}} = \hat{k}_1(1 - \hat{\lambda}) - \hat{k}_2|\dot{\gamma}^p|\hat{\lambda} \tag{8.26}$$

with the plastic viscosity then being given by $k = k_0 + \hat{k}_3\hat{\lambda}$ (a linear dependency). The evolution equation in Eq. 8.26 is identical to that of Eq. 8.18, but with new coefficients $\hat{k}_1$, $\hat{k}_2$, $\hat{k}_3$ and k_0 having been introduced to determine how k will evolve in time. This evolution can easily be implemented into the flow rule of Eq. 8.11, while keeping the kinematic and isotropic hardening behavior that has been discussed thus far.

The timescale for restructuring of the k parameter will now be determined by the values of $\hat{k}_1$ and $\hat{k}_2$, which will not necessarily be equal to k_1 and k_2 respectively. Significantly smaller values of $\hat{k}_1$ were required in order to predict the long term increase in stress that is observed in Fig. 8-6, indicating that the k parameter increases much more slowly than σ_y. In Fig. 8-17, we show that by introducing this new dependency of k on $\hat{\lambda}$, all of the essential features of Fig. 8-6 are reproduced (including the magnitude of the stress maximum, and a long term increase in stress). For the simulation in Fig. 8-17, all of the IKH fitting coefficients are the same as those used in Fig. 8-6, while the new coefficients are set as follows: $\hat{k}_1 = 5 \times 10^{-4}$ s^{-1}, $\hat{k}_2 = 5 \times 10^{-4}$, $\hat{k}_3 = 0.7$ Pa.s and $k_0 = 0.62$ Pa.s.

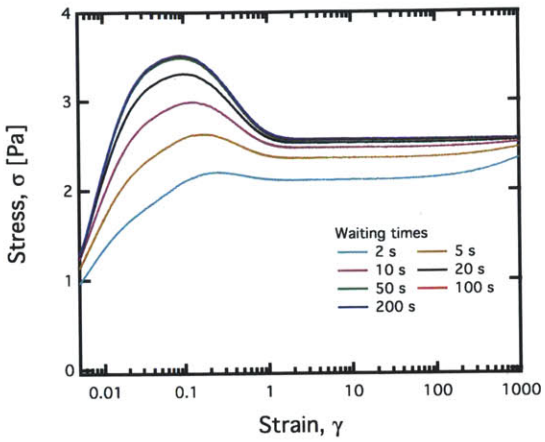

Figure 8-17: Simulation of startup of steady shear for different waiting times for the IKH model with an additional dependency of k on a new paramter $\hat{\lambda}$, as given in Eq. 8.26.

Care needs to be taken when specifying the initial conditions for the simulations in Fig. 8-17. The imposed shear rate $\dot{\gamma}$ is high enough to erase any memory of λ at the end of each application of shear rate (thus setting $\lambda = 0$), and then the waiting time will set the initial value of λ before startup of steady shear. However, the parameter $\hat{\lambda}$ will depend on both the waiting time, and the value it had at the end of the previous startup of steady shear. Its value must therefore be carried over between sequences of aging steps and startup steps in the simulations. Furthermore, the first startup test begins with a value of $\hat{\lambda} = 0$, because the experiments in Fig. 8-6 were conducted immediately after pre-shearing the material at a high shear rate (enough to cause $\hat{\lambda}$ to approach zero).

Genealogy of Models

The isotropic and kinematic hardening mechanisms which have been utilized in the IKH model are taken from plasticity theory, however several limits of the model can be taken to reduce it to simpler forms. In Fig. 8-18, we illustrate a "genealogy" of constitutive models, where the elastic variant (Fig. 8-9 (c)) of the IKH model is shown as a simplified, 1-dimensional version of the plasticity models used by Anand and coworkers [11, 10, 96]. The IKH model can simplify to several other constitutive

models under certain limits (light blue boxes). It is also related in a broader sense to other thixotropy models that are encountered in the rheology literature - among them the Souza-Mendes model [58] and the Mujumdar model [152] (shown in orange boxes). In each individual box, the number of fitting coefficients is indicated in the blue circle.

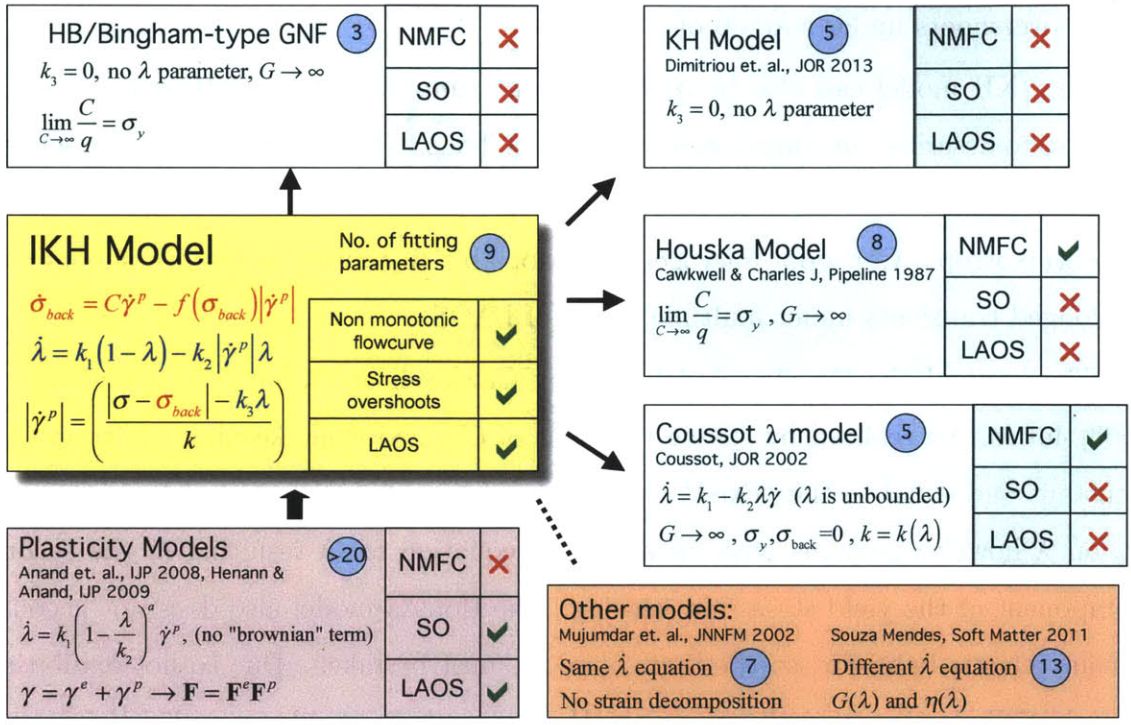

Figure 8-18: Genealogy diagram showing the relationship between the IKH model and other constitutive models used for thixotropic systems. Models in the light blue boxes can be reached by setting specific limits of the IKH model. The models in the orange boxes are more broadly related.

One important distinction between the IKH model and the plasticity models is the different form of the evolution equation for λ . The plasticity models are thus unable to predict a NMFC, due to the absence of a Brownian build up term in their evolution equation of λ. Hence, this aspect is the only distinction in the IKH model when compared to the plasticity models that are mentioned here.

The IKH model can be quite easily reduced to the Bingham generalized Newtonian fluid model by setting $k_3 = 0$, and then taking the limit of $G \to \infty$ and $C \to \infty$ while

keeping the ratio C/q constant and equal to the yield stress. This results in the back stress σ_{back} immediately responding to a given stress level by either saturating at $\pm\sigma$ if $|\sigma| < \sigma_y$ or saturating at $\pm\sigma_y$ if $|\sigma| > \sigma_y$. An alternative way to reduce the IKH model to a Bingham model would be to eliminate the back stress σ_{back} and set λ to a constant. Note that the neither the Binghan model nor the Herschel Bulkley model are capable of predicting NMFC's, the correct LAOS response of the material, or stress overshoots under startup of steady shear.

The IKH model can also be quite easily be simplified to the KH model used in Chap. 6 to describe non-thixotropic yield stress fluids. This is accomplished by setting $k_3 = 0$. While the KH model was shown to predict the correct LAOS behavior for a nonthixotropic Carbopol microgel, it is not able to predict stress overshoots and prolonged transients under multiple cycles of LAOS.

The limit of the Houska model used by Cawkwell and Charles [44] and others [163, 46] can be realized by taking the limit of $C \to \infty$ while keeping the ratio C/q constant and equal to the "fixed" component of the yield stress. The dependence of σ_y on λ however remains with an evolution equation for λ resulting in the second component of the yield stress not varying. The Houska model also does not account for any elastic behavior, so the limit $G \to \infty$ must be taken. Due to not exhibiting any elastic behavior at small strains, the Houska model is unable to predict the correct LAOS behavior of our model crude oil.

Finally, the IKH model can (in a somewhat more complex manner) be simplified to the toy λ-model employed by Coussot et. al. in order to account for viscosity bifurcations in thixotropic yield stress fluids [53]. This limit can be achieved by setting both yield parameters σ_y and σ_{back} equal to zero, taking the limit of $G \to \infty$, and making k a function of λ. Coussot also employs a different evolution equation for λ, which results in λ being unbounded in time. While Coussot's model can qualitatively capture the nature of the NMFC, it cannot quantitatively capture many other aspects associated with the response of the material to LAOS or startup of steady shear.

The IKH model is more broadly related to the Mujumdar [152] and Souza Mendes [58] models because these models exhibit critical differences from the IKH model.

The Mujumdar model does not explicitly decompose strain into elastic and plastic components - as a result the authors necessarily introduce a critical strain γ_c into the model which is used to determine whether or not the structure of the material is breaking. The Mujumdar model does, however, use the same form of the evolution equation for λ that the IKH model employs. On the other hand, the Souza Mendes model uses a different form for the evolution equation of λ - specifically the stress σ enters this equation and is assumed to be the driving force for destroying the material microstructure. We avoid introducing this type of behavior into the IKH model due to the measurements of constant G' and G'' as a function of time in the linear regime of deformation. Souza Mendes also writes the linear viscoelastic moduli G and η as functions of λ. This may be required for a more complete form of the IKH model, however measurements of G' and G'' as a function of t_w have indicated that the linear viscoelastic moduli are weakly dependent on the structure of the material.

8.5 Conclusions

The core theme of this chapter was to present a study on thixotropy in the context of a model waxy crude oil. This study is the capstone of this thesis, as it builds from the work presented on shear heterogeneities in Chaps. 3-5, and from the study of EVP behavior in Chaps. 6-7.

RheoPIV measurements have been conducted on the model waxy crude oil (introduced in Chap. 5) in order to develop an appropriate preparation protocol which can be used prior to conducting rheological measurements of the fluid. We further used RheoPIV measurements in order to elucidate the nature of flow instabilities that occur in the material - these are the result of a measurable non-monotonic flowcurve that the material exhibits. We contrast this unstable flow to the standard shear banding scenario often envisioned for other complex fluids that have an underlying non-monotonicity in their flowcurve. The material instability observed in the model crude oil consists of spatially and temporally fluctuating values of local shear rate and shear stress within the material, with a constant globally applied shear rate and

average shear stress.

The constitutive model developed here was built on the KH model framework that was introduced and discussed in detail in Chaps. 6-7. This constitutive model was used to capture the behavior of the fluid under our set of 3 "canonical" flow scenarios which were proposed. These are measurements of the steady flowcurve of the material ($\hat{\sigma}$ vs. $\hat{\dot{\gamma}}$), startup of steady shear following different waiting times t_w, and LAOStrain. An added benefit of the modeling approach is that the model is extendable to a frame invariant, 3-dimensional tensorial form (such as that discussed in Chap. 7) that can be utilized in simulations of more complex flow scenarios. The IKH model was fitted to the 10% wax in oil model system in its "slurry state" at 27°C - under these isothermal conditions it was capable of capturing the aging behavior exhibited by the fluid, and the subsequent effect that this aging has on the response to deformations.

Chapter 9

Final Remarks and Outlook

This central focus of this thesis has been on developing an understanding of the rheological complexity of precipitate containing crude oils. Three particular rheological phenomena that are exhibited by these crude oils have been studied by utilizing and developing a number of experimental and analytical tools. At the completion of this study, we arrive at the following conclusions:

First, the ability to detect shear heterogeneities in these fluids is crucial if one wishes to probe the nonlinear rheology of these fluids. Chap. 5 demonstrated that these crude oils can exhibit complex spatio-temporal fluctuations in their local shear rate when they undergo a steady *apparent* shearing deformation within a cone-plate rheometer. This forces us to reevaluate bulk rheological data by taking these shear heterogeneities into account.

Second, a framework for nonlinear rheological characterization is necessary to probe the inherently nonlinear elasto-viscoplastic behavior of these fluids. The particular framework that is identified and developed in this work is stress-controlled large amplitude oscillatory shear (LAOStress). We have shown that the LAOStress framework naturally incorporates the strain-decomposition ideas that are typically associated with a yielding response in a material. While the LAOStress framework is purely descriptive, in Chap. 6 it served as a tool for developing constitutive models that capture the yielding behavior of these fluids.

Finally, we have shown that the constitutive response of these crude oils can be well

described using a modeling framework borrowed from the plasticity literature. This framework possesses several key components. First: Strain is additively decomposed into a (reversible) elastic part and an (irreversible) plastic part. Second: Isotropic and kinematic hardening mechanisms can be used to account for a dynamic change in the size and center of a material's yield surface. Third: These modeling components can be generalized to a frame invariant, thermodynamically consistent, 3D tensorial form. In Chap. 8 we illustrated how one particular model (the IKH model) is successful at capturing the fully thixotropic, elasto-viscoplastic behavior of a model waxy crude oil. Chaps. 6 and 7 also showed how a simpler version of this (the KH model) improves on the currently available EVP models in the rheology literature. These improvements include capturing transient creeping flow below the yield stress, and regularizing the yielding behavior by introducing an evolving internal variable.

Although the three phenomena studied in this work (shear heterogeneities, elasto-viscoplastic behavior, and thixotropy) are endemic to precipitate-containing crude oils, they are also exhibited by other complex fluids. This extends the utility of this work beyond the scope of the petroleum industry. The results in Chaps. 5 and 6 in particular are relevant to fluids commonly encountered in the consumer product industry, since surfactant solutions and Carbopol gels are frequently introduced into these products to control their rheology.

There are several potential avenues for continuing this work - some may involve improving the predictive capabilities of the thixotropic EVP model proposed here (the IKH model). For example, nonlocal terms can be introduced into the constitutive model, in order to predict the nature of the flow instabilities that were observed in Chap. 8 at low imposed shear rates. An additional way to improve the model would be to capture the continuous, temperature-dependent transition that the material exhibits as it is cooled from above T_{wa} (where it behaves as a Newtonian liquid) to below T_{wa} where it begins to exhibit thixotropic, elastoviscoplastic behavior. An improved IKH model would also account for the difference in material behavior when it is in its "slurry state" vs. its "strong gel" state (see Chaps. 5 and 8). This would require introducing a much larger set of material parameters and evolution equations,

which account for both volume fraction of wax variation with temperature, as well as how shear history (i.e. the preparation protocol) affects the ultimate state of the wax-oil gel.

The ultimate goal of such work would be to develop a temperature-dependent elasto-viscoplastic and thixotropic model, which can then be implemented into simulations of non-isothermal flow in pipelines. This would substantially expand on the capabilities of the temperature-dependent models that are available today, which typically assume a generalized Newtonian fluid and do not account for elastic or yielding behavior [164, 82]. Such a model would greatly assist in flow assurance applications involving the optimizing of operating conditions for pipelines that transport waxy crude oil.

On the experimental side, scaled up experiments where real or model waxy crude oils are pumped through large-scale flow loops would be useful for comparison with results from simulations. We have shown that the 1-dimensional IKH model can accurately describe experimental data from simple shear flows. However for pipe flow experiments where the total pressure drops are large, it may be necessary to also account for the compressibility of the fluid and use a more general 3D form of the IKH model. A successful comparison of simulations and experiments would further verify the validity of the IKH model as a constitutive framework.

The challenges faced by flow assurance specialists in the oil industry are certainly varied and complex. However, the development of a constitutive law framework for precipitate containing crude oils will have important implications for flow assurance strategies. We hope that this thesis has laid the groundwork for developing classes of models by providing a detailed account of the rheological complexity of these fluids.

Appendix A

Experimental Artifacts in LAOStress and LAOStrain

A.1 Effect of Instrument Inertia in LAOStress

When carrying out dynamic stress-controlled experiments on a single head rheometer such as an ARG2, the rheometer typically controls the total torque applied, which is distributed between the instrument geometry, and the sample. In the present work, the total torque (which was sampled before any filtering using an auxiliary sample program on the ARG2) was converted to the shear stress acting on the sample using an appropriate geometry factor ($2\pi R^3/3$ with R being the radius of the cone-plate geometry). For greater accuracy, one would want to subtract any contribution of the inertial torque from the measured signal before applying this geometry factor.

For small enough frequencies and strain amplitudes, we expect that influences from the inertial torque can be neglected and we seek to provide a dimensionless constraint that quantifies this expectation. The total torque $\mathcal{T}$ can be additively decomposed into an 'inertia torque', $\mathcal{T}_i$ and the sample torque, $\mathcal{T}_s$ such that $\mathcal{T} = \mathcal{T}_i + \mathcal{T}_s$. The inertia torque is related to the angular orientation of the geometry, ϕ, and the instrument moment of inertia I as follows:

$$\mathcal{T}_i = I\frac{d^2\phi}{dt^2} \tag{A.1}$$

To be able to neglect the effects that instrument inertia has on an experiment, it is desired for the ratio $\mathcal{T}_i/\mathcal{T}_s$ to be small. For the particular experiments carried out in this work (stress-controlled oscillations with stress amplitude σ_0 and frequency ω, in a cone and plate geometry), one can estimate the values of $\mathcal{T}_i$ and $\mathcal{T}_s$ as follows:

$$\mathcal{T}_s \sim \frac{2\sigma_0\pi R^3}{3} \tag{A.2}$$

$$\mathcal{T}_i \sim I\omega^2\gamma_0\Theta_0 \tag{A.3}$$

Where R is the radius of the cone-plate geometry, Θ_0 is the cone angle, and γ_0 is the strain amplitude of the deformation, which naturally depends on the type of material being probed. We define a dimensionless inertia number In which estimates the relative magnitude of the inertia torque to the sample torque as follows:

$$In = \frac{3I\omega^2\Theta_0\gamma_0}{2\pi\sigma_0 R^3} \tag{A.4}$$

The strain amplitude of deformation cannot be determined a priori. For the present work we can determine γ_0 from the experiments presented in Fig. 6-8, and based on these values of γ_0, we find $In < 0.05$ for all the experiments. The test in Fig. 6-8 for which In is largest is that where the imposed frequency is $\omega = 5$ rad/s and the stress amplitude is 200 Pa. To illustrate that the cutoff of $In \leq 0.05$ is acceptable, we plot the corrected stress-strain curve on top of the uncorrected stress strain curve in Fig. A-1. As Fig. A-1 shows, there is little change in the overall shape of the Lissajous curve for this particular frequency. In particular, the value of J'_M evaluated from the two different curves differs by less than 3 %. However, a quantitative comparison of the measure J'_L at this particular value of ω and σ_0 is rather difficult to obtain, due to a substantial amount of noise being introduced into the corrected stress signal at higher values of $\sigma(t)$.

Another way to measure the importance of inertia in a stress-controlled test is by

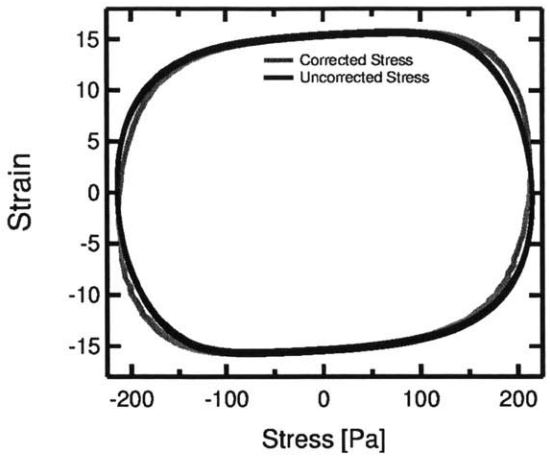

Figure A-1: Comparison of corrected and uncorrected Lissajous curves for LAOS experiment with $\omega = 5$ rad/s and $\sigma_0 = 200$ Pa

looking at the relative "spectral purity" of the periodic torque wave $\mathcal{T}_s(t)$ imposed on the sample. For stress-controlled LAOS, the rheometer will typically impose a total torque such that $\mathcal{T}(t) = \mathcal{T}_0 \cos \omega t$. Due to the nonlinear nature of the material response, the torsional angle $\phi(t)$ will contain higher harmonics. As a result, $\mathcal{T}_i(t)$ will also contain higher harmonics, as a consequence of the definition in Eq. A.1. There is therefore no guarantee that the oscillating torque, $\mathcal{T}_s(t) = \mathcal{T}(t) - \mathcal{T}_i(t)$ applied to the sample will only contain a single harmonic in its waveform. For each of the experiments presented in this work, $\mathcal{T}(t)$ can be corrected for inertia to obtain the true sample torque $\mathcal{T}_s(t)$. An FFT of $\mathcal{T}_s(t)$ can then be taken and the relative magnitude of the third harmonic to the first harmonic ($\mathcal{T}_3/\mathcal{T}_1$) can be determined. This gives the LAOS experimentalist an idea of how pure the spectral content of the stress input into the material is. In Fig. A-2 we show the ratio $\mathcal{T}_3/\mathcal{T}_1$ for the LAOStress measurements presented in this work. From the figure, it is apparent that the ratio increases beyond a noise threshold ($\sim 0.2\%$) for the highest stress amplitudes, but never increases beyond 3% at the highest frequency and stress amplitude

A coarse estimate of the limiting strain amplitude, γ_0, can also be determined as a criterion before carrying out experiments. For values of σ_0 below the yield stress, we expect $\gamma_0 \sim \sigma_0/G$ (i.e. the material will behave primarily as an elastic

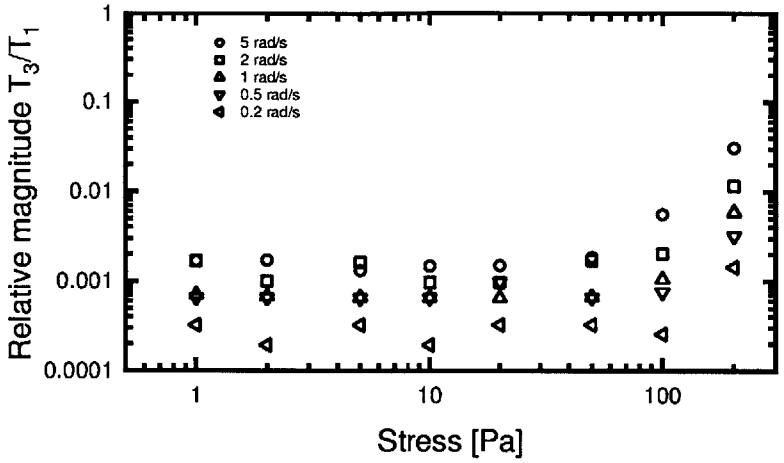

Figure A-2: Plot of the relative size of the third harmonic to the first harmonic in the periodic sample stress waveform, $\mathcal{T}_s(t)$

solid). For values of σ_0 above the yield stress, however, the material will deform with a maximum shear rate (given by the Herschel-Bulkley equation) of $\left(\frac{\sigma_0-\sigma_y}{k}\right)^{1/m}$. If we multiply this shear rate by the period, $2\pi/\omega$, we obtain an estimate for the total accumulated viscoplastic strain in the material. We also need to add the accumulated elastic strain to the material as well (σ_0/G), so when we add these two terms we obtain the following estimate for γ_0 above the yield stress:

$$\gamma_0 \sim \frac{\sigma_0}{G} + \left(\frac{\sigma_0 - \sigma_y}{k}\right)^{1/m} \frac{2\pi}{\omega} \tag{A.5}$$

Using these estimates for the strain amplitude both below and above the yield stress, we can modify the dimensionless inertia number defined in Eq. A.4. In the absence of any knowledge of γ_0, In can then be determined as follows for a soft solid gel:

$$In = \frac{3I\omega^2\Theta_0}{2\pi R^3 G} \qquad \text{for } \sigma < \sigma_y \tag{A.6}$$

$$In = \frac{3I\omega^2\Theta_0}{2\sigma_0\pi R^3}\left(\sigma_0/G + \left(\frac{\sigma_0 - \sigma_y}{k}\right)^{1/m} \frac{2\pi}{\omega}\right) \qquad \text{for } \sigma \geq \sigma_y \tag{A.7}$$

A suitable upper bound constraint can then be placed on the value of In, which allows the range of test frequencies and imposed stresses for which inertial effects are

negligible to be evaluated before stress-controlled experiments are actually performed.

Finally, we reiterate the fact that the analysis in this section assumes that experiments are being performed with a single head stress controlled rheometer. This is a different scenario than say, that studied by Walters [207] for the Weissenberg Rheogoniometer. In Walters' case, it is necessary to consider the coupled system dynamics arising from the fluid, the plate and the torsional spring, under displacement controlled conditions. For a single-head stress-controlled rheometer, a torsional spring is not present in the system. Rather, there is a rigid coupling between the electromechanical system applying the torque, and the rotating (and accelerating) test fixture.

A.2 Uniqueness of Strain Decomposition

We consider the case in which we have a sinusoidally imposed stress $\sigma(t)$ as given in Eq. 6.6 (and inertial effects are negligible), with the strain $\gamma(t)$ being decomposed into a Fourier series as given in Eq. 6.7. Based on the Fourier decomposition of Eq. 6.7, we desire to find a strain decomposition $\gamma = \gamma' + \gamma''$ such that γ' is a single-valued function of stress, and $\dot{\gamma''}$ is a single-valued function of stress.

A.2.1 Strain Decomposition

We propose that the following decomposition satisfies the criteria of γ' being a single-valued function of σ and $\dot{\gamma}''$ being a single-valued function of σ:

$$\gamma'(t) = \sum_{n \text{ odd}} J'_n \sigma_0 \cos n\omega t \tag{A.8}$$

$$\gamma''(t) = \sum_{n \text{ odd}} J''_n \sigma_0 \sin n\omega t \tag{A.9}$$

To show this, we must show that if $\sigma(t_1) = \sigma(t_2)$, then $\gamma'(t_1) = \gamma'(t_2)$, i.e. for two different times at which the stress is equal, the value of γ' must be equal. For $\sigma(t_1) = \sigma(t_2)$ we must have $\cos\omega t_1 = \cos\omega t_2$. Due to the fact that cosine is an even

function, this only holds if:

$$\omega t_1 = -\omega t_2 \tag{A.10}$$

Using equation A.10 we can obtain a relationship between the higher harmonics in equation A.8 at times t_1 and t_2.

$$\cos n\omega t_1 = \cos(-n\omega t_2) = \cos n\omega t_2 \tag{A.11}$$

Where the last equality follows because cosine is an even function regardless of the value of n. As a result of equation A.11, all the terms in equation A.8 are the same if they are evaluated at either t_1 or t_2, as long as the stress is the same at times t_1 and t_2. Because of this, γ' is a single-valued function of stress. It follows that $\dot{\gamma}''$ is also a single-valued function of stress, because it consists of only cosine terms (it is the time derivative of sine terms), and the same logic applies.

A.2.2 Uniqueness of Strain Decomposition

We now show that the strain decomposition in equations A.8 and A.9 is unique, in the sense that no other strain decomposition gives an apparent elastic contribution γ' which is a single-valued function of the stress σ and an apparent plastic strain rate $\dot{\gamma}''$ which is a single-valued function of the stress σ. We propose an alternative elastic strain, γ'^1. This γ'^1 would have the following Fourier decomposition:

$$\gamma'^1 = \sum_{n \text{ odd}} \{a_n \sigma_0 \sin n\omega t + b_n \sigma_0 \cos n\omega t\} \tag{A.12}$$

Using equation A.10 we can obtain a relation between the sine terms in Eq. A.12 at t_1 and t_2:

$$\sin n\omega t_1 = \sin(-n\omega t_2) = -\sin n\omega t_2 \tag{A.13}$$

Where the last equality follows from the odd property of the sine function. It is therefore impossible for $\gamma'^1(t_1) = \gamma'^1(t_2)$ unless all the b_n are zero. This leaves us only nonzero a_n. Any choice of a_n will give a γ'^1 which is a single-valued function of stress,

however by the properties of the strain decomposition we can obtain the viscoplastic strain through the following:

$$\gamma''^1 = \gamma - \gamma'^1 \tag{A.14}$$

The only way that $\dot{\gamma}''^1$ will also be a single-valued function of stress is if $a_n = J'_n$ - i.e. we can only have sine terms in γ''^1 such that $\dot{\gamma}''^1$ will only contain cosine terms.

A.3 Effect of slip on shear stress distribution in a cone-plate geometry

It is fairly well known that the presence of wall slip for flow of a Newtonian or non-Newtonian fluid in a cone and plate geometry can cause a non uniform stress in the sample [168, 184]. In this section we will explore some of the possible scenarios that may result from the presence of wall slip in cone and plate flow.

A.3.1 Newtonian Fluid with a Navier Slip Law

For a Newtonian fluid, the stress–strain rate relation is as follows

$$\sigma = \eta\dot{\gamma}_r \tag{A.15}$$

Where $\dot{\gamma}_r$ is the real shear rate experienced by the fluid in the bulk. For this particular scenario, we consider a Navier–like slip law, given by the following

$$v_s = \beta\sigma \tag{A.16}$$

Where β is the slip coefficient and v_s is the slip velocity. For this particular scenario, we must distinguish between the real (or true) shear rate $\dot{\gamma}_r$ and the apparent shear rate $\dot{\gamma}_a$. In a cone and plate geometry where the cone angle is small, the real and

apparent shear rate can be related through the slip velocity as follows:

$$\dot{\gamma}_r = \dot{\gamma}_a - \frac{2v_s(r)}{r\tan\Theta_0} \tag{A.17}$$

In equation A.17 we explicitly state that the slip velocity is a function of the radial coordinate r. We also expect that the stress σ will depend on r, as will $\dot{\gamma}_r$. However, $\dot{\gamma}_a$ will not depend on the radial coordinate.

By combining equations A.15, A.16 and A.17, it is possible to obtain an expression relating the shear stress to the radial coordinate r, which is as follows

$$\sigma(r) = \frac{r\eta\dot{\gamma}_a}{r + \frac{2\eta\beta}{\tan\Theta_0}} \tag{A.18}$$

Note how in the case where there is no slip, i.e. $\beta = 0$, the above expression simplifies to the usual cone–plate result, where $\sigma = \eta\dot{\gamma}$ with $\dot{\gamma} = \dot{\gamma}_a = \dot{\gamma}_r$. It is also instructive to consider the limit of this expression as $r \to \infty$

$$\lim_{r\to\infty} \sigma(r) = \eta\dot{\gamma}_a \tag{A.19}$$

Equation A.19 above shows that at large values of r, the stress approaches that which we would expect for a cone–plate geometry where slip was not present. For a cone–plate apparatus with radius R, a relevant dimensionless parameter to consider is $C = \frac{2\eta\beta}{R\tan\Theta_0}$. In the rest of this section we will look at the effect this parameter has on the total torque exerted by the rheometer on the geometry, $\mathcal{T}$. However, by inspection one might expect small values of C to result in small deviations of the value of $\mathcal{T}$ from that expected for a Newtonian fluid where there is no slip present. For illustrative purposes, we include a plot of how the shear stress σ varies with r in Figure A-3.

The plot in A-3 shows that in general the stress σ is lower at a given apparent shear rate when there is slip present. This lower stress will result in a generally lower

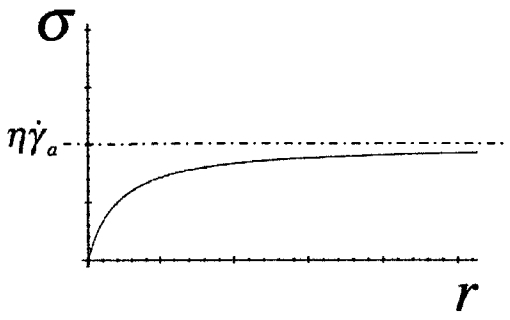

Figure A-3: Figure showing dependence of the stress σ on the radial position r

value of $\mathcal{T}$. We can obtain an analytic expression of $\mathcal{T}$ through the following integral

$$\mathcal{T} = \int_0^R \frac{2\pi r^3 \eta \dot{\gamma}_a}{r + \frac{2\eta\beta}{\tan\Theta_0}} dr \tag{A.20}$$

By making the substitution $r' = r/R$ we can rewrite the above integral as follows

$$\mathcal{T} = \frac{2\pi R^3 \eta \dot{\gamma}_a}{3} \left[3 \int_0^1 \frac{r'^3}{r' + C} dr' \right] \tag{A.21}$$

Where the term in the square brackets is a dimensionless parameter with value between 0 and 1, and the term outside the parentheses includes the well known stress factor ($\frac{2\pi R^3}{3}$) used to determine stress from a measured torque for a fluid undergoing steady shear in a cone–plate geometry with no slip present. The term $\eta\dot{\gamma}_a$ can be termed the "apparent stress", i.e. the stress that the fluid would experience if it were undergoing the applied, or apparent shear rate $\dot{\gamma}_a$. So, to calculate the viscosity η for the case of a Newtonian fluid with a Navier like slip law, it is only necessary to apply the correction factor in the square brackets in order to obtain the correct result for η.

A.3.2 Bingham fluid with a Navier Slip Law

Another scenario that may arise is steady shear of a Bingham fluid with a Navier slip law at the fluid-wall interface. For a Bingham fluid the shear rate is related to the stress as follows:

$$|\sigma| = \sigma_y + \eta|\dot{\gamma}_r| \tag{A.22}$$

For $|\sigma| > \sigma_y$, and when $|\sigma| < \sigma_y$, $|\dot{\gamma}_r| = 0$. By combining the above equation with Eqs. A.16 and A.17 and suppressing magnitude signs (we assume stresses and shear rates are positive) we obtain the following conditional relationship between σ and r:

$$\sigma(r) = \frac{\dot{\gamma}_a r \tan\Theta_0}{2\beta} \qquad \text{for } r < \frac{2\beta\sigma_y}{\dot{\gamma}_a \tan\Theta_0} \tag{A.23}$$

$$\sigma(r) = \frac{r\eta\dot{\gamma}_a + r\sigma_y}{r + \frac{2\eta\beta}{\tan\Theta_0}} \qquad \text{for } r \geq \frac{2\beta\sigma_y}{\dot{\gamma}_a \tan\Theta_0} \tag{A.24}$$

Hence, the stress increases linearly with r, until it reaches the yield stress σ_y. It then continues to increase in a nonlinear fashion, approaching the limit of $\sigma = \sigma_y \eta\dot{\gamma}_a$ as $r \to \infty$.

Several other scenarios can be considered for steady shear - for example, a "Bingham-like" slip law can be specified where wall slip only occurs above a critical stress. This may be more appropriate for elasto-viscoplastic materials.

A.3.3 Linear Viscoelastic Fluid (LVE) with a Navier Slip Law under Oscillatory Shear

Next, we study the impact of wall slip on stress heterogeneities under oscillatory shearing conditions. We consider a linear viscoelastic fluid (LVE) under oscillatory shear, $\dot{\gamma}_a = \gamma_0 \sin\omega t$ which slips according to the Navier slip law. The slip law is given by equation A.16, and the stress $\sigma(r,t)$ (a function of both time and radial position) is given by the following equation:

$$\sigma(r,t) = G'\gamma_r(r,t) + \frac{G''}{\omega}\dot{\gamma}_r(r,t) \tag{A.25}$$

Where $\dot{\gamma}_r(r,t)$ is the real strain experienced by the fluid, which depends on both radial position and time. This term is related to the apparent strain through equation A.17, with the slight modification that apparent strain, real strain and slip velocity are now functions of time. By combining equations A.16, A.17 and A.25, we obtain the following differential equation for the true strain as a function of time (for which we

now drop the subscript r, and just write as γ):

$$\frac{d\gamma}{dt}\left(1+\frac{2\beta G''}{\omega r\tan\Theta_0}\right)+\frac{2\beta G'}{r\tan\Theta_0}\gamma=\omega\gamma_0\cos\omega t \tag{A.26}$$

This is a first order linear ODE which can be solved using the integrating factor. To simplify the integration with respect to time we write $A=\frac{2\beta G'}{r\tan\Theta_0}$ and $B=\left(1+\frac{2\beta G''}{\omega r\tan\Theta_0}\right)$. Then we obtain the following expression for the real strain as a function of both radius r and time t:

$$\gamma(r,t)=\frac{\omega\gamma_0}{A^2+B^2\omega^2}\left(A\cos\omega t+B\omega\sin\omega t\right) \tag{A.27}$$

The radial dependency in the strain is hidden in the A and B parameters. We will ignore this until we get to the point where we will integrate the local stress to obtain the torque. For now however, we can write the expression for $\sigma(r,t)$ by combining equations A.27 and A.25. The following expression is obtained:

$$\sigma(r,t)=\left(\frac{G'\omega^2\gamma_0 B-G''\omega\gamma_0 A}{A^2+B^2\omega^2}\right)\sin\omega t+\left(\frac{G'\omega\gamma_0 A+G''\omega^2\gamma_0 B}{A^2+B^2\omega^2}\right)\cos\omega t \tag{A.28}$$

At this point we will consider the relative phase of this torque (relative with respect to the applied apparent strain γ_a). This is equal to the ratio of the magnitude of the sine and cosine terms of equation A.28, and simplifies to the following expression:

$$\tan\delta_\sigma=\frac{G''}{G'}+\frac{2\beta}{\omega r\tan\Theta_0}\left(\frac{G'^2+G''^2}{G'}\right) \tag{A.29}$$

Note how when $\beta=0$, equation A.29 gives $\tan\delta_\sigma=\frac{G''}{G'}$, which is the expected result for no slip conditions. An important consequence of our slip law (equation A.16) is that our slip velocity (which we measure in our PIV system, for a particular value of r) will have the same phase as the local stress at that value of r, so the expression in equation A.29 also describes the relative phase of the slip velocity (again relative to the imposed sinusoidal apparent strain).

Next, we will verify whether or not the torque applied on the geometry, $\mathcal{T}(t)$ has the

same phase as the local stress and slip velocity at a point where we might be locally measuring the slip velocity. Due to the radial dependency of $\tan\delta_\sigma$, which is shown in equation A.29, it seems likely that the two probably do not have the same phase. In order to obtain an expression for torque, we must evaluate the following integral:

$$\mathcal{T}(t) = \int_0^R 2\pi r^2 \sigma(r,t) dr \tag{A.30}$$

We combine equations A.30 and A.28 to obtain the following:

$$\mathcal{T}(t) = \left[\int_0^R \left(\frac{G'\omega^2\gamma_0 B - G''\omega\gamma_0 A}{A^2 + B^2\omega^2}\right) dr\right] \sin\omega t + \left[\int_0^R \left(\frac{G'\omega\gamma_0 A + G''\omega^2\gamma_0 B}{A^2 + B^2\omega^2}\right) dr\right] \cos\omega t \tag{A.31}$$

In order to carry out the integration, we need to now write the parameters A and B in their full form, because they depend on r. Furthermore, if we want to determine the tangent of the phase of the torque ($\delta_\mathcal{T}$) we need to take the ratio of the two integrals in equation A.31. We write the expression for $\tan\delta_\mathcal{T}$ below:

$$\tan\delta_\mathcal{T} = \frac{G''}{G'} + \frac{\int_0^R \frac{\frac{2\beta\omega r^3}{\tan\Theta_0}[G'^2+G''^2]}{\frac{4\beta^2}{\tan^2\Theta_0}[G'^2+G''^2]+\frac{4\omega\beta G''r}{\tan\Theta_0}+\omega^2r^2} dr}{\int_0^R \frac{G'\omega^2\gamma_0 r^4}{\frac{4\beta^2}{\tan^2\Theta_0}[G'^2+G''^2]+\frac{4\omega\beta G''r}{\tan\Theta_0}+\omega^2r^2} dr} \tag{A.32}$$

Again, this phase reduces to $\frac{G''}{G'}$ for the case when $\beta = 0$, or no slip – this is another desired result. In order to simplify the expression in equation A.33, we introduce some dimensionless parameters. They are $C' = \frac{\beta G'}{\omega R}$ and $C'' = \frac{\beta G''}{\omega R}$. These parameters can be thought of as comparisons of the slip stress to the viscous and elastic bulk stress - they are similar to the parameter C discussed in section A.3.1. We also introduce a non-dimensional radius $\tilde{r} = \frac{r}{R}$. By introducing these dimensionless variables we can non-dimensionalize the integrals written in equation A.33, and obtain the following expression.

$$\tan\delta_\mathcal{T} = \frac{G''}{G'} + \frac{2}{\tan\Theta_0}\left(\frac{C'^2 + C''^2}{C'}\right) \frac{\int_0^1 \frac{\tilde{r}^3}{\frac{C'^2+C''^2}{\tan^2\Theta_0}+\frac{C''}{\tan\Theta_0}\tilde{r}+\tilde{r}^2} d\tilde{r}}{\int_0^1 \frac{\tilde{r}^4}{\frac{C'^2+C''^2}{\tan^2\Theta_0}+\frac{C''}{\tan\Theta_0}\tilde{r}+\tilde{r}^2} d\tilde{r}} \tag{A.33}$$

Now using our dimensionless parameters, we can also rewrite equation A.29 in order to compare it to equation A.33

$$\tan \delta_\sigma = \frac{G''}{G'} + \frac{2}{\tan \Theta_0} \left(\frac{C'^2 + C''^2}{C'} \right) \tag{A.34}$$

Equations A.34 and A.33 are identical except for the quotient of integral term which multiplies the second term in the case of equation A.33. Because this quotient of integral terms is not always equal to zero, there is typically going to be a phase difference between the locally measured slip velocity and the bulk averaged torque. Therefore in general $(\delta_\sigma - \delta_\mathcal{T}) \neq 0$. This will result in "hysteresis" when the Lissajous curves of torque vs. slip velocity are plotted for this situation.

Using the RheoPIV device (v1) described in Chap. 3, it is possible to observe this type of hysteresis in Lissajous curves of torque vs. slip velocity for certain types of fluids. We will demonstrate this behavior for a 0.5% U10 Carbopol microgel solution under an oscillatory shearing deformation. This microgel's bulk rheology is slightly different to the fluid used in Chap. 6 because it is a different variant of Carbopol. As a result its yield stress is somewhat higher, with $\sigma_y \simeq 150$ Pa. The RheoPIV measurements were carried out using a 50mm diameter, 4° cone-plate geometry with smooth walls (to promote wall slip). Slip velocities were measured at a radial location of $r = 23$ mm.

Figure 2 shows the curves obtained for this microgel under an imposed oscillatory torque at a number of different torque amplitudes and frequencies. This is essentially a LAOStress experiment, however due to the presence of wall slip the rheometer is not able to impose a radially homogenous shear stress on the sample. The cyclic curves point towards the material exhibiting a nonlinear dependency of wall slip on stress (because they are not elliptical shapes). These types of nonlinear slip laws have been observed by previous workers [189] where a quadratic dependency of slip velocity on shear stress was proposed to describe this behavior.

Despite this nonlinear behavior, our observations in Fig. A-4 still imply that there is a phase difference between the slip velocity and the apparent stress (which is related

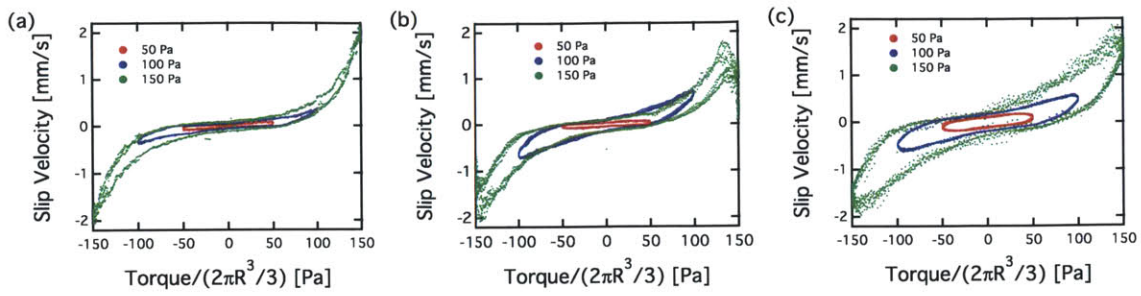

Figure A-4: Family of curves of slip velocity plot vs. apparent stress (or $\mathcal{T}/(2\pi R^3/3)$). For a 0.5% Carbopol microgel. Both torque amplitude and frequency are varied. In (a) a frequency of 0.5 rad/s is imposed, in (b) a frequency of 1 rad/s is imposed, and in (c) a frequency of 2 rad/s is imposed. More hysteresis in the curves can be observed as the frequency increases.

to the torque through the geometry factor $2\pi R^3/3$). One might be tempted to posit that such a behavior is a result of a dynamic slip law, where slip velocity is related to stress through a differential equation [91]. However, given the preceding analysis, we can also say that this behavior is be due to radial heterogeneities in the stress (which the rheometer cannot control).

The analysis which provided us with Eqs A.33 and A.34 assumed a linear viscoelastic material, with a Navier slip law. These assumptions do not hold for the data in Fig. A-4, since local stresses are approaching the material's yield stress (so the bulk response will not be linear viscoelastic), and Carbopol does not appear to exhibit a linear slip law. Nevertheless, we can graphically represent the same type of hysteresis that was observed in Fig. A-4 for an LVE material undergoing an oscillatory deformation $\gamma_a = \gamma_0 \sin \omega t$ when wall slip is present, at a number of different frequencies ω. Specifically, we can cross plot the slip velocity $v_s(r,t)$ and the torque $\mathcal{T}(t)$ for a particular geometry and radial location r, and for a material with a given set of viscoelastic parameters. These plots (which were generated using Mathcad) are given in Fig. A-5. The particular set parameters that were chosen for these plots were $G' = 200$ Pa, $G'' = 20$ Pa, $\beta = 3 \times 10^{-5}$ m/Pa.s, $R = 25$ mm, $r = 25$ mm, and $\Theta_0 = 4°$. Although the shape of the curves is elliptical, a similar growth in the hysteresis with frequency is observed, as it is in Fig. A-4.

Finally, Mathcad was used to generate a plot of the phase difference between the

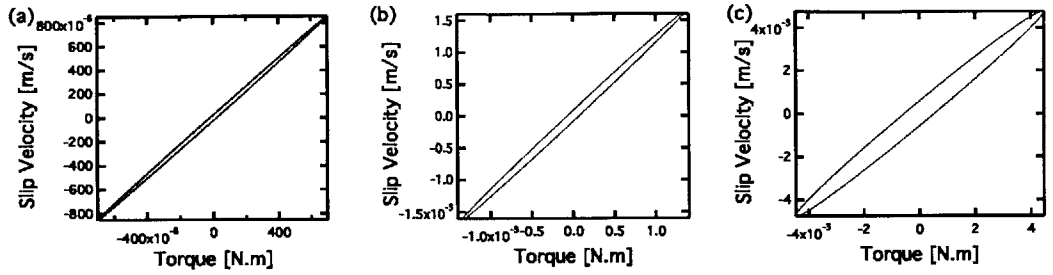

Figure A-5: Lissajous plots of slip velocity vs. torque for a LVE material undergoing an oscillatory deformation with an apparent strain amplitude of $\gamma_0 = 1$ and at a frequency of (a) 1 rad/s, (b) 2 rad/s and (c) 10 rad/s.

stress $\sigma(r,t)$ and the torque $\mathcal{T}$ as a function of frequency. This quantifies the amount of hysteresis that was observed in the curves in Fig. A-5. Fig. A-6 shows an increase in the phase difference between the stress and the torque (which is equal to the phase difference between the slip velocity and the torque, because stress and slip velocity are in phase).

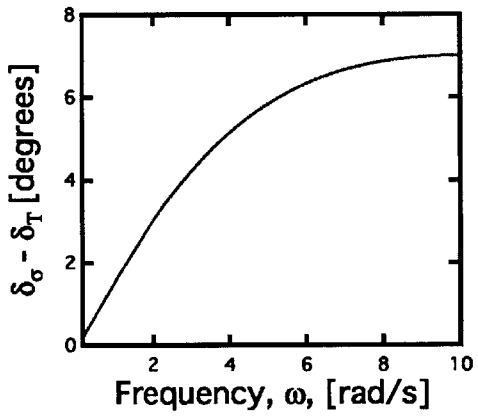

Figure A-6: Plot of the phase difference between $\sigma(r,t)$ and $\mathcal{T}$ as a function of frequency. This plot assumes a LVE material with a Navier slip law under an imposed apparent oscillatory strain $\gamma_a = \gamma_0 \sin \omega t$. The same set of parameters that were used for Fig. A-5 were used to generate this figure.

Appendix B

Asymptotic limits of KH model

B.1 Creep

In this section, we derive the asymptotic expansion that was given in Sec. 6.4.4 for the 1D KH model under a constant applied stress σ (i.e. a creep test). We begin by stating the evolution equations that the material follows:

$$\dot{A} = \dot{\gamma}^p \left(1 - qA(t)\right) \tag{B.1}$$

$$\dot{\gamma}^p = \left(\frac{\sigma - CA(t)}{k}\right)^{1/m} \tag{B.2}$$

Note that the initial condition for this set of evolution equations is $A = 0$.

B.1.1 Special case where $\sigma = \sigma_y$

We will first consider the special case for when the applied stress equals the yield stress, i.e. $\sigma = \sigma_y = C/q$. We are interested in obtaining a long time asymptotic expression for how A evolves in time, which we can then use to determine how the apparent viscosity varies, $\eta^+ \equiv \sigma/\dot{\gamma}(t) = \sigma/\dot{\gamma}^p(t)$. We are neglecting elastic strains because these will respond immediately to the step in the stress, and they do not affect the long time evolution in the strain. For long times, A will approach a value

equal to $1/q$. We will therefore seek a solution of the following form:

$$A \simeq \frac{1}{q} - \frac{a_\infty}{t^x} \tag{B.3}$$

Where a_∞ is an unknown prefactor, and x is an unknown exponent. We can take the derivative of Eqn. B.3 above and obtain an expression for $\dot{A}$

$$\dot{A} \simeq \frac{a_\infty x}{t^{x+1}} \tag{B.4}$$

We also can substitute Eqn. B.3 into Eqns. B.1 and B.2, and then combine these two in order to obtain another expression for $\dot{A}$

$$\dot{A} \simeq \left(\frac{Ca_\infty}{kt^x}\right)^{1/m} \left(\frac{qa_\infty}{t^x}\right) \tag{B.5}$$

Comparing the exponent of t in Eqns. B.4 and B.5 gives $x = m$, while comparing the prefactors gives $a_\infty = \frac{k}{C}\left(\frac{m}{q}\right)^m$. We can therefore rewrite Eqn B.3:

$$A \simeq \frac{1}{q} - \frac{km^m}{Cq^m t^m} \tag{B.6}$$

Inserting Eqn. B.6 above into Eqn. B.2 then results in the following aymptotic expression of the plastic strain rate $\dot{\gamma}^p$:

$$\dot{\gamma}^p \simeq \frac{m}{qt} \tag{B.7}$$

Eqn. B.7 above can then be inserted into the definition of the apparent viscosity, $\eta^+ \equiv \sigma/\dot{\gamma}(t) = \sigma/\dot{\gamma}^p(t)$, in order to obtain an expression for the change in apparent viscosity over time:

$$\eta^+ \simeq \frac{Ct}{m} \tag{B.8}$$

Thus, when the applied stress is equal to the yield stress, the apparent viscosity for long times increases linearly with time t. This is observed in our simulations in Sec. 6.4.4

B.1.2 Case where $\sigma < \sigma_y$

For long times with creep experiments where the stress σ is below the yield stress, a similar approach can be taken as in Sec. B.1.1. We seek a solution of the following form:

$$A \simeq \frac{\sigma}{C} - \frac{b}{t^x} \tag{B.9}$$

Where b is an unknown prefactor, and x is an unknown exponent. We can take the derivative of Eqn. B.9 above and obtain an expression for $\dot{A}$

$$\dot{A} \simeq \frac{bx}{t^{x+1}} \tag{B.10}$$

We also can substitute Eqn. B.9 into Eqns. B.1 and B.2, and then combine these two in order to obtain another expression for $\dot{A}$

$$\dot{A} \simeq \left(\frac{Cb}{kt^x}\right)^{1/m} \left(1 - \frac{q\sigma}{C}\right) \tag{B.11}$$

Note that when inserting Eqn B.9 into Eqn. B.1, we approximate the term $1 - qA(t)$ as $1 - q\sigma/C$. Comparing the exponents and prefactors in Eqn. B.11 with those of Eqn. B.10 gives the following expression for x and b

$$x = \frac{m}{1-m} \tag{B.12}$$

$$b = \left[\left(1 - \frac{q\sigma}{C}\right)\left(\frac{1-m}{m}\right)\right]^{\frac{m}{m-1}} \left(\frac{C}{k}\right)^{\frac{1}{m-1}} \tag{B.13}$$

The expressions above can then be inserted into either Eqn. B.11 or B.10, which can in turn be inserted into Eqn. B.2. This will provide an expression of the rate of plastic strain $\dot{\gamma}^p$. This is then used to determine the apparent viscosity $\eta^+ \equiv \sigma/\dot{\gamma}^p$, which is as follows:

$$\eta^+ \simeq \sigma \left[\left(1 - \frac{q\sigma}{C}\right)\left(\frac{1-m}{m}\right)\left(\frac{C}{k}\right)t\right]^{\frac{1}{1-m}} \tag{B.14}$$

The equation above can then be rewritten in terms of a characteristic timescale t_c and a characteristic viscosity scale η_c as is given in Eqns. 6.29-6.31.

B.2 Small amplitude oscillatory shear

Under small amplitude oscillatory shear, it is necessary to keep track of the direction of deformation, so we must modify Eqn. B.2 in order to account for changes in the sign of σ and γ^p.

$$\dot{\gamma}^p = \left(\frac{|\sigma - CA|}{k}\right)^{1/m} \text{sign}(\sigma - CA) \tag{B.15}$$

B.2.1 Case where $m = 1$

It is possible to obtain analytical expressions for $G'(\omega)$ and $G''(\omega)$ for the KH model for the special case when $m = 1$. For SAOS, we impose an oscillatory stress $\sigma = \sigma_0 \sin \omega t$, with $\sigma_0 \ll \sigma_y = C/q$. Under these conditions we can compare the magnitude of the terms on the right hand side of Eqn. B.1 and since $qA \ll 1$ we can ignore the second term. As a result, A can be approximated by the following differential equation:

$$\dot{A} \simeq \dot{\gamma}^p \tag{B.16}$$

For small oscillatory stresses, we therefore have $A \simeq \gamma^p$. Inserting this (and the expression $\sigma = \sigma_0 \sin \omega t$) into Eqn. B.15 then gives the following first order linear ODE:

$$\dot{\gamma}^p + \frac{C}{k}\gamma^p = \frac{\sigma_0}{k} \sin \omega t \tag{B.17}$$

The above equation can easily be solved using an integrating factor, allowing us to arrive at the following expression for $\gamma(t)$:

$$\gamma = \sigma_0 \left(\frac{1}{G} + \frac{C}{C^2 + k^2\omega^2}\right) \sin \omega t + \sigma_0 \left(\frac{-k\omega}{C^2 + k^2\omega^2}\right) \cos \omega t \tag{B.18}$$

Note that in the above expression, we provide the total strain $\gamma = \gamma^e + \gamma^p$, so a term with the elastic modulus G enters into the equation (and this term is in phase with the driving sinusoidal stress). The coefficients of the sine and cosine terms in the parentheses in Eqn. B.18 above are the linear compliances $J'(\omega)$ and $J''(\omega)$ respectively. These can be converted to the linear viscoelastic moduli $G'(\omega)$ and

$G''(\omega)$ [77], giving the following expressions:

$$G'(\omega) = \frac{GC^2 + Gk^2\omega^2 + G^2C}{G^2 + C^2 + 2GC + k^2\omega^2} \tag{B.19}$$

$$G''(\omega) = \frac{G^2k\omega}{C^2 + k^2\omega^2 + 2GC + G^2} \tag{B.20}$$

The expressions for $G'(\omega)$ and $G''(\omega)$ above are the same as those for a standard 3-parameter viscoelastic model, with a spring (with modulus G) in series with a Kelvin element (with a spring with modulus C and a dashpot with viscosity coefficient k). The KH model for $m = 1$ essentially reduces to this linear viscoelastic model for small deformations.

B.2.2 Case where $m < 1$

We again impose an oscillatory stress $\sigma = \sigma_0 \sin \omega t$, with $\sigma_0 \ll \sigma_y = C/q$. We seek a linear solution for the plastic strain rate γ^p of the following form:

$$\gamma^p = \gamma_0 \sin(\omega t + \delta) = a_1 \sin \omega t + b_1 \cos \omega t \tag{B.21}$$

Where γ_0 is the magnitude of the plastic strain and δ is a phase angle. The constants a_1 and b_1 are related to γ_0 and δ through the trigonometric identity for sine. The time derivative of this solution $\dot{\gamma}^p = \omega\gamma_0 \cos(\omega t + \delta)$. The solution can also be inserted into Eqn. B.15 and this can be compared with the time derivative of Eqn. B.21.

$$\omega\gamma_0 \cos(\omega t + \delta) \underbrace{=}_{?} \left(\frac{|\sigma_0 \sin \omega t - C\gamma_0 \sin(\omega t + \delta)|}{k} \right)^{1/m} \text{sign}\left(\sigma_0 \sin \omega t - C\gamma_0 \sin(\omega t + \delta)\right) \tag{B.22}$$

Note that the equality above does not strictly hold, because the term on the left hand side is a phase shifted sinusoidal wave, while the term on the right hand size is a periodic waveform distorted from a pure sinusoid due to the presence of the $1/m$ exponent. In the limit of $m \to \infty$, the periodic function on the right will approach a square waveform.

Nonetheless, we can reach an approximate solution by equating the phase and

amplitude of these waveforms. This will provide two equations which will allow us to determine expressions for δ and γ_0 (which can in turn be used to obtain G' and G'').

$$\sqrt{\omega^2 a_1^2 + \omega^2 b_1^2} = \left(\frac{\sqrt{(\sigma_0 - Ca_1)^2 + (Cb_1)^2}}{k} \right)^{1/m} \qquad \text{(Equating the amplitudes)} \tag{B.23}$$

$$\frac{\sigma_0 - Ca_1}{-Cb_1} = \frac{-b_1}{a_1} \qquad \text{(Equating the phases)} \tag{B.24}$$

With Eqns. B.23 and B.24 above we can, in principle, solve for a_1 and b_1, and in turn use those expressions to determine the linear viscoelastic moduli. However, due to the presence of the $1/m$ exponent in Eqn. B.23, an analytical solution has eluded us.

B.2.3 Increasing the strain amplitude - G' and G'' under LAOStrain

For larger strain amplitudes, higher harmonics begin to arise in the periodic stress waveform in the material, and the linear viscoelastic moduli will not be sufficient to characterize the material response. G' and G'' will also begin to vary as a function of the strain amplitude. In Fig. B-1 below, we plot G' and G'' as a function of strain amplitude γ_0 for the KH model (simulated with the same fitting parameters used for the Carbopol microgel in Chap. 6, at a frequency of $\omega = 1$ rad/s). The predicted values of G' and G'' for the KH model are overlaid on measured values of G' and G'' for the same Carobopol microgel that was studied in Chap. 6. The KH model predicts the signature change of G' and G'' that is exhibited by this microgel, and many other EVP materials as they begin to yield at larger strains [180, 181]. Specifically, G' plateaus at low strain amplitudes and decreases monotonically at larger amplitudes. G'' on the other hand, exhibits an overshoot at the point where it crosses over with G', and then monotonically decreases. The crossover point where G'' becomes larger than G' is frequently labeled as a yield strain, as it indicates the point where the material transitions from a primarily solid-like behavior to a primarily liquid-like behavior.

The expressions in Eq. B.23 and B.24 have not provided us with analytical forms for G' and G'' for small values of γ_0, However, when Fig. B-1 is expanded to lower values of γ_0, we observe $G' \to G$ and $G'' \to 0$ as $\gamma_0 \to 0$. For the case where $m = 1$ however, G'' will approach a nonzero value as $\gamma_0 \to 0$ (and the expression for this value is given in Eq. B.20).

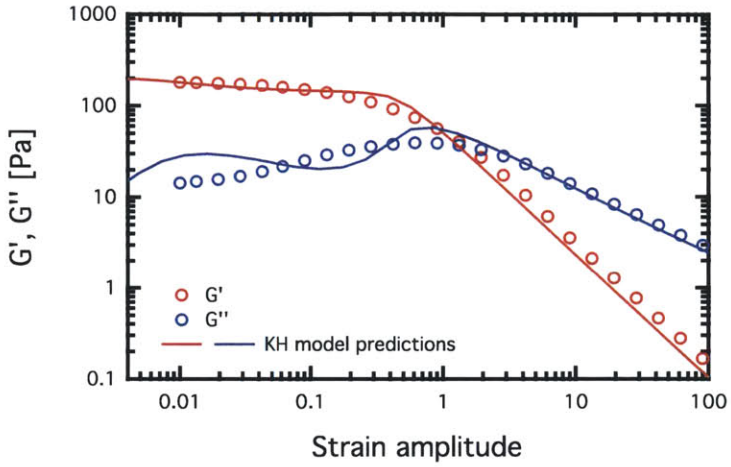

Figure B-1: G' and G'' measured for Carbopol as a function of γ_0, and determined for the KH model through numerical simulations. The KH model parameters used are $m = 0.43$, $G = 350$ Pa, $k = 23$ Pa.s^m, $C = 540$ Pa, $q = 12$.

The only disagreement between the KH model and the experimental data occurs at low strain amplitudes, where the KH model overestimates the value of G''. However, it still predicts a value of G'' which is a factor of 3 lower than G'. This is indicative of a material response that is primarily elastic. For the case where $m < 1$, the KH model also predicts that $G'' \to 0$ as $\gamma_0 \to 0$. This means that strictly speaking, in the linear viscoelastic regime the material behaves as an elastic solid with modulus G. To prevent this from occurring, one can modify the relationship specifying the rate of plastic flow $|\dot{\gamma}^p|$ to the following:

$$|\dot{\gamma}^p| = \left(\frac{|\sigma - \sigma_{\text{back}}|}{k} \right)^{(1/m)} + \left(\frac{|\sigma - \sigma_{\text{back}}|}{\eta} \right) , \tag{B.25}$$

where η is a large, Newtonian viscosity parameter. The second term in Eq. B.25 above allows for a small amount of linear viscous flow to occur at vanishingly small

strain amplitudes. This in turn results in a nonzero value of G'' as $\gamma_0 \to 0$.

Bibliography

[1] J. M. Adams, S. M. Fielding, and P. D. Olmsted. The interplay between boundary conditions and flow geometries in shear banding: Hysteresis, band configurations, and surface transitions. *Journal of Non-Newtonian Fluid Mechanics*, 151(1-3):101 – 118, 2008.

[2] J. M. Adams and P. D. Olmsted. Nonmonotonic Models are Not Necessary to Obtain Shear Banding Phenomena in Entangled Polymer Solutions. *Physical Review Letters*, 102(6), 2009.

[3] R. J. Adrian. Particle-Imaging techniques for experimental fluid-mechanics. *Annual Review of Fluid Mechanics*, 23:261–304, 1991.

[4] R. J. Adrian. Twenty years of particle image velocimetry. *Experiments in Fluids*, 39:159–169, 2005.

[5] R. J. Adrian and J. Westerweel. *Particle Image Velocimetry.* Cambridge, 2011.

[6] E. C. Aifantis. The physics of plastic deformation. *International Journal of Plasticity*, 3(3):211–247, 1987.

[7] A. Aiyejina, D. P. Chakrabarti, A. Pilgrim, and M. Sastry. Wax formation in oil pipelines: A critical review. *International Journal of Multiphase Flow*, 37(7):671 – 694, 2011.

[8] K. Akbarzadeh, A. Hammami, A. Kharrat, D. Zhang, S. Allenson, J. Creek, S. Kabir, A. J. Jamaluddin, A. G. Marshall, R. P. Rodgers, O. C. Mullins, and T. Solbakken. Asphaltenes - problematic but rich in potential. *Schlumberger Oilfield Review*, 19(2):22–43, 2007.

[9] S. Ali, D. Norman, D. Wagner, J. Ayoub, J. Desroches, H. Morales, P. Prince, D. Shepherd, E. Toffanin, J. Troscoso, and S. White. Combined stimulation and sand control. *Schlumberger Oilfield Review*, 14(2):30–47, 2002.

[10] N. M. Ames, V. Srivastava, S. Chester, and L. Anand. A thermo-mechanically coupled theory for large deformations of amorphous polymers. Part II: Applications. *International Journal of Plasticity*, 25(8):1495–1539, 2009.

[11] L. Anand, N. M. Ames, V. Srivastava, and S. Chester. A thermo-mechanically coupled theory for large deformations of amorphous polymers. Part I: Formulation. *International Journal of Plasticity*, 25(8):1474–1494, 2008.

[12] C. A. Angell. Formation of Glasses from Liquids and Biopolymers. *Science*, 267(5206):1924–1935, 1995.

[13] P. J. Armstrong and C. O. Frederick. A mathematical representation of the multiaxial Bauschinger effect. *Materials at High Temperatures*, 24:1–26, 1966.

[14] K. Atalik and R. Keunings. On the occurrence of even harmonics in the shear stress response of viscoelastic fluids in large amplitude oscillatory shear. *Journal of Non-Newtonian Fluid Mechanics*, 122(1-3):107–116, 2004.

[15] P. Ballesta, R. Besseling, L. Isa, G. Petekidis, and W. C. K. Poon. Slip and Flow of Hard-Sphere Colloidal Glasses. *Physical Review Letters*, 101(25), 2008.

[16] H. A. Barnes. A review of the slip (wall depletion) of polymer solutions, emulsions and particle suspensions in viscometers: its cause, character, and cure. *Journal of Non-Newtonian Fluid Mechanics*, 56(3):221–251, 1995.

[17] H. A. Barnes. Thixotropy - A review. *Journal of Non-Newtonian Fluid Mechanics*, 70(1-2):1–33, 1997.

[18] H. A. Barnes. The yield stress–a review of $\pi\alpha\nu\tau\alpha\ \rho\epsilon\iota$–everything flows? *Journal of Non-Newtonian Fluid Mechanics*, 81(1-2):133 – 178, 1999.

[19] H. A. Barnes, J. F. Hutton, and K. Walters. *An introduction to Rheology*. Elsevier, 1989.

[20] H. A. Barnes and K. Walters. The yield stress myth. *Rheologica Acta*, 24(4):323–32x, 1985.

[21] Q. Barral, G. Ovarlez, X. Chateau, J. Boujlel, B. Rabideau, and P. Coussot. Adhesion of yield stress fluids. *Soft Matter*, 6(6):1343–1351, 2010.

[22] J. Bauschinger. Über die veränderung der position der elastizitätsgrenze des eisens und stahls durch strecken und quetschen und durch erwärmen und abkühlen und durch oftmals wiederholte beanspruchungen. *Mitteilung aus dem Mechanisch-technischen Laboratorium der Königlichen polytechnischen Hoschschule in München*, 13:1–115, 1886.

[23] L. Bécu, S. Manneville, and A. Colin. Spatiotemporal dynamics of wormlike micelles under shear. *Physical Review Letters*, 93(1):018301, 2004.

[24] J.-F. Berret. Transient rheology of wormlike micelles. *Langmuir*, 13(8):2227–2234, 1997.

[25] J.-F. Berret, D. C. Roux, and G. Porte. Isotropic-to-nematic transition in wormlike micelles under shear. *Journal de Physique II*, 4(8):1261–1279, 1994.

[26] V. Bertola, F. Bertrand, H. Tabuteau, D. Bonn, and P. Coussot. Wall slip and yielding in pasty materials. *Journal of Rheology*, 47(5):1211–1226, 2003.

[27] S. Betancourt, T. Davies, R. Kennedy, C. Dong, H. Elshahawi, O. C. Mullins, J. Nighswander, and M. O'Keefe. Advancing fluid-property measurements. *Schlumberger Oilfield Review*, 19(3):56–70, 2007.

[28] E. C. Bingham. An investigation of the laws of plastic flow. *U.S. Bureau of Standards Bulletin*, 13:309–353, 1916.

[29] R. B. Bird, R. C. Armstrong, and O. Hassager. *Dynamics of Polymeric Liquids Vol. 1.* John Wiley and Sons, second edition, 1987.

[30] B. Bloys, N. Davis, B. Smolen, L. Bailey, O. Houwen, P. Reid, J. Sherwood, L. Fraser, and M. Hodder. Designing and managing drilling fluid. *Schlumberger Oilfield Review*, 6(2):33–43, 1994.

[31] L. Bocquet, A. Colin, and A. Ajdari. Kinetic theory of plastic flow in soft glassy materials. *Physical Review Letters*, 103(3), 2009.

[32] P. Boltenhagen, Y. Hu, E. F. Matthys, and D. J. Pine. Observation of bulk phase separation and coexistence in a sheared micellar solution. *Physical Review Letters*, 79(12), 1997.

[33] P. E. Boukany and S.-Q. Wang. Use of particle-tracking velocimetry and flow birefringence to study nonlinear flow behavior of entangled wormlike micellar solution: From wall slip, bulk disentanglement to chain scission. *Macromolecules*, 41(4):1455–1464, 2008.

[34] P. E. Boukany and S.-Q. Wang. Exploring the transition from wall slip to bulk shearing banding in well-entangled DNA solutions. *Soft Matter*, 5(4):780–789, 2009.

[35] K. Breuer. *Microscale Diagnostic Techniques*, section 2.5.3, pages 70–73. Springer, 2005.

[36] M. M. Britton and P. T. Callaghan. Two-phase shear band structures at uniform stress. *Physical Review Letters*, 78(26):4930–4933, 1997.

[37] M. M. Britton and P. T. Callaghan. Shear banding instability in wormlike micellar solutions. *European Physical Journal B*, 7(2), 1999.

[38] A. Calin, M. Wilhelm, and C. Balan. Determination of the non-linear parameter (mobility factor) of the Giesekus constitutive model using LAOS procedure. *Journal of Non-Newtonian Fluid Mechanics*, 165(23–24):1564 – 1577, 2010.

[39] P. Callaghan. Rheo NMR and shear banding. *Rheologica Acta*, 47:243–255, 2008. 10.1007/s00397-007-0251-2.

[40] C. J. Campbell and J. H. Laherrere. The end of cheap oil. *Scientific American*, 278(6), 1998.

[41] J. O. Carnali and M. S. Naser. The use of dilute solution viscometry to characterize the network properties of carbopol microgels. *Colloid & Polymer Science*, 270:183–193, 1992.

[42] M. E. Cates and S. M. Fielding. Rheology of giant micelles. *Advances in Physics*, 55(7):799 – 879, 2006.

[43] M. Cawkwell and M. Charles. Characterization of canadian arctic thixotropic gelled oils utilizing an eight parameter model. *Journal of Pipelines*, 7:251–256, 1989.

[44] M. G. Cawkwell and M. E. Charles. An improved model for start-up of pipelines containing gelled crude-oil. *Journal of Pipelines*, 7(1):41–52, 1987.

[45] C. Chang, D. V. Boger, and Q. D. Nguyen. Yielding of waxy crude oils. *Industrial and Engineering Chemistry*, 37:1551–1559, 1998.

[46] C. Chang, O. Nguyen, and H. Ronningsen. Isothermal start-up of pipeline transporting waxy crude oil. *Journal of Non-Newtonian Fluid Mechanics*, 87(2-3):127–154, 1999.

[47] A. Chawathe, U. Ozdogan, K. S. Glaser, Y. Jalali, and M. Riding. A plan for success in deep water. *Schlumberger Oilfield Review*, 21(1):26–35, 2009.

[48] D. C.-H. Cheng. Yield stress: A time-dependent property and how to measure it. *Rheologica Acta*, 25:542–554, 1986.

[49] W. C. Chin. Modern flow assurance methods: clogged pipelines, wax deposition, hydrate plugs. *Offshore*, 60(9):92, 2000.

[50] K. S. Cho, K. Hyun, K. H. Ahn, and S. J. Lee. A geometrical interpretation of large amplitude oscillatory shear response. *Journal of Rheology*, 49(3):747–758, 2005.

[51] P. Coussot, A. I. Leonov, and J. M. Piau. Rheology of concentrated dispersed systems in a low molecular weight matrix. *Journal of Non-Newtonian Fluid Mechanics*, 46(2–3):179–217, 1993.

[52] P. Coussot, Q. D. Nguyen, H. T. Huynh, and D. Bonn. Avalanche behavior in yield stress fluids. *Physical Review Letters*, 88(128302), 2002.

[53] P. Coussot, Q. D. Nguyen, H. T. Huynh, and D. Bonn. Viscosity bifurcation in thixotropic, yielding fluids. *Journal of Rheology*, 46(3):573–589, May 2002.

[54] P. Coussot, J. S. Raynaud, F. Bertrand, P. Moucheront, J. P. Guilbaud, H. T. Huynh, S. Jarny, and D. Lesueur. Coexistence of liquid and solid phases in flowing soft-glassy materials. *Physical Review Letters*, 88(21):218301, 2002.

[55] P. Coussot, L. Tocquer, C. Lanos, and G. Ovarlez. Macroscopic vs. local rheology of yield stress fluids. *Journal of Non-Newtonian Fluid Mechanics*, 158(1-3, Sp. Iss. SI):85–90, 2009.

[56] C. J. Davies, A. J. Sederman, C. J. Pipe, G. H. McKinley, L. F. Gladden, and M. L. Johns. Rapid measurement of transient velocity evolution using gervais. *Journal of Magnetic Resonance*, 202(1):93 – 101, 2010.

[57] D. De Kee and C. F. Chan Man Fong. Rheological properties of structured fluids. *Polymer Engineering & Science*, 34(5):438–445, 1994.

[58] P. R. de Souza Mendes. Thixotropic elasto-viscoplastic model for structured fluids. *Soft Matter*, 7:2471–2483, 2011.

[59] P. R. de Souza Mendes and R. L. Thompson. A critical overview of elasto-viscoplastic thixotropic modeling. *Journal of Non-Newtonian Fluid Mechanics*, 187–188:8–15, 2012.

[60] M. Denn. Extrusion instabilities and wall slip. *Annual Review of Fluid Mechanics*, 33:265–287, 2001.

[61] J. A. Dijksman, G. H. Wortel, L. T. H. van Dellen, O. Dauchot, and M. van Hecke. Jamming, yielding, and rheology of weakly vibrated granular media. *Physical Review Letters*, 107, 2011.

[62] T. Divoux, C. Barentin, and S. Manneville. From stress-induced fluidization processes to herschel-bulkley behaviour in simple yield stress fluids. *Soft Matter*, 7:8409–8418, 2011.

[63] T. Divoux, C. Barentin, and S. Manneville. Stress overshoot in a simple yield stress fluid: An extensive study combining rheology and velocimetry. *Soft Matter*, 7:9335–9349, 2011.

[64] T. Divoux, D. Tamarii, C. Barentin, and S. Manneville. Transient shear banding in a simple yield stress fluid. *Physical Review Letters*, 104(20):208301, 2010.

[65] D. Doraiswamy, A. N. Mujumdar, I. Tsao, A. N. Beris, S. C. Danforth, and A. B. Metzner. The cox–merz rule extended: A rheological model for concentrated suspensions and other materials with a yield stress. *Journal of Rheology*, 35(4):647–685, 1991.

[66] K. Dullaert and J. Mewis. Thixotropy: Build-up and breakdown curves during flow. *Journal of Rheology*, 49(6):1–18, 2005.

[67] K. Dullaert and J. Mewis. A structural kinetics model for thixotropy. *Journal of Non-Newtonian Fluid Mechanics*, 139(1–2):21–30, 2006.

[68] C. Eisenmann, C. Kim, J. Mattsson, and D. A. Weitz. Shear Melting of a Colloidal Glass. *Physical Review Letters*, 104(3), 2010.

[69] R. H. Ewoldt. *Nonlinear viscoelastic materials: bioinspired applications and new characterization measures.* PhD thesis, Massachusetts Institute of Technology, 2009.

[70] R. H. Ewoldt, C. Clasen, A. E. Hosoi, and G. H. McKinley. Rheological fingerprinting of gastropod pedal mucus and synthetic complex fluids for biomimicking adhesive locomotion. *Soft Matter*, 3(5):634–643, 2007.

[71] R. H. Ewoldt, A. E. Hosoi, and G. H. McKinley. New measures for characterizing nonlinear viscoelasticity in large amplitude oscillatory shear. *Journal of Rheology*, 52(6):1427–1458, 2008.

[72] R. H. Ewoldt and G. H. McKinley. On secondary loops in laos via self-intersection of Lissajous–Bowditch curves. *Rheologica Acta*, 49:213–219, 2010.

[73] R. H. Ewoldt, P. Winter, J. Maxey, and G. H. McKinley. Large amplitude oscillatory shear of pseudoplastic and elastoviscoplastic materials. *Rheological Acta*, 49(2):191–212, 2010.

[74] M. A. Fardin, B. Lasne, O. Cardoso, G. Grégoire, M. Argentina, J. P. Decruppe, and S. Lerouge. Taylor-like vortices in shear-banding flow of giant micelles. *Phys. Rev. Lett.*, 103(2):028302, Jul 2009.

[75] M. A. Fardin, D. Lopez, J. Croso, G. Grégoire, O. Cardoso, G. H. McKinley, and S. Lerouge. Elastic turbulence in shear banding wormlike micelles. *Phys. Rev. Lett.*, 104(17):178303, 2010.

[76] K. Feindel and P. Callaghan. Anomalous shear banding: multidimensional dynamics under fluctuating slip conditions. *Rheologica Acta*, 49:1003–1013, 2010.

[77] J. D. Ferry. *Viscoelastic Properties of Polymers.* John Wiley and Sons, third edition, 1980.

[78] S. M. Fielding, M. E. Cates, and P. Sollich. Shear banding, aging and noise dynamics in soft glassy materials. *Soft Matter*, 5(12):2378–2382, 2009.

[79] S. M. Fielding, P. Sollich, and M. E. Cates. Aging and rheology in soft materials. *Journal of Rheology*, 44(2):323–369, 2000.

[80] S. N. Ganeriwala and C. A. Rotz. Fourier transform mechanical analysis for determining the nonlinear viscoelastic properties of polymers. *Polymer Engineering & Science*, 27(2):165–178, 1987.

[81] P. Gao, J. Zhang, and G. Ma. Direct image-based fractal characterization of morphologies and structures of wax crystals in waxy crude oils. *Journal of Physics - Condensed Matter*, 18(50):11487–11506, 2006.

[82] E. Ghanaei and D. Mowla. Prediction of waxy oil rheology by a new model. *Energy & Fuels*, 24(3):1762–1770, 2010.

[83] A. J. Giacomin, R. B. Bird, L. M. Johnson, and A. W. Mix. Large-amplitude oscillatory shear flow from the corotational Maxwell model. *Journal of Non-Newtonian Fluid Mechanics*, 166(19–20):1081–1099, 2011.

[84] A. J. Giacomin, R. S. Jeyaseelan, T. Samurkas, and J. M. Dealy. Validity of separable BKZ model for large amplitude oscillatory shear. *Journal of Rheology*, 37(5):811–826, 1993.

[85] T. Gibaud, C. Barentin, and S. Manneville. Influence of boundary conditions on yielding in a soft glassy material. *Physical Review Letters*, 101(25), 2008.

[86] T. Gibaud, C. Barentin, N. Taberlet, and S. Manneville. Shear-induced fragmentation of laponite suspensions. *Soft Matter*, 5(16):3026–3037, 2009.

[87] T. Gibaud, D. Frelat, and S. Manneville. Heterogeneous yielding dynamics in a colloidal gel. *Soft Matter*, 6:3482–3488, 2010.

[88] R. Glowinski and A. Wachs. On the numerical simulation of viscoplastic fluid flow. *Handbook of Numerical Analysis*, 16:483–717, 2011.

[89] J. D. Goddard. Material instability in complex fluids. *Annual Review of Fluid Mechanics*, 35(1):113–133, 2003.

[90] J. Goyon, A. Colin, G. Ovarlez, A. Ajdari, and L. Bocquet. Spatial cooperativity in soft glassy flows. *Nature*, 454(7200):84–87, 2008.

[91] M. Graham. Wall slip and the nonlinear dynamics of large-amplitude oscillatory shear flows. *Journal of Rheology*, 39(4):697–712, 1995.

[92] A. K. Gurnon and N. J. Wagner. Large amplitude oscillatory shear (LAOS) measurements to obtain constitutive equation model parameters: Giesekus model of banding and nonbanding wormlike micelles. *Journal of Rheology*, 56(2):333–351, 2012.

[93] M. Gurtin, E. Fried, and L. Anand. *The Mechanics and Thermodynamics of Continua*. Cambridge, 2010.

[94] S. G. Hatzikiriakos and J. M. Dealy. Wall Slip of Molten High-Density Polyethylenes .2. Sliding Rheometer Studies. *Journal of Rheology*, 35(4):497–523, 1991.

[95] M. E. Helgeson, P. A. Vasquez, E. W. Kaler, and N. J. Wagner. Rheology and spatially resolved structure of cetyltrimethylammonium bromide wormlike micelles through the shear banding transition. *Journal of Rheology*, 53(3):727–756, 2009.

[96] D. L. Henann and L. Anand. A large deformation theory for rate-dependent elastic–plastic materials with combined isotropic and kinematic hardening. *International Journal of Plasticity*, 25(10):1833 – 1878, 2009.

[97] W. H. Herschel and T. Bulkley. Measurement of consistency as applied to rubber-benzene solutions. *Am. Soc. Test Proc.*, 26(2):621–633, 1926.

[98] A. Hess and N. Aksel. Yielding and structural relaxation in soft materials: Evaluation of strain-rate frequency superposition data by the stress decomposition method. *Phys. Rev. E*, 84, 2011.

[99] Y. T. Hu. Steady-state shear banding in entangled polymers? *Journal of Rheology*, 54(6):1307–1323, 2010.

[100] Y. T. Hu, P. Boltenhagen, and D. J. Pine. Shear thickening in low-concentration solutions of wormlike micelles. I. direct visualization of transient behavior and phase transitions. *Journal of Rheology*, 42(5):1185–1208, 1998.

[101] Y. T. Hu, C. Palla, and A. Lips. Comparison between shear banding and shear thinning in entangled micellar solutions. *Journal of Rheology*, 52(2):379–400, 2008.

[102] M. K. Hubbert. Energy From Fossil Fuels. *Science*, 109(2823):103–109, 1949.

[103] K. Hyun, M. Wilhelm, C. O. Klein, K. S. Cho, J. G. Nam, K. H. Ahn, S. J. Lee, R. H. Ewoldt, and G. H. McKinley. A review of nonlinear oscillatory shear tests: Analysis and application of large amplitude oscillatory shear (LAOS). *Progress in Polymer Science*, 36(12):1697–1753, 2011.

[104] Y. W. Inn, K. F. Wissbrun, and M. M. Denn. Effect of edge fracture on constant torque rheometry of entangled polymer solutions. *Macromolecules*, 38(22):9385–9388, 2005.

[105] Y. Jiang and P. Kurath. Characteristics of the Armstrong-Frederick type plasticity models. *International Journal of Plasticity*, 12(3):387 – 415, 1996.

[106] M. W. Johnson Jr. and D. Segalman. A model for viscoelastic fluid behavior which allows non-affine deformation. *Journal of Non-Newtonian Fluid Mechanics*, 2(3):255–270, 1977.

[107] C. Kalelkar, A. Lele, and S. Kamble. Strain-rate frequency superposition in large-amplitude oscillatory shear. *Physical Review E*, 81, 2010.

[108] M. Kanè, M. Djabourov, and J. Volle. Rheology and structure of waxy crude oils in quiescent and under shearing conditions. *Fuel*, 83(11-12):1591–1605, 2004.

[109] M. Kanè, M. Djabourov, J.-L. Volle, J.-P. Lechaire, and G. Frebourg. Morphology of paraffin crystals in waxy crude oils cooled in quiescent conditions and under flow. *Fuel*, 82:127–135, 2002.

[110] M. Keentok and S. Xue. Edge fracture in cone-plate and parallel plate flows. *Rheologica Acta*, 38(4):321–348, 1999.

[111] R. J. Ketz, R. K. Prud'homme, and W. W. Graessley. Rheology of concentrated microgel solutions. *Rheologica Acta*, 27:531–539, 1988.

[112] A. S. Khan and S. Huang. *Continuum Theory of Plasticity.* Wiley, 1995.

[113] C. O. Klein, H. W. Spiess, A. Calin, C. Balan, and M. Wilhelm. Separation of the nonlinear oscillatory response into a superposition of linear, strain hardening, strain softening, and wall slip response. *Macromolecules*, 40(12):4250–4259, 2007.

[114] E. Kroner. Allgemeine kontinuumstheorie der versetzungen und eigenspannungen. *Archive for Rational Mechanics and Analysis*, 4:273–334, 1960.

[115] P. Kundu and I. Cohen. *Fluid Mechanics.* Academic Press, 2008.

[116] R. G. Larson. Instabilities in viscoelastic flows. *Rheologica Acta*, 31:213–263, 1992.

[117] R. G. Larson. *The Structure and Rheology of Complex Fluids.* Oxford University Press, ninth edition, 1999.

[118] J. Läuger and H. Stettin. Differences between stress and strain control in the non-linear behavior of complex fluids. *Rheologica Acta*, 49:909–930, 2010.

[119] H. S. Lee, P. Singh, W. H. Thomason, and H. S. Fogler. Waxy oil gel breaking mechanisms: Adhesive versus cohesive failure. *Energy and Fuels*, 22(1):480–487, 2008.

[120] J. Lemaitre and J.-L. Chaboche. *Mechanics of Solid Materials.* Cambridge, 1990.

[121] S. Lerouge and J.-F. Berret. Shear-induced transitions and instabilities in surfactant wormlike micelles. In K. Dusek and J.-F. Joanny, editors, *Polymer Characterization*, volume 230 of *Advances in Polymer Science*, pages 1–71. Springer Berlin / Heidelberg, 2010.

[122] M. P. Lettinga and S. Manneville. Competition between Shear Banding and Wall Slip in Wormlike Micelles. *Physical Review Letters*, 103(24), 2009.

[123] X. Li, S.-Q. Wang, and X. Wang. Nonlinearity in large amplitude oscillatory shear (LAOS) of different viscoelastic materials. *Journal of Rheology*, 53(5):1255–1274, 2009.

[124] M. R. Lopez-Gonzalez, W. M. Holmes, and P. T. Callaghan. Rheo-nmr phenomena of wormlike micelles. *Soft Matter*, 2:855–869, 2006.

[125] C. W. Macosko. *Rheology:Principles, Measurements, and Applications.* Wiley, 1994.

[126] W. C. MacSporran and R. P. Spiers. The dynamic performance of the weissenberg rheogoniometer iii. large amplitude oscillatory shearing — harmonic analysis. *Rheologica Acta*, 23:90–97, 1984.

[127] F. Mahaut, X. Chateau, P. Coussot, and G. Ovarlez. Yield stress and elastic modulus of suspensions of noncolloidal particles in yield stress fluids. *Journal of Rheology*, 52(1):287–313, 2008.

[128] S. Manneville. Recent experimental probes of shear banding. *Rheologica Acta*, 47:301–318, 2008.

[129] S. Manneville, L. Bécu, P. Grondin, and A. Colin. High-frequency ultrasonic imaging: A spatio-temporal approach of rheology. *Colloids and Surfaces A: Physicochemical and Engineering Aspects*, 270-271:195 – 204, 2005. Liquids and MesoScience.

[130] S. Manneville, J.-B. Salmon, L. Bécu, A. Colin, and F. Molino. Inhomogeneous flows in sheared complex fluids. *Rheologica Acta*, 43:408–416, 2004.

[131] S. Manneville, J.-B. Salmon, and A. Colin. A spatio-temporal study of rheo-oscillations in a sheared lamellar phase using ultrasound. *The European Physical Journal E: Soft Matter and Biological Physics*, 13:197–212, 2004.

[132] F. H. Marchesini, A. A. Alicke, P. R. de Souza Mendes, and C. M. Ziglio. Rheological characterization of waxy crude oils: Sample preparation. *Energy & Fuels*, 26(5):2566–2577, 2012.

[133] B. M. Marín-Santibáñez, J. Pérez-González, L. de Vargas, F. Rodríguez-González, and G. Huelsz. Rheometrypiv of shear-thickening wormlike micelles. *Langmuir*, 22(9):4015–4026, 2006.

[134] L. Martinie, H. Buggisch, and N. Willenbacher. Apparent elongational yield stress of soft matter. *Journal of Rheology*, 57(2):627–646, 03 2013.

[135] C. Masselon, A. Colin, and P. D. Olmsted. Influence of boundary conditions and confinement on nonlocal effects in flows of wormlike micellar systems. *Physical Review E*, 81(2):021502, 2010.

[136] C. Masselon, J.-B. Salmon, and A. Colin. Nonlocal effects in flows of wormlike micellar solutions. *Physical Review Letters*, 100(3):038301–, 2008.

[137] G. H. McKinley, A. Öztekin, J. A. Byars, and R. A. Brown. Self-similar spiral instabilities in elastic flows between a cone and a plate. *Journal of Fluid Mechanics*, 285:123–164, 1995.

[138] S. P. Meeker, R. T. Bonnecaze, and M. Cloitre. Slip and flow in pastes of soft particles: Direct observation and rheology. *Journal of Rheology*, 48(6):1295–1320, 2004.

[139] S. P. Meeker, R. T. Bonnecaze, and M. Cloitre. Slip and flow in soft particle pastes. *Physical Review Letters*, 92(19):198302, 2004.

[140] A. F. Mendez-Sanchez, J. Perez-Gonzalez, L. de Vargas, J. R. Castrejon-Pita, A. A. Castrejon-Pita, and G. Huelsz. Particle image velocimetry of the unstable capillary flow of a micellar solution. *Journal of Rheology*, 47(6):1455–1466, 2003.

[141] P. Menut, S. Seiffert, J. Sprakel, and D. A. Weitz. Does size matter? elasticity of compressed suspensions of colloidal- and granular-scale microgels. *Soft Matter*, 8:156–164, 2012.

[142] J. Mewis. Thixotropy - a general review. *Journal of Non-Newtonian Fluid Mechanics*, 6(1):1–20, 1979.

[143] J. Mewis and N. J. Wagner. Thixotropy. *Advances in Colloid and Interface Science*, 147–148(0):214–227, 2009.

[144] E. Michel, J. Appell, F. Molino, J. Kieffer, and G. Porte. Unstable flow and non-monotonic flow curves of transient networks. *Journal of Rheology*, 45(6):1465–1477, 2001.

[145] E. Miller and J. P. Rothstein. Transient evolution of shear-banding wormlike micellar solutions. *Journal of Non-Newtonian Fluid Mechanics*, 143(1):22 – 37, 2007.

[146] P. C. F. Møller, A. Fall, and D. Bonn. Origin of apparent viscosity in yield stress fluids below yielding. *Europhysics Letters*, 87(3):38004, 2009.

[147] P. C. F. Møller, A. Fall, V. Chikkadi, D. Derks, and D. Bonn. An attempt to categorize yield stress fluid behavior. *Phil. Trans. R. Soc. A*, 367(1909):5139–5155, 2009.

[148] P. C. F. Møller, J. Mewis, and D. Bonn. Yield stress and thixotropy: on the difficulty of measuring yield stresses in practice. *Soft Matter*, 2(4):274–283, 2006.

[149] P. C. F. Møller, S. Rodts, M. A. J. Michels, and D. Bonn. Shear banding and yield stress in soft glassy materials. *Physical Review E*, 77(4):041507, 2008.

[150] M. Mooney. Explicit formulas for slip and fluidity. *Journal of Rheology*, 2(2):210–222, 04 1931.

[151] F. Moore. The rheology of ceramic slip and bodies. *Transactions of the British Ceramic Society*, 58:470–494, 1959.

[152] A. Mujumdar, A. N. Beris, and A. B. Metzner. Transient phenomena in thixotropic systems. *Journal of Non-Newtonian Fluid Mechanics*, 102(2):157 – 178, 2002.

[153] O. Muránsky, C. J. Hamelin, M. C. Smith, P. J. Bendeich, and L. Edwards. The effect of plasticity theory on predicted residual stress fields in numerical weld analyses. *Computational Materials Science*, 54(0):125–134, 2012.

[154] T. S. K. Ng, G. H. McKinley, and R. H. Ewoldt. Large amplitude oscillatory shear flow of gluten dough: A model power-law gel. *Journal of Rheology*, 55(3):627–654, 2011.

[155] P. Nghe, G. Degré, P. Tabeling, and A. Ajdari. High shear rheology of shear banding fluids in microchannels. *Applied Physics Letters*, 93(20):204102, 2008.

[156] T. J. Ober, J. Soulages, and G. H. McKinley. Spatially resolved quantitative rheo-optics of complex fluids in a microfluidic device. *Journal of Rheology*, 55(5):1–33, 2011.

[157] D. O. Olagunju. Effect of free surface and inertia on viscoelastic parallel plate flow. *Journal of Rheology*, 38(1):151–168, 1994.

[158] P. D. Olmsted. Perspectives on shear banding in complex fluids. *Rheologica Acta*, 47:283–300, 2008.

[159] P. D. Olmsted, O. Radulescu, and C.-Y. D. Lu. Johnson–Segalman model with a diffusion term in cylindrical couette flow. *Journal of Rheology*, 44(2):257–275, 2000.

[160] F. K. Oppong and J. R. de Bruyn. Diffusion of microscopic tracer particles in a yield-stress fluid. *Journal of Non-Newtonian Fluid Mechanics*, 142(1–3):104 – 111, 2007.

[161] G. Ovarlez, Q. Barral, and P. Coussot. Three-dimensional jamming and flows of soft glassy materials. *Nature Materials*, 9(2):115–119, 02 2010.

[162] F. W. Padgett, D. G. Hefley, and A. Henriksen. Wax crystallization - a preliminary report. *Industrial and Engineering Chemistry*, 18(8):832–835, 1926.

[163] K. Paso, T. Kompalla, H. J. Oschmann, and J. Sjöblom. Rheological degradation of model wax-oil gels. *Journal of Dispersion Science and Technology*, 30(4):472–480, 2009.

[164] K. S. Pedersen and H. P. Ronningsen. Effect of precipitated wax on viscosity - A model for predicting non-Newtonian viscosity of crude oils. *Energy & Fuels*, 14(1):43–51, 2000.

[165] T. K. Perkins and J. B. Turner. Starting behavior of gathering lines and pipelines filled with gelled prudhoe bay oil. *Journal of Petroleum Technology*, 23(3):301–308, 1971.

[166] C. J. S. Petrie and M. M. Denn. Instabilities in polymer processing. *AIChE Journal*, 22(2):209–236, 1976.

[167] H. Petter Rønningsen. Rheological behaviour of gelled, waxy north sea crude oils. *Journal of Petroleum Science and Engineering*, 7(3-4):177–213, 1992.

[168] J. M. Piau. Carbopol gels: Elastoviscoplastic and slippery glasses made of individual swollen sponges Meso- and macroscopic properties, constitutive equations and scaling laws. *Journal of Non-Newtonian Fluid Mechanics*, 144(1):1–29, 2007.

[169] F. Pignon, A. Magnin, and J.-M. Piau. Thixotropic colloidal suspensions and flow curves with minimum: Identification of flow regimes and rheometric consequences. *Journal of Rheology*, 40(4):573–587, 1996.

[170] C. J. Pipe, N. J. Kim, P. A. Vasquez, L. P. Cook, and G. H. McKinley. Wormlike micellar solutions: II. comparison between experimental data and scission model predictions. *Journal of Rheology*, 54(4):881–913, 2010.

[171] A. C. Pipkin. *Lectures on Viscoelasticity Theory.* Springer, 1972.

[172] D. J. Plazek. What's wrong with the moduli charley brown? or get the h out and go to l. *Journal of Rheology*, 36(8):1671–1690, 1992.

[173] D. Quemada. Rheological modelling of complex fluids: IV: Thixotropic and "thixoelastic" behaviour. start-up and stress relaxation, creep tests and hysteresis cycles. *The European Physical Journal of Applied Physics*, 5(2):191–207, 1999.

[174] M. Raffel, C. Willert, S. Werely, and J. Kompenhans. *Particle Image Velocimetry, A Practical Guide.* Springer, 2007.

[175] J. Ratulowski, A. Amin, A. Hammami, M. Muhammad, M. Riding, and Schlumberger. Flow assurance and subsea productivity: Closing the loop with connectivity and measurements. In *SPE Annual Technical Conference and Exhibition, 26-29 September 2004, Houston, Texas*, AIP Conference Proceedings. Society of Petroleum Engineers, 2004.

[176] H. Rehage and H. Hoffmann. Viscoelastic surfactant solutions - model systems for rheological research. *Molecular Physics*, 74(5):933–973, 1991.

[177] M. J. Reimers and J. M. Dealy. Sliding plate rheometer studies of concentrated polystyrene solutions: Nonlinear viscoelasticity and wall slip of two high molecular weight polymers in tricresyl phosphate. *Journal of Rheology*, 42(3):527–548, 1998.

[178] G. P. Roberts and H. A. Barnes. New measurements of the flow-curves for Carbopol dispersions without slip artefacts. *Rheologica Acta*, 40:499–503, 2001.

[179] S. A. Rogers. A sequence of physical processes determined and quantified in laos: An instantaneous local 2d/3d approach. *Journal of Rheology*, 56(5):1129–1151, 2012.

[180] S. A. Rogers, P. T. Callaghan, G. Petekidis, and D. Vlassopoulos. Time-dependent rheology of colloidal star glasses. *Journal of Rheology*, 54(1):133–158, 2010.

[181] S. A. Rogers, B. M. Erwin, D. Vlassopoulos, and M. Cloitre. Oscillatory yielding of a colloidal star glass. *Journal of Rheology*, 55(4):733–752, 2011.

[182] S. A. Rogers, B. M. Erwin, D. Vlassopoulos, and M. Cloitre. A sequence of physical processes determined and quantified in LAOS: Application to a yield stress fluid. *Journal of Rheology*, 55(2):435–458, 2011.

[183] S. A. Rogers and M. P. Lettinga. A sequence of physical processes determined and quantified in large-amplitude oscillatory shear (laos): Application to theoretical nonlinear models. *Journal of Rheology*, 56(1):1–25, 2012.

[184] W. B. Russel and M. C. Grant. Distinguishing between dynamic yielding and wall slip in a weakly flocculated colloidal dispersion. *Colloids and Surfaces A: Physicochemical and Engineering Aspects*, 161(2):271–282, 2000.

[185] J.-B. Salmon, A. Colin, S. Manneville, and F. M. C. Molino. Velocity profiles in shear-banding wormlike micelles. *Phys. Rev. Lett.*, 90(22):228303, 2003.

[186] P. Saramito. A new elastoviscoplastic model based on the Herschel–Bulkley viscoplastic model. *Journal of Non-Newtonian Fluid Mechanics*, 158(1-3):154–161, 2009.

[187] V. Schmitt, F. Lequeux, A. Pousse, and D. Roux. Flow behavior and shear induced transition near an isotropic/nematic transition in equilibrium polymers. *Langmuir*, 10(3):955–961, 1994.

[188] J. Sestak, M. E. Charles, M. G. Cawkwell, and M. Houska. Start-up of gelled crude oil pipelines. *Journal of Pipelines*, 6:15–24, 1987.

[189] J. R. Seth, M. Cloitre, and R. T. Bonnecaze. Influence of short-range forces on wall-slip in microgel pastes. *Journal of Rheology*, 52(5):1241–1268, 2008.

[190] V. Sharma, K. Park, and M. Srinivasarao. Colloidal dispersion of gold nanorods: Historical background, optical properties, seed-mediated synthesis, shape separation and self-assembly. *Materials Science & Engineering Reports*, 65(1-3):1–38, 2009.

[191] P. Singh, R. Venkatesan, H. S. Fogler, and N. Nagarajan. Formation and aging of incipient thin film wax-oil gels. *AIChE Journal*, 46(5):1059–1074, 2000.

[192] P. Singh, R. Venkatesan, H. S. Fogler, and N. Nagarajan. Morphological evolution of thick wax deposits during aging. *AIChE Journal*, 47(1):6–18, 2001.

[193] S. Skorski and P. D. Olmsted. Loss of solutions in shear banding fluids driven by second normal stress differences. *Journal of Rheology*, 55(6):1219–1246, 2011.

[194] P. Sollich. Rheological constitutive equation for a model of soft glassy materials. *Physical Review E*, 58:738–759, 1998.

[195] J. G. Speight. *The Chemistry and Technology of Petroleum.* CRC Press, fourth edition, 2007.

[196] C. Sui and G. B. McKenna. Instability of entangled polymers in cone and plate rheometry. *Rheologica Acta*, 46(6):877–888, 2007.

[197] P. Tapadia, S. Ravindranath, and S. Q. Wang. Banding in entangled polymer fluids under oscillatory shearing. *Physical Review Letters*, 96(19):196001, MAY 19 2006.

[198] P. Tapadia and S. Wang. Direct visualization of continuous simple shear in non-newtonian polymeric fluids. *Physical Review Letters*, 96(1):016001, 2006.

[199] E. Toorman. Modelling the thixotropic behaviour of dense cohesive sediment suspensions. *Rheologica Acta*, 36(1):56–65, 1997.

[200] M. Tsoskounogiou, G. Ayerides, and E. Tritopoulou. The end of cheap oil: Current status and prospects. *Energy Policy*, 36(10):3797–3806, 2008.

[201] I. Vardoulakis and E. C. Aifantis. A gradient flow theory of plasticity for granular materials. *Acta Mechanica*, 87(3-4):197–217, 1991.

[202] R. Venkatesan, N. Nagarajan, K. Paso, Y. Yi, A. Sastry, and H. Fogler. The strength of paraffin gels formed under static and flow conditions. *Chemical Engineering Science*, 60(13):3587–3598, 2005.

[203] R. Venkatesan, J. A. Ostlund, H. Chawla, P. Wattana, M. Nyden, and H. S. Fogler. The effect of asphaltenes on the gelation of waxy oils. *Energy and Fuels*, 17(6):1630–1640, 2003.

[204] R. F. G. Visintin, R. Lapasin, E. Vignati, P. D'Antona, and T. P. Lockhart. Rheological behavior and structural interpretation of waxy crude oil gels. *Langmuir*, 21(14):6240–6249, 2005.

[205] R. F. G. Visintin, T. P. Lockhart, R. Lapasin, and P. D'Antona. Structure of waxy crude oil emulsion gels. *Journal of Non-Newtonian Fluid Mechanics*, 149:34–39, 2008.

[206] A. Wachs, G. Vinay, and I. Frigaard. A 1.5d numerical model for the start up of weakly compressible flow of a viscoplastic and thixotropic fluid in pipelines. *Journal of Non-Newtonian Fluid Mechanics*, 159(1–3):81 – 94, 2009.

[207] K. Walters. *Rheometry*. Halsted Press, 1975.

[208] S.-Q. Wang, S. Ravindranath, and P. E. Boukany. Homogeneous shear, wall slip, and shear banding of entangled polymeric liquids in simple-shear rheometry: A roadmap of nonlinear rheology. *Macromolecules*, 44(2):183–190, 2011.

[209] L. T. Wardhaugh and D. V. Boger. Flow Characteristics of Waxy Crude Oils - Application to Pipeline Design. *AIChE Journal*, 37(6):871–885, 1991.

[210] L. T. Wardhaugh and D. V. Boger. The measurement and description of the yielding behavior of waxy crude oil. *Journal of Rheology*, 35(6):301–308, 1991.

[211] M. Wilhelm. Fourier-transform rheology. *Macromolecular Materials and Engineering*, 287(2):83–105, 2002.

[212] M. Wilhelm, D. Maring, and H.-W. Spiess. Fourier-transform rheology. *Rheologica Acta*, 37:399–405, 1998.

[213] H. Winter. The critical gel - The universal material state between liquid and solid. In Borsali, R and Pecora, R, editor, *Structure and Dynamics of Polymer and Colloidal Systems*, pages 439–470, PO Box 17, 3300 AA Dordrecht Netherlands, 2002. NATO, SPRINGER. Conference of the NATO-Advanced-Study-Institute on Structure and Dynamics of Polymer and Colloidal Systems, Les Houches, France, Sep 14-24, 1999.

[214] H. H. Winter and M. Mours. Rheology of polymers near liquid-solid transitions. *Advance in Polymer Science*, 134:165–234, 1997.

[215] B. Yesilata, C. Clasen, and G. H. McKinley. Nonlinear shear and extensional flow dynamics of wormlike surfactant solutions. *Journal of Non-Newtonian Fluid Mechanics*, 133(2-3):73–90, 2006.

[216] A. Yoshimura and R. K. Prudhomme. Wall slip corrections for couette and parallel disk viscometers. *Journal of Rheology*, 32(1):53–67, 1988.

[217] A. S. Yoshimura and R. K. Prud'homme. Response of an elastic bingham fluid to oscillatory shear. *Rheologica Acta*, 26:428–436, 1987.

[218] A. S. Yoshimura and R. K. Prud'homme. Wall slip effects on dynamic oscillatory measurements. *Journal of Rheology*, 32(6):575–584, 1988.

[219] F. Yziquel, P. Carreau, M. Moan, and P. Tanguy. Rheological modeling of concentrated colloidal suspensions. *Journal of Non-Newtonian Fluid Mechanics*, 86(1–2):133 – 155, 1999.

[220] L. Zhou, L. Cook, and G. H. McKinley. Probing shear-banding transitions of the VCM model for entangled wormlike micellar solutions using large amplitude oscillatory shear (LAOS) deformations. *Journal of Non-Newtonian Fluid Mechanics*, 165(21-22):1462 – 1472, 2010.